UNIVERSITY OF SÃO PAULO
SÃO CARLOS INSTITUTE OF CHEMISTRY

Mailde da Silva Ozório

The Role of Dimensionality of Hybrid Organic-Inorganic Perovskites in the Structural, Energetic and Optoelectronic Properties

São Carlos

2022

Mailde da Silva Ozório

The Role of Dimensionality of Hybrid Organic-Inorganic Perovskites in the Structural, Energetic and Optoelectronic Properties

Thesis presented to São Carlos Institute of Chemistry from the University of São Paulo as requisite to obtain the degree of Doctor of Science.

Research area: Physical Chemistry

Supervisor: Prof. Juarez Lopes Ferreira da Silva

São Carlos

2022

Assinatura: 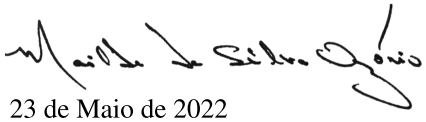

Data: 23 de Maio de 2022

Ficha Catalográfica elaborada pela Seção de Referência e Atendimento ao Usuário do SBI/IQSC

Ozório, Mailde da Silva
The role of dimensionality of hybrid organic-inorganic perovskites in the structural, energetic and optoelectronic properties / Mailde da Silva Ozório. — São Carlos, 2022.
150 f.

Tese (Doutorado em Físico-Química) — Instituto de Química de São Carlos / Universidade de São Paulo, 2022.

Orientador: Prof. Dr. Juarez Lopes Ferreira da Silva

1. Lead-free Perovskites. 2. Tin Perovskites. 3. Zero-dimensional Perovskites. 4. Solar cells. 5. DFT. I. Título.

Wilneide do C. Marchi Maiorano - CRB: 3978/8

It is with genuine gratitude and warm regard that I dedicate this Ph.D. thesis to my parents, Ana Clara and Carlos Antônio.

ACKNOWLEDGEMENTS

I thank my supervisor Prof. Dr. Juarez L. F. Da Silva for the knowledge transmitted and the opinions and criticisms that showed me the correct path to improve this work. I thank my parents and siblings who, even from a distance, supported me on this journey. Thanks to my colleagues Rafael Besse, Julian F. R. V. Silveira, Alexandre C. Dias, Ana Flávia Nogueira, Juarez L. F. Da Silva, Willian X. C. Oliveira, and Srikanth Malladi for the scientific discussions and collaboration in my Ph.D. works. I also thank my colleague Vivianne K. Ocampo Restrepo for the friendly talks we have during my time in the QTNano group. Thanks to the national scientific and technological development council (CNPq) for financial support and also to the Advanced Scientific Computing Laboratory (LCCA) from the University of São Paulo (USP) and the National Computer Laboratory (LNCC) by the computational resources (SDumont), without which it would be impossible to complete this project on time.

I extend my thanks to the professors and staff of the São Carlos Institute of Chemistry (IQSC-USP) for their sympathy and for making the institute pleasant and conducive to learning and scientific production. Thank you all very much!

—

"There is nothing more stimulating than a case where everything goes against you."
Arthur Conan Doyle

ABSTRACT

OZÓRIO, Mailde S. **The Role of Dimensionality of Hybrid Organic-Inorganic Perovskites in the Structural, Energetic and Optoelectronic Properties**. 2022. 150p. Thesis (Doctor of Science) - São Carlos Institute of Chemistry, University of São Paulo, São Carlos, 2022.

Perovskites are promising materials in the optoelectronic field, in particular, as a light-absorbing layer in solar cells. However, stable and non-toxic alternatives for mainstream lead perovskites must be designed for eco-friendly applications. In the quest for lead-free perovskites, we perform three studies: (*i*) the role of $CH(NH_2)_2^+$ (formamidinium), $CH_3PH_3^+$ (methylphosphonium), and $CH_3NH_3^+$ (methylammonium) as *A*-cations on the structural-stability and optoelectronic properties of lead-free $A\mathrm{SnI}_3$ perovskites; (*ii*) the characterization of three novel bismuth zero-dimensional (0D) perovskites, namely, $C_{20}H_{20}N_4Bi_2I_{10}$, $C_{42}H_{39}N_6Bi_2I_9$, and $C_{30}H_{25}N_6BiI_6 \cdot 2\,H_2O$; and (*iii*) the effect of the inorganic complex replacement in the $C_{20}H_{20}N_4B_2X_{10}$ and $C_{30}H_{25}N_6BX_6 \cdot 2\,H_2O$ 0D perovskites, where $B = \{Sb^{3+}, Bi^{3+}\}$ and $X = \{Cl^-, Br^-, I^-\}$. To achieve our goals, we performed density-functional-theory calculations by considering Grimme's D3 van der Waals correction to the PBE exchange-correlation functional. Overall, the anisotropy of *A*-cation yields intrinsic octahedra distortions and also plays a major role in the relative energy of phases. For instance, the dipole-dipole interactions depend on the alignment/orientation of *A*-cations, and can drive the $A\mathrm{SnI}_3$ structures to the lowest energy, and the weak H···I interactions enhance the structural cohesion by increasing the Coulombic attraction between *A*-cations and inorganic framework. The inorganic framework dominates the density of states and band structures around the Fermi level, as well as the optical properties, e.g., the absorption curves, suggest that conventional perovskite structure (cubic, tetragonal, and orthorhombic 3D corner-sharing SnI_6 octahedra) harvest a wider range of solar energy than the low-dimensional structures, which display all wide optical bandgap energy and are not suitable as harvesting materials for solar cells. Regarding the three novel 0D perovskites, the most significant transitions occur inside the octahedra, which probably justifies the similar optical responses. The 0D perovskites display a greater degree of structural deformation of octahedra as the number of shared iodides increases, an aspect corroborated by theoretical-experimental data. Overall, the band structures of 0D perovskites are very flat, and spin-orbit coupling is more significant for the I-based systems. By considering $C_{20}H_{20}N_4B_2X_{10}$ and $C_{30}H_{25}N_6BX_6 \cdot 2\,H_2O$ as model, we identified a more expressive effect of X than B on both structural and the electronic properties, where the valence band is largely determined by the X *p*-states, and the bandgap decrease as Cl^- is replaced with Br^-, and then I^-.

Keywords: Lead-free perovskites, Tin perovskites, Zero-dimensional perovskites.

RESUMO

OZÓRIO, Mailde S. **O papel da dimensionalidade de Perosvkitas Híbridas Orgânicas-Inorgânicas nas Propriedades Estruturais, Energéticas e Optoeletrônicas**. 2022. 150p. Tese (Doutorado em Ciências) - Instituto de Química de São Carlos, Universidade de São Paulo, São Carlos, 2022.

Perovskitas são materiais promissores no campo optoeletrônico, em particular, como camada de absorção de energia em células solares. No entanto, alternativas estáveis e não tóxicas às perovskitas de chumbo devem ser desenvolvidas para aplicações ecologicamente corretas. Considerando materiais livres de chumbo, realizamos três estudos: (*i*) o papel dos *A*-cátions $CH(NH_2)_2^+$ (formamidínio), $CH_3PH_3^+$ (metilfosfônio) e $CH_3NH_3^+$ (metilamônio) nas propiedades estruturais e optoeletrônicas de perovskitas $A SnI_3$; (*ii*) a caracterização de três novas perovskitas zero-dimensional de bismuto, $C_{20}H_{20}N_4Bi_2I_{10}$, $C_{42}H_{39}N_6Bi_2I_9$ e $C_{30}H_{25}N_6BiI_6 \cdot 2\,H_2O$; e (*iii*) o efeito da substituição do complexo inorgânico nas perovskitas $C_{20}H_{20}N_4B_2X_{10}$ e $C_{30}H_{25}N_6BX_6 \cdot 2\,H_2O$, onde $B = \{Sb^{3+}, Bi^{3+}\}$ e $X = \{Cl^-, Br^-, I^-\}$. Para atingir nossos objetivos, realizamos cálculos da teoria do funcional de densidade considerando a correção de Grimme D3 van der Waals para o funcional de troca e correlação PBE. No geral, a anisotropia do *A*-cátion resulta em distorções nos octaedros, e desempenha um papel importante na energia relativa das fases. Por exemplo, as interações dipolo-dipolo dependem do alinhamento/orientação dos *A*-cátions e podem conduzir as estruturas $A SnI_3$ para uma energia mais baixa, e as interações fracas H···I aumentam a coesão estrutural devido as atrações Coulombiana entre *A*-cátions e estrutura inorgânica. A estrutura inorgânica domina a densidade de estados e estruturas de bandas ao redor do nível de Fermi, bem como as propriedades ópticas. Por exemplo, curvas de absorção sugerem que a perovskitas com estrutura convencional (cúbica, tetragonal e ortorrômbica, com octaedros SnI_6 conectados em 3D) absorvem mais energia solar do que as perovskitas de baixa dimensão. As transições mais significativas observadas em perovskitas 0D foram dentro do octaedro, o que justifica o porquê os novos materiais apresentaram respostas ópticas semelhantes. As perovskitas 0D apresentam maior grau de deformação estrutural dos octaedros à medida que o número de iodetos compartilhados aumenta, aspecto corroborado por dados teórico e experimentais. No geral, as estruturas de banda das perovskitas 0D são planas e o acoplamento spin-órbita é mais significativo em sistemas contendo I. Ao considerar $C_{20}H_{20}N_4B_2X_{10}$ e $C_{30}H_{25}N_6BX_6 \cdot 2\,H_2O$, identificamos um efeito mais expressivo de *X* do que *B* nas propriedades estruturais, ópticas e eletrônicas, onde a banda de valência é amplamente determinada pelos estados *X p*, e o intervalo de banda diminui quando Cl^- é substituído por Br^-, e então I^-.

Palavras-chave: Perovskitas sem chumbo, Perovskitas de estanho, Perovskitas 0D.

LIST OF FIGURES

Figure 1 – Schematic representation of the planar-regular and inverted architectures. The mesoscopic architecture reassembles the planar-regular with the exception that it contains a mesoporous material in contact with the perovskite layer. 32

Figure 2 – **a)**- Crystal structure of a cubic perovskite, where the A-cation sites (green sphere) represent MA = $CH_3NH_3^+$, FA = $HC(NH_2)_2^+$, Cs^+ and so forth. The B-cations (blue sphere) are usually bivalent, while X (purple spheres) are monovalent anions (e.g., Cl^-, Br^- and I^-). **b)**- Each A-cation is surrounded by eight equivalent BX_6^{4-} moieties. 34

Figure 3 – Schematic representation of three-dimensional (3D) and low-dimensional (2D, 1D, and 0D) perovskite structures. 36

Figure 4 – Kohn-Sham self-consistent field. 45

Figure 5 – a) Schematic representation of the $A$$SnI_3$ perovskites unit cells, where blue, silver and purple spheres stand for the A-cation, Sn, and I sites, respectively. The different orientations of arrows in the blue spheres suggest the numerous orientations calculated for the A-cation in the inorganic-framework cage of $A$$SnI_3$ perovskites. Conferring to the experimental evidence, we considered two formula units for the tetragonal phase of $FASnI_3$. b) The column on the right side exhibits the $A$$SnI_3$ volume per formula unit, as well as the relative total energy (ΔE_{tot}) obtained by contemplating the perfect cubic structure (C) as energy reference for the remaining pseudo-hexagonal/hexagonal (PH/H), pseudo-cubic (PC), tetragonal (T), and orthorhombic (O) phases. . . . 59

Figure 6 – All H···I distances and XHI angles (X = C, N or P) versus the relative total energy of $A$$SnI_3$ perovskites. 61

Figure 7 – All XHI angles (X = C, N or P) versus the H···I distances for $A$$SnI_3$ perovskites. The red, dark green and light blue color represents the fitting of all data of NHI, CHI and PHI angles versus distance curve, respectively. The light green and blue curves represent the fitting for lowest energy perovskites dots. 62

Figure 8 – The lowest-energy structures for a) $MASnI_3$ b) $MPSnI_3$ and c) $FASnI_3$ cubic, orthorhombic, tetragonal, and hexagonal phases. Relative total energy using the cubic structure as reference are given in meV/f.u.. By the side of the cubic and hexagonal structures (in parenthesis) are indicated the respective values of pseudo-cubic and pseudo-hexagonal structures. 63

Figure 9 – The effective Bader charge analysis of each element, and site of $A\mathrm{SnI_3}$ perovskites (A, Sn, I, C, N, P, and sum of H) of the pseudo-hexagonal (PH), hexagonal (H), pseudo-cubic (PC), cubic (C), tetragonal (T), and orthorhombic (O) phases. 67
Figure 10 – Top: electron density accumulation (green) and depletion (purple) in the $A\mathrm{SnI_3}$ perovskites obtained by electron density difference between the charge of $A\mathrm{SnI_3}$ and the respective frozen-isolated fragments (A + $\mathrm{SnI_3}$). Bottom: Plane along tin-iodide bond lengths showing the electron localization function, which increase from blue to red. 68
Figure 11 – Plots of band structure and density of states per formula unit for the pseudo-hexagonal/hexagonal (PH/H), pseudo-cubic/cubic (PC/C), tetragonal (T), and orthorhombic (O) phases of $\mathrm{MASnI_3}$, $\mathrm{MPSnI_3}$ and $\mathrm{FASnI_3}$ perovskites. The VBM was set to 0 eV in all cases. 69
Figure 12 – Comparison of the band structure of pseudo-hexagonal (PH), hexagonal (H), pseudo-cubic (PC), cubic (C), tetragonal (T), and orthorhombic (O) phases by considering the whole $A\mathrm{SnI_3}$ perovskite and the frozen inorganic-framework fragment without the A-cation (indicated by **X**). The VBM was set to 0 eV in all cases. 70
Figure 13 – Absorption coefficient for the pseudo-hexagonal(PH), hexagonal (H), pseudo-cubic (PC), cubic (C), tetragonal (T), and orthorhombic (O) phases of $\mathrm{MASnI_3}$, $\mathrm{MPSnI_3}$ and $\mathrm{FASnI_3}$ perovskites. The vertical lines show the fundamental bandgap values. 71
Figure 14 – Crystal structures of the three novel lead-free zero-dimensional perovskites: $\mathrm{C_{20}H_{20}N_4Bi_2I_{10}}$, $\mathrm{C_{42}H_{39}N_6Bi_2I_9}$, and $\mathrm{C_{30}H_{25}N_6BiI_6 \cdot 2\,H_2O}$. The dashed lines indicate the unit cell. The kind of $\mathrm{BiI_6}$ connectivity and the unit formula of each 0D perovskite structure are shown below the unit cell representation. 76
Figure 15 – Density of states and band structure calculated at PBE+D3 level for all three 0D perovskites: $\mathrm{C_{20}H_{20}N_4Bi_2I_{10}}$, b) $\mathrm{C_{42}H_{39}N_6Bi_2I_9}$, and c) $\mathrm{C_{30}H_{25}N_6BiI_6 \cdot 2\,H_2O}$. 81
Figure 16 – a) Experimental absorption curves from 1 eV to 4 eV for the perovskites $\mathrm{C_{20}H_{20}N_4Bi_2I_{10}}$ (**1**), $\mathrm{C_{42}H_{39}N_6Bi_2I_9}$ (**2**) and $\mathrm{C_{30}H_{25}N_6BiI_6 \cdot 2\,H_2O}$ (**3**) with the corresponding optical bandgap energy b) Theoretical absorption coefficient calculated at PBE+D3 level for perovskites **1**, **2** and **3**. The PBE+D3 fundamental bandgap energy (orange line), the onset of the intra-octahedra transitions (purple line), and the optical banda-gap energy found as x-interception by the extrapolation done to the absorption coefficient curve (gray line) are also given. 83

Figure 17 – Effective Bader charge (e) and electron localization function (ELF) calculated at PBE+D3 level for the inorganic moieties of the perovskites a) $C_{20}H_{20}N_4Bi_2I_{10}$, b) $C_{42}H_{39}N_6Bi_2I_9$ and c) $C_{30}H_{25}N_6BiI_6 \cdot 2\,H_2O$. In the ELF plots, blue regions mean charge depletion and red represent the regions of charge accumulation. 84
Figure 18 – Schematic representation of the experimentally-determined $C_{20}H_{20}N_4Bi_2I_{10}$ and $C_{30}H_{25}N_6BiI_6 \cdot 2\,H_2O$ crystal structures,[1] which were employed as models to investigate the role of inorganic halide complex via the Bi^{3+} and I^- species substitution. 89
Figure 19 – Equilibrium volume (V_0), average of B-X bond lengths ($d_{av}^{B\text{-}X}$), effective coordination number of B-cation (ECN^B), $X-B-X$ bond angle variance (BAV), shortest distance of octahedra-cation ($d^{\text{c-a}}$) and cation-cation ($d^{\text{c-c}}$) for all B_2X_{10} and BX_6 studied 0D perovskites. . . . 91
Figure 20 – Decomposition of the bulk cohesive energy of 0D perovskites (E_{coh}^{bulk}) into organic-inorganic binding energy ($E_b^{org-inorg}$), the cohesive energy of the organic (E_{coh}^{org}) and inorganic (E_{coh}^{org}) fragments, and their dependence with the effective Bader charge of the inorganic fragments (Q). 94
Figure 21 – Local density of states per octahedra unity for the antimony and bismuth-based zero-dimensional perovskites obtained at PBE+D3 level. 95
Figure 22 – Band structures were calculated with PBE+D3 without SOC effects (black lines) and considering SOC effects (dashed-blue lines) for all 0D perovskite systems. 96
Figure 23 – Absorption coefficient of whole 0D perovskite (black lines) and their respective organic cationic (magenta lines) and inorganic anionic (teal lines) fragments. All results were obtained at the PBE+D3 level within DFT formalism. 98
Figure 24 – The blue line interception on the photon energy axes gives the optical bandgap energy of 0D perovskites by considering the Tauc plot procedure for direct-allowed transitions. The absorption coefficient (α) of the ordinate quantity $(\alpha h\nu)^{1/2}$ comes from the TB+scissor+BSE approach, as published in our work.[2] 99
Figure 25 – a) Different representation of the initial non-optimized cubic $CH_3NH_3SnI_3$ structure employed on our **k**-points density analyses. Each octahedral of the corner are equivalent, thus each one contributes with $\frac{1}{8}$ for the single cell. The picture shows different projections of the C–N bond length of the organic cation in the cage formed by octahedra. b) Orthorhombic $CH_3NH_3SnI_3$ perovskite structure. 125

Figure 26 – PBE results for cubic $CH_3NH_3SnI_3$ perovskite: volume, lattice parameters, and relative cubic deviation in relation to the values found with the highest **k**-points density. 127
Figure 27 – PBE results for cubic $CH_3NH_3SnI_3$: relative total energy in relation to the energy found with highest **k**-points density. 127
Figure 28 – Cubic deviation, relative volume, and relative total energy as a function of cutoff energy. 131
Figure 29 – $MASnI_3$ perovskites: bond length of X−H, C−N of *A*-cation and from C and N of to iodide of inorganic framework. 133
Figure 30 – $MPSnI_3$ perovskites: bond length of X−H, C−P of *A*-cation and from C and P of to iodide of inorganic framework. 134
Figure 31 – $FASnI_3$ perovskites: bond length of X−H, C−N of *A*-cation and from C and N of to iodide of inorganic framework. 135
Figure 32 – **k**-path selection for the band structure calculations of a) B_2X_{10}-based and b) BX_6-based zero-dimensional structures. 137
Figure 33 – Band structure of perovskite $C_{20}H_{20}N_4Bi_2I_{10}$ calculated with PBE+D3. The indirect fundamental bandgap energy is 0.9756 eV with the top of valence band at V point and the bottom of conduction band at R point. The direct fundamental bandgap energy is 1.0143 eV and occurs at R point. 138
Figure 34 – Band structure of perovskite $C_{42}H_{39}N_6Bi_2I_9$ calculated at PBE+D3 level. The indirect fundamental bandgap energy is 1.53 eV. The top of valence band is at Γ point and the bottom of conduction band in three degenerated points located between the path of Γ and X points. The fundamental direct bandgap energy is 1.53 eV and occurs at Γ point. . 139
Figure 35 – Band structure of perovskite $C_{30}H_{25}N_6BiI_6 \cdot 2\,H_2O$ calculated with PBE+D3. The direct fundamental bandgap energy is 1.406 eV and occurs at **R** point. 140
Figure 36 – Total and local density of states for PBE+D3 optimized $C_{20}H_{20}N_4Bi_2I_{10}$ perovskite. The fundamental bandgap energy is 0.9802 eV 141
Figure 37 – Total and local density of states for PBE+D3 optimized $C_{42}H_{39}N_6Bi_2I_9$ perovskite. The fundamental bandgap energy is 1.530 eV. 142
Figure 38 – Total and local density of states for PBE+D3 optimized $C_{30}H_{25}N_6BiI_6 \cdot 2\,H_2O$ perovskite. The fundamental bandgap energy is 1.406 eV. 143
Figure 39 – Density of states calculated with HSE06 for perovskite $C_{20}H_{20}N_4Bi_2I_{10}$. The fundamental bandgap energy is 1.8004 eV 144
Figure 40 – Density of states obtained with HSE06 for perovskite $C_{42}H_{39}N_6Bi_2I_9$. The fundamental bandgap energy is 2.3525 eV 145

Figure 41 – Density of states obtained with HSE06 for perovskite $C_{30}H_{25}N_6BiI_6 \cdot 2\,H_2O$. The fundamental bandgap energy is 2.24 eV . . . 146
Figure 42 – Local density of states per octahedron unity obtained at PBE+D3 level for the bismuth zero-dimensional perovskites. 147
Figure 43 – Local density of states per octahedron unity obtained at PBE+D3 level for the antimony zero-dimensional perovskites. 148
Figure 44 – Representation of zero-dimensional perovskite structures: $C_{20}H_{20}N_4B_2X_{10}$ and $C_{30}H_{25}N_6BX_6 \cdot 2\,H_2O$. 149
Figure 45 – Electron localization function of 0D perovskites: charge depletion (blue) and accumulation (red). 150

LIST OF TABLES

Table 1 – Structural and energetic properties obtained for the lowest energy of $A\mathrm{SnI_3}$ perovskite structures: enthalpy of formation, ΔH_f^o), bulk cohesive energy, E_{coh}, the average I···H distance of stronger hydrogen bond interactions of $-\mathrm{NH}_x{}^+/-\mathrm{PH_3}^+$ group, $d^{\mathrm{N}}_{\mathrm{I}\cdots\mathrm{H}}$, and of $-\mathrm{CH_3}$ group, $d^{\mathrm{C}}_{\mathrm{I}\cdots\mathrm{H}}$, difference of hydrogen bond lengths of $-\mathrm{NH}_x{}^+$ and $-\mathrm{CH_3}$ groups, $\Delta d_{\mathrm{I}\cdots\mathrm{H}}$), effective coordination number of tin, $\mathrm{ECN}^{\mathrm{Sn}}$, average tin-iodide bond lengths, $d_{av}^{\mathrm{Sn-I}}$, I–Sn–I angle of octahedron diagonal, Θ, I–Sn–I angle involving adjacent iodide species, θ, and the lattice parameters (a_0, b_0 and c_0) of pseudo-hexagonal (PH), hexagonal (H), pseudo-cubic (PC), cubic (C), tetragonal (T), and orthorhombic (O) phases. The experimental values are indicated below the respective theoretical results when available. 64

Table 2 – Direct fundamental/optical bandgap energy at PBE+D3 level, ($E^f_{g,\mathrm{PBE+D3}}/E^{opt}_{g,\mathrm{PBE+D3}}$), and HSE06 fundamental bandgap energy ($E^f_{g,\mathrm{HSE06}}$) for the pseudo-hexagonal (PH), hexagonal (H), pseudo-cubic (PC), cubic (C), tetragonal (T), and orthorhombic (O) phases of $A\mathrm{SnI_3}$ perovskites. The fundamental indirect bandgap values of pseudo-hexagonal and hexagonal structures are given below the direct bandgap values. All bandgap values are given in eV. 72

Table 3 – Structural properties of perovskite $\mathrm{C_{20}H_{20}N_4Bi_2I_{10}}$ calculated by employing the PBE exchange-correlation functional with (PBE+D3) and without Van der Waals D3 corrections (PBE): lattice parameters, and internal structural properties, i.e., average bond length between the halide and metallic cation (d_{av}^{B-X}), effective coordination number of B-cation (ECN^B), and average B_xX_y volume ($V_{B_xX_y}$) The deviation from experimental results of bismuth-iodide perovskites (Δ) are also reported.[1] 78

Table 4 – Tests to define the position of hydrogen atoms in the perovskite $\mathrm{C_{30}H_{25}N_6BiI_6\cdot 2\,H_2O}$ by comparing the theoretical-experimental percentage deviations (Δ) of lattice parameters, bismuth-iodide average bond length ($d_{av}^{\mathrm{Bi-I}}$), average non-adjacent I–Bi–I average bond angle (Θ_{av}), adjacent I–Bi–I average bond angle (θ_{av}), and average effective coordination number of bismuth ($\mathrm{ECN}^{\mathrm{Bi}}$). All calculations were performed employing the D3 van der Waals correction and the PBE functional (PBE+D3). 79

Table 5 – Theoretical (PBE+D3 calculations) and experimental values of lattice parameters, and average values for: the bond lengths of Bi–I ($d_{av}^{\mathrm{Bi-I}}$), non-adjacent bond angle of I–Bi–I (Θ_{av}), adjacent bond angle of I–Bi–I (θ_{av}), and average effective coordination number of bismuth ($\mathrm{ECN^{Bi}}$). The experimental-theoretical deviation (Δ) and the respective population standard deviation (σ) by considering two octahedra (two unit cells for perovskite $C_{30}H_{25}N_6BiI_6 \cdot 2\,H_2O$) are given for all three structures. . . . 80

Table 6 – Optical bandgap energy (in eV) found for the perovskites $C_{20}H_{20}N_4Bi_2I_{10}$, $C_{42}H_{39}N_6Bi_2I_9$ and $C_{30}H_{25}N_6BiI_6 \cdot 2\,H_2O$ through the interception of photon energy axis by the extrapolation done to the absorption coefficient curve ($E_{g,\mathrm{PBE+D3}}^{opt}$), employing the HSE06 shift ($E_{g,\mathrm{HSE06}}^{opt}$), and according to experimental data ($E_{g,\mathrm{Exp.}}^{opt}$). 82

Table 7 – Lattice parameters, volume of the unit cell (V_0), and volume of $[Bi_xI_y]^{z-}$ ($V_{B_xX_y}$) of the $C_{30}H_{25}N_6BX_6 \cdot 2\,H_2O$ and $C_{20}H_{20}N_4B_2X_{10}$ perovskites calculated at PBE and PBE+D3 levels. The chemical formula of the structures were abbreviated as BX_6 and B_2X_{10}, where $B = \{Bi^{3+}, Sb^{3+}\}$, and $X = \{Cl^-, Br^-, I^-\}$. The experimental results (Exp.) are shown for bismuth-iodide systems.[1] 90

Table 8 – Cohesive energy of the 0D perovskites (E_{coh}), cohesive energy of the inorganic framework ($E_{coh}^{inorg.}$), and organic spacer cations ($E_{coh}^{org.}$). Sum of the organic-inorganic binding energy ($E_b^{inorg-org}$) with the cohesive energy of organic and inorganic moieties with of 0D perovskites ($E_{coh}^{sum} = E_{coh}^{inorg.} + E_{coh}^{org.} + E_b^{inorg-org}$), and their difference with the cohesive energy of the whole system ($\Delta = E_{coh} - E_{coh}^{sum}$). 93

Table 9 – Fundamental bang gap energy (E_g) of all zero-dimensional bismuth- and antimony-based perovskites with PBE+D3 and PBE+D3+SOC approaches (bold). 97

Table 10 – Band structure properties: Electronic fundamental bandgap energy (E_g) using different level of approximations (PBE+D3, PBE+D3+SOC, HSE06, HSE06+SOC) at the Γ-point. Optical bandgap ($E_g^{optical}$) employing the TB+$\Delta_{scissor}$+BSE framework as described in our published work.[2] The values of the experimental optical bandgap energy ($E_{g,exp.}^{optical}$) are also provided when available.[1] All properties are provided in eV. 100

Table 11 – Cubic $CH_3NH_3SnI_3$ perovskites optimization: **k**-points density (KD), **k**-points mesh (KM), number of **k**-points (NK), volume (V), cubic volume (a_0^c), lattice parameters (a_0, b_0, c_0), cubic deviation (CD) and the relative deviation (considering all significant numbers) of parameters in relation to the highest **k**-points density. 126

Table 12 – Orthorhombic $CH_3NH_3SnI_3$ perovskites optimization: **k**-points density (KD), **k**-points mesh (KM), Number of **k**-points (NK), volume (V), lattice parameters, and the relative deviation (considering all significant numbers) of aforementioned parameters in relation to the highest **k**-pints density. 128
Table 13 – Cubic $CH_3NH_3SnI_3$ perovskites optimization: relative total energy (ΔE_{tot}), average ($d^N_{\mathrm{I-H}}$) and standard deviation ($\sigma^N_{\mathrm{I-H}}$) of stronger hydrogen bond of $-NH_3{}^+$ group, average ($d^C_{\mathrm{I-H}}$) and standard deviation ($\sigma^C_{\mathrm{I-H}}$) of stronger hydrogen bond of $-CH_3$ group, difference of the average hydrogen bonds of $-NH_3{}^+$ and $-CH_3$ ($\Delta d_{\mathrm{I-H}}$), effective coordination number ($\mathrm{ECN}^{\mathrm{Sn}}$), average ($d^{\mathrm{Sn-I}}_{av}$) and standard deviation of Sn–I bond lengths ($\sigma^{\mathrm{Sn-I}}$), octahedra diagonal I–Sn–I angle (Θ) and standard deviation (σ^{Θ}), adjacent I–Sn–I angle (θ) and standard deviation (σ^{θ}), distortion index (DI), and bond angle variance (BAV). 129
Table 14 – Orthorhombic $CH_3NH_3SnI_3$ perovskites optimization: relative total energy (ΔE_{tot}), average ($d^N_{\mathrm{I-H}}$) and standard deviation ($\sigma^N_{\mathrm{I-H}}$) of stronger hydrogen bond of $-NH_3{}^+$ group, average ($d^C_{\mathrm{I-H}}$) and standard deviation ($\sigma^C_{\mathrm{I-H}}$) of stronger hydrogen bond of $-CH_3$ group, difference of the average hydrogen bonds of $-NH_3{}^+$ and $-CH_3$ ($\Delta d_{\mathrm{I-H}}$), octahedra effective coordination number ($\mathrm{ECN}^{\mathrm{Sn}}$), average ($d^{\mathrm{Sn-I}}_{av}$) and standard deviation of Sn–I bond lengths ($\sigma^{\mathrm{Sn-I}}$), octahedra diagonal I–Sn–I angle (Θ) and standard deviation (σ^{Θ}), octahedra adjacent I–Sn–I angle (θ) and standard deviation (σ^{θ}), distortion index (DI), and bond angle variance (BAV). 130
Table 15 – ENCUT analyses (NBANDS default) for cubic hybrid $CH_3NH_3SnI_3$ perovskites optimization: **k**-points mesh (KM), Number of **k**-points (NK), volume (V), cubic volume (a^c_0), lattice parameters (a_0, b_0, b_0), relative total energy (ΔE_{tot}), cubic deviation (CD) and the relative deviation of aforementioned parameters in relation to the highest **k**-pints density. . . 130
Table 16 – ENCUT test (NBANDS default) for cubic $CH_3NH_3SnI_3$ perovskites optimization: relative total energy (ΔE_{tot}), average ($d^N_{\mathrm{I-H}}$) and standard deviation ($\sigma^N_{\mathrm{I-H}}$) of stronger hydrogen bond of $-NH_3{}^+$ group, average ($d^C_{\mathrm{I-H}}$) and standard deviation ($\sigma^C_{\mathrm{I-H}}$) of stronger hydrogen bond of $-CH_3$ group, difference of the average hydrogen bonds of $-NH_3{}^+$ and $-CH_3$ ($\Delta d_{\mathrm{I-H}}$), octahedra effective coordination number ($\mathrm{ECN}^{\mathrm{Sn}}$), average ($d^{\mathrm{Sn-I}}_{av}$) and standard deviation of Sn–I bond lengths ($\sigma^{\mathrm{Sn-I}}$), octahedra I–Sn–I diagonal angle (Θ), octahedra adjacent I–Sn–I angle (θ), and respective standard deviation (σ^{Θ})/(σ^{θ}), distortion index (DI), and bond angle variance (BAV). 131

Table 17 – Structural parameters of the cubic (C), pseudo-cubic (PC), orthorhombic (O), tetragonal (T), hexagonal (H), pseudo-hexagonal (PH) lowest energy phases of $A\mathrm{SnI_3}$ perovskites: average ($d^{N/P}_{\mathrm{I-H}}$) and standard deviation ($\sigma^{N/P}_{\mathrm{I-H}}$) of stronger hydrogen bond of $-\mathrm{NH}_x{}^+/-\mathrm{PH_3}^+$ group, average ($d^{C}_{\mathrm{I-H}}$) and standard deviation ($\sigma^{C}_{\mathrm{I-H}}$) of stronger hydrogen bond of $-\mathrm{CH_3}$ group, difference of the average hydrogen bonds of $-\mathrm{NH}_x{}^+/-\mathrm{PH_3}^+$ and $-\mathrm{CH_3}$ ($\Delta d_{\mathrm{I-H}}$), octahedra effective coordination number ($\mathrm{ECN}^{\mathrm{Sn}}$), average ($d^{\mathrm{Sn-I}}_{av}$) and standard deviation of Sn–I bond lengths ($\sigma^{\mathrm{Sn-I}}$), octahedra diagonal I–Sn–I angle (Θ) and standard deviation (σ^{Θ}), octahedra adjacent I–Sn–I angle (θ) and standard deviation (σ^{θ}), distortion index (DI), and bond angle variance (BAV). 132

LIST OF ABBREVIATIONS AND ACRONYMS

BAV	Bond angle variance.
CBM	Conduction band minimum.
CD	Cubic deviation.
CM	Center of mass.
DFT	Density-functional theory.
DI	Distortion index.
ECN	Effective coordination number.
ELF	Electron localization function.
ENCUT	Energy cutoff.
ETL	Electron transport layer.
FTO	Fluorine-doped tin oxide.
GGA	Generalized gradient approximation.
HF	Hartree–Fock.
HK	Hohenberg–Kohn.
HSE06	Heyd–Scuseria–Ernzerhof.
HTL	Hole transport layer.
ITO	Indium tin oxide.
KD	**k**-points density.
KM	**k**-points mesh.
KS	Kohn–Sham.
NBANDS	Number of bands.
NK	Number of **k**-points.
PAW	Projector augmented wave.
PBE	Perdew–Burke–Ernzerhof.

PCE	Power conversion efficiency.
QD	Quantum dots.
VASP	Vienna *Ab initio* simulation package.
VBM	Valence band maximum.
vdW	van der Waals.
WHO	World health organization.

CONTENTS

1 INTRODUCTION 29
1.1 Why Study Perovskite Materials? 29
1.2 Perovskite Solar Cells 31
1.3 Perovskite Materials 35
1.3.1 Three-Dimensional Halide Perovskites 36
1.3.2 Low-Dimensional Halide Perovskites 37
1.4 Open Questions 39
1.5 Objectives 39

2 METHODOLOGY 41
2.1 Many-Body Problem 41
2.2 Born-Oppenheimer Approximation 41
2.3 Density-Functional Theory 42
2.3.1 Hohenberg-Kohn Theorems 43
2.3.2 Kohn-Sham Formalism 44
2.3.3 Exchange-Correlation Functionals 46
2.3.4 Van der Waals Corrections 46
2.4 Periodic Boundary Conditions 47
2.5 Projector Augmented Wave Method 48
2.5.1 The Linear Transforming Operator 49
2.5.2 Transforming Operators 51
2.5.3 Charge Density 52
2.5.4 Kinetic Energy 53
2.5.5 The PAW Total Energy 53
2.5.6 Hamiltonian Operator 54
2.5.7 Forces in the PAW method 54
2.5.8 PAW: Approximations 54
2.5.9 Difference between Blöchl and Kresse Implementations 55
2.6 Optical Properties 55

3 THE STRUCTURAL, ENERGETIC AND OPTOELECTRONIC PROPERTIES OF TIN PEROVSKITES 57
3.1 Computational Details 57
3.2 Bulk of Tin Perovskites 58
3.3 Relative Energy Stability 59
3.3.1 The Effect of *A*-cation Size 59

3.3.2 Hydrogen Bond Interactions . . . 60
3.3.3 The Role of Dipole-dipole Interactions . . . 60
3.4 Stability of Tin Perovskites . . . 63
3.5 Structural Properties . . . 65
3.6 Charge Density Analysis . . . 66
3.7 Optical and Electronic Properties . . . 68
3.8 Summary . . . 73

4 NOVEL ZERO-DIMENSIONAL HYBRID PEROVSKITES . . . 75
4.1 Computational Details . . . 75
4.2 Crystal Structure of Zero-Dimensional Perovskites . . . 76
4.3 Equilibrium Structural Parameters . . . 78
4.4 Electronic Structure . . . 81
4.5 Optical Properties . . . 82
4.6 Chemical Bonding Analysis . . . 84
4.7 Summary . . . 85

5 ROLE OF THE INORGANIC HALIDE COMPLEXES SUBSTITUTION IN THE PHYSICAL PROPERTIES OF LEAD-FREE ZERO-DIMENSIONAL PEROVSKITES . . . 87
5.1 Computational Details . . . 87
5.2 Zero-Dimensional Perovskite Structures . . . 88
5.2.1 Equilibrium Lattice Parameters . . . 88
5.2.1.1 Local Structural Parameters . . . 91
5.3 Cohesive Energy . . . 92
5.4 Electronic and Optical Properties . . . 95
5.4.1 Density of States and Band Structure . . . 95
5.4.2 Absorption Coefficient . . . 96
5.5 Summary . . . 100

6 CONCLUSIONS . . . 103
6.1 Scientific Papers . . . 105
6.1.1 Perovskites Systems . . . 105
6.1.1.1 List of Published Articles . . . 105
6.1.2 Other Works . . . 106

BIBLIOGRAPHY . . . 107

APPENDIX A – TIN-BASED PEROVSKITES . . . 125
A.1 Convergence Test . . . 125

A.2 ASnI$_3$ Perovskites 132

APPENDIX B – ZERO-DIMENSIONAL PEROVSKITES 137
B.1 Band Structures 137
B.2 Density of States 141

1 INTRODUCTION

Perovskite materials are widely studied today because of their unique characteristics that allow broad applicability. The number of perovskite articles increased fast since the first perovskite solar cell production in 2009.[3] For instance, perovskite researchers worldwide published more than 16000 papers from January 2009 to December 2019.[4] However, it still exists many open questions in the perovskite field. As visionary Richard Feynman used to say, there is plenty of history at the bottom, and this statement applies perfectly to the microscopic properties behind the noteworthy perovskite features. The space here is small to account for all interesting experimental and theoretical studies already reported about halide perovskites. Out of many published works, here it's presented a brief review by considering relevant topics, for instance, composition, dimensionality, application as solar cells, and open questions.

1.1 Why Study Perovskite Materials?

All-inorganic and hybrid organic-inorganic perovskite systems have been under much research spotlight in the last years because of their real possibility of achieving widespread applications, i.e., perovskite studies have been motivated by the promising scale-up of low-cost solar cells, and other standout uses in the optoelectronic field. For instance, the singular optoelectronic properties of perovskites have resulted in a plethora of proposed applications beyond solar cells, including resistive random-access memory,[5] light-emitting-diodes,[6] photodetectors,[7] solar-to-fuels conversion,[8] photocatalysis,[9] electroluminescent devices,[10] scintillation,[11] and X-ray detectors.[12] In particular, regarding the application as a light-absorbing layer in solar cells, perovskite may have a good impact on decreasing the fossil fuel demand by representing an inexpensive and sustainable energy source. Strikingly, perovskite solar cells have been considered cheap substitutes for expensive conventional crystalline silicon cells. However, the durability of perovskite solar cells must be improved, which is essential for commercialization.[13] In addition to its cost advantages, perovskites solar cells have outstanding features such as tunable bandgap energy,[14–16] extended light-harvesting,[17] high exciton lifetime,[16] high charge-carrier mobility, long diffusion lengths,[13,14,16,18] and low-cost processing methods, which allows producing flexible/printable devices as well as building tandem solar cells.[19]

In part, the perovskite interest has been motivated by early investigations of lead perovskites, namely, the $CH_3NH_3PbI_3$ (henceforth $MAPbI_3$, where $MA \equiv CH_3NH_3^+$, i.e., the methylammonium cation) and related materials. The first $MAPbI_3$ perovskite solar cell was able to convert 3.8 %[3] of the solar daylight energy into electricity, making the race for better efficiency begin. Twelve years later, the efficiency of perovskite cells achieved

values higher than 25.0 %,[20–22] and it exits a real possibility of outperforming the power conversion efficiency (PCE) limit of 33.7 % estimated with the Shockley–Queisser limit of a single-junction cell.[23,24] As a result of the fast-growing efficiency, this class of material has become a promising pathway to solving the increasing energy consumption/demand from fossil fuels. And, since the renewable and clean solar energy potential is higher than the human primary energy consumption, solar energy is a benign replacement for fossil fuels.[25]

Despite the various required attempts to stabilize the devices, all singular features have been put perovskite solar cells as promising substitutes for the conventional silicon cells. However, the commercialization of $MAPbI_3$ and related lead perovskites have been hindered or questioned because of instability caused by moisture, heat, extended light exposure, and lead toxicity, which may yield problems in the fabrication, installation, and discard.[26] Internal factors also add to the list of negative points, for instance, ion migration, instability of other layers, and reactions between the interfaces.[27,28] Recycling procedures and encapsulation cannot exclude dangers arising from the scale-up production of lead-based perovskite technologies.[29–31] Recently, lead was classified as one of the ten most harmful materials for human life and the environment by the WHO (World Health Organization).[32] Thus, lead-free perovskites alternatives with long-term stability have received increased importance. The focus was a high efficiency in the first years of the perovskite solar cell study but more recently started to address also the stability.[32] In this sense, stable and efficient lead-free perovskites are perfect targets.

Inspired by the efficient perovskite-solar-cell devices designed with the pristine $MAPbI_3$ perovskite, which have shown significant efficiency, but low stability under operating conditions, many components have been examined for complete/partial substitution of each site of ABX_3 perovskites as a trail for obtaining stable-efficient devices. Among the library of ions employed in the design of new perovskites, single/mixed FA (FA $\equiv$ $HC(NH_2)_2{}^+$),[33] MA,[34] Cs^+,[35] Rb^+[36] have been used as *A*-cations, monovalent-cations (e.g., Ag^+), divalent cations (e.g., Pb^{2+}, Sn^{2+}, Ge^{2+}, Mg^{2+}, Cu^{2+}), and trivalent cations (e.g. Bi^{3+}, Sb^{3+}) have been the options for *B*-sites;[37] concerning the *X*-sites, halide anions (Cl^-, Br^-, I^-) are the major library of employed ions. Studies have shown higher performance for perovskite materials displaying a mixing of ions in each site of ABX_3,[38] e.g., materials with double CsFA,[39] triple CsMAFA,[40] and quadruple RbCsMAFA[41] mixture of *A*-cations have been obtained with enhanced properties compared to non-mixed/pristine ones.

Different replacement candidates for hazardous lead content of the archetypal $MAPbI_3$ and related materials have been proposed to obtain eco-friendly perovskite materials. In particular, tin-based perovskites have shown promising efficiencies,[42] which can be explained by the comparable electronic properties with Pb-based counterparts.

However, $A\mathrm{Sn}X_3$ perovskites experience the same deterioration process of Pb-perovskites, which influenced a complete or partial substitution of cation and halide sites of both lead and tin-based perovskites to enhance the stability.[43–45] However, other destabilizing factors occur in tin perovskites, including the self-doping process provoked by tin oxidation and the non-uniformity of films.[46,47] All combined destabilizing factors contribute to yield instability and low device efficiencies of $A\mathrm{Sn}X_3$ perovskite. Hence, it is urgent to improve the atomic-scale understanding of perovskite materials to enhance stability and PCE.

1.2 Perovskite Solar Cells

Perovskite solar cells are formed by stacking thin films, where the perovskite layer absorbs photon energy equal to or higher than its bandgap energy. The perovskite layer stays between two important-selective contact layers, the electron-transport-layer (ETL) and the hole-transport-layer (HTL). Selectively, the holes and photo-excited electrons are collected, respectively, by the HTL and ETL. As sketched in Figure 1, based on the film's disposition, the solar cells have different architectures, where the main architectures are the planar-regular, planar-inverted and mesoporous.[48] In cells with planar-regular architecture (glass/FTO/ETL/perovskite/HTL/metal), the light incidence occurs to the side of transparent conducting oxide, which commonly is an indium tin oxide (ITO) or fluorine-doped tin oxide (FTO). Planar-inverted architecture has ETL and HTL inverted compared to the regular architecture, i.e., glass/FTO/HTL/perovskite/ETL/metal; hence, the light incidence occurs by the side of HTL, which must have higher transmittance. Under the HTL (regular structure) or ETL (inverted structure) is deposited a metal (e.g., Au, Ag, and Al) that completes the circuit yielding to the carrier formation.[48] One benefit of photovoltaic applications of perovskite solar cells is the possibility of inexpensive scale-up production. The production methods include vapor-assisted process, one-step(two-step) depositions, and sequential deposition methods. For instance, the one-step deposition of the pristine $MAPbI_3$ perovskite follows a few steps (*i*) organic solvent solution of PbI_2 and MAI precursor added on top of the TiO_2 layer and spin-coated. (*ii*) increase in the spinning rate until the $MAPbI_3$ layer formation, and (*iii*) the film annealing. Further details of perovskite fabrication are in the work of Jeong-Hyeok[49] and Jamal.[50]

Organic compounds have been used as charge carrier transport layers in perovskite solar cells, with poly(3,4-ethylenedioxythiophene) polystyrene sulfonate (PEDOT:PSS),[51] 2,2',7,7'-Tetrakis[N,N-di(4-methoxyphenyl)amino]-9,9'-spirobifluorene (spiro-OMETAD),[52] poly(triaryl amine) (PTAA),[53] and poly(3-hexylthiophene) (P3HT)[54] used as the HTL, while [6,6]-phenyl-C61-butyric acid methyl ester (PCBM),[55] C_{60}[56] and fullerene-derived compounds used as the ETL. Nevertheless, research has been done to replace organic HTL by inorganic compounds, including CuSCN,[57] CuI[58] and NiO_x.[59,60] Among the ETL candidates, the inorganic TiO_2 has been the most employed, but other inorganic

Figure 1 – Schematic representation of the planar-regular and inverted architectures. The mesoscopic architecture reassembles the planar-regular with the exception that it contains a mesoporous material in contact with the perovskite layer.

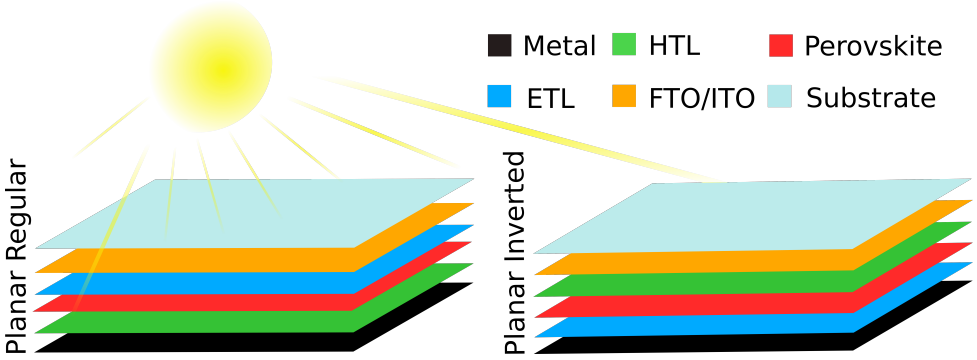

Source: Source: Done by Mailde S. Ozório

metal oxides have also employed, such as ZnO[60] and SnO_2.[61] In particular, SnO_2 has been considered a promising replacement of the traditional TiO_2 ETL.[62] Although organic-based transport layers give high efficiency and hysteresis reduction, metallic oxides present higher mobility for charge carriers and also higher stability.[60] Additionally, organic-based transport materials are synthesized in multiple steps and increase the cost of the cells. For instance, high purity spiro-OMETAD is about ten times more expensive than gold and platinum.[63]

Many perovskite materials were employed as a light-absorbing layer in perovskite solar cells, where $MAPbI_3$ perovskite has been widely investigated. In the $MAPbI_3$, Pb^{2+} occupies the center of octahedra and it is hexacoordinated by iodide (PbI_6^{4-}), while MA is coordinated by 12 iodide ions. Eight PbI_6^{4-} octahedra form the cavity occupied by the MA cation. $MAPbI_3$ perovskite is a cubic structure with $Pm\bar{3}m$ space group at high temperature ($T > 330\,K$). The cubic to the tetragonal phase transition at 330 K causes a symmetry reduction from $Pm\bar{3}m$ to $I4/mcm$. A further transition occurs at ~160 K, where the tetragonal phase transforms to the orthorhombic phase with space group $Pnma$.[64]

Solar cells based on $MAPbI_3$ and their derivatives face some commercialization roadblocks despite having relevant features. These perovskites suffer from instability caused by moisture, migration of ions, extended light exposure, instability of perovskite neighbor layers, reactions between interfaces, and lead toxicity, which may yield problems in the fabrication, installation, and discard.[26–28] On degradation mechanism promoted by oxygen and light exposure, one proposed: (*i*) $MAPbI_3 \xrightarrow{\text{light}} MAPbI_3{}^*$, follow (*ii*) $O_2 \xrightarrow{MAPbI_3{}^*} O_2{}^{\bullet-}$ and, then, (*iii*) $MAPbI_3 + O_2{}^{\bullet-} \longrightarrow CH_3NH_2 + PbI_2 + \frac{1}{2}I_2 + H_2O$. Thus, oxygen receives one photo-excited electron from the perovskite surface and generates superoxide ($O_2{}^{\bullet-}$), which decomposes the perovskite layer by deprotonating the MA-cation.[65] Although light is essential for the functioning of the perovskite solar cell, extended light exposure yields to degradation, ion migration, TiO_2 deterioration (ETL), formation of structural defects,

phase separation in mixed-halide perovskites, and distortion of octahedron.[32] Thus, to achieve the desired scalability, perovskite solar cells technology must be improved to present long-term extrinsic stability under real operating conditions, which implies a lifetime of about 25 years under higher heat, sunlight radiation, external bias, and atmospheric environment (presence of moisture, oxygen, nitrogen, and other gases).

The mainstream perovskite materials suffer from an irreversible degradation when contacting aprotic polar solvents like water.[66] The perovskite structures form hydrated compounds because of hydrogen-bonding interactions with the halide. For instance, to describe the degradation mechanism of the pristine $MAPbI_3$ perovskite, the following chemical equations have been proposed: $4MAPbI_3 + 4\,H_2O \longleftrightarrow 4\,[MAPbI_3 \cdot H_2O] \longleftrightarrow (MA)_4PbI_6 \cdot 2\,H_2O + 3\,PbI_2 + 2\,H_2O$. This equation suggests the reversibility of the process. However, in the presence of higher moisture, the process becomes irreversible and, thus, the perovskite structure degradation occurs $(MA)_4PbI_6 \cdot 2\,H_2O \longrightarrow 4\,MAI + PbI_2 + 2\,H_2O$.[67]

One of the many procedures developed to minimize the stability and toxicity problems is encapsulation, which considers one additional layer to protect susceptible layers from external degrading factors like oxygen and moisture exposure. However, the benefits of encapsulation have been examined because of possible negative consequences, including the increase in cost, reduction of efficiency, and damage to the device's flexibility. The encapsulation cannot avoid disaster and dangers from the large-scale production of lead perovskites.[29–31] In fact, lead is one of the top ten materials most harmful to the environment and human life.[32] Thus, to enhance the stability of perovskite solar cells, other approaches rather than encapsulation are preferable.[68] Some alternatives include testing hydrophobic HTL, additives, non-hygroscopic polymer between HTL and perovskite layers, molecule adsorptions on perovskite surface, and the reduction of perovskite dimensionality.[32] However, not only the perovskite layer suffers from the degradation process. The performance of perovskite solar cells also depends on the stability of other layers (ETL, HTL, and either of the metal contact).

Finding lead-free perovskites with long-term stability is one urgent scientific ambition that has received major attention. In this sense, the focus of the perovskite solar cell study moved from efficiency to addressing the toxicity and stability more recently,[32] which implies more efforts to obtain stable and eco-friendly devices without scarifying the efficiency. Despite efforts worldwide, the ideal perovskite solar cells remain a dream by generating many open questions to be achieved. For instance, from an atomistic point of view, achieving an in-depth understanding of microscopic properties that help boost stability and efficiency is deeply desired. This issue triggered complete/partial replacement of AB-cations and of X-halide sites to improve the structural stability of ABX_3 perovskites.[43–45] In particular, to obtain eco-friendly and stable perovskite materials, different candidates for lead replacement were proposed, e.g., the lead has been substituted

Figure 2 – **a)**- Crystal structure of a cubic perovskite, where the *A*-cation sites (green sphere) represent MA = $CH_3NH_3^+$, FA = $HC(NH_2)_2^+$, Cs^+ and so forth. The *B*-cations (blue sphere) are usually bivalent, while *X* (purple spheres) are monovalent anions (e.g., Cl^-, Br^- and I^-). **b)**- Each *A*-cation is surrounded by eight equivalent BX_6^{4-} moieties.

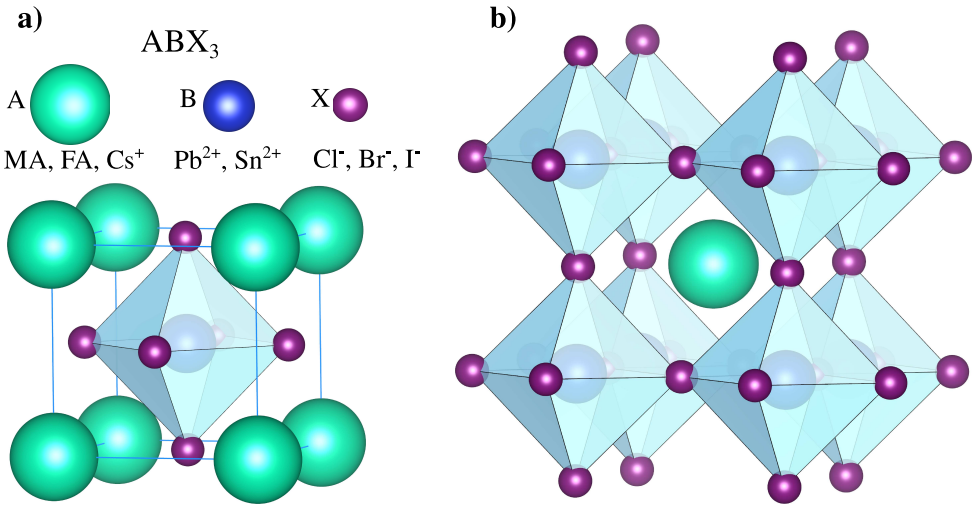

Source: Source: Done by Mailde S. Ozório

by Sn^{2+}, Ge^{2+}, Mn^{2+}, and Cu^{2+}. However, only tin has shown comparable efficiencies,[42] which have been explained by the similarity between tin and lead electronic properties.

Tin perovskites suffer from the same intrinsic and extrinsic degradation process as their lead counterparts, as well as from the non-uniformity of films and the self-doping process induced by tin oxidation.[46,47] While relativistic effects protect lead from oxidation, Sn^{2+} can easily oxidize to Sn^{4+}.[69,70] All these factors have contributed to yield lower device efficiencies of $ASnX_3$ perovskites compared to lead-based ones. Among lead-based perovskites, $FAPbI_3$ (FA represents the formamidinium cation, i.e., $HC(NH_2)_2^+$) is a material with the potential to provide better performance than $MAPbI_3$ because of its wide absorption range of the solar spectrum. However, stable perovskites and high-quality films $FAPbI_3$ formation are more difficult than with $MAPbI_3$.[71] Photo-luminescence and X-Ray diffraction show that $CH_3NH_3Pb\,(I_{1-x}Br_x)_3$ and other halide mixed perovskites suffer from reversible segregation of phases, e.g., in regions rich in iodine and bromine, when subjected to light excitation. Therefore, mixing halide sites leads to instabilities and problems regarding the operation and applicability of these materials.[72,73] Phase segregation and how to avoid it is complicated because the mechanism associated with segregation and restoration is not understood.[74] One suggests these processes may occur because the physical properties of hybrid perovskites differ from pure organic and inorganic semiconductors.[75]

1.3 Perovskite Materials

The perovskite term was employed for the first time to label materials with the same crystal structure as $CaTiO_3$ and named after Russian mineralogist L. A. Perovski.[76] Convectional perovskite structures have a general ABX_3 formula, where A and B are cations, and X usually stands for halide or oxide. As shown in Figure 2, the perovskite structure displays a three-dimensional (3D) corner-sharing connectivity of the anionic BX_6 octahedra, with the A-cation providing the charge compensation for the neutrality of the whole system. Nowadays, under the umbrella name of perovskites are included many structures with different crystal structures to the conventional $CaTiO_3$ perovskite, e.g., zero- (0D), one- (1D), and two-dimensional (2D) perovskites. A schematic representation of perovskite dimensionality is shown in Figure 3. As a consequence of the large structural versatility, "perovskite" materials have emerged with many singular properties, which have allowed their use for the most diverse purpose, as well as promising applications spanning ionic and magnetic conductors, superconductors, semiconductors, ferroelectrics, dielectrics, and photovoltaics.[19]

The size of A-cation play significant role in the stability of the crystalline structure, where the ideal size has been estimated by octahedra factor, $\mu = r_{\mathrm{B}}/r_{\mathrm{X}}$, and the Goldschmidt tolerance factor, $\tau = (r_{\mathrm{A}} + r_{\mathrm{X}})/\sqrt{2}(r_{\mathrm{B}} + r_{\mathrm{X}})$, in which the ionic radii of A, B and X are represented by r_{A}, r_{B} and r_{X}, respectively.[70] In principle, for a perfect cubic structure $\tau = 1$, which is not satisfied for many cations in the A positions that are much small or larger.[64] However, cubic/distorted perovskites structures are empirically favored in the range of $0.8 < \tau < 1.0$. For $\tau < 0.8$ and $\tau > 1.0$ increase the possibility of the formation of lower symmetry tetragonal and orthorhombic phases as well as non-perovskite structures (e.g. 2D-layered, 1D-chain, and 0D-isolated BX_6 octahedra).[32,64] For instance, the effective ionic radii of MA, Cs^+, Pb^{2+} and I^- are, respectively, 217 pm, 188 pm, 119 pm and 220 pm.[32,77] Thus, the tolerance factor of $CsPbI_3$ (0.85) and $MAPbI_3$ (0.91) fits in the range of stable perovskite structure, thus, suggest that cations accommodate well in the cage formed by 3D corner-sharing PbI_6 octahedra.

Mixed compositions of cations and anions give τ values of stable perovskite structures, i.e., compared to non-alloyed ABX_3 perovskites, alloyed $(A_yA'_{1-y})B(X_zX'_{1-z})_3$ perovskites tend to present improved structural stability. To obtain the tolerance factor of mixed perovskites with $(A_yA'_{1-y})B(X_zX'_{1-z})_3$ chemical formula it is necessary adjustments to acquire approximated effective ionic radii of A-cations ($r_A(eff)$) and X-anions ($r_X(eff)$), which can be predicted by $r_A(eff) = yr_A + (1-y)r'_A$ and $r_X(eff) = zr_X + (1-z)r'_X$, respectively.[32] The effective ionic radii of each organic cation (r_{eff}) come from Kieslich's method,[78] $r_{eff} = r_{mass} + r_i$, where r_{mass} stands for the distance between the center of mass (CM) of cation and the furthest non-hydrogen atom i to the CM, and r_i correspond to the Shannon effect ionic radii of atom i. The $(MA_{0.15}FA_{0.85})Pb(Br_{0.15}I_{0.85})_3$ perovskite

Figure 3 – Schematic representation of three-dimensional (3D) and low-dimensional (2D, 1D, and 0D) perovskite structures.

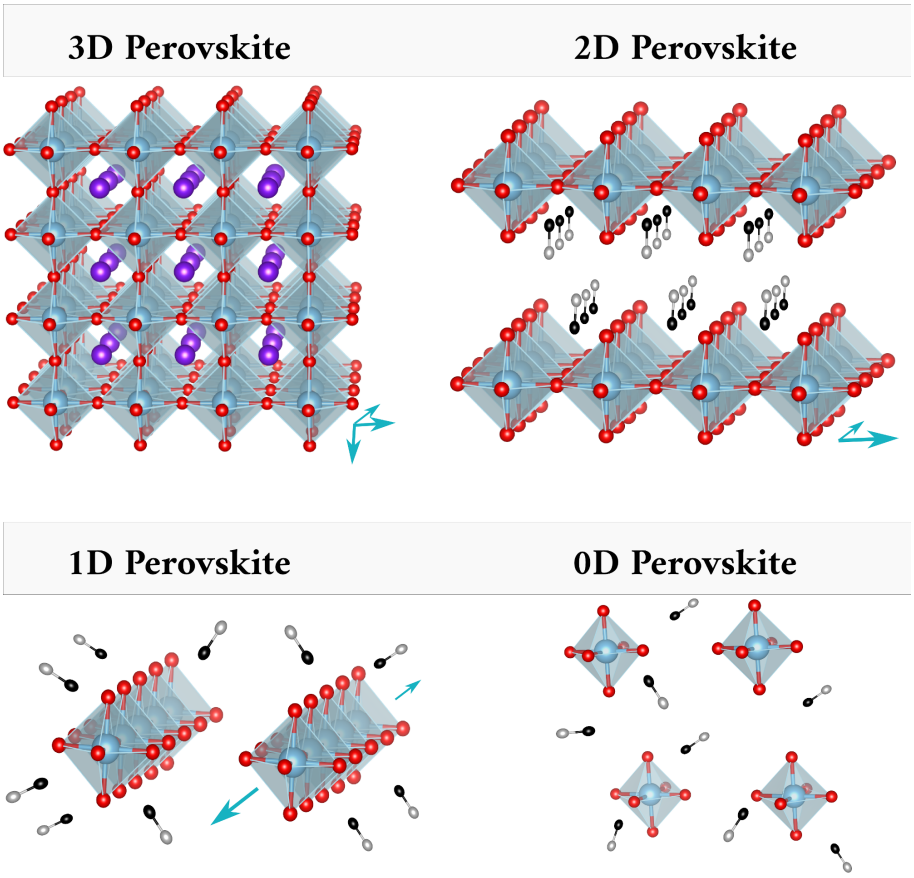

Source: Source: Done by Mailde S. Ozório

presents an effective tolerance factor of 0.98. Despite being a good starting point for ions selections, the effective tolerance factor can fail in predicting the structural stability of mixed perovskite. Indeed, other factors play a decisive role in determining the intrinsic stability, such as the absence of purity and ion migration.[32]

1.3.1 Three-Dimensional Halide Perovskites

Among three-dimensional (3D) halide perovskites, the archetypal methylammonium lead iodide ($MAPbI_3$) structure has been widely studied and also motivated studies of its derivatives, in part due to their fast-growing efficiency as a light-absorbing layer in solar cells.[3] A myriad of three-dimensional ABX_3 halide perovskite structures has been reported so far. On the basis of *A*-cation composition, the perovskites can be hybrid organic-inorganic or all-inorganic with $MAPbI_3$, and $CsPbI_3$ as respective examples. The most common examples of *A*-cations are methylammonium ($CH_3NH_3^+$, MA), formamidinium ($CH(NH_2)_2^+$, FA), Cs^+ and Rb^+. Examples of *B*-cations are Pb^{2+}, Sn^{2+}, Ge^{2+} and Cu^{2+},[13,42] which also can be alloyed. Lead replacement by lead-free alternatives has been a straightforward strategy to eliminate the toxicity of perovskite

materials. In its turn, in perovskite materials for photovoltaic applications, the X-site usually stands for halide ions (Cl^-, Br^- and I^-), a mixture of them,[75] or either the mixture of halide with other ions, such as thiocyanate and tetrafluoride.[79,80] The changes in halide composition usually result in a wide response to the optoelectronic properties (e.g., the optical absorption wavelength).[32] Due to their high reactivity, F rarely occurs, but some compounds have been reported experimentally.[81]

Due to problems of toxicity and stability of lead-halide single $A^+Pb^{2+}X_3$ perovskites, the 3D lead-free halide double perovskite $A_2^+B^+B'^{3+}X_6$ structures have been garnering increasing interest, for instance, the class of Cs_2AgBiX_6 perovskites, where two Pb-bivalent cation is substituted by a monovalent (B^+) and a trivalent cation (B^{3+}), while X usually represent one or more halide elements.[82–84] These structures share the same 3D inorganic-framework connectivity of the $A^+B^{2+}X_3$ structures, but within an increased flexibility due two different corner-sharing octahedra units, i.e., each BX_6 unit is surrounded by six $B'X_6$ units and vice-versa.[85] Another example of 3D structure has a $A_2^+B^{4+}X_6$ general formula (e.g., Cs_2SnI_6[86] and Cs_2PtI_6[87]), and they are vacancy ordered perovskite-like structures because they do not have similar 3D corner-sharing BX_6 octahedra of a conventional perovskite structure.[88]

1.3.2 Low-Dimensional Halide Perovskites

One additional avenue to address the toxicity and stability issues of archetypal perovskite is to move towards lead-free low-dimensional perovskite, which has promising prospects because of their increased structural flexibility, i.e., varied shapes and sizes compared to the 3D ones. Low-dimensional perovskites have inorganic octahedra interspersed by organic cations in one, two or three directions, creating two-dimensional perovskites (2D)[89,90] threads (one-dimensional perovskites, 1D),[91,92] or simply small interspersed octahedra clusters (zero-dimensional perovskites, 0D).[1,93] 2D halide perovskites include nanosheets and nanoplatelets; nanowires and nanorods are archetypal examples of 1D perovskites; 0D perovskites include nanoparticles and quantum dots (QD),[94] where quantum dots solar cells fabricated with $Cs_{0.5}FA_{0.5}PbI_3$ presented certified PCE of 16.6 eV in a short time.[95]

2D perovskites are generally derivative of 3D structures by slicing along one crystallographic plane.[88] Ruddlesden–Popper hybrid organic-inorganic 2D halide perovskites has the general $A'_2A_{n-1}B_nX_{3n+1}$ chemical formula, where A' represents a bulky aromatic or long-chain aliphatic alkylammonium spacer cation with a huge library of possibilities (e.g., 2-phenylethylammounium (PEA) and butylammonium (BA)), while A stands for monovalent cations (e.g., MA and FA), B is usually a divalent cation (e.g. Sn^{2+} and Ge^{2+}), X represents a halide, and n refers to the number of inorganic-octahedra layers.[96] The stability of those 2D perovskites tends to decrease as large as the number of

layers. The electron mobility reduces with the reduction of the number of layers, which yields the bandgap energy to become large and not desirable for some particular applications, such as solar cell absorbing layer. Among 2D perovskites, the double perovskite derivatives have been found of considerable interest. 2D low-dimensional halide double perovskites consist of layered sheets of alternated corner-sharing BX_6 and $B^{'}X_6$ units, and they are derivatives from the respective 3D $A_2BB^{'}X_6$ double perovskites by taking a slice along a particular plane.[97] Another type of layered double perovskites experimentally observed have the $A_4M^{+2}B_2^{3+}X_{12}$ general formula, e.g., $Cs_4CuSb_2Cl_{12}$.[98]

One-dimensional perovskites can display one-dimensional corner-, edge-, and face-sharing metal-halide connectivity.[76,88] 1D perovskites allow larger structural versatility than their 3D counterparts because they can accommodate organic cations of different lengths in addition to the inorganic and small organic cations. Many 1D perovskites have been reported, for instance, hybrid organic-inorganic structures $C_4N_2H_{14}PbBr_4$,[99] and all-inorganic structures $CsCu_2X_3$ ($X = Cl^-$, Br^- or I^-).[100] All-inorganic 1D perovskites show increased structural stability because of the absence of organic moieties degradation compared to the hybrid ones. However, despite the wide structural versatility, research in this class of low-dimensional perovskites is still in the initial stage.[76]

In its turn, many lead-based hybrid organic-inorganic 0D perovskites revealed outstanding white,[101] blue-violet,[102] and blue[103] light emission. Among all-inorganic ones, many studies have been focused in the class of lead-based Cs_4PbBr_6 0D perovskite,[104–108] which have singular properties, including super-paramagnetism of green emission crystals,[107] improved stability, intrinsic emission of Pb-cation, and higher exciton binding energy.[109] Overall, the increased quantum confinement effects of low-dimensional perovskite result into different electronic properties than of 3D counterparts,[20,21] and as a result, a wide range of new applications, including spintronics,[110] light-emitting diodes,[111] lasers,[112] catalysts,[113] X-Ray and γ-Ray detection[114] and capacitors.[115]

The non-toxic Sb^{3+} and Bi^{3+} are prominent inside octahedron of 0D perovskites, i.e., antimony and bismuth (B) form stable halide-anionic complexes with a large variety of size and shapes, e.g., isolated octahedron (BX_6^{3-}),[116,117] edge-sharing ($B_2X_{10}^{4-}$),[113,118] and face-sharing ($B_2X_9^{3-}$).[1] Hybrid and all-inorganic 0D perovskites turned up with photoluminescence quantum yields[118,119] increased air-stability,[93] and high-exciton-binding energy features.[120] The structural versatility of the organic/inorganic cations and the halide-anionic complexes have a significant role in these features. As a result, several works have explored different applications for low-dimensional Bi-based perovskites, including solar cells,[121,122] capacitors,[115] photodetectors[123] and X-Ray imaging.[124] In particular, two face-sharing $Bi_2I_9^{3-}$ octahedra perovskites, the MA_3BiI_9 and $Cs_3Bi_2I_9$ 0D perovskites displayed PCE of 1.64 %[121] and 3.00 %,[122] respectively.

Hydrophobic interactions between the organic cations and inorganic octahedra can

boost the stability of low-dimensional perovskite structures by avoiding the physisorption of oxygen and water molecules.[26] On the other hand, compared to the traditional 3D structures, the PCE decrease in the low-dimensional perovskites,[125] which is a consequence of the reduction of carrier mobility caused by the quantum confinement effects promoted by the organic components' interspersion. In this context, a construction based on the mixing of different dimensionality structures emerges as one suitable route to overcome the reduction of efficiency of low-dimensional perovskites.[125] To that finality, it is important to find an in-depth understanding of the properties behind the features of low-dimensional perovskites. In particular, the vast structural flexibility of 0D perovskites suggests their potential for being included in these constructions.[126] Therefore, there is a great interest in investigating and designing new 0D perovskites materials for photovoltaics applications.

1.4 Open Questions

Perovskite is one of the hottest topics of research, which features suggest a myriad of applications. However, the perovskite field has many unanswered questions, which include the design of stable, efficient, and durable perovskite solar cells under operating conditions. It is important to achieve a better understanding of the mechanisms triggering the useful perovskite features, and the limitations hindering their optoelectronic applications. Despite many works worldwide to overcome related issues, even the most studied perovskites are not yet completely understood.[127] As a result, this stimulated the interest in the low-dimensional perovskites, which requires further theoretical and experimental investigations to explore their broad properties that arise from their structural versatility. From the experimental side, better fabrication methods are desirable for obtaining defect-free or defect-tolerant bulk crystals, as well as thin films of high quality. From a theoretical perspective, it is urgent a further understanding of perovskite materials, which includes the discovery and design of materials and establishing the link between mechanism, functionality, and structure.[88] Inter-facial processes, multi-scale dynamics, and crystal engineering were suggested as the next step of halide perovskite atomistic simulations.[128]

1.5 Objectives

Given the issues associated with employing lead in perovskite technologies, much effort has been done towards the design of lead-free and stable perovskite structures. In particular, our main goals were the investigation of lead-free materials with different structures, namely, tin iodide $A\mathrm{SnI_3}$ perovskites, and the characterization of three novel zero-dimensional (0D) structures, which were experimentally determined by X-Ray diffraction analysis. Two of those 0D structures were employed as a model to understand the physical-chemical effects of replacing the inorganic sites of zero-dimensional perovskite structures. Below is a brief description of the goals achieved in this Ph.D. thesis.

- ***A*SnI$_3$ Perovskites:** We investigated changes in the physical-chemistry properties of ASnI$_3$ perovskites induced by orientation/alignment of the A-cations in the inorganic cage of different polymorphic ASnI$_3$ phases (cubic, tetragonal, orthorhombic, and hexagonal). This work resulted in one scientific paper untitled "*The role of the A-cations in the polymorphic stability and optoelectronic properties of lead-free ASnI$_3$ perovskites*".[129] The main results of this work are given in Chapter 3.

- **Novel Zero-dimensional Perovskites:** As a result of a theoretical-experimental effort, we investigated for the first time three new zero-dimensional perovskite structures, namely, $C_{20}H_{20}N_4Bi_2I_{10}$, $C_{42}H_{39}N_6Bi_2I_9$ and $C_{30}H_{25}N_6BiI_6.2\,H_2O$ 0D perovskites, in which octahedra morphology changes from one system to another. The results were published under the title "*Novel Zero-dimensional Lead-free Bismuth Based Perovskites: From Synthesis to Structural and Optoelectronic Characterization*".[1] In this thesis we present the theoretical results regarding the structural, electronic, and optical properties of these three new 0D lead-free bismuth-based perovskites (see Chapter 4).

- **Effect of Halide Anionic Complex:** By considering the experimental-determined $C_{20}H_{20}N_4Bi_2I_{10}$ and $C_{30}H_{25}N_6BiI_6.2\,H_2O$ structures as models, we investigate the effect of Bi^{3+} and I^- substitution of in the structural, electronic, energetic and optical properties. We considered Sb^{3+}/(Cl^- and Br^-) as a replacement of Bi^{3+}/I^- sites. Those substitutions allowed a better understanding of the role of the halide anionic complex in the physical-chemical properties of 0D perovskites. The results were published under the name "*Theoretical Investigation of the Role of Anion and Trivalent Cation Substitution in the Physical Properties of Lead-Free Zero-Dimensional Perovskites*".[2] The theoretical results are given in Chapter 5.

2 METHODOLOGY

In this thesis, the methodology is organized in the following sections: (*i*) Many-body problem, (*ii*) Born-Oppenheimer approximation, (*iii*) Density-functional theory, (*iv*) Periodic-boundary conditions, and (*v*) Projector-augmented-wave method (PAW).

2.1 Many-Body Problem

Quantum mechanics allow a better understanding of matter through the description of the material properties at the microscopical-atomistic level. In particular, the quantum mechanics formalism presents essential strategies to explore multi-electronic systems, which comprise the use of the Schrödinger equation to solve a problem of N electrons and M nuclei, i.e., the many-body problem. The many-body Hamiltonian of the time-independent Schrödinger equation is given by:

$$\hat{H}\Psi_k(\{\mathbf{r}_i\},\{\mathbf{R}_j\}) = E_k\Psi_k(\{\mathbf{r}_i\},\{\mathbf{R}_j\}), \tag{2.1}$$

where $\{\mathbf{r}_i\} = \mathbf{r}_1$, $\mathbf{r}_2$, ...,$\mathbf{r}_N$, and $\{\mathbf{R}_j\} = \mathbf{R}_1$, $\mathbf{R}_2$, ...,$\mathbf{R}_M$ represent, respectively, the set of all electronic and nuclear spatial coordinates. $\Psi_k(\{\mathbf{r}_i\},\{\mathbf{R}_j\})$ is the wave function that describes the many-body system, and E_k represents the energy eigenvalue. Finally, $\hat{H}$ represents the non-relativistic Hamiltonian operator, which is given by $\hat{H} = \hat{T}_n + \hat{T}_e + \hat{V}_{ne} + \hat{V}_{nn} + \hat{V}_{ee}$, where the two first right-side terms are kinetic energy operators, $\hat{T}_n$ representing the nuclei kinetic energy and $\hat{T}_e$ the electron kinetic energy. The last three represent the Coulomb electrostatic interactions, where $\hat{V}_{ne}$, $\hat{V}_{nn}$ and $\hat{V}_{ee}$ indicate, in this order, the nuclei-electron attraction, the nuclei-nuclei, and electron-electron repulsion. The mathematical expression of the kinetic energy and Coulomb electrostatic interaction operators, in atomic units,[1] are given by

$$\hat{T}_n = -\frac{1}{2}\sum_{i=1}^{M}\frac{\nabla^2_{\mathbf{R}_i}}{M_i}\ , \qquad \hat{T}_e = -\frac{1}{2}\sum_{i=1}^{N}\nabla^2_{\mathbf{r}_i}$$

$$\hat{V}_{ne} = -\sum_{i=1}^{N}\sum_{j=1}^{M}\frac{Z_j}{|\mathbf{r}_i-\mathbf{R}_j|}\ , \quad \hat{V}_{nn} = \sum_{i=1}^{M}\sum_{j>i}^{M}\frac{Z_iZ_j}{|\mathbf{R}_i-\mathbf{R}_j|} \quad \text{and} \quad \hat{V}_{ee} = \sum_{i=1}^{N}\sum_{j>i}^{N}\frac{1}{|\mathbf{r}_i-\mathbf{r}_j|}\ , \tag{2.2}$$

where Z_i and Z_j represent, respectively, the charges of i and j nuclei.

2.2 Born-Oppenheimer Approximation

The Schrödinger equation has analytical solutions for simple systems with non-complicated Hamiltonian form, such as hydrogen atoms, isoelectronic species, free

[1] Atomic units $\hbar = 1,\ m_e = 1,\ e = 1$ and $4\pi\epsilon_0 = 1$

particles, and the harmonic oscillator. However, numeric methods and approximations are required to solve the time-independent Schrödinger equation for complicated multiple-electronic systems. Among several procedures for solving the time-independent Schrödinger equation of multi-electronic systems (systems composed of many N electrons and M nuclei, e.g., clusters, molecules, nanoparticles, and condensed state solid materials), one comprises the approximation performed by the splitting of many-body wave functions into two parts, i.e., one for the electronic (ψ), and other for nuclear (χ) that satisfy the $\Psi_k(\{\mathbf{r}_i\};\{\mathbf{R}_j\}) = \psi(\{\mathbf{r}_i\},\{\mathbf{R}_j\}')\chi(\{\mathbf{R}_j\})$ product.

The mentioned procedure is well-known as the Born-Oppenheimer approximation (BO-approximation) in honor of its developers, Max Born and J. Robert Oppenheimer.[130] The BO-approximation is valid when there is a negligible coupling between nuclear and electronic states, in other words, when the electronic-vibrational decoupling occurs. The justification for the BO-approximation arises from the relative velocity of electron and nuclei, i.e., since nuclear mass is around 1800× higher than the electron mass, the nuclei move slower than electrons. Thus, according to the slow change of nuclear coordinate, the electronic cloud instantly follows the motion of nuclei. Hence, the electronic distribution is obtained for a set of fixed nuclei coordinates in the context of the BO-approximation. The function χ depends only on the nuclear coordinates, and for each nuclear coordinates exists one corresponding wave function. Similarly, ψ depends on the electronic coordinates, and it is parametrically dependent on nuclei coordinates. Consequently, each set of fixed nuclear positions determines one different electronic wave function.

For each set of nuclei coordinates the nuclear kinetic energy can be neglected and Coulomb's potential for nuclear repulsion, $\hat{V}_{nn}$, becomes just an additive constant in the electronic Hamiltonian ($\hat{H}_e + \hat{V}_{nn}$, where $\hat{H}_e$ has only the contributions of N electrons in an electric field generated by M fixed nuclei, i.e., $\hat{H}_e = \hat{T}_e + \hat{V}_{ne} + \hat{V}_{ee}$). Therefore, in the BO-approximation, finding the total energy of a system composed of N electrons and M-fixed nuclei consists of solving the following Schrödinger equation: $\left[\hat{H}_e + \hat{V}_{nn}\right]\Psi_k(\{\mathbf{r}_i\},\{\mathbf{R}_j\}) = E_k(\{\mathbf{R}_j\})\Psi(\{\mathbf{r}_i\},\{\mathbf{R}_j\})$, where the $\hat{V}_{nn}$ operator becomes just an additive constant to the total energy of the system, which is given by: $E_k(\{\mathbf{R}_j\}) = \varepsilon_k(\{\mathbf{R}_j\}) + \hat{V}_{nn}$, where $\varepsilon_k(\mathbf{R}_j)$ represents the eigenvalue that satisfies the following electronic equation: $\hat{H}_e\psi(\{\mathbf{r}_i\},\{\mathbf{R}_j\}') = \varepsilon_k(\mathbf{R}_j)\psi(\{\mathbf{r}_i\},\{\mathbf{R}_j\}')$, where $\mathbf{R}'$ represents that the electronic wave functions parametrically depend on the nuclei coordinates. Hence, due to the decoupling of the global wave function, it is possible to solve the time-independent electronic Schrödinger equation without solving the respective nuclear Schrödinger equation.

2.3 Density-Functional Theory

Density functional theory (DFT) is a well-succeeded quantum mechanic technique that allows predicting useful information from matter through computational simulations.

Instead of many-electron wave functions, DFT is based on electronic density to predict the stationary ground state energy of electronic structures $\rho(\mathbf{r})$.[131] One of the major advantages of DFT front of the wave-function approaches is the computation time. Neglecting the spin coordinates, the wave functions depend on $3N$ (where N is the number of electrons) spatial coordinates, and the use of electronic density allows to reduce a problem of $3N$ degrees of freedom for one, the electron density $\rho(\mathbf{r})$ with only 3 spatial variables (x, y, z). In systems with many atoms, this approach becomes computationally more feasible than methods based on wave functions. As a result of the low computational cost and good experimental-theoretical agreement for many simulated materials, the DFT[132,133] has been employed to characterize the properties of several materials, including clusters,[134] and solid-state systems at the atomistic level.[1,2,129]

2.3.1 Hohenberg-Kohn Theorems

The starting point of DFT comes from two fundamental theorems formulated by Pierre Hohenberg and Walter Kohn in the 1960's decade.[132] These theorems, so-called Hohenberg-Kohn theorems, consider a system composed of N interacting electrons driven by the many-body Hamiltonian. They say:

Theorem 01 *the ground state of any interacting many-particles system is a unique functional of the electron density ρ_0 of the ground-state density, $|\psi_0\rangle = |\psi[\rho_0]\rangle$.*

Theorem 02 *A universal functional for energy in terms of density $\rho(\mathbf{r})$ can be defined for any external potential $V_{ext}(\mathbf{r})$. For a given external potential, the exact energy of the ground-state is the global minimum of this functional, and the density that minimizes the functional is the exact ground-state density.*

The first theorem establishes that exists an one-to-one correspondence between the external potential $v(\mathbf{r})$ and the ground-state density $\rho(\mathbf{r})$ of a N interacting electron cloud. Any change in potential affects the electron density, but the density will be kept constant if the external potential is unchanged. Thus, up to an additive constant, the ground-state density corresponds to a unique external potential and one wave function. Besides determining the external potential, the density determines the total number of N electrons by integration,

$$\int \rho\left(\mathbf{r}\right) d\mathbf{r} = N \ , \tag{2.3}$$

and implicitly all properties determined by the Hamiltonian in a BO-approximation,[131] for instance, the ground state energy. The proof of the first theorem comes from the *reductio ad absurdum* procedure. It assumes that two different external potentials yield the same ground-state density. From these conditions, an *absurdum* relation (i.e., $E_0 + E_0^{'} < E_0 + E_0^{'}$) is found, which shows that two different external potentials do not have the same ground-state density.

For a gaseous system composed of N interacting electrons, the total energy as a function of electron density can be expressed by $E[\rho(\mathbf{r})] = V_{ext}[\rho(\mathbf{r})] + F_{\mathrm{HK}}[\rho(\mathbf{r})]$, where $V_{ext}[\rho(\mathbf{r})]$ gives the external potential contribution generated by the M nuclei and $F_{\mathrm{HK}}[\rho(\mathbf{r})]$ represents the universal Hohenberg–Kohn functional, which corresponds to the sum of the kinetic energy, $T[\rho(\mathbf{r})]$, and the electronic repulsion, $V_{ee}[\rho(\mathbf{r})]$, in an interacting electron gas ($F_{\mathrm{HK}}[\rho(\mathbf{r})] = T[\rho(\mathbf{r})] + V_{ee}[\rho(\mathbf{r})]$).

According to the second theorem, $E[\rho(\mathbf{r})] \geq E[\rho_0(\mathbf{r})] \equiv E_0$, i.e., the electron density that minimizes the total energy functional is the ground-state density ($\rho_0(\mathbf{r})$), where E_0 represents the energy of the ground state. However, in the Hohenberg-Kohn formalism, the exact expression of $F_{\mathrm{HK}}[\rho(\mathbf{r})]$ is not known, which makes necessary an approximation for obtaining the energy. This problem was solved in a formalism proposed by Kohn-Sham.

2.3.2 Kohn-Sham Formalism

The formalism proposed by Walter Kohn and Lu Sham in 1965, the so-called Kohn-Sham method,[133] consists of describing a system composed of N non-interacting electrons with the same electron density of the real system. In this formalism, the total electronic energy is partitioned as follows:

$$E[\rho(\mathbf{r})] = \sum_{i=1}^{N} \left\langle \phi_i^{\mathrm{KS}}(\mathbf{r}) \left| -\frac{1}{2}\nabla^2 \right| \phi_i^{\mathrm{KS}}(\mathbf{r}) \right\rangle + \frac{1}{2} \iint \frac{\rho(\mathbf{r})\rho(\mathbf{r}')}{|\mathbf{r}-\mathbf{r}'|} d\mathbf{r} d\mathbf{r}' + \\ + \int \rho(\mathbf{r}) v(\mathbf{r}) d\mathbf{r} + E_{xc}[\rho(\mathbf{r})] \ , \tag{2.4}$$

the first term of the equation represents the kinetic energy, which is obtained by Kohn–Sham orbitals (ϕ^{KS}), which determine the electronic density through the $\rho(\mathbf{r}) = \sum_{i=1}^{N} f_i |\phi_i^{\mathrm{KS}}(\mathbf{r})|^2$ expression, where f_i is the occupation of electronic states. The second term of the equation (2.4) is the Hartree's potential energy, while the third term represents the interaction energy between the electron density, $\rho(\mathbf{r})$, and the field created by M static nuclei. Finally, the fourth term includes the exchange energy, electronic correlation, a correction for electron self-interaction in Hartree potential, and a correction for kinetic energy because of the difference between the non-interacting electron system and the real system.

According to the second Hohenberg-Kohn theorem, the global minimum of the energy (equation (2.4)) comes from the exact ground-state density, but the energy functional can also be minimized concerning the Kohn-Sham orbitals using the orthogonality condition

$$\int \phi_i^{\mathrm{KS}}(\mathbf{r})^* \phi_j^{\mathrm{KS}}(\mathbf{r}) d\mathbf{r} = \delta_{ij} \ , \tag{2.5}$$

The minimization of the energy functional is given by

$$\delta \left[E[\phi_i^{\mathrm{KS}}(\mathbf{r})] - \sum_{i=1}^{N} \sum_{j=1}^{N} \epsilon_{ij} \left(\int \phi_i^{\mathrm{KS}}(\mathbf{r})^* \phi_j^{\mathrm{KS}}(\mathbf{r}) d\mathbf{r} \right) \right] = 0 \ , \tag{2.6}$$

Figure 4 – Kohn-Sham self-consistent field.

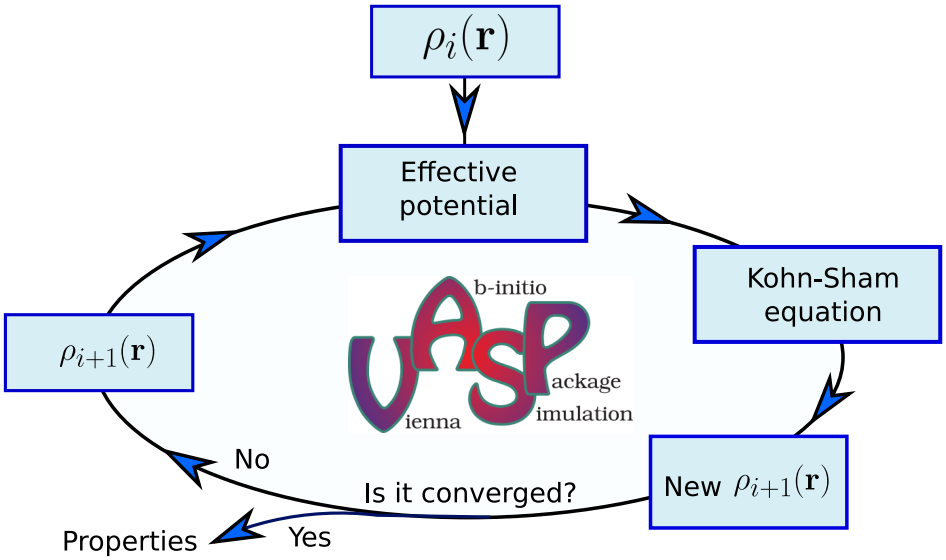

Source: **Source:** Done by Mailde S. Ozório

where ϵ_{ij} represents Lagrange multipliers. Performing a variational calculation, one obtains a set of single-particle Schrödinger equations, which originate the so-called Kohn-Sham equations given by

$$\left[-\frac{1}{2}\nabla^2_{\mathbf{r}} + V_{eff}(\mathbf{r})\right]\phi_i^{\mathrm{KS}}(\mathbf{r}) = \epsilon_i^{\mathrm{KS}}\phi_i^{\mathrm{KS}}(\mathbf{r}) \ , \tag{2.7}$$

$$V_{eff}(\mathbf{r}) = v(\mathbf{r}) + \int \frac{\rho(\mathbf{r})}{|\mathbf{r}-\mathbf{r}'|}d\mathbf{r}' + \frac{\delta E_{xc}[\rho(\mathbf{r})]}{\delta\rho(\mathbf{r})} \ , \tag{2.8}$$

where $V_{eff}(\mathbf{r})$ is the effective Kohn–Sham potential, which is composed of three potentials that are the same for all electrons in the system. The first represents the external potential, the second the Hartree potential, and the last one the exchange-correlation potential.

As shown in Figure 4, the KS equations must be self-consistently solved. The initial-trial electron density, $\rho_i(\mathbf{r})$, is used to generate the effective potential that determines the Kohn-Sham single-particle orbitals, which are used to obtain a new density $\rho_{\mathrm{i+1}}(\mathbf{r}) = \sum_{i=1}^{N} f_i|\phi_i^{\mathrm{KS}}(\mathbf{r})|^2$ (where $i+1$ changes within the cycle completion). This procedure is repeated until the convergence criteria are satisfied with no difference between the two consecutive electron densities. From the converged results, one obtains the ground-state density, which gives the KS orbitals, the potentials, and all remaining observables.

Hence, Kohn-Sham proposed one interesting way to determine the kinetic-energy from a non-interacting electron system by considering the anti-symmetry of the wave function, and the electronic density can be determined by the Kohn-Sham orbitals.

2.3.3 Exchange-Correlation Functionals

In principle, DFT provides the exact solution to the electronic many-body problem. However, the exact formula of the universal exchange-correlation functional ensured by the Hohenberg-Kohn theorem is not known. Therefore, several approaches have been developed to describe the exchange-correlation functional. This section describes only the approximations used in this project, the Generalized Gradient Approximation (GGA)[135] and the hybrid HSE06.[136–139]

The GGA approximation is a semi-local approach that considers the local electron density at the point $\mathbf{r}$ and the gradient of the density at the same $\mathbf{r}$ point. We have the equation

$$E_{xc}^{\mathrm{GGA}}[\rho(\mathbf{r})] = \int \rho(\mathbf{r}) f_{xc}(\rho(\mathbf{r}), |\nabla\rho(\mathbf{r})|) d\mathbf{r} \ , \tag{2.9}$$

where the form of the f_{xc} function is not unique, therefore it is the differential among different formulations, e.g., Perdew-Wang functional (PW91), and Perdew–Burke–Ernzerhof functionals (PBE, PBEsol).

The hybrid HSE06 functional is derived from the hybrid PBE0 functional,[140] which has the following form,

$$E_{xc}^{\mathrm{PBE0}} = 0.75{\times}E_{x}^{\mathrm{PBE}} + 0.25{\times}E_{x}^{\mathrm{HF}} + E_{c}^{\mathrm{PBE}} \ , \tag{2.10}$$

where E_x^{PBE} and E_c^{PBE} are the exchange and correlation contributions from the semilocal PBE functional. The PBE0 functional has 25% of the exchange energy of the Hartree-Fock method, that is 25% of

$$E_{x}^{\mathrm{HF}} = \sum_{j=i}^{N}\sum_{i=1}^{N} \int\int \phi_i^{\mathrm{KS}}(\mathbf{r})^* \phi_j^{\mathrm{KS}}(\mathbf{r}')^* \frac{1}{|\mathbf{r}-\mathbf{r}'|} \phi_i^{\mathrm{KS}}(\mathbf{r}') \phi_j^{\mathrm{KS}}(\mathbf{r}) d\mathbf{r} d\mathbf{r}' \ , \tag{2.11}$$

where $\phi_i(\mathbf{r})^{\mathrm{KS}}$ and $\phi_j(\mathbf{r})^{\mathrm{KS}}$ are Kohn-Sham orbitals. In the HSE06 functional the non-local term E_x^{HF} has a short-range (SR) and a long-range (LR) contribution. Due to the small non-local dependency, the long-range contribution can be represented by the semi-local contribution of the PBE potential. Therefore, the HSE06 functional can be expressed by

$$E_{xc}^{\mathrm{HSE06}} = 0.75{\times}E_{x}^{\mathrm{PBE,SR}}(\omega) + 0.25{\times}E_{x}^{\mathrm{HF,SR}}(\omega) + E_{x}^{\mathrm{PBE,LR}} + E_{c}^{\mathrm{PBE}} \ , \tag{2.12}$$

where the term $E_x^{\mathrm{PBE,\,LR}}$ represents the long-range semi-local contribution, while $E_x^{\mathrm{PBE,\,SR}}(\omega)$ and $E_x^{\mathrm{HF,\,SR}}(\omega)$ represent, respectively, short-range semi-local and non-local contributions. For $\omega = 0$ the HSE06 functional is equivalent to the PBE0 functional, and for $\omega \to \infty$ it converges asymptotically to the PBE functional. In this project $\omega = 0.11$ bohr^{-1} was used, which provides a balance between quality of results and computational cost.[141]

2.3.4 Van der Waals Corrections

Van der Waals interactions are present in many systems, in particular hybrid perovskites, and they represent a large set of interactions, such as dipole-dipole, a

dipole with induced-dipole, and London dispersion forces.[142] The last corresponds to instantaneously fluctuations of electronic density, which are not accurately described by the local functional (LDA) as well as semi-local functional (e.g., GGA-based functional). Hence, efforts to include those interactions resulted in the development of corrections to the total energy of DFT approach, i.e., the addition of the dispersion energy, E_{disp}, to the KS total energy of a converged calculation: $E_{\mathrm{DFT}} = E_{\mathrm{KS}} + E_{\mathrm{disp}}$.

One of the available methods to obtain the dispersion energy is called DFT-D3,[143] in which the energy dispersion has contributions of two-body ($E^{(2)}$) and three-body ($E^{(3)}$), i.e., $E_{disp} = E^{(2)} + E^{(3)}$. However, the three-body term yields to bad results to lattice parameters and, hence, it is not recommended for solid systems.[144] For this reason, the three-body term is not implemented in the VASP code (Vienna *Ab initio* Simulation package),[145,146] which was the package employed to run the calculations of the current thesis. The terms of DFT-D3 are given by:

$$E^{(2)} = \sum_{XY} \sum_{n=6,8,10,\ldots} s_n \frac{C_n^{XY}}{r_{XY}^n} f_{d,n}(R_{XY}) \quad \text{and} \quad E^{(3)} = \sum_{XYZ} f_{d,(3)}(\bar{R}_{XYZ}) E^{XYZ} \ , \qquad (2.13)$$

where the sum is over all XY pairs in the first equation. To assure the accuracy, s_n is an adjustable factor for all $n > 6$. However, n is truncated in $n = 8$ because for $n > 8$ the results do not have an improvement and the additional term lead to instability for more complicated systems.[143] The term C_n^{XY} corresponds to average coefficient of the n-th order of XY pair, which inter-molecular distance is R_{XY} and, finally, $f_{d,n}$ represents the "damping" function that determines the range of dispersion of energy correction.

2.4 Periodic Boundary Conditions

The structure of a perfect solid system can be interpreted as many connected unit cells that repeat periodically in the crystal forming the Bravais lattice, which is defined by $\mathbf{v}_1$, $\mathbf{v}_2$ and $\mathbf{v}_3$ translation vectors ($\mathbf{T} = a_1\mathbf{v}_1 + a_2\mathbf{v}_2 + a_3\mathbf{v}_3$, with a_i integer numbers). Hence, the atoms of the unit cells have a new position $\mathbf{r}'$ when translated from the initial position $\mathbf{r}$ by the translation vector $\mathbf{T}$, i.e., $\mathbf{r}' = \mathbf{r} + \mathbf{T}$ and the solid is invariant to the translation vector. The periodic potential at $\mathbf{r}$ must be equal at $\mathbf{r}'$, i.e. the relation $U(\mathbf{r}) = U(\mathbf{r} + \mathbf{T})$ must be satisfied in a periodic system.

As a consequence of the Blöchl Theorem, due to the periodicity of the system given by $u_{n,\mathbf{k}}(\mathbf{r})e^{i\mathbf{k}\,\cdot\,\mathbf{r}} = u_{n,\mathbf{k}}(\mathbf{r}+\mathbf{T})e^{i\mathbf{k}\,\cdot\,\mathbf{r}}$, the Kohn-Sham eigenfunctions $\psi(\mathbf{r})$ of a periodic system can be described by the product $\psi(\mathbf{r}) = u_{n,\mathbf{k}}(\mathbf{r})e^{i\mathbf{k}.\mathbf{r}}$ of a plane wave function $e^{i\mathbf{k}.\mathbf{r}}$, and a periodic function $u_{\mathbf{k}}(\mathbf{r})$. In these equations, the $\mathbf{k}$ wave vectors are related to the crystal momentum and for each $\mathbf{k}$ exists a set of solutions, which can be indicated by a band index n. The $\mathbf{k}$ vector set forms the reciprocal space, whose associated primitive cell is well-known as the first Brillouin zone. Any periodic properties of real space can be represented in the reciprocal space, e.g., a translation vector $\mathbf{G}$ can be easily defined as

$\mathbf{G} = h_1\mathbf{g}_1 + h_2\mathbf{g}_2 + h_3\mathbf{g}_3$, with h_i and $\mathbf{g}_i$, respectively, integer numbers and primitive wave vectors in the reciprocal space; and finally the periodic function can be rewritten as:

$$\psi_{n,\mathbf{k}}(\mathbf{r}) = \frac{1}{\sqrt{\Omega}} \sum_{\mathbf{G}}^{\frac{1}{2}|\mathbf{k}+\mathbf{G}|^2 \leq E_c} c(\mathbf{k}+\mathbf{G}) e^{i(\mathbf{k}+\mathbf{G})\cdot\mathbf{r}} \ , \tag{2.14}$$

where $\mathbf{k}$ and Ω represent, respectively, the wave vectors and the volume of unit cell of the first Brillouin zone. The optimization of $c(\mathbf{k}+\mathbf{G})$ is the key-point to the total energy minimization, and, just the periodic functions with the kinetic energy lower than the cutoff energy ($\frac{1}{2}|\mathbf{k}+\mathbf{G}|^2 \leq E_c$) are included in the basis set. Thus, the total energy ($E_\mathbf{k}$) are given by the sum of the kinetic energy contribution and the effective potential $V_{eff}(\mathbf{G})$, i.e., $E_\mathbf{k} = \frac{1}{2}|\mathbf{k}+\mathbf{G}|^2 \leq E_c + V_{eff}(\mathbf{G})$.

2.5 Projector Augmented Wave Method

Due to the high kinetic energy of electrons close to the nuclei region, the application of plane waves to describe the core electrons becomes an enormous challenge for periodic systems calculations. However, since the core electrons have a minor role in the physical-chemistry properties of the materials compared to the valence electrons, many methods have been developed to turn such calculations more reasonable. Among these methods are the pseudo-potential (PP), linear augmented plane-wave (LAPW), and one of the most important, the so-called Projector Augmented Wave (PAW) method, which brings ideas from both PP and LAPW methods, i.e., the PAW method is an all-electron method that combines ideas that comes from the LAPW linear method with the simplicity of the pseudo-potential approach.

In particular, the PAW is an *ab initio* electronic structure calculations technique developed by P. E. Blöchl.[147] PAW is an exact implementation technique for *ab initio* density functional theory calculations, and it is implemented in a large number of codes for electronic structures calculations, e.g., VASP, ABINIT, and Quantum EXPRESSO. The PAW method allows greater computational cost-efficiency for density functional theory calculations by considering local and semi-local auxiliary wave functions to build Kohn-Sham orbitals with the correct description of regions close to nuclei in addition to the behavior of the plane waves for valence electrons. It defines a spherical region with radius R^n around each nucleus (n), where R^n is the delimiting frontier between an augmented region (inside the sphere) and an interstice region (outside the sphere). Since one wave function is used to describe both regions, the PAW procedure can be characterized as an all-electron method, but the wave functions inside and outside the sphere have different descriptions.

2.5.1 The Linear Transforming Operator

In the PAW method, the electrons of the augmented region are described by auxiliary wave functions ($\tilde{\Psi}_n$), while electrons outside the augmented region are described by the all electron wave function Ψ_n. This method is possible because the KS orbitals are expanded in plane waves, where the wave function of a single electron (Ψ_n) is obtained through the linear transformation of an auxiliary wave function ($\tilde{\Psi}_n$), i.e. $|\Psi_n\rangle = \mathcal{T}|\tilde{\Psi}_n\rangle$ with $\mathcal{T} = 1 + \sum_a \sum_i (|\phi_i^a\rangle - |\tilde{\phi}_i^a\rangle)\langle\tilde{p}_i^a|$, which just modifies the wave function of the augmented region. In the end, the wave function that describes the complete system is defined by $|\Psi_n\rangle = |\tilde{\Psi}_n\rangle + \sum_a \sum_i (|\phi_i^a\rangle - |\tilde{\phi}_i^a\rangle) \left\langle \tilde{p}_i^a | \tilde{\Psi}_n \right\rangle$, where (from left-to-right sequence) $|\tilde{\Psi}_n\rangle$ represents the auxiliary wave function; for each atom a, the $|\phi_i^a\rangle$ is the partial wave function in the augmented region, and $|\tilde{\phi}_i^a\rangle$ is an auxiliary pseudo-wave function that cancels the plane waves part of an auxiliary function inside the augmented sphere. Finally, $\tilde{p}_i^a$ represents a projected function, which takes part in the linear transformation $\mathcal{T}$. Hence, the exact wave function in the PAW method is obtained by performing a linear combination of (*i*) auxiliary wave functions, (*ii*) partial wave functions, and (*iii*) subtracting the term added to the plane wave functions in the augmented region.

The behavior of wave functions change depending on the region of space, for instance, rapid oscillations close to the nuclei and a very smooth behavior in the bonding region. In particular, the rapid oscillations of wave functions near the core region is a drawback for simulations of materials due to the increasing demand of computational resources. Hence, the augmented wave methods brought the strategy to solve the difficulties of performing electronic structures calculations by considering the split of wave functions into two parts, i.e., the use of smooth auxiliary wave functions inside an atom-centered sphere and other convenient basis set outside the sphere. For instance, through the PAW method, the first step is to use the linear transformation operator $\mathcal{T}$, which transforms the smooth auxiliary wave function of the core region ($|\tilde{\Psi}\rangle_n$) onto the all-electron wave function for the bonding region ($|\Psi\rangle$), i.e., $|\Psi\rangle_n = \mathcal{T}|\tilde{\Psi}_n\rangle$, and $\mathcal{T}$ takes the form:

$$\mathcal{T} = 1 + \sum_a \mathcal{T}^a \tag{2.15}$$

where a is an atom index, and $\mathcal{T}^a$ is different from zero inside a spherical augmentation region Ω_a enclosing atom a. Inside Ω_a, the smooth auxiliary wave function can be expanded in partial auxiliary waves $\tilde{\phi}_i^a$, i.e., $|\tilde{\Psi}_n\rangle = \sum_i c_{ni}^a |\tilde{\phi}_i^a\rangle$; where c_{ni}^a are expansion coefficients, and for each $\tilde{\phi}_i^a$ exist one all-electron partial wave ϕ_i^a satisfying $|\phi_i^a\rangle = \mathcal{T}|\tilde{\phi}_i^a\rangle$. Thus, since $|\Psi\rangle_n = \mathcal{T}|\tilde{\Psi}_n\rangle$, applying the $\mathcal{T}$ operator to the $|\tilde{\Psi}_n\rangle$ expression

$$\begin{aligned} |\tilde{\Psi}_n\rangle &= \sum_i c_{ni}^a |\tilde{\phi}_i^a\rangle \\ \mathcal{T}|\tilde{\Psi}_n\rangle &= \sum_i c_{ni}^a \mathcal{T}|\tilde{\phi}_i^a\rangle \\ |\Psi_n\rangle &= \sum_i c_{ni}^a |\phi_i^a\rangle \end{aligned} \tag{2.16}$$

we can conclude, due to the linearity of operator $\mathcal{T}$, that both smooth and all-electron wave functions have the same expansion coefficients c^a_{ni}, i.e., $c^a_{ni} = \left\langle \tilde{p}^a_i | \tilde{\Psi}_n \right\rangle$, where $\tilde{p}^a_i$ are smooth projector functions that must satisfy $\sum_i |\tilde{\phi}^a_i\rangle\langle\tilde{p}^a_i| = 1$ and $\langle \tilde{p}^a_i | \tilde{\phi}^a_j \rangle = \delta_{ij}$ inside each Ω_a region. Outside Ω_a, $\mathcal{T}$ does not modify the wave function. In other words, this imply that $|\Psi\rangle_n \equiv |\tilde{\Psi}_n\rangle$ as well as $\tilde{\phi}^a_i \equiv \phi^a_i$ outside the augmentation region.

From the equality $\sum_i |\tilde{\phi}^a_i\rangle\langle\tilde{p}^a_i| = 1$, we can write:

$$\mathcal{T}^a = \sum_i \mathcal{T}^a |\tilde{\phi}^a_i\rangle\langle\tilde{p}^a_i|. \tag{2.17}$$

Since $|\phi^a_i\rangle = \mathcal{T}|\tilde{\phi}^a_i\rangle$, it follows that $|\phi^a_i\rangle = (1 + \sum_{a'} \mathcal{T}^{a'})|\tilde{\phi}^a_i\rangle$, which implies that $|\phi^a_i\rangle = (1 + \mathcal{T}^a)|\tilde{\phi}^a_i\rangle \leftrightarrow \mathcal{T}^a = (|\phi^a_i\rangle - |\tilde{\phi}^a_i\rangle)$ for all i and a. Thus, equation 2.17 becomes:

$$\mathcal{T}^a = \sum_i (|\phi^a_i\rangle - |\tilde{\phi}^a_i\rangle)\langle\tilde{p}^a_i| \tag{2.18}$$

Replacing 2.18 in 2.15, we have:

$$\mathcal{T} = 1 + \sum_a \sum_i (|\phi^a_i\rangle - |\tilde{\phi}^a_i\rangle)\langle\tilde{p}^a_i|. \tag{2.19}$$

Thus, using 2.19, the Kohn-Sham all-electron wave function ($|\Psi\rangle_n = \mathcal{T}|\tilde{\Psi}_n\rangle$) can be written as:

$$|\Psi_n\rangle = |\tilde{\Psi}_n\rangle + \sum_a \sum_i (|\phi^a_i\rangle - |\tilde{\phi}^a_i\rangle) \left\langle \tilde{p}^a_i | \tilde{\Psi}_n \right\rangle, \tag{2.20}$$

which one may represent in the compact way:

$$|\Psi_n\rangle = |\tilde{\Psi}_n\rangle + \sum_a (|\Psi^a_n\rangle - |\tilde{\Psi}^a_n\rangle), \tag{2.21}$$

by introducing two one-center expansions $\Psi^a_n = \sum_i |\phi^a_i\rangle\langle\tilde{p}^a_i|\tilde{\Psi}_n\rangle$ and $\tilde{\Psi}^a_n = \sum_i |\tilde{\phi}^a_i\rangle\langle\tilde{p}^a_i|\tilde{\Psi}_n\rangle$. Or in the simplified notation as shown in the PAW original paper:

$$|\Psi_n\rangle = |\tilde{\Psi}_n\rangle + \sum_i (|\phi_i\rangle - |\tilde{\phi}_i\rangle) \left\langle \tilde{p}_i | \tilde{\Psi}_n \right\rangle. \tag{2.22}$$

In summary, we have:

- $|\phi^a_i\rangle$: the all-electron partial wave functions, which are used as atomic basis-set for the all-electron Kohn-Sham wave function ($|\Psi_n\rangle$) inside the augmentation sphere (Ω_a region).
- $|\tilde{\phi}^a_i\rangle$: smooth auxiliary partial wave function, which are used as basis-set for the smooth auxiliary wave function ($|\tilde{\Psi}_n\rangle$), and coincide with $|\phi^a_i\rangle$ outside the Ω_a region (i.e., $|\tilde{\phi}^a_i\rangle = |\phi^a_i\rangle$).
- $\langle\tilde{p}^a_i|$: smooth projector functions, which satisfy the conditions $\sum_i |\tilde{\phi}^a_i\rangle\langle\tilde{p}^a_i| = 1$ and $\langle \tilde{p}^a_i | \tilde{\phi}^a_j \rangle = \delta_{ij}$ inside each Ω_a region.

2.5.2 Transforming Operators

Due to the role of auxiliary wave function ($\tilde{\Psi}_n$) as a variational parameter, the PAW method allows that observable quantities from the all-electron wave-function Ψ_n be obtained from $\tilde{\Psi}_n$. In other words, by considering the transformation $|\Psi\rangle_n = \mathcal{T}|\tilde{\Psi}_n\rangle$, one expectation value $\langle A\rangle$ obtained as $\langle A\rangle = \sum_n f_n \langle \Psi_n | A | \Psi_n\rangle$ can also be obtained from $\langle A\rangle = \sum_n f_n \left\langle \tilde{\Psi}_n \middle| \tilde{A} \middle| \tilde{\Psi}_n \right\rangle$, where n refers to the band index, f_n to the occupation of the state, and $\tilde{A}$ is given by:

$$\tilde{A} = \mathcal{T}^\dagger \hat{A} \mathcal{T}. \tag{2.23}$$

By replacing equation 2.19 into 2.23, we have:

$$\tilde{A} = \left(1 + \sum_a \mathcal{T}^a\right)^\dagger A \left(1 + \sum_a \mathcal{T}^a\right) = A\left[1 + \sum_a \left(\mathcal{T}^{a\dagger} + \mathcal{T}^a + \mathcal{T}^{a\dagger}\mathcal{T}^a\right)\right] \tag{2.24}$$

Replacing 2.18 into 2.24 (replacing 2.19 into 2.23 gives similar result, but the equations become more complex to be solved), we found:

$$\begin{aligned}\tilde{A} = A\Bigg\{1 + \sum_a \Bigg[&\sum_i |\tilde{p_i}^a\rangle \left(\langle\phi_i^a| - \langle\tilde{\phi}_i^a|\right) + \sum_j \left(|\phi_j^a\rangle - |\tilde{\phi}_j^a\rangle\right)\langle\tilde{p_j}^a| \\ &+ \left(\sum_i |\tilde{p_i}^a\rangle \left(\langle\phi_i^a| - \langle\tilde{\phi}_i^a|\right) \sum_j \left(|\phi_j^a\rangle - |\tilde{\phi}_j^a\rangle\right)\langle\tilde{p_j}^a|\right)\Bigg]\Bigg\}\end{aligned} \tag{2.25}$$

Since $\sum_j |\tilde{\phi}_j^a\rangle\langle\tilde{p}_j^a| = 1$, the equation above can be rewritten as:

$$\begin{aligned}\tilde{A} = A\Bigg\{1 + \sum_a \Bigg[&\sum_i |\tilde{p_i}^a\rangle \left(\langle\phi_i^a| - \langle\tilde{\phi}_i^a|\right) \sum_j |\tilde{\phi}_j^a\rangle\langle\tilde{p}_j^a| + \sum_i \langle\tilde{\phi}_i^a|\tilde{p}_i^a\rangle \sum_j \left(|\phi_j^a\rangle - |\tilde{\phi}_j^a\rangle\right)\langle\tilde{p_j}^a| \\ &+ \left(\sum_i |\tilde{p_i}^a\rangle \left(\langle\phi_i^a| - \langle\tilde{\phi}_i^a|\right) \sum_j \left(|\phi_j^a\rangle - |\tilde{\phi}_j^a\rangle\right)\langle\tilde{p_j}^a|\right)\Bigg]\Bigg\}\end{aligned} \tag{2.26}$$

$$\tilde{A} = A\left\{1 + \sum_a \left[\sum_i \langle\tilde{\phi}_i^a|\tilde{p}_i^a\rangle \sum_j \left(|\phi_j^a\rangle - |\tilde{\phi}_j^a\rangle\right)\langle\tilde{p_j}^a| + \sum_i |\tilde{p_i}^a\rangle \left(\langle\phi_i^a| - \langle\tilde{\phi}_i^a|\right) \sum_j |\phi_j^a\rangle\langle\tilde{p_j}^a|\right]\right\} \tag{2.27}$$

$$\tilde{A} = A\left\{1 + \sum_a \left[\sum_{i,j} |\tilde{p}_i^a\rangle \left(\langle\phi_i^a|\phi_j^a\rangle - \langle\tilde{\phi}_i^a|\tilde{\phi}_j^a\rangle\right)\langle\tilde{p_j}^a|\right]\right\} \tag{2.28}$$

Or more simply (in the original notation):

$$\tilde{A} = A\left[1 + \sum_{i,j} |\tilde{p}_i\rangle \left(\langle\phi_i|\phi_j\rangle - \langle\tilde{\phi}_i|\tilde{\phi}_j\rangle\right)\langle\tilde{p_j}|\right] \tag{2.29}$$

$$\tilde{A} = A + \sum_{i,j} |\tilde{p}_i\rangle \left(\langle \phi_i | A | \phi_j \rangle - \left\langle \tilde{\phi}_i | A | \tilde{\phi}_j \right| \right) \rangle \langle \tilde{p}_j |. \tag{2.30}$$

While the overlap matrix of all-electron representation is given by the unity operator, the overlap operator $\tilde{S}$ of the PAW method is given by ($\tilde{S} = \mathcal{T}^\dagger \mathcal{T}$) the term in square brackets in the equation 2.29:

$$\tilde{S} = 1 + \sum_{i,j} |\tilde{p}_i\rangle \left(\langle \phi_i | \phi_j \rangle - \langle \tilde{\phi}_i | \tilde{\phi}_j \rangle \right) \langle \tilde{p}_j |, \tag{2.31}$$

that reduces to the unity operator if the $\langle \phi_i | \phi_j \rangle = \langle \tilde{\phi}_i | \tilde{\phi}_j \rangle$ condition is imposed. Moreover, the smooth auxiliary wave functions are orthogonal with respect to the overlap operator, i.e. $\langle \tilde{\Psi}_n | \tilde{S} | \tilde{\Psi}_m \rangle = \delta_{nm}$.

2.5.3 Charge Density

We already mentioned before that the expectation value of some operator A in the PAW method can be alternatively obtained as:

$$\langle A \rangle = \sum_n f_n \left\langle \tilde{\Psi}_n \left| \tilde{A} \right| \tilde{\Psi}_n \right\rangle \tag{2.32}$$

From the description of equation 2.30, the equation 2.32 assumes the following form:

$$\langle A \rangle = \sum_n f_n \left\langle \tilde{\Psi}_n \left| \left(A + \sum_{i,j} |\tilde{p}_i\rangle \left(\langle \phi_i | A | \phi_j \rangle - \left\langle \tilde{\phi}_i | A | \tilde{\phi}_j \right| \right) \right\rangle \langle \tilde{p}_j | \right) \right| \tilde{\Psi}_n \right\rangle \tag{2.33}$$

In order to evaluate the charge density ($n(\mathbf{r})$), in the equation 2.33, we determine the expectation value of the real-space projection operator $|\mathbf{r}\rangle\langle\mathbf{r}|$ (i.e., $A = |\mathbf{r}\rangle\langle\mathbf{r}|$).

$$n(\mathbf{r}) = \sum_n f_n \left\langle \tilde{\Psi}_n \left| \left(|\mathbf{r}\rangle\langle\mathbf{r}| + \sum_{i,j} |\tilde{p}_i\rangle \left(\langle \phi_i | \mathbf{r}\rangle\langle\mathbf{r}| \phi_j \rangle - \left\langle \tilde{\phi}_i | \mathbf{r}\rangle\langle\mathbf{r}| \tilde{\phi}_j \right| \right) \right\rangle \langle \tilde{p}_j | \right) \right| \tilde{\Psi}_n \right\rangle, \tag{2.34}$$

which can be written as:

$$\begin{aligned} n(\mathbf{r}) = \sum_n f_n \left\langle \tilde{\Psi}_n | \mathbf{r}\rangle\langle\mathbf{r}| \tilde{\Psi}_n \right\rangle + \sum_{n,(i,j)} f_n \left\langle \tilde{\Psi}_n | \tilde{p}_i \right\rangle \langle \phi_i | \mathbf{r}\rangle \langle \mathbf{r} | \phi_j \rangle \left\langle \tilde{p}_j | \tilde{\Psi}_n \right\rangle \\ - \sum_{n,(i,j)} f_n \left\langle \tilde{\Psi}_n | \tilde{p}_i \right\rangle \left\langle \tilde{\phi}_i | \mathbf{r} \right\rangle \left\langle \mathbf{r} | \tilde{\phi}_j \right\rangle \left\langle \tilde{p}_j | \tilde{\Psi}_n \right\rangle. \end{aligned} \tag{2.35}$$

Thus, as suggest in the equation 2.35, the PAW charge density can be given by three terms $n(\mathbf{r}) = \tilde{n}(\mathbf{r}) + n^1(\mathbf{r}) - \tilde{n}^1(\mathbf{r})$, where $\tilde{n}$ represents a pseudo-charge density from the smooth auxiliary wave function ($\tilde{\Psi}_n$), and is given by:

$$\tilde{n}(\mathbf{r}) = \sum_n f_n \left\langle \tilde{\Psi}_n | \mathbf{r} \right\rangle \left\langle \mathbf{r} | \tilde{\Psi}_n \right\rangle, \tag{2.36}$$

On the other hand, n^1 and $\tilde{n}^1$ are onsite charge densities treated on a radial support grid, and they are given by:

$$n^1(\mathbf{r}) = \sum_{n,(i,j)} f_n \left\langle \tilde{\Psi}_n | \tilde{p}_i \right\rangle \langle \phi_i | \mathbf{r} \rangle \langle \mathbf{r} | \phi_j \rangle \left\langle \tilde{p}_j | \tilde{\Psi}_n \right\rangle, \tag{2.37}$$

and

$$\tilde{n}^1(\mathbf{r}) = \sum_{n,(i,j)} f_n \left\langle \tilde{\Psi}_n | \tilde{p}_i \right\rangle \left\langle \tilde{\phi}_i | \mathbf{r} \right\rangle \left\langle \mathbf{r} | \tilde{\phi}_j \right\rangle \left\langle \tilde{p}_j | \tilde{\Psi}_n \right\rangle. \tag{2.38}$$

2.5.4 Kinetic Energy

As done for the charge density, in order to obtain the kinetic energy (E_k), we determine the expectation value of the quasi-local operator $-\nabla^2/2$ in the equation 2.33, which is needed to evaluate the kinetic energy.

$$E_k = \sum_n f_n \left\langle \tilde{\Psi}_n \left| \left(-\frac{1}{2}\nabla^2 + \sum_{i,j} |\tilde{p}_i\rangle \left(\left\langle \phi_i \left| -\frac{1}{2}\nabla^2 \right| \phi_j \right\rangle - \left\langle \tilde{\phi}_i | - \frac{1}{2}\nabla^2 | \tilde{\phi}_j | \right\rangle \right) \langle \tilde{p}_j | \right) \right| \tilde{\Psi}_n \right\rangle, \tag{2.39}$$

which can be written as:

$$E_k = \sum_n f_n \left\langle \tilde{\Psi}_n | - \frac{1}{2}\nabla^2 | \tilde{\Psi}_n \right\rangle + \sum_{n,(i,j)} f_n \left\langle \tilde{\Psi}_n | \tilde{p}_i \right\rangle \left\langle \phi_i | - \frac{1}{2}\nabla^2 | \phi_j \right\rangle \left\langle \tilde{p}_j | \tilde{\Psi}_n \right\rangle - \sum_{n,(i,j)} f_n \left\langle \tilde{\Psi}_n | \tilde{p}_i \right\rangle \left\langle \tilde{\phi}_i | - \frac{1}{2}\nabla^2 | \tilde{\phi}_j \right\rangle \left\langle \tilde{p}_j | \tilde{\Psi}_n \right\rangle. \tag{2.40}$$

Thus, from equation 2.40, the PAW kinetic energy is given by three terms $E_k = \tilde{E}_k + E_k^1 - \tilde{E}_k^1$, where $\tilde{E}_k$ represents the kinetic-energy from the smooth auxiliary wave function ($\tilde{\Psi}_n$), and is given by:

$$\tilde{E}_k = \sum_n f_n \left\langle \tilde{\Psi}_n | - \frac{1}{2}\nabla^2 | \tilde{\Psi}_n \right\rangle, \tag{2.41}$$

On the other hand, E_k^1 and $\tilde{E}_k^1$ are onsite kinetic energy treated on a radial support grid, and they are given by:

$$E_k^1 = \sum_{n,(i,j)} f_n \left\langle \tilde{\Psi}_n | \tilde{p}_i \right\rangle \left\langle \phi_i | - \frac{1}{2}\nabla^2 | \phi_j \right\rangle \left\langle \tilde{p}_j | \tilde{\Psi}_n \right\rangle, \tag{2.42}$$

and

$$\tilde{E}_k^1 = \sum_{n,(i,j)} f_n \left\langle \tilde{\Psi}_n | \tilde{p}_i \right\rangle \left\langle \tilde{\phi}_i | - \frac{1}{2}\nabla^2 | \tilde{\phi}_j \right\rangle \left\langle \tilde{p}_j | \tilde{\Psi}_n \right\rangle. \tag{2.43}$$

2.5.5 The PAW Total Energy

As the charge density and expectation value, the PAW total energy can be divided in $E = \tilde{E} + E^1 - \tilde{E}^1$, which have the following form:

$$\tilde{E} = \sum_n f_n \left\langle \tilde{\Psi}_n \left| -\frac{1}{2}\nabla^2 \right| \tilde{\Psi}_n \right\rangle + \frac{1}{2} \int d\mathbf{r} \int d\mathbf{r}' \frac{(\tilde{n} + \hat{n})(\tilde{n} + \hat{n})}{\mathbf{r} - \mathbf{r}'} + \int d\mathbf{r} \tilde{n} \bar{v} + \int d\mathbf{r} \tilde{n} \epsilon_{xc}(\tilde{n}) \tag{2.44}$$

$$E^1 = \sum_{n,(i,j)} f_n \left\langle \tilde{\Psi}_n | \tilde{p}_i \right\rangle \left\langle \phi_i \left| -\frac{1}{2}\nabla^2 \phi_j \right| \right\rangle \left\langle \tilde{p}_j | \tilde{\Psi}_n \right\rangle + \frac{1}{2} \int d\mathbf{r} \int d\mathbf{r}' \frac{(n^1 + n^Z)(n^1 + n^Z)}{|\mathbf{r} - \mathbf{r}'|} + \int d\mathbf{r} n^1 \epsilon_{xc}(n^1) \tag{2.45}$$

$$\tilde{E}^1 = \sum_{n,(i,j)} f_n \left\langle \tilde{\Psi}_n | \tilde{p}_i \right\rangle \left\langle \tilde{\phi}_i \left| -\frac{1}{2}\nabla^2 \right| \tilde{\phi}_j \right\rangle \left\langle \tilde{p}_j | \tilde{\Psi}_n \right\rangle + \frac{1}{2} \int d\mathbf{r} \int d\mathbf{r}' \frac{(\tilde{n}^1 + \hat{n})(\tilde{n}^1 + \hat{n})}{|\mathbf{r} - \mathbf{r}'|} + \int d\mathbf{r} \tilde{n}^1 \epsilon_{xc}(\tilde{n}^1) \tag{2.46}$$

where n^Z and $\hat{n}$ reassemble the point charge density of the nucleus, and compensation charge density, respectively. In its turn, ϵ_{xc} represents the exchange-correlation energy, and $\bar{v}$ represents an arbitrary potential that vanishes ($\tilde{n} = \tilde{n}^1$) in the augmentation sphere.

2.5.6 Hamiltonian Operator

Like the charge density (n), the potential has the form $v(\mathbf{r}) = \tilde{v}(\mathbf{r}) + v^1(\mathbf{r}) - \tilde{v}^1(\mathbf{r})$, which allows the Hamiltonian of the smooth auxiliary wave-function to be written as:

$$\tilde{H} = -\frac{1}{2}\nabla^2 + \tilde{v} + \sum_{i,j} |\tilde{p}_i\rangle \left(\langle \tilde{\phi}_i | - \frac{1}{2}\nabla^2 + v^1 | \phi_j \rangle - \langle \tilde{\phi}_i | - \frac{1}{2}\nabla^2 + \tilde{v} | \tilde{\phi}_j \rangle \right) \langle \tilde{p}_j |. \tag{2.47}$$

And this Hamiltonian relates to the smooth auxiliary wave function as $\tilde{H}\tilde{\Psi}_n = \epsilon_n \tilde{S}\tilde{\Psi}_n$, where $\tilde{S}$ is the overlap operator as given by equation 2.31.

2.5.7 Forces in the PAW method

In the PAW method the forces are given by three components, i.e., $F = F_R^1 + F_R^2 + F_R^3$, where

$$F_R^1 = \int d\mathbf{r} \nabla \hat{n}_R' \int d\mathbf{r}' \frac{\tilde{n} + \hat{n}'}{\mathbf{r} - \mathbf{r}'} + \int d\mathbf{r} \tilde{n} (\nabla \hat{v}_R + \nabla \bar{v}_R) - \int d\mathbf{r} \tilde{n}^c \nabla \tilde{v} - \sum_{R'} \nabla_{R|Q} U_{R,R'} \tag{2.48}$$

$$F_R^{(2)} = -\sum_{i,j} \nabla_R \Theta_{ij} \left(\left\langle \phi_i | - \frac{1}{2}\nabla^2 + v^1 | \phi_j \right\rangle - \left\langle \tilde{\phi}_i | - \frac{1}{2}\nabla^2 + \tilde{v}^1 | \tilde{\phi}_j \right\rangle \right) \tag{2.49}$$

$$F_R^{(3)} = -\sum_{n,m} \frac{f_n + f_m}{2} \left\langle \tilde{\Psi}_n \left| \tilde{H} \right| \tilde{\Psi}_m \right\rangle \left\langle \tilde{\Psi}_m \left| \nabla_R \tilde{O} \right| \tilde{\Psi}_n \right\rangle \tag{2.50}$$

2.5.8 PAW: Approximations

At first glance, the PAW method is exact for DFT calculations, and requires an infinite number of atom-centered partial wave functions and projectors. However, for practical purposes some approximations are required in the PAW implementation. For instance, consider the frozen core approximation in order to turn calculations less cumbersome. Moreover, it is a common practice to consider finite basis set as well as finite number of partial waves and projectors.

2.5.9 Difference between Blöchl and Kresse Implementations

The PAW derivation of the energy functional of Kresse[148] follows closely the derivation of Blöchl, but with changes in exchange correlation energy as well as the decomposition of the Hartree energy. In particular the exchange-correlation term in the Blöchl formalism follows the expression:

$$E_{xc}^{Blöchl} = E_{xc}[\tilde{n} + \tilde{n}_c] + \sum_a \left(E_{xc}^a\left[n^a + n_c^a\right] - E_{xc}^a\left[\tilde{n}^a + \tilde{n}_c^a\right]\right). \tag{2.51}$$

On the other hand, Kresse's expression for the exchange–correlation energy follow the form:

$$E_{xc}^{Kresse} = E_{xc}[\tilde{n} + \tilde{n}_c + \hat{n}] + \sum_a \left(E_{xc}^a\left[n^a + n_c^a\right] - E_{xc}^a\left[\tilde{n}^a + \tilde{n}_c^a + \hat{n}^a\right]\right), \tag{2.52}$$

where the difference between the formulas is a term ($\hat{n}$) for valence compensation of charge density.[149]

2.6 Optical Properties

The analysis of optical properties, such as absorption coefficient, is an important way to evaluate the photovoltaic potential of perovskite materials. To estimate the optical properties of the perovskites, we calculated the absorption coefficient by considering the following equation:

$$\alpha(\omega) = \frac{2\kappa\omega}{c} \tag{2.53}$$

were κ, ω, and c represent, in this order, the extinction coefficient, the incident photon frequency, and the light speed in the vacuum. The complex refractive index ($\tilde{n}$) is given by $\tilde{n} = n + ik$, where n and k represent the refractive index and extinction coefficient. The complex refractive index can be related to the real (ϵ_1) and imaginary (ϵ_2) part of frequency-dependent dielectric function ($\tilde{\epsilon}$) as $\tilde{\epsilon} = \tilde{n}^2 = \epsilon_1 + i\epsilon_2$. Thus, from the equality relation $\epsilon_1 + i\epsilon_2 = n^2 + 2nik - k^2$, we conclude that $\epsilon_1 = n^2 - k^2$ and $\epsilon_2 = 2nk$, which a simple algebraic procedure gives the following equation for k:

$$\kappa = \left[\frac{\sqrt{\epsilon_1^2 + \epsilon_2^2} - \epsilon_1}{2}\right]^{\frac{1}{2}}, \tag{2.54}$$

which substitution in the equation 2.53 gives the absorption coefficient formula employed in the current work:

$$\alpha(\omega) = \frac{\sqrt{2}\omega}{c}\left[\sqrt{\epsilon_1^2 + \epsilon_2^2} - \epsilon_1\right]^{\frac{1}{2}}. \tag{2.55}$$

To compute the absorption coefficient as a function of incident photon energy, we calculated the frequency-dependent dielectric matrix, which was derived by considering

the PAW methodology.[150] Thus, neglecting local field effects, the imaginary part of the dielectric matrix can be obtained using the equation:

$$\epsilon_2(\omega) = \frac{4\pi^2 e^2}{\Omega} \lim_{q\to 0} \frac{1}{q^2} \sum_{c,v,\mathbf{k}} 2w_{\mathbf{k}} \delta(\epsilon_{c\mathbf{k}} - \epsilon_{v\mathbf{k}} - \omega) \times \langle u_{c\mathbf{k}+\mathbf{e}_\alpha q} | u_{v\mathbf{k}} \rangle \langle u_{v\mathbf{k}} | u_{c\mathbf{k}+\mathbf{e}_\beta q} \rangle. \quad (2.56)$$

The indices v and c refer to valence and conduction band states. The terms $u_{c\mathbf{k}}$ and $\mathbf{e}_{\beta q}$ represent, respectively, the cell periodic part at the k-point $\mathbf{k}$ and the unit vectors for the Cartesian directions. The real part of the dielectric matrix is obtained through the usual Kramers-Kronig transformation:

$$\epsilon_1(\omega) = 1 + \frac{2}{\pi} P \int_0^\infty \frac{\epsilon_2(\omega')\omega'}{\omega'^2 - \omega^2} d\omega' \quad (2.57)$$

where P designates the principal value.

3 THE STRUCTURAL, ENERGETIC AND OPTOELECTRONIC PROPERTIES OF TIN PEROVSKITES

Henceforth, we present the investigation of lead-free $A\mathrm{SnI_3}$ perovskites within different A-cations and polymorphous phases. In summary, to address the energetic-structural stability, we investigated the enthalpy of formation and cohesive energy of cubic, hexagonal, tetragonal and orthorhombic phases by considering the effects of orientation of A-cation, as well as their effects in the relative total energy, lattice parameters, unit-cell volume, dipole moment, and hydrogen-bonding interactions. Equally important, we also analyzed the electronic and optical properties, for instance, charge transfer and absorption coefficient. The main results are organized into the sections: (*i*) computational details, (*ii*) bulk of tin perovskites, (*iii*) relative energy stability, (*iv*) stability of tin perovskites, (*v*) structural properties, (*vi*) charge density analysis, (*vii*) optoelectronic properties, and (*viii*) summary.

3.1 Computational Details

The DFT calculations were done in the VASP package (version 5.4.1), which supports solving the many-body problem of a periodic system through the DFT methodology by considering the plane-waves basis set and the PAW method.[147,148] To improve the description of the interactions between organic and inorganic parts of the hybrid organic-inorganic $A\mathrm{SnI_3}$ perovskites, the D3 van der Waals (vdW) correction proposed by Grimme[143,151] were added to the DFT total energy calculations, which were obtained using the Perdew–Burke–Ernzerhof (PBE) exchange-correlation energy functional[135] for the self-consistent optimizations. Furthermore, we applied the hybrid HSE06 functional[136] for enhanced characterization of the fundamental bandgap energy of the lowest energy $A\mathrm{SnI_3}$ perovskites. Because of the slow convergence of the stress-tensor as a function of the number of plane waves, we employed cutoff energy of 841.82 eV to obtain the equilibrium volume of $A\mathrm{SnI_3}$ perovskites. From equilibrium structures, we employed cutoff energy of 473 eV to calculate physical-chemistry properties of $A\mathrm{SnI_3}$ perovskites, including enthalpy of formation, cohesive energy, band structure, density of states, and optical properties. The employed cutoff energy of 473 eV is 12.5 % larger than the largest value among the recommended cutoff energy of the $A\mathrm{SnI_3}$ elements species (Sn, I, Bi, O, H, C, N/P) of `POTCARs`, which is a VASP input file consisting of pseudo-potential information. Regarding the optical calculations, for obtaining an accurate description of the optical bandgap, we used a `CSHIFT` parameter of 1 meV for the Kramers–Kronig transformation.

We calculated the equilibrium volume of pseudo-hexagonal, hexagonal, pseudo-cubic, cubic, orthorhombic, and tetragonal structures of the $A\mathrm{SnI_3}$ perovskites. To compare the energetic stability of the different phases, all $A\mathrm{SnI_3}$ calculations were done employing a

k-point density of 40 $Å^{-1}$, which coincide to a **k**-mesh of 6×6×6 for the pseudo-cubic and cubic structures. Except for the high-cost HSE06 calculations, we increased the **k**-point density to 80 $Å^{-1}$ for other properties, such as optical responses and density of states.

3.2 Bulk of Tin Perovskites

In order to acquire a deep understanding on how the substitution and orientation of the *A*-cation affect the physical-chemistry properties of different phases of lead-free $ASnI_3$ perovskites, we selected three organic *A*-cations, namely, the MP ($CH_3PH_3^+$) and two mainstream organic cation in the perovskite field, i.e., the FA ($HC(NH_2)_2^+$) and MA ($CH_3NH_3^+$). The MP and MA organic cations have similar shape within the respective presence of P and N the only differentiation. The size of cations increases on the basis of the effective radii from MA (2.17 Å) to FA (2.53 Å).[78] We calculated cubic/pseudo-cubic, tetragonal, orthorhombic and hexagonal/pseudo-hexagonal structures for $ASnI_3$ perovskites, and preferably considering crystal phases with some experimental evidence. For instance, through X-Ray diffraction analyses it was identified that the cubic ($Pm\bar{3}m$) $MASnI_3$ structure occurs at 295 K, which undergoes to the tetragonal ($I4/mcm$) structure at 140 K in a solid-to-solid phase transition.[152,153] Likewise, the orthorhombic phase of $FASnI_3$ ($Pnma$) observed at 100 K goes to the tetragonal phase ($P4/mbm$) at 175 K, and then a phase-transition to form the cubic phase ($Pm\bar{3}m$) at 275 K.[153,154] On the contrary, to the best of our knowledge, experimental $MPSnI_3$ crystal structures have not been reported until the moment, but the experimental interest in the synthesis exits.[155]

Regarding the connectivity, the cubic, tetragonal and orthorhombic phases of $ASnI_3$ perovskites exhibit three-dimensional (3D) corner-sharing connectivity of the SnI_6 octahedra. They have a 3D framework connection along the three axes and differ from each other by the unit cell size, as well as the net dipole moment and orientation of *A*-cations. To analyze the role of inorganic framework connectivity, we further incorporated a low-dimensional hexagonal $ASnI_3$ structure ($P6_3mc$), which was experimentally reported for $FAPbI_3$,[156,157] and it has a unit cell composed of two formula units ($Z = 2$) with a 1D (one-dimensional) face-sharing connectivity of SnI_6 octahedra in the [001] direction, while no SnI_6 connectivity along the [100] and [010] directions.

To achieve our goals, we performed the calculations by preserving the Bravais lattice of the different structures, which means that we employed constraints to the tetragonal, orthorhombic, and perfect cubic phases satisfy $\alpha = \beta = \gamma = 90°$. In addition, we considered the constrains $a_0 = b_0 \neq c_0$, $a_0 \neq b_0 \neq c_0$, and $a_0 = b_0 = c_0$, respectively, for tetragonal, orthorhombic and cubic structures. No constrains were applied for the low-dimensional pseudo-hexagonal structures, and for the pseudo-cubic structures angles constrains were considered ($\alpha = \beta = \gamma = 90°$). The procedure provided a path to investigate the outcome of SnI_6 dimensionality in the $ASnI_3$ physical-chemistry properties, as well as the effects

induced by the orientations and alignments of A-cations at the respective Wyckoff positions of ASnI$_3$ polymorphs.

3.3 Relative Energy Stability

As indicated in Figure 5, the relative energy stability of the ASnI$_3$ structures shows clear dependence on how the organic A-cations are orientated/aligned in the inorganic cage, which has also been verified for the lead-based MAPbI$_3$ counterpart.[158] To explain the role of the orientations of A-cations in the relative stability of ASnI$_3$ phases, we analyzed intrinsic parameters, including A-cation size, dipole-dipole, and the hydrogen-bond interactions.

Figure 5 – a) Schematic representation of the ASnI$_3$ perovskites unit cells, where blue, silver and purple spheres stand for the A-cation, Sn, and I sites, respectively. The different orientations of arrows in the blue spheres suggest the numerous orientations calculated for the A-cation in the inorganic-framework cage of ASnI$_3$ perovskites. Conferring to the experimental evidence, we considered two formula units for the tetragonal phase of FASnI$_3$. b) The column on the right side exhibits the ASnI$_3$ volume per formula unit, as well as the relative total energy (ΔE_{tot}) obtained by contemplating the perfect cubic structure (C) as energy reference for the remaining pseudo-hexagonal/hexagonal (PH/H), pseudo-cubic (PC), tetragonal (T), and orthorhombic (O) phases.

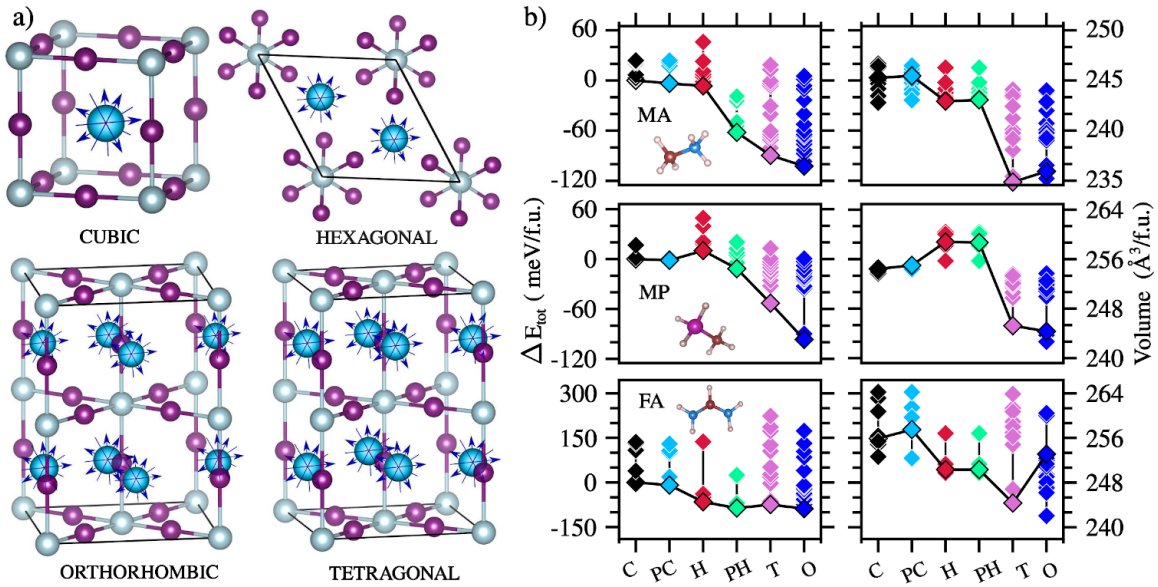

Source: Reprinted from OZÓRIO, M.S.; SRIKANTH, M.; BESSE, R.; DA SILVA, J. L. F. **Physical Chemistry Chemical Physics**, v. 23, n.3, p. 2286–2297, 2021[129]

3.3.1 The Effect of A-cation Size

The average and standard deviation volume per formula unit are 242.50 ± 3.16Å^3 for MASnI$_3$, and of 254.60 ± 5.07Å^3/253.23 ± 3.56Å^3 for FASnI$_3$/MPSnI$_3$ perovskites, which is a direct effect of the A-cations steric radius expanding from MA (2.03 Å), FA (2.24 Å) to

MP (2.38 Å).[159] The size of *A*-cations show an almost irrelevant response in determining the relative energy of a particular $A\mathrm{SnI_3}$ polymorphs, which may be associated with the very similar values of the N(P)−H and C−N(P) bond lengths. Replacing the organic *A*-cation does not yield a substantial change in the relative energy trend of polymorphs. Hence, the results suggest the role of other factors in the equilibrium volume rather than of *A*-cations size, which can be visualized by how the *A*-cations orientations affect the equilibrium volume.

3.3.2 Hydrogen Bond Interactions

In order to understand if/how the role of hydrogen bond interactions influence the $A\mathrm{SnI_3}$ polymorphs relative energy stability, we considered all H···I (hydrogen-iodide distance) and XHI angles (X = N, P or C) within a cutoff radius of 3.5 Å. As shown in Figure 6, we noticed shorter and directional H···I distances for NH···I/PH···I than CH···I for all $A\mathrm{SnI_3}$ perovskites, where the CH···I distances is wider than 3.0 Å (see Figure 7). The *A*-cations are somewhat dislocated from the unit cell center, i.e., the C−I distances are larger than P−I/N−I because of the weak PH···I/NH···I hydrogen bond interactions of the $-\mathrm{PH_3}/-\mathrm{NH}_x$ groups,[160] which displayed a linear relation between the hydrogen bonds (H-bonds) and NHI/PHI angles, and by increasing the angles towards 180° the bond lengths become smaller. However, the weak hydrogen bond has a minor effect in contributing to the relative energy stability tendencies because all structures have similar behavior regarding the H-bonds.

Despite being weak, the H-bond interactions play a significant role in the structural cohesion of those $A\mathrm{SnI_3}$ perovskites because they are attractive forces between the *A*-cations and the inorganic framework. For instance, the MA and MP have three hydrogen donors ($-\mathrm{NH_3}$ and $-\mathrm{PH_3}$) that helps stabilize the structure, while the planar cation FA has four hydrogen atoms from $-(\mathrm{NH_2})_2$. As a result, the cohesive energy values of Table 1 suggest higher structural cohesion for $\mathrm{FASnI_3}$ than for the $\mathrm{MASnI_3}$ structures, and both with high structural cohesion than $\mathrm{MPSnI_3}$. Although MA- and MP-cations display similar geometry, the weaker structural cohesion of $\mathrm{MPSnI_3}$ relates to the very weak H···I bond interactions involving the $-\mathrm{PH_3}$ moiety. The MA > MP sequence for the cohesive energy per hydrogen donor agrees with the strengths sequence of the shortest H-bonds of those moieties (see Table 1). It's well know the negative effect of moisture and oxygen-rich environment on the stability of Sn−I bonds,[161,162] thus, $\mathrm{MPSnI_3}$ structures may be more affected by oxygen and water molecules than $\mathrm{MASnI_3}$ and $\mathrm{FASnI_3}$ because of their weaker structural cohesion.

3.3.3 The Role of Dipole-dipole Interactions

The dipole moments we found for the *A*-cation molecules correspond to 2.34 D for MA, 1.95 D for MP and 0.26 D for FA, which are in an excellent agreement with

Figure 6 – All H···I distances and XHI angles (X = C, N or P) versus the relative total energy of ASnI$_3$ perovskites.

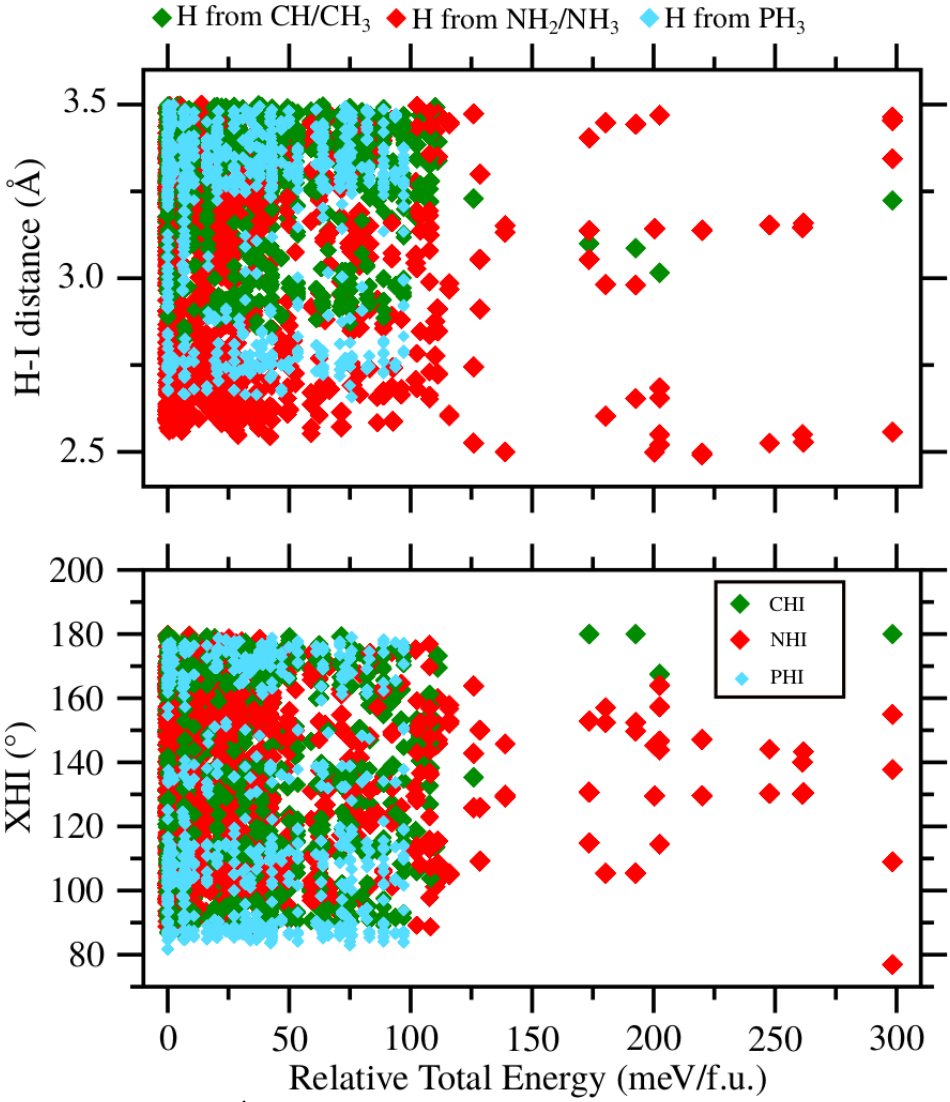

Source: Reprinted from OZÓRIO, M.S.; SRIKANTH, M.; BESSE, R.; DA SILVA, J. L. F. **Physical Chemistry Chemical Physics**, v. 23, n.3, p. 2286–2297, 2021[129]

preceding values reported in the literature.[163–166] As for lead-based perovskites,[166] A-cations orientations influence in the relative energy of the ASnI$_3$ structures. The net dipole moment change as the orientation of anisotropic A-cations change, and as a result, the A-cations change the dipole-dipole interactions in the unit-cell and its images. Based on structural analysis, since there is only one cation in the unit cell, the net dipole moment will not be zero in the cubic/pseudo-cubic structures. Affected by the weak H···I interactions, the A-cations orientate towards the inorganic layers of pseudo-hexagonal/hexagonal structures, and the null resulting dipole moment is not achieved because of the reduced dimensionality and symmetry of the inorganic framework. Proper alignment of the organic cation in the orthorhombic and tetragonal structures resulted in a null/almost-null net dipole moment.

The head-to-tail orientation of MA results in a null/(almost null) net dipole

Figure 7 – All XHI angles (X = C, N or P) versus the H···I distances for ASnI$_3$ perovskites. The red, dark green and light blue color represents the fitting of all data of NHI, CHI and PHI angles versus distance curve, respectively. The light green and blue curves represent the fitting for lowest energy perovskites dots.

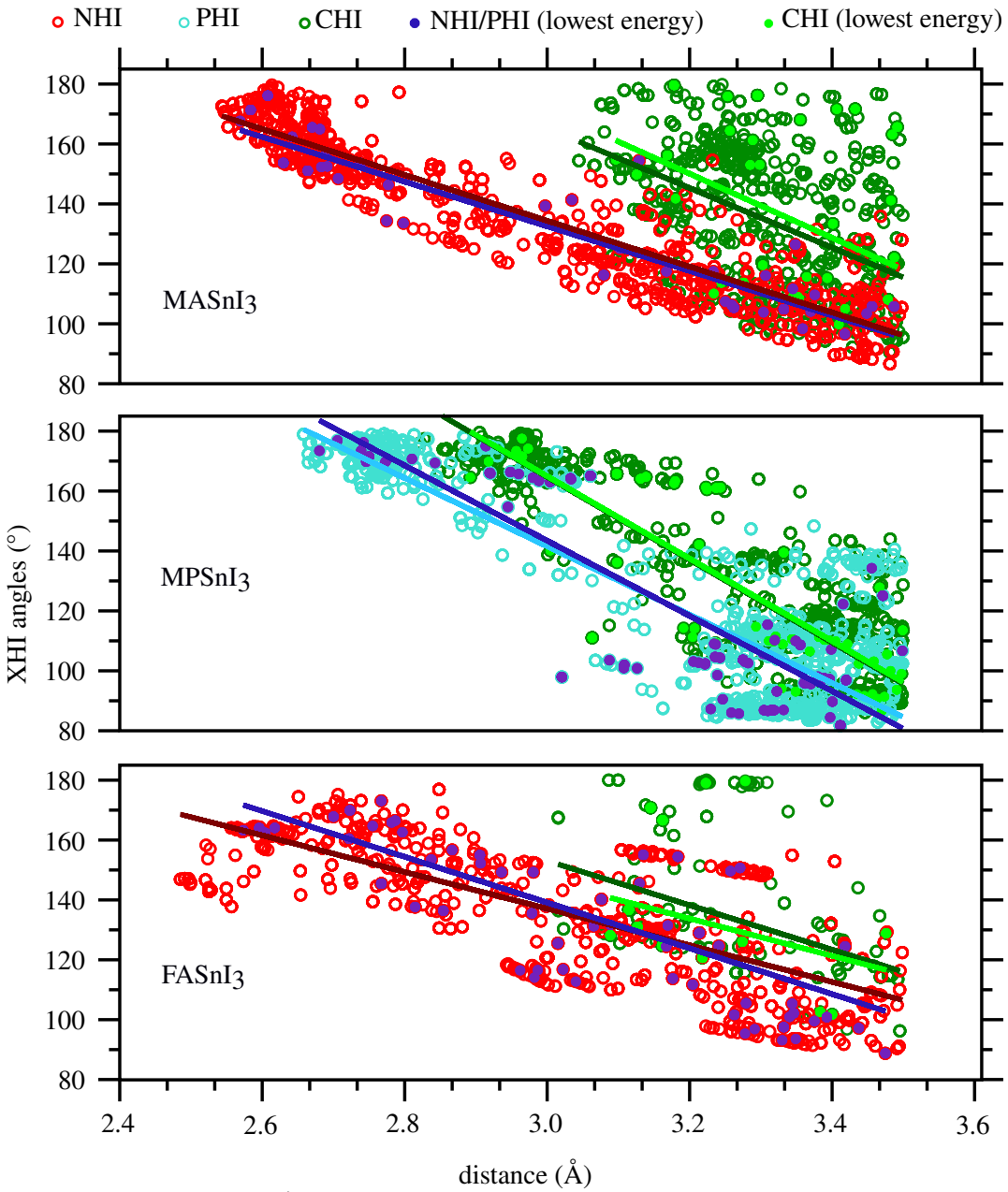

Source: Reprinted from OZÓRIO, M.S.; SRIKANTH, M.; BESSE, R.; DA SILVA, J. L. F. **Physical Chemistry Chemical Physics**, v. 23, n.3, p. 2286–2297, 2021[129]

moment, which contributes to reduce the relative total energy ΔE_{tot} of the tetragonal and orthorhombic phases of MASnI$_3$ perovskites (see Figure 8). On the contrary, the dipole moment cancellation does not occur completely in the lowest-energy orthorhombic phase of MPSnI$_3$ and FASnI$_3$ perovskites because of weakened dipole-dipole interactions in the MPSnI$_3$ and FASnI$_3$ structures, and the dipole moment of FA- and MP-cation plays minor effects on ΔE_{tot}. Indeed, the resulting dipole moment is null for structures degenerated

Figure 8 – The lowest-energy structures for a) $MASnI_3$ b) $MPSnI_3$ and c) $FASnI_3$ cubic, orthorhombic, tetragonal, and hexagonal phases. Relative total energy using the cubic structure as reference are given in meV/f.u.. By the side of the cubic and hexagonal structures (in parenthesis) are indicated the respective values of pseudo-cubic and pseudo-hexagonal structures.

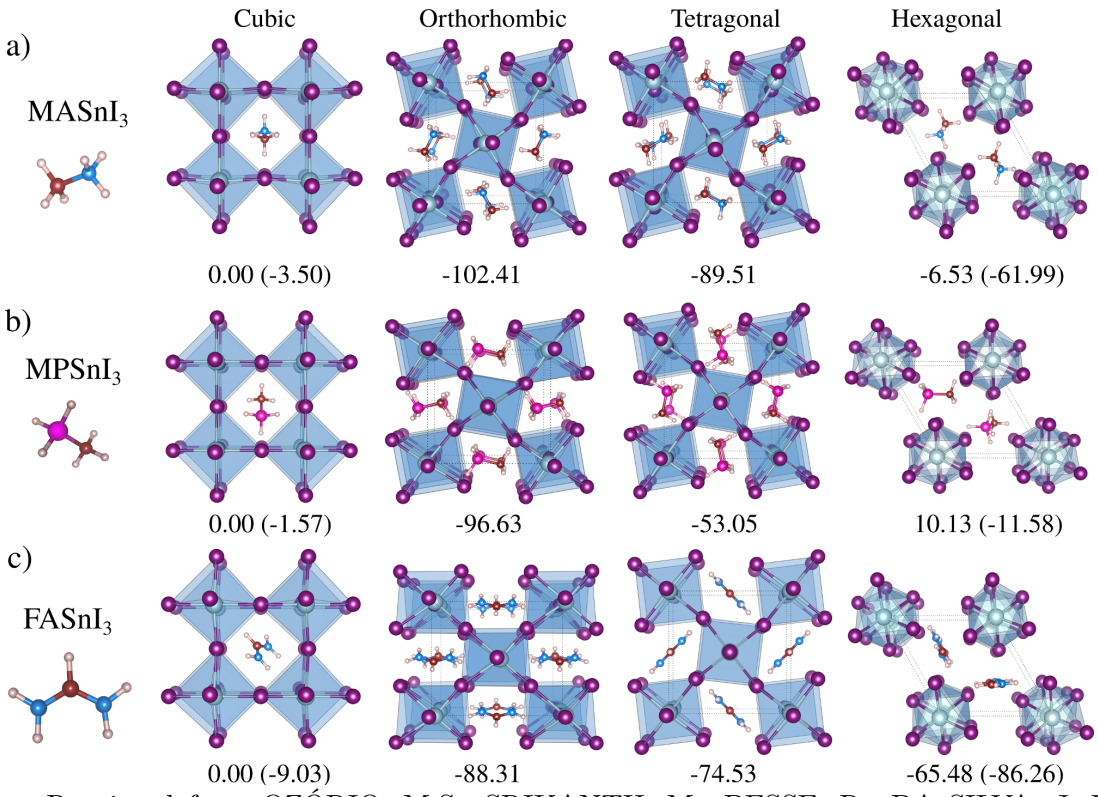

Source: Reprinted from OZÓRIO, M.S.; SRIKANTH, M.; BESSE, R.; DA SILVA, J. L. F. **Physical Chemistry Chemical Physics**, v. 23, n.3, p. 2286–2297, 2021[129]

with the lowest-energy of $FASnI_3$ and $MPSnI_3$ orthorhombic structures, i.e., with energy difference of only 6 meV/f.u. and 3 meV/f.u. for $MPSnI_3$ and $FASnI_3$, respectively. Different combinations of relative orientations of A-cations occur in the $ASnI_3$ polymorphs. The reduced variability of structures causes the decrease in the ΔE_{tot} range among structures. Overall, contrary to the A-cation size and the hydrogen bond interaction, dipole-dipole interactions have a significant influence on the relative energy configurations.

3.4 Stability of Tin Perovskites

The structural stability is a crucial guideline for experimental syntheses and even can help predict perovskite materials with feasible applications. To achieve knowledge about the stability of perovskites, the enthalpy of formation (ΔH_f^o) is a better criterion than the relative total energy.[167] At $T = 0\,\mathrm{K}$, the enthalpy measure the spontaneity of $AI_{(s)} + SnI_{2(s)} \xrightarrow{0\,\mathrm{K}} ASnI_{3(s)}$ reactions ($\Delta H_f^o \equiv \Delta G_f^o$), given by the equation of state:

$$\Delta G_f^o = E(ASnI_{3(s)}) - E(AI_{(s)}) - E(SnI_{2(s)}) \ , \tag{3.1}$$

Table 1 – Structural and energetic properties obtained for the lowest energy of $A\mathrm{SnI_3}$ perovskite structures: enthalpy of formation, ΔH_f^o), bulk cohesive energy, E_{coh}, the average I···H distance of stronger hydrogen bond interactions of $-\mathrm{NH}_x{}^+/-\mathrm{PH_3}{}^+$ group, $d^{\mathrm{N}}_{\mathrm{I\cdots H}}$, and of $-\mathrm{CH_3}$ group, $d^{\mathrm{C}}_{\mathrm{I\cdots H}}$, difference of hydrogen bond lengths of $-\mathrm{NH}_x{}^+$ and $-\mathrm{CH_3}$ groups, $\Delta d_{\mathrm{I\cdots H}}$), effective coordination number of tin, $\mathrm{ECN^{Sn}}$, average tin-iodide bond lengths, $d_{av}^{\mathrm{Sn-I}}$, I–Sn–I angle of octahedron diagonal, Θ, I–Sn–I angle involving adjacent iodide species, θ, and the lattice parameters (a_0, b_0 and c_0) of pseudo-hexagonal (PH), hexagonal (H), pseudo-cubic (PC), cubic (C), tetragonal (T), and orthorhombic (O) phases. The experimental values are indicated below the respective theoretical results when available.

		ΔH_f^o (meV/f.u.)	E_{coh} (eV/f.u.)	$d^{\mathrm{N/P}}_{\mathrm{I-H}}$ (Å)	$d^{C}_{\mathrm{I-H}}$ (Å)	$\mathrm{ECN^{Sn}}$ (NNN)	$d_{av}^{\mathrm{Sn-I}}$ (Å)	Θ^{ISnI} (deg.)	a_0 (Å)	b_0 (Å)	c_0 (Å)
$\mathrm{MASnI_3}$	C	−32.11	−39.329	2.71	3.32	5.75	3.14	171.05	6.26	6.26	6.26
	C						3.12[153]		6.24	6.24	6.24[152]
	PC	−35.60	−39.333	2.71	3.32	5.70	3.14	170.75	6.29	6.20	6.29
	O	−134.51	−39.432	2.61	3.12	6.00	3.16	180.00	8.91	12.54	8.45
	T	−121.62	−39.419	2.65	3.18	6.00	3.16	180.00	8.67	8.67	12.50
	T								8.73	8.73	12.50[152]
	H	−38.64	−39.336	2.84	3.32	5.74	3.20	176.04	8.52	8.52	7.73
	PH	−94.09	−39.391	2.73	3.24	5.89	3.20	176.81	8.72	8.46	8.71
$\mathrm{MPSnI_3}$	C	−219.34	−35.130	2.93	3.12	5.62	3.17	174.75	6.34	6.34	6.34
	PC	−220.91	−35.132	2.94	3.13	5.53	3.18	174.68	6.41	6.31	6.30
	O	−315.96	−35.227	3.02	3.20	5.76	3.17	175.13	9.15	12.63	8.45
	T	−272.39	−35.183	3.05	3.09	6.00	3.16	180.00	8.83	8.83	12.57
	H	−209.21	−35.120	2.90	3.15	5.96	3.20	177.01	8.83	8.83	7.67
	PH	−230.91	−35.142	2.89	3.17	5.91	3.20	176.84	9.06	8.59	7.69
$\mathrm{FASnI_3}$	C	40.17	−44.116	2.78	3.28	5.49	3.18	171.13	6.35	6.35	6.35
	C						3.16[153]		6.31	6.31	6.31[154]
	PC	31.14	−44.125	2.81	3.22	5.21	3.19	169.93	6.28	6.29	6.52
	O	−48.14	−44.204	2.77	3.11	5.22	3.19	171.63	8.40	12.52	9.63
	O								8.82	12.42	8.86[154]
	T	−34.36	−44.190	2.99	3.22	5.97	3.14	176.69	8.88	8.88	6.19
	T								8.86	8.86	6.25[154]
	H	−25.31	−44.181	2.86	3.13	5.72	3.20	175.53	8.58	8.58	7.85
	PH	−46.09	−44.202	2.88	3.15	5.73	3.20	175.72	8.52	8.64	7.91

Source: Reprinted from OZÓRIO, M.S.; SRIKANTH, M.; BESSE, R.; DA SILVA, J. L. F. **Physical Chemistry Chemical Physics**, v. 23, n.3, p. 2286–2297, 2021[129]

where $E(A\mathrm{SnI}_{3(\mathrm{s})})$, $E(\mathrm{SnI}_{2(\mathrm{s})})$, and $E(A\mathrm{I}_{(\mathrm{s})})$, represent the respective bulk compounds total energy. The bulk total energy of MAI, FAI and $\mathrm{SnI_2}$ were achieved by performing the structural optimization of the experimental structures.[168–170] The bulk total energy of MPI was obtained from the relaxed structure resulted by the replacing of N for P in $\mathrm{MAI}_{(\mathrm{s})}$. The required energy for the perovskites formation at $T = 0\,\mathrm{K}$ is shown in Table 1.

The values we found for ΔG_f^o suggest that the $MASnI_3$ and $FASnI_3$ perovskite phases have lower thermodynamic stability at 0 K than the respective $MPSnI_3$ phases. Our results show that $MPSnI_3$ is thermodynamically stable as lead-based counterparts, which stability was predicted in previous theoretical works.[171–173] As shown by the cohesive energy, structure-wise $MPSnI_3$ may be more affected by intrinsic and extrinsic factors, which could explain its actual lack of experimental synthesis. For more cohesive $MASnI_3$ and $FASnI_3$ perovskites, higher structural stability is expected within $FASnI_3$ more stable than $MASnI_3$, which is in line with the relative stability upon illumination.[174]

Experimental analysis of both $FASnI_3$ and $MASnI_3$ perovskites reveals that the orthorhombic phase is the most stable at low temperature, which suffers a phase-transition to the tetragonal and next to the cubic phase with a continued increase of temperature.[154,175] Therefore, our DFT calculations (0 K) are in line with the experimental findings by predicting higher stability of the orthorhombic phase at low temperatures. We found slightly unstable cubic and pseudo-cubic phases of $FASnI_3$. Overall, changes in the stability trends may occur if one considers entropy effects, e.g., within cubic, tetragonal, and even hexagonal structures being more stable at high temperatures.

3.5 Structural Properties

The *A*-cation's size, orientation, anisotropy and hydrogen bonds parameters yield to intrinsic SnI_6 octahedra tilting. To understand how those effects influence the symmetry of the structures, we used FINDSYM program[176] to get the space group of the perovskite structures. To the best of our knowledge, it does not exist experimental reports on the space group of orthorhombic $MASnI_3$ phase.[152,175] Then, we calculated various orientations/alignments of MA-cation in the cage of an orthorhombic cell displaying the size of the orthorhombic $MAPbI_3$ counterpart.[177,178] Our calculation suggest that the lowest energy orthorhombic phase of $MASnI_3$ have a $a^-b^+a^-$ tilting (Glazer tilting notation)[179] and space group *Pnma* (point group D_{2h}). As observed for the orthorhombic $MASnI_3$ phase, an anti-ferroelectric alignment of MA-cation also occurs in the tetragonal phase. The lowest-energy of the $MASnI_3$ tetragonal phase displayed the same octahedral tilting and symmetry of the orthorhombic phase, which may be explained by the high dipole moment of MA-cation.

We have observed different orthorhombic phases for $FASnI_3$ perovskites in the literature, such as *Pnma*, *Amm*2, and *Imm*2.[154,156,180] Here, the lowest energy orthorhombic $FASnI_3$ phase has lower symmetry (*Cc* space group), and it is close in energy with a *Pbam* space group structure, which has experimental evidence.[181] In its turn, the inorganic frame of the lowest-energy tetragonal $FASnI_3$ phase shows an $a^0a^0c^+$ octahedra-network tilting towards the *c*-axis and satisfies the rules of $P4/mbm$ space group. The orthorhombic $MPSnI_3$ phase displays different tilting than that of $MASnI_3$

because of the MP-cation orientation/alignment. The $MPSnI_3$ tetragonal phase has an anti-ferroelectric alignment of cations, and a $a^-b^+a^-$ octahedra tilting. These results suggest the effects of organic cation features on the inorganic-frame tilting of perovskites.

At high temperature a net spherical environment for the A-cations arises from the free and random cation motion. However, as lower the temperature, the degree of freedom of the A-cations drastically reduce, and because of the frozen picture of MP (Schönflies symmetry is C_{3v}), MA (C_{3v}), and FA (C_{2v}) cations generally causes the symmetry to reduce from O_h to $P1$ in the pseudo-cubic/cubic structures. The octahedra SnI_6 tilting causes internal distortions, such as deviation of tin effective coordination number from the ideal value ($ECN^{Sn} = 6$), tin off-center in I–Sn–I segments, as well as deviation from the ideal 90°/180° angles of ISnI adjacent/diagonal bond angles.

As stated in Table 1, the alignment of the MA-cations contributes to decreasing structural distortions and canceling the dipole moment in the tetragonal and orthorhombic $MASnI_3$ perovskites. Cubic/pseudo-cubic structures can be used to assimilate the impact of octahedra distortions. The a_0, b_0, and c_0 parameters are a direct measurement of the three diagonal of the unit cell octahedron, which is equivalent to the distance between adjacent tin cations and also the distance between non-adjacent iodide ions. In conclusion, all factors that trigger octahedra distortions affect the lattice parameters, the unit cell volume, and dependent properties.

We found negligible theoretical-experimental deviations for the a_0 and c_0 lattice parameters of the $MASnI_3$ tetragonal structures, respectively, only $-0.69\,\%$ and $0.00\,\%$.[152] For tetragonal $FASnI_3$ structure, the lattice parameters deviations are also small, i.e., $0.23\,\%$ for a_0 and $0.97\,\%$ for c_0. The experimental lattice for $MASnI_3$ and $FASnI_3$ perovskites[152–154] exhibit satisfactory agreement with our theoretical results (see Table 1), i.e., the theoretical-experimental deviation is of $0.64\,\%$ and $-0.32\,\%$ for $FASnI_3$ and $MASnI_3$, respectively.

3.6 Charge Density Analysis

We considered the Bader charge partition[182,183] to get information about charge transfer and the charge depletion/accumulation of lowest energy $ASnI_3$ perovskites. Represented by Q^{B}_{eff}, the effective Bader charges were calculated as the difference of valence electrons (Z_{val}) of neutral atoms and their respective Bader charge (Q^{B}), i.e., $Q^{B}_{eff} = Z_{val} - Q^{B}$. As stated in Figure 9, the net charge transfer within the A-cations is the sum of the Bader charges of each constituent atom. By subtracting the densities of separated organic (A-cation) and inorganic constituents from the $ASnI_3$ density we got the electron density difference of lowest-energy $ASnI_3$ systems.

The results suggest that carbon of both FA- and MA-cations are charge donors to

Figure 9 – The effective Bader charge analysis of each element, and site of ASnI$_3$ perovskites (A, Sn, I, C, N, P, and sum of H) of the pseudo-hexagonal (PH), hexagonal (H), pseudo-cubic (PC), cubic (C), tetragonal (T), and orthorhombic (O) phases.

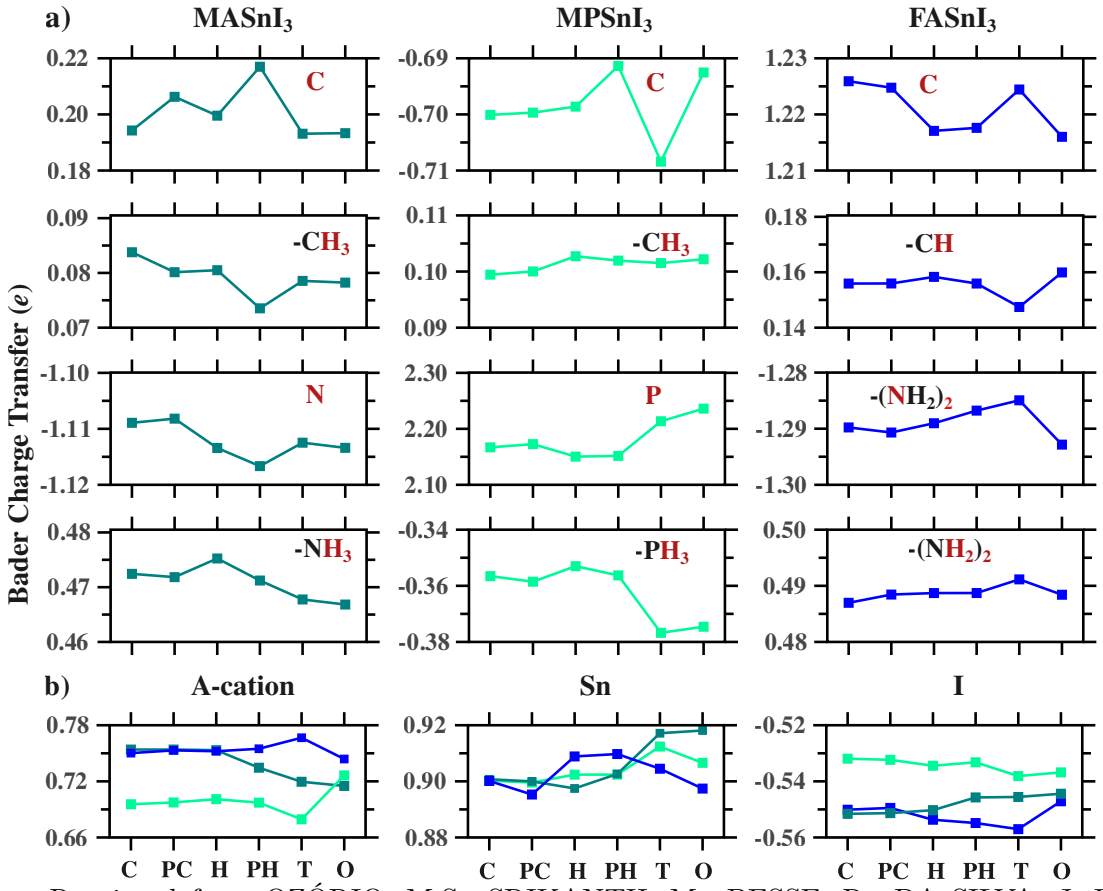

Source: Reprinted from OZÓRIO, M.S.; SRIKANTH, M.; BESSE, R.; DA SILVA, J. L. F. **Physical Chemistry Chemical Physics**, v. 23, n.3, p. 2286–2297, 2021[129]

N, which also accepts electronic charges from the hydrogen of the $-NH_x$ group. Charge reduction in hydrogen contributes to the Coulomb attractions of H···I, i.e., to the formation of weak hydrogen bonds. It occurs about 0.75 e of charge transfer from the organic cation to the inorganic framework, which is in line with previous works,[184] and arises mainly from NH_x moieties because of high electronegativity of iodide compared to the hydrogen of the $-N-H\cdots I$ moiety. Carbon acts as an acceptor of electrons in the MPSnI$_3$ perovskites, which justifies the charge depletion in the $-PH_3$ segments. The electronic coupling of P and H orbitals causes a small accumulation of charge on the hydrogen atoms of PH_3 moieties. As a result, it occurs a shorter charge transfer from the hydrogen of $-PH_3$ group to the iodide of the inorganic framework because the coulomb attractions between them are reduced, which justify the weaker H···I interaction and stability of MPSnI$_3$ compared to MASnI$_3$ and FASnI$_3$ perovskites. As shown in Figure 9, the inorganic frame is not formed by pure ionic Sn–I bonds, i.e., the effective charge on Sn/I of 0.90 e/−0.55 e deviates from the values 2.00 e/−1.00 e expected for a pure ionic behavior.

Figure 10 – Top: electron density accumulation (green) and depletion (purple) in the ASnI$_3$ perovskites obtained by electron density difference between the charge of ASnI$_3$ and the respective frozen-isolated fragments (A + SnI$_3$). Bottom: Plane along tin-iodide bond lengths showing the electron localization function, which increase from blue to red.

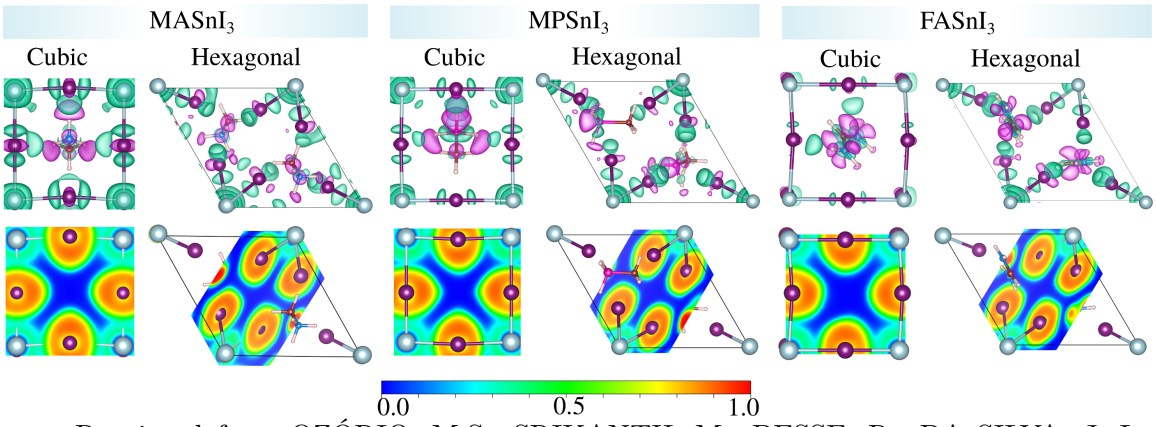

Source: Reprinted from OZÓRIO, M.S.; SRIKANTH, M.; BESSE, R.; DA SILVA, J. L. F. **Physical Chemistry Chemical Physics**, v. 23, n.3, p. 2286–2297, 2021[129]

As shown in Figure 10, the electron localization function (ELF) and density difference analysis yielded further evidence for the character of SnI$_6$ bond length and the charge transfer. Our results show that NH$_x$ and PH$_3$ groups are the major source of charge transfer from A-cation to the inorganic frame. Then, there is a good agreement between the charge density analysis and the strength of the hydrogen bonds in those moieties. In addition, as shown in the ELF plots (see Figure 10), all ASnI$_3$ perovskites have Sn–I bond lengths displaying an intermediate ionic-covalent character.

3.7 Optical and Electronic Properties

To find further information concerning the optical and electronic properties of the lowest-energy ASnI$_3$ phases, we evaluated more properties such as density of states, band structures, absorption coefficient, and so on. Figure 11 show the local density of states and band structures for ASnI$_3$ phases, which highlights the inorganic part prevailing the band structures and density of states, i.e., the overlap of I p, Sn s-, and Sn p-states of SnI$_6$ moieties. Among the investigated ASnI$_3$ perovskites, MASnI$_3$ systems have the minor contribution of MA-cation states to the valence and conduction bands. The MA-cation states do not display a significant role 4.00 eV above or below the valence band maximum (VBM). As a result, band structures of the frozen SnI$_3^-$ inorganic framework display similar behavior to the bands of whole MASnI$_3$ perovskites (see Figure 12). The states of FA and MP organic cations have some smaller (but significant) contributions to the band structure of FASnI$_3$ and MPSnI$_3$, respectively. For FASnI$_3$ perovskites, a similar

Figure 11 – Plots of band structure and density of states per formula unit for the pseudo-hexagonal/hexagonal (PH/H), pseudo-cubic/cubic (PC/C), tetragonal (T), and orthorhombic (O) phases of $MASnI_3$, $MPSnI_3$ and $FASnI_3$ perovskites. The VBM was set to 0 eV in all cases.

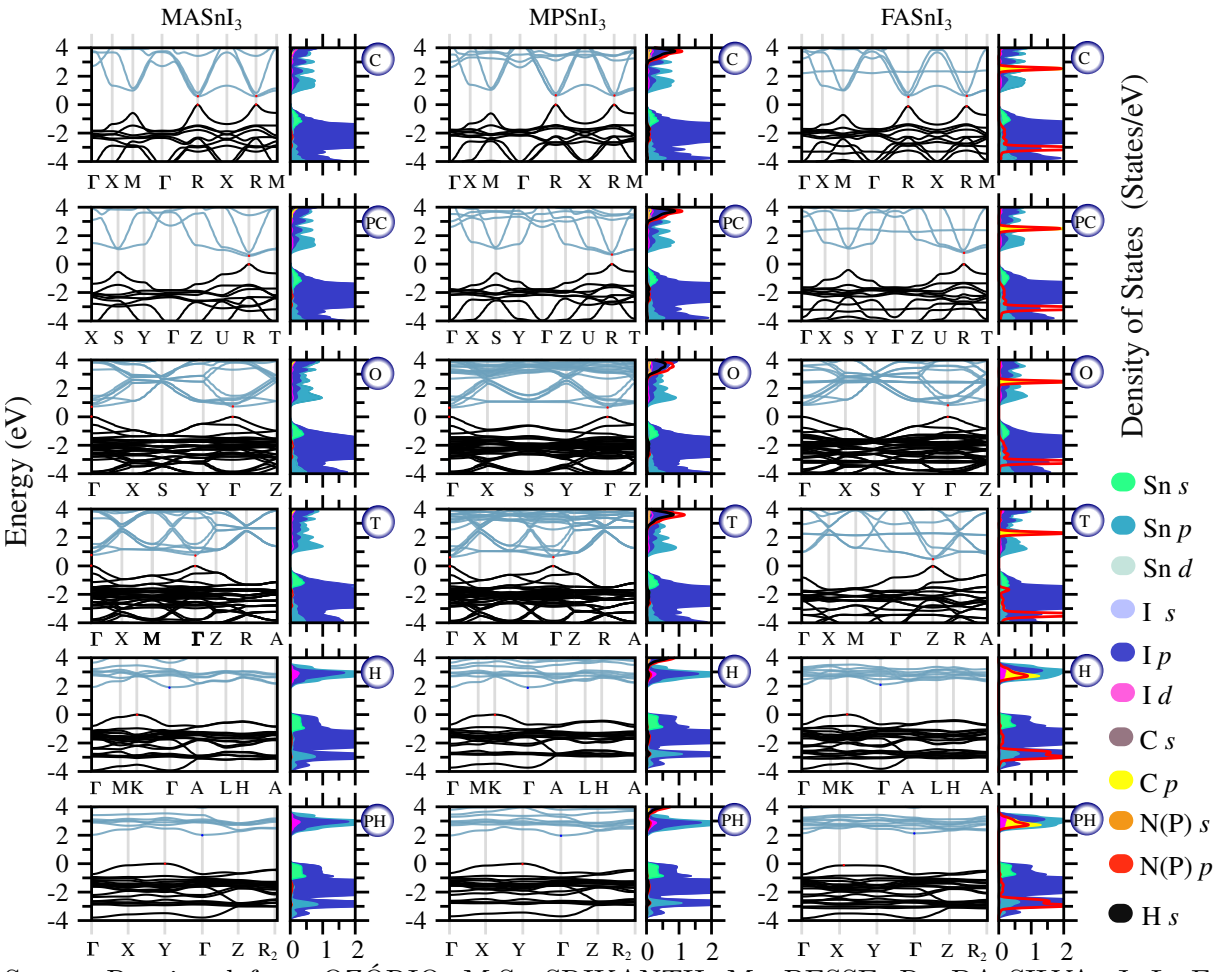

Source: Reprinted from OZÓRIO, M.S.; SRIKANTH, M.; BESSE, R.; DA SILVA, J. L. F. **Physical Chemistry Chemical Physics**, v. 23, n.3, p. 2286–2297, 2021[129]

contribution of C *s*- and N *p*-states appears near ±2.00 eV above VBM, while localized N *p*-states occur almost ±3.00 eV below the VBM.

The density of states and band structure plots are in perfect agreement by suggesting small-direct fundamental bandgap energy for cubic/pseudo-cubic, tetragonal, and orthorhombic perovskite structures, and wide-indirect fundamental bandgap energy for hexagonal/pseudo-hexagonal non-perovskite structures. Band structure plots show close trends for structures of the same phase. The band structures of non-perovskite systems are very flat, while those of perovskite are more dispersed, which could be explained by the difference in connectivity. Cubic/pseudo-cubic structures have the direct fundamental bandgap energy at $(\frac{1}{2}, \frac{1}{2}, \frac{1}{2})\frac{2\pi}{a_0}$ (R point), tetragonal and orthorhombic phases have direct fundamental bandgap at $(0, 0, 0)\frac{2\pi}{a_0}$ (Γ point). By exception, the direct fundamental bandgap of $FASnI_3$ tetragonal phase occurs at $(0, 0, \frac{1}{2})\frac{2\pi}{a_0}$ (the Z point).

Figure 12 – Comparison of the band structure of pseudo-hexagonal (PH), hexagonal (H), pseudo-cubic (PC), cubic (C), tetragonal (T), and orthorhombic (O) phases by considering the whole $A\mathrm{SnI_3}$ perovskite and the frozen inorganic-framework fragment without the A-cation (indicated by **X**). The VBM was set to 0 eV in all cases.

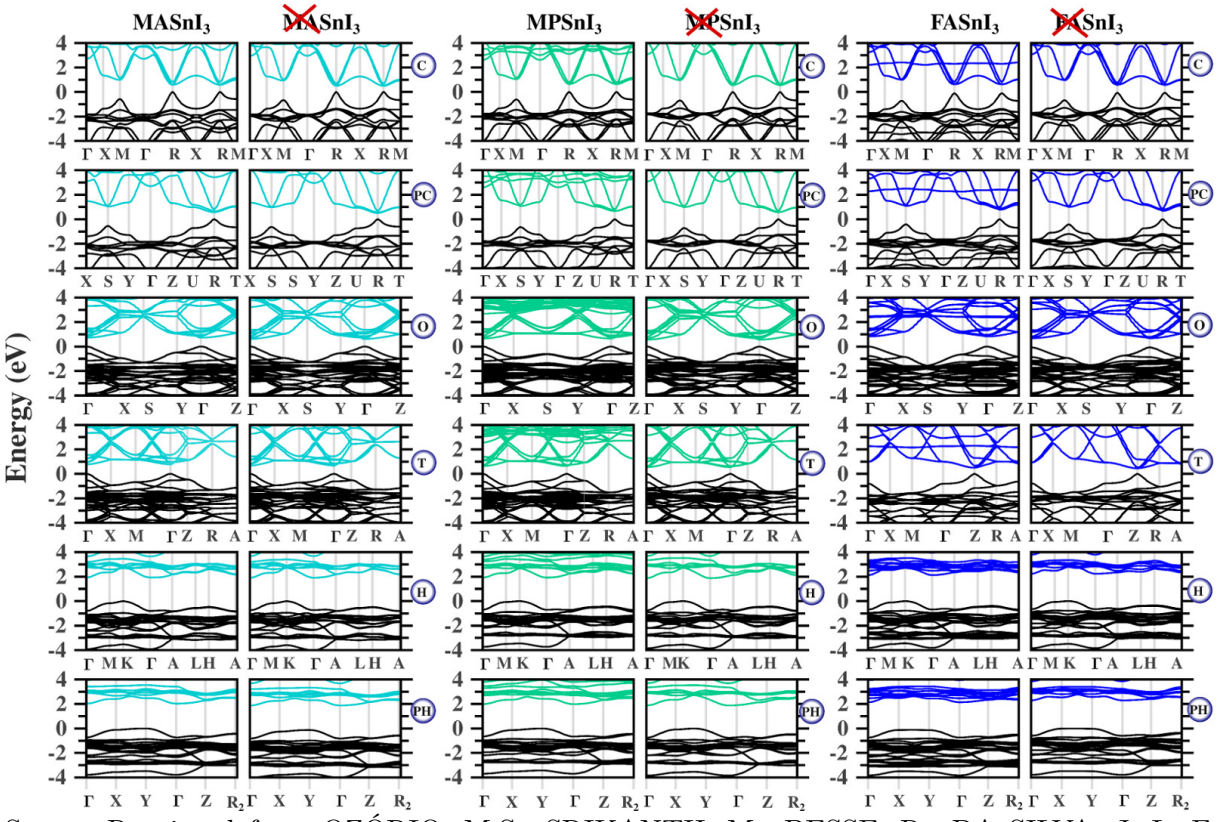

Source: Reprinted from OZÓRIO, M.S.; SRIKANTH, M.; BESSE, R.; DA SILVA, J. L. F. **Physical Chemistry Chemical Physics**, v. 23, n.3, p. 2286–2297, 2021[129]

In order to extract additional information about $A\mathrm{SnI_3}$ perovskites, from the frequency-dependent imaginary dielectric-function, we got the absorption coefficient for all lowest-energy $A\mathrm{SnI_3}$ perovskites. We show the results in Figure 13. We found high absorption coefficients ($> 10^5\,\mathrm{cm^{-1}}$) for all $A\mathrm{SnI_3}$, in which onset of the absorption starts in the near-infrared for perovskite structures, while of the hexagonal/pseudo-hexagonal occurs in the ultra-violet. As a result, the hexagonal/pseudo-hexagonal non-perovskite phases require higher photon energy compared to 3D perovskite structures, which make the low-dimensional hexagonal/pseudo-hexagonal structures inappropriate to be used as a light-adsorbing layer in a solar cell. The 3D inorganic-framework connectivity of perovskite structures seems to be desirable for achieving the features of perovskite-based solar cells, e.g., a broader absorption range of solar energy. In fact, 52 % of sunlight reaching the earth's surface corresponds to the infrared region, 43 % occurs in the visible-light range, and only 5 % corresponds to the ultraviolet photons.[185] Overall, the onset of absorption

Figure 13 – Absorption coefficient for the pseudo-hexagonal(PH), hexagonal (H), pseudo-cubic (PC), cubic (C), tetragonal (T), and orthorhombic (O) phases of $MASnI_3$, $MPSnI_3$ and $FASnI_3$ perovskites. The vertical lines show the fundamental bandgap values.

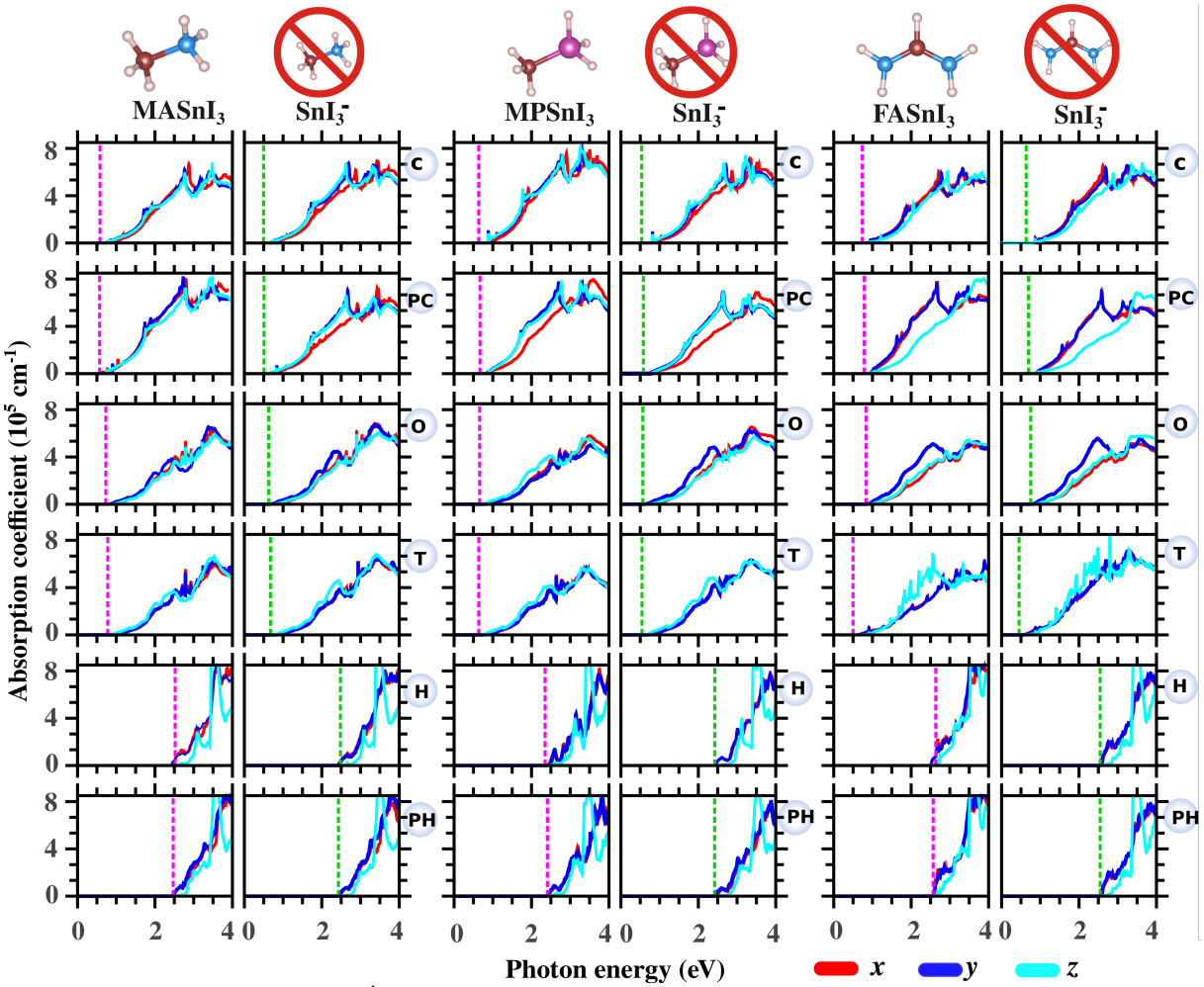

Source: Reprinted from OZÓRIO, M.S.; SRIKANTH, M.; BESSE, R.; DA SILVA, J. L. F. **Physical Chemistry Chemical Physics**, v. 23, n.3, p. 2286–2297, 2021[129]

energy is at the same point as the fundamental bandgap energy for all phases; and the transitions are allowed by symmetry.

The *A*-cations play a minor role on the absorption coefficient of those $ASnI_3$ perovskites, to conclude that we calculate separated the absorption coefficient of inorganic part (SnI_3^-) and compared to that of whole $ASnI_3$ structure, which displayed no significant difference in the trends (see Figure 13). The absorption coefficient of perovskites and non-perovskite structures display an enormous difference regarding the absorbed photon energy. Accordingly, our results suggest that any factor that can affect the connectivity of the inorganic framework may also affect the absorption coefficient. As a result, we expect that more large *A*-cations than those investigated in this work may affect the optoelectronic properties if able to break the inorganic-framework connectivity. Thus, we

Table 2 – Direct fundamental/optical bandgap energy at PBE+D3 level, ($E^{f}_{g,\mathrm{PBE+D3}}/E^{opt}_{g,\mathrm{PBE+D3}}$), and HSE06 fundamental bandgap energy ($E^{f}_{g,\mathrm{HSE06}}$) for the pseudo-hexagonal (PH), hexagonal (H), pseudo-cubic (PC), cubic (C), tetragonal (T), and orthorhombic (O) phases of $A\mathrm{SnI_3}$ perovskites. The fundamental indirect bandgap values of pseudo-hexagonal and hexagonal structures are given below the direct bandgap values. All bandgap values are given in eV.

		$E^{f}_{g,\mathrm{PBE+D3}}$	$E^{f}_{\mathrm{g,HSE06}}$	**k**-point	$E^{opt}_{g,\mathrm{PBE+D3}}$
$\mathrm{MASnI_3}$	C	0.58	0.91	R	0.58
	PC	0.57	0.90	R	0.57
	O	0.73	1.10	Γ	0.73
	T	0.78	1.15	Γ	0.78
	H	2.42	3.17	M"	2.42
		1.93	2.59	K-Γ	
	PH	2.47	3.20	V2	2.47
		2.03	2.59	Y-Γ	
$\mathrm{MPSnI_3}$	C	0.64	0.99	R	0.64
	PC	0.67	1.02	R	0.67
	O	0.66	1.03	Γ	0.66
	T	0.64	0.99	Γ	0.64
	H	2.35	3.31	M	2.35
		1.92	2.58	K-Γ	
	PH	2.41	3.16	Y	2.41
		1.98	2.54	Y-Γ	
$\mathrm{FASnI_3}$	C	0.73	1.10	R	0.73
	PC	0.79	1.15	R	0.79
	O	0.83	1.21	Γ	0.83
	T	0.50	0.84	Z	0.50
	H	2.51	3.41	Y	2.51
		2.12	2.71	K-Γ	
	PH	2.57	3.36	V2	2.57
		2.25	2.82	X-Γ	

Source: Reprinted from OZÓRIO, M.S.; SRIKANTH, M.; BESSE, R.; DA SILVA, J. L. F. **Physical Chemistry Chemical Physics**, v. 23, n.3, p. 2286–2297, 2021[129]

found good insights into the optoelectronic properties despite neglecting the entropy effects to describe the high-temperature phases.

The fundamental and estimated optical bandgap energy we got with PBE+D3 calculation for the lowest-energy $A\mathrm{SnI_3}$ phases are outlined in Table 2. A preceding literature report claimed that satisfactory theoretical-experimental agreement for fundamental bandgap energy of lead-based perovskites results from error cancellations between relativist spin-orbit coupling and GGA result. For tin perovskites, however, the GGA calculations underestimate the experimental fundamental bandgap energy

of ASnI$_3$ structures because of their reduced spin-orbit coupling effects compared to lead-iodide ones.[186,187] Because of inorganic-connectivity reduction, SnI$_6$ corner-sharing structures (perovskite structures) have the fundamental bandgap energy closer to each other than the one-directional SnI$_6$ face-sharing hexagonal/pseudo-hexagonal structures. Our results for the fundamental bandgap energy show good agreement with preceding GGA-based calculations,[186–189] which was experimentally estimated as 1.20 eV for the tetragonal MASnI$_3$ phase, and 1.41 eV for orthorhombic FASnI$_3$.[156] Hence, the high-cost HSE06 functional present better experimental agreement to the tetragonal MASnI$_3$ phase than GGA-functional, within an absolute difference of only 0.05 eV. However, experimental-theoretical deviations can be minimized by increasing the exact exchange energy of Hartree-Fock,[186] but considerable deviations can also come from the structural difference between calculated and experimental structures.

3.8 Summary

In this chapter, we presented an *ab initio* investigation based on DFT calculations to investigate the role of orientation/alignment, size, dipole, and hydrogen bonding interactions of three distinct organic cations in the physical-chemistry properties of ASnI$_3$ perovskites. We reported for the first time the study of MPSnI$_3$, and its comparison with the MASnI$_3$ and FASnI$_3$ perovskites. Under an agreement with experimental phase transitions trends, we found that the orthorhombic phase of ASnI$_3$ systems displays higher structural stability at low temperatures than the other phases (e.g., cubic, tetragonal, and hexagonal phases). The effect of dipole moment on the relative stability of ASnI$_3$ structures shows a more decisive role than other investigated factors, including the size of cation and hydrogen bonds. Hydrogen bonding interactions cause a major impact on driving the higher structural stability of tin perovskites. In fact, by acting as an attractive force between the inorganic framework and A-cation, the weak hydrogen bonding interactions enhance the structural cohesion.

Regarding the optoelectronic properties, the effect of A-cation is secondary. Besides the absorption coefficient, we found that the inorganic framework formed by SnI$_6$ octahedra dominates the band structure and density of states around the Fermi level. The SnI$_6$ connectivity affects all optoelectronic properties. Small fundamental bandgap energy, dispersive bands, and a broader absorption of photon energy are some characteristics of the 3D ASnI$_3$ perovskites. Wide fundamental bandgap, flat bands, and reduced absorption range of solar spectra characterize the 1D hexagonal/pseudo-hexagonal ASnI$_3$ structures.

4 NOVEL ZERO-DIMENSIONAL HYBRID PEROVSKITES

.

Zero-dimensional perovskites display inorganic octahedra clusters interspersed with organic/inorganic cations in three-dimensional directions.[1,108] This class of materials has increased quantum confinement effects, improved structural stability, and extensive flexibility of shape and sizes compared to the 3D archetypal perovskite structures.[1,108] Non-toxic bismuth and antimony employed in the constructions of octahedra of 0D perovskites form stable anionic complexes with halide with different morphologies.[1,117,118] Because of the versatility of octahedra composition and a large library of stabilizers inorganic/organic cations, 0D perovskites have peculiar features, e.g., high exciton binding energy,[120] increased air-stability,[93] and photoluminescence quantum yields.[118,119] As a result, 0D systems found many potential applications, including spintronics,[110] capacitors,[115] light-emitting diodes,[111] lasers,[112] catalysts,[113] photodetectors[123] and X-Ray imaging.[124] Solar cells based on 0D perovskites display low efficiency,[121,122] but a construction based on the mixing of different perovskite dimensionality appears as one suitable route to overcome the lowered efficiency of low-dimensional structures,[125] and the large structural flexibility of 0D perovskites suggest their potential in these constructions.[126] Overall, it is urgent to study the microscopic origins behind the 0D perovskites features.

This chapter presents the theoretical analysis of three novel lead-free and stable bismuth-based 0D perovskites synthesized by our experimental collaborators. The theoretical results are organized in the following sections: (*i*) computational details, (*ii*) crystal structure of zero-dimensional perovskites, (*iii*) equilibrium structural parameters, (*iv*) electronic structure, (*v*) optical properties, (*vi*) chemical bonding analysis, and the (*vii*) summary of the results.

4.1 Computational Details

We used the GGA-PBE exchange-correlation functional for all self-consistent optimizations. The vdW D3 correction proposed by Grimme[143,151] was employed to enhance the description interactions between the organic and inorganic parts of the 0D bismuth-based perovskites. We applied plane-wave cutoff energy of 841.82 eV to achieve the equilibrium volume of 0D perovskites via stress-tensor calculations. Once found the equilibrium volume, we run all remaining calculations (e.g., optical properties, the density of states, and band structures.) with a plane-wave cutoff energy of 473.53 eV. The convergence criteria for the total energy and atomic force were 1×10^{-5} eV and 0.025 eV Å^{-1}, respectively. For the stress-tensor calculations of 0D perovskites (see Figure 14), the Brillouin zone was sampled by employing a **k**-point density of 20 Å^{-1}, which yielded

Figure 14 – Crystal structures of the three novel lead-free zero-dimensional perovskites: $C_{20}H_{20}N_4Bi_2I_{10}$, $C_{42}H_{39}N_6Bi_2I_9$, and $C_{30}H_{25}N_6BiI_6 \cdot 2\,H_2O$. The dashed lines indicate the unit cell. The kind of BiI_6 connectivity and the unit formula of each 0D perovskite structure are shown below the unit cell representation.

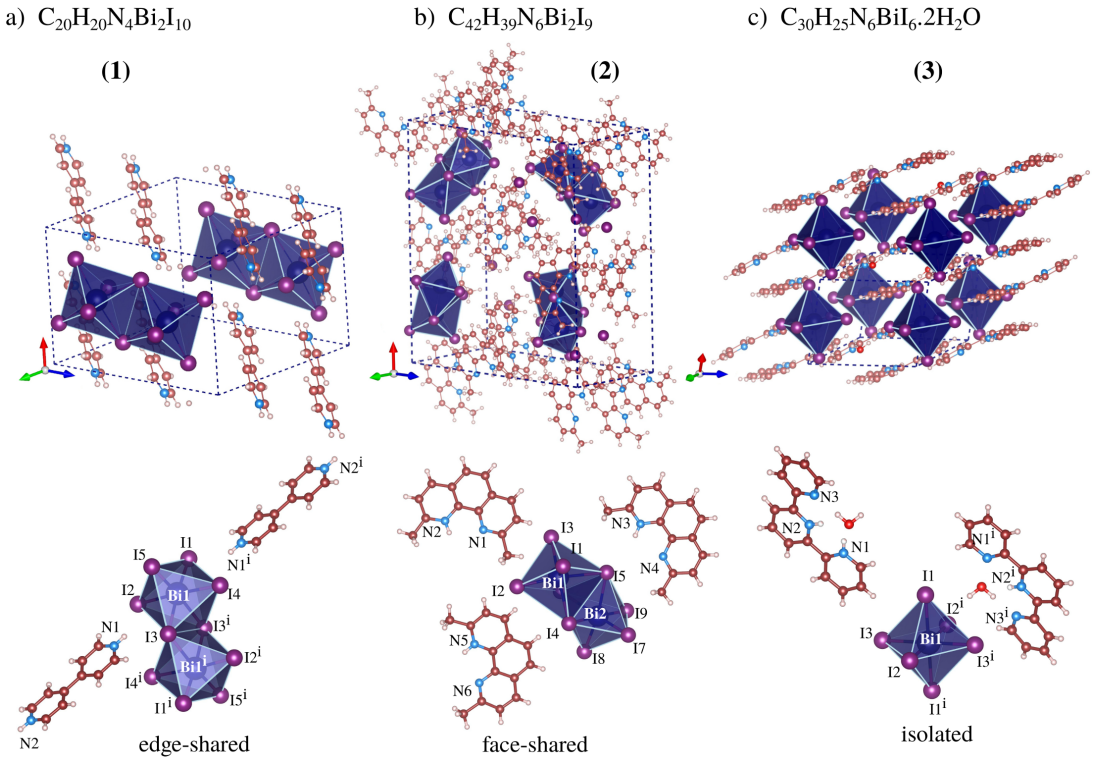

Source: Reprinted from OZÓRIO, M. S.; OLIVEIRA, W. X. C.; SILVEIRA, J. F. R. V.; NOGUEIRA, A. F.; DA SILVA, J. L. F. **Materials Advances**, v. 1, n. 9, p. 3439–3448, 2020[1]

to **k**-point meshes of 2×2×2 for perovskites $C_{20}H_{20}N_4Bi_2I_{10}$ and $C_{30}H_{25}N_6BiI_6 \cdot 2\,H_2O$, and 1×2×1 for $C_{42}H_{39}N_6Bi_2I_9$. For the electronic calculations (e.g., optical properties and density of states calculations), we employed a **k**-point density of 40 $Å^{-1}$, which generated **k**-meshes of 5×4×4 , 2×4×2 , and 5×5×4 for perovskites $C_{20}H_{20}N_4Bi_2I_{10}$, $C_{42}H_{39}N_6Bi_2I_9$, and $C_{30}H_{25}N_6BiI_6 \cdot 2\,H_2O$, respectively.

4.2 Crystal Structure of Zero-Dimensional Perovskites

The crystal structures of the three novel 0D perovskites are shown in Figure 14. The $[Bi_xI_y]^{z-}$ octahedra of those 0D perovskites are interspersed by large organic cations, namely, bpy = 4,4'-bipyridine, dmphen = 2,9-dimethyl-1,10-phenantroline, and terpy = 2,2';6',2"-terpyridine. The di-protonated bpy (H_2bpy^{2+}) is present in the perovskite $C_{20}H_{20}N_4Bi_2I_{10}$; the mono-protonated dmphen ($Hdmphen^{+}$) occurs in the perovskite $C_{42}H_{39}N_6Bi_2I_9$, and the combination of di-protonated (H_2terpy^{2+}) and mono-pronated ($Hterpy^{+}$) cations occur in the perovskite $C_{30}H_{25}N_6BiI_6 \cdot 2\,H_2O$. The inorganic moieties have different morphologies in these 0D compounds, i.e., edge-sharing bi-octahedra

($Bi_2I_{10}{}^{4-}$ in the $C_{20}H_{20}N_4Bi_2I_{10}$ perovskite), face-sharing bi-octahedra ($Bi_2I_9{}^{3-}$ in the perovskite $C_{42}H_{39}N_6Bi_2I_9$) or either isolated octahedron ($BiI_6{}^{3-}$ in the perovskite $C_{30}H_{25}N_6BiI_6 \cdot 2\,H_2O$).

As shown in Figure 14a, the triclinic unit cell ($P\bar{1}$) of $C_{20}H_{20}N_4Bi_2I_{10}$ has two H_2bpy^{2+} organic cation and one edge-sharing $[Bi_2I_{10}]^{4-}$ moiety, which is composed of two $[BiI_5]^{2-}$ identical square-based pyramids. The Bi–I bond lengths are between 2.9508(5) and 3.2562(5) Å, and iodide ions shared by fused octahedra have elongated Bi–I bonds, e.g., I3–$Bi1^i$ = 3.2562(5) Å and Bi1–I3 = 3.2062(5) Å, and the bridge angle Bi1–I3–$Bi1^i$ corresponds to 95.29(1)°. As a result of the non-symmetrical Bi–I bonds lengths and bridge angles, each fused BiI_6 octahedron is distorted, and the iodine ligands out-of bridge plane are kind of bent in direction of each other with a low bond angle (I2–Bi1–I4 = 176.25(1)°). The distance between the two bismuth cations ($Bi_1 \cdots Bi_1{}^i$) is equal to 4.7758(5) Å. The inter-molecular distance that determines the interaction between the organic cation H_2bpy^{2+} units with terminal iodide anions of $[Bi_2I_{10}]^{4-}$ is 2.921 Å to 3.086 Å.

The orthorhombic perovskite $C_{42}H_{39}N_6Bi_2I_9$ has space group $Pna2_1$, and for each $[Bi_2I_9]^{3-}$ unit it exists three monovalent $Hdmphen^+$ cation. As stated in Figure 14b, $[Bi_2I_9]^{3-}$ units have two octahedra fused by one face. The unit cell has four face-sharing $[Bi_2I_9]^{3-}$ octahedra, which one with distinct orientations and far disconnected by the large $Hdmphen^+$ organic cations also displayed with distinct orientations. Three connected aromatic rings characterize the $Hdmphen^+$ cations, which exhibit large planarity and surface area. In its turn, $[Bi_2I_9]^{3-}$ occupies the blank space left from the stacking of $Hdmphen^+$ cations, but contacts near octahedra generate a supramolecular chain approximately normal to the stacking of organic cations where the shortest anion-anion distance is 3.667(1) Å. As noticed for the perovskite $C_{20}H_{20}N_4Bi_2I_{10}$, larger bond lengths occur for the bridge iodide ligands. The bond lengths varied from 3.1471(9) to 3.3590(8) Å for shared ligands. As expected from face-sharing eclipsed octahedra dimmers, a slight twist angle of 2.0(5) Å occurs. We found an inter-metallic bismuth-bismuth distance of 4.2175(7) Å (Bi1···Bi2), and H···I distances bigger or equal to 2.967 Å, which suggest the existence of weak hydrogen bond interactions.

In its turn, as represented in Figure 14c, the triclinic structure ($P\bar{1}$) of perovskite $C_{30}H_{25}N_6BiI_6 \cdot 2\,H_2O$ has a mono-metallic $[BiI_6]^{3-}$ complex, two water molecule, and two organic cations, i.e., one mono-protonated 2,2':6,2"-terpyridine molecule ($Hterpy^+$), and other di-protonated (H_2terpy^{2+}). Each $[BiI_6]^{3-}$ octahedron of perovskite $C_{30}H_{25}N_6BiI_6 \cdot 2\,H_2O$ is far distanced. For instance, the distance between two bismuth cations is 10.947(2) Å. The octahedron display very low structural distortions, hence, there exists a negligible difference among all six Bi–I bonds. In this array, the cations chains are spaced of 10.822(2) Å from each other.

4.3 Equilibrium Structural Parameters

To verify the role of the van der Waals correction in our theoretical description of 0D structures, we optimized the perovskite $C_{20}H_{20}N_4Bi_2I_{10}$ with (PBE+D3) and without the D3 van der Waals correction (PBE). According to Table 3, the comparison of PBE and PBE+D3 results for lattice parameters and internal properties suggests the D3 van der Waals correction has a decisive contribution to a better description of the structural properties of 0D perovskites. Indeed, the PBE+D3 results display the lowest deviation from the experimental findings, being more suitable for the theoretical characterization of those hybrid 0D perovskites.

Table 3 – Structural properties of perovskite $C_{20}H_{20}N_4Bi_2I_{10}$ calculated by employing the PBE exchange-correlation functional with (PBE+D3) and without Van der Waals D3 corrections (PBE): lattice parameters, and internal structural properties, i.e., average bond length between the halide and metallic cation (d_{av}^{B-X}), effective coordination number of B-cation (ECN^B), and average B_xX_y volume ($V_{B_xX_y}$) The deviation from experimental results of bismuth-iodide perovskites (Δ) are also reported.[1]

Method	a_0 (Å)	b_0 (Å)	c_0 (Å)	α (°)	β (°)	γ (°)	d_{av}^{B-X} (Å)	ECN^B (NNN)	$V_{B_xX_y}$ (Å^3)
PBE+D3	8.80	11.02	11.74	115.33	100.71	100.13	3.11	5.75	80.05
Δ (%)	−0.34	−0.09	−0.42	0.77	1.01	0.04	0.65	2.50	2.46
PBE	9.00	11.36	12.43	117.21	98.88	99.67	3.13	5.75	81.24
Δ (%)	1.93	6.16	5.43	2.41	−0.82	−0.42	1.24	2.50	3.99

Source: Reprinted from OZÓRIO, M. S.; OLIVEIRA, W. X. C.; SILVEIRA, J. F. R. V.; NOGUEIRA, A. F.; DA SILVA, J. L. F. **Materials Advances**, v. 1, n. 9, p. 3439–3448, 2020[1]

Once we recognized the relevance of van der Waals correction, all calculations were done by considering the PBE+D3 approach. In particular, as shown in Table 4, we applied the D3 van der Waals correction to all PBE calculations to identify the undermined hydrogen position of perovskite $C_{30}H_{25}N_6BiI_6 \cdot 2\,H_2O$. The principal shortcoming of X-Ray experimental structures originates from the unpredictability of the hydrogen atoms' positions in some compounds. Perovskite $C_{20}H_{20}N_4Bi_2I_{10}$ dispenses the need for further checking the positions of hydrogen atoms of the H_2bpy^{2+} units, which are well-defined. Despite the degrees of freedom, the sites of $Hdmphen^+$ units are symmetrical, and the perovskite $C_{42}H_{39}N_6Bi_2I_9$ structure has little bearing. Perovskite $C_{30}H_{25}N_6BiI_6 \cdot 2\,H_2O$ has more degrees of freedom because of the presence of two organic cations (one di-protonated H_2terpy^{2+} and one mono-protonated $Hterpy^+$) and of two water molecules, which interact with the organic cations via O···H hydrogen bond interactions. The modeling of different

Table 4 – Tests to define the position of hydrogen atoms in the perovskite $C_{30}H_{25}N_6BiI_6 \cdot 2\,H_2O$ by comparing the theoretical-experimental percentage deviations (Δ) of lattice parameters, bismuth-iodide average bond length ($d_{av}^{\mathrm{Bi-I}}$), average non-adjacent I–Bi–I average bond angle (Θ_{av}), adjacent I–Bi–I average bond angle (θ_{av}), and average effective coordination number of bismuth ($\mathrm{ECN}^{\mathrm{Bi}}$). All calculations were performed employing the D3 van der Waals correction and the PBE functional (PBE+D3).

	Exp.	DFT[a]	Δ	DFT[b]	Δ	DFT[c]	Δ	DFT[d]	Δ	DFT[e]	Δ
a_0 (Å)	10.67	11.28	5.72	10.94	2.53	11.12	4.12	10.66	−0.09	10.86	1.78
b_0 (Å)	10.82	10.53	−2.68	10.71	−1.02	10.80	−0.18	10.68	−1.29	10.77	−0.46
c_0 (Å)	10.95	11.15	1.83	10.77	−1.64	10.57	−3.47	10.98	0.27	10.74	−1.92
α (°)	81.04	83.12	2.57	80.57	−0.58	81.05	0.01	81.17	0.16	81.76	0.89
β (°)	61.71	63.78	3.35	60.64	−1.73	60.37	−2.17	61.69	−0.03	61.47	−0.39
γ (°)	61.46	56.20	−8.56	60.88	−0.94	60.94	−0.85	61.80	0.55	61.84	0.62
$d_{av}^{\mathrm{Bi_1-I}}$ (Å)	3.08	3.10	0.65	3.10	0.65	3.11	0.97	3.10	0.65	3.11	0.97
$\Theta_{av}^{\mathrm{Bi_1}}$ (°)	180.00	177.20	−1.56	178.65	−0.75	178.64	−0.76	179.17	−0.46	177.94	−1.31
$\theta_{av}^{\mathrm{Bi_1}}$ (°)	90.00	89.99	−0.01	90.00	0.00	90.00	0.00	90.00	0.00	90.00	0.00
$\mathrm{ECN}^{\mathrm{Bi_1}}$	6.00	5.96	−0.67	5.97	0.50	5.98	−0.33	6.00	0.00	5.99	−0.17
	Exp.	DFT[a]	Δ	DFT[b]	Δ	DFT[c]	Δ	DFT[d]	Δ	DFT[e]	Δ
a_0 (Å)	10.67	11.28	5.72	10.93	2.44	10.93	2.44	11.05	3.56	10.71	0.37
b_0 (Å)	10.82	10.53	−2.68	10.69	−1.20	10.72	−0.92	10.72	−0.92	10.74	−0.74
c_0 (Å)	10.95	11.15	1.83	10.77	−1.64	10.56	−3.56	10.67	−2.56	10.89	−0.55
α (°)	81.04	83.12	2.57	80.60	−0.54	80.49	−0.68	81.22	0.22	81.96	1.14
β (°)	61.71	63.78	3.35	60.59	−1.81	60.63	−1.75	60.27	−2.33	61.47	−0.39
γ (°)	61.46	56.20	−8.56	61.22	−0.39	61.04	−0.68	61.58	−0.19	62.18	1.17
$d_{av}^{\mathrm{Bi_1-I}}$ (Å)	3.08	3.10	0.65	3.10	0.65	3.10	0.65	3.11	0.97	3.11	0.97
$\Theta_{av}^{\mathrm{Bi_1}}$ (°)	180.00	177.20	−1.56	178.71	−0.72	178.69	−0.73	178.74	0.70	178.32	−0.93
$\theta_{av}^{\mathrm{Bi_1}}$ (°)	90.00	89.99	−0.01	90.00	0.00	90.00	0.00	90.00	0.00	90.00	0.00
$\mathrm{ECN}^{\mathrm{Bi_1}}$	6.00	5.96	−0.67	5.97	0.50	5.97	0.50	5.97	0.50	5.99	−0.17

Source: Reprinted from OZÓRIO, M. S.; OLIVEIRA, W. X. C.; SILVEIRA, J. F. R. V.; NOGUEIRA, A. F.; DA SILVA, J. L. F. **Materials Advances**, v. 1, n. 9, p. 3439–3448, 2020[1]

hydrogen positions may yield multiple non-degenerated configurations with different structural outputs and a massive deviation from the experimental results.

To perform the stress-tensor calculations, we examined several starting configurations of perovskite $C_{30}H_{25}N_6BiI_6 \cdot 2\,H_2O$ by modifying the hydrogen atoms' positions of the two water molecules and the positions of hydrogen atoms between the two organic cations. Table 4 shows the optimization results of ten trial positions, and the respective experimental-theoretical deviation (Δ). Most parameters were compared, including lattice parameters and internal properties like bond lengths/angles. Through stress-tensor optimization, the initial positions of hydrogen atoms yield different local minima with different structural parameters. For instance, as shown in Table 4, the theoretical-experimental deviation of the lattice parameter within this set was as high as 8 %.

The results reveal the need to address the ambiguities and the uncertainty of the positions of hydrogen atoms in complex systems. Testing different initial positions for hydrogen atoms allowed us to determine the best theoretical-experimental agreement and give clues about the correct positions of hydrogen atoms non-properly determined by X-Ray analysis. We identified the DFT^d calculations as our best theoretical description of perovskite $C_{30}H_{25}N_6BiI_6 \cdot 2\,H_2O$, i.e., by giving the best theoretical-experimental agreement.

Table 5 summarizes the structural characterization of all three novel 0D perovskites, including both internal and external parameters properties. We found a low theoretical-experimental deviation from experimental results for all the structural parameters. In particular, for the lattice parameters (a_0, b_0, c_0, α, β, γ) the deviation are ranging from $-1.3\,\%$ to $1.0\,\%$. Thus, the results are solid and validate the method we employed.

Table 5 – Theoretical (PBE+D3 calculations) and experimental values of lattice parameters, and average values for: the bond lengths of Bi–I ($d_{av}^{\mathrm{Bi-I}}$), non-adjacent bond angle of I–Bi–I (Θ_{av}), adjacent bond angle of I–Bi–I (θ_{av}), and average effective coordination number of bismuth ($\mathrm{ECN}^{\mathrm{Bi}}$). The experimental-theoretical deviation (Δ) and the respective population standard deviation (σ) by considering two octahedra (two unit cells for perovskite $C_{30}H_{25}N_6BiI_6 \cdot 2\,H_2O$) are given for all three structures.

	$C_{20}H_{20}N_4Bi_2I_{10}$			$C_{42}H_{39}N_6Bi_2I_9$			$C_{30}H_{25}N_6BiI_6 \cdot 2\,H_2O$		
	Exp.	DFT	Δ	Exp.	DFT	Δ	Exp.	DFT	Δ
a_0 (Å)	8.83	8.80	−0.34	23.55	23.32	−0.98	10.67	10.66	−0.09
b_0 (Å)	10.70	11.02	−0.09	10.43	10.37	−0.58	10.82	10.68	−1.29
c_0 (Å)	11.79	11.74	−0.42	21.92	21.85	−0.32	10.95	10.98	0.27
α (°)	114.45	115.33	0.77	90.00	90.00	0.00	81.04	81.17	0.16
β (°)	99.70	100.71	1.01	90.00	90.00	0.00	61.71	61.69	−0.03
γ (°)	100.09	100.13	0.04	90.00	90.00	0.00	61.46	61.80	0.55
$d_{av}^{\mathrm{Bi_1-I}}$ (Å)	3.09	3.11	0.65	3.10	3.12	0.65	3.08	3.10	0.65
$d_{av}^{\mathrm{Bi_2-I}}$ (Å)				3.12	3.13	0.32			
$\Theta_{av}^{\mathrm{Bi_1}}$ (°)	174.79	174.83	0.02	171.61	170.66	−0.55	180.00	179.17	−0.46
$\Theta_{av}^{\mathrm{Bi_2}}$ (°)				172.00	172.31	0.18			
$\theta_{av}^{\mathrm{Bi_1}}$ (°)	89.96	89.97	0.01	90.02	90.06	0.04	90.00	90.00	0.00
$\theta_{av}^{\mathrm{Bi_2}}$ (°)				89.88	89.89	0.01			
$\mathrm{ECN}^{\mathrm{Bi_1}}$	5.61	5.74	2.32	5.32	5.48	3.01	6.00	6.00	0.00
$\mathrm{ECN}^{\mathrm{Bi_2}}$				5.09	5.40	6.09			
σ			0.76			1.62			0.36

Source: Reprinted from OZÓRIO, M. S.; OLIVEIRA, W. X. C.; SILVEIRA, J. F. R. V.; NOGUEIRA, A. F.; DA SILVA, J. L. F. **Materials Advances**, v. 1, n. 9, p. 3439–3448, 2020[1]

The results reveal little experimental-theoretical deviation for the local structure parameters, except for the effective coordination number of bismuth ($\mathrm{ECN}^{\mathrm{Bi}}$), which

displays deviations as high as 2 %/6 % for perovskites $C_{20}H_{20}N_4Bi_2I_{10}$/$C_{42}H_{39}N_6Bi_2I_9$, which is consistent with fused octahedra. In fact, an increasing structural distortion from an ideal octahedron (i.e., equal Bi–I bond lengths, IBiI bond angles of 90° or 180°) occurs when the number of shared iodide increases. The isolated octahedron of perovskite $C_{30}H_{25}N_6BiI_6 \cdot 2\,H_2O$ displays the lowest structural distortion. The face-sharing octahedra of perovskite $C_{42}H_{39}N_6Bi_2I_9$ exhibit the highest distortion, followed by the edge-sharing octahedra of perovskite $C_{20}H_{20}N_4Bi_2I_{10}$. Thus, we expect that greater deviations may occur in structures with more complex fused octahedra since the discrepancies increase with the octahedron fusion degree.

4.4 Electronic Structure

Figure 15 – Density of states and band structure calculated at PBE+D3 level for all three 0D perovskites: $C_{20}H_{20}N_4Bi_2I_{10}$, b) $C_{42}H_{39}N_6Bi_2I_9$, and c) $C_{30}H_{25}N_6BiI_6 \cdot 2\,H_2O$.

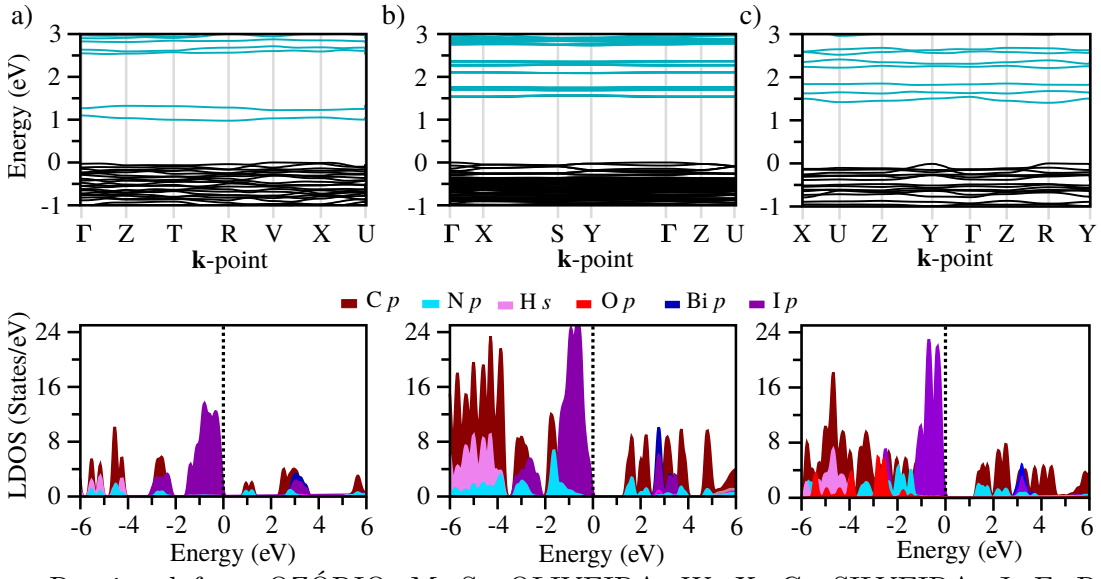

Source: Reprinted from OZÓRIO, M. S.; OLIVEIRA, W. X. C.; SILVEIRA, J. F. R. V.; NOGUEIRA, A. F.; DA SILVA, J. L. F. **Materials Advances**, v. 1, n. 9, p. 3439–3448, 2020[1]

Because of the discrete nature separation of inorganic moiety by the large organic cations, which severely decreases carrier mobility, the three 0D perovskites display nearly flat band structures, Figure 15. Despite the band structures appearing equally flat for all 0D perovskites, compound $C_{42}H_{39}N_6Bi_2I_9$ presented considerably larger hole and electron effective mass than the remaining ones. This fact can be justified by the greater distance between inorganic moieties when compared to $C_{20}H_{20}N_4Bi_2I_{10}$ and $C_{30}H_{25}N_6BiI_6 \cdot 2\,H_2O$ perovskites. Our PBE+D3 (HSE06, frozen PBE+D3 structures) calculations reveal that all materials are semiconductors with fundamental bandgap energy of 0.98 eV (1.80 eV), 1.53 eV (2.35 eV), 1.41 eV (2.24 eV) for perovskites $C_{20}H_{20}N_4Bi_2I_{10}$, $C_{42}H_{39}N_6Bi_2I_9$ and

$C_{30}H_{25}N_6BiI_6 \cdot 2\,H_2O$, in this order. Thus, because of the non-local Fock exchange, the results found with HSE06 are larger than PBE results.

Valence band maxima (VBM) and conduction band minima (CBM) are at V/R for perovskite $C_{20}H_{20}N_4Bi_2I_{10}$ within $(\frac{1}{2}, -\frac{1}{2}, 0)\frac{2\pi}{a_0}/\ (\frac{1}{2}, \frac{1}{2}, \frac{1}{2})\frac{2\pi}{a_0}$ coordinates; for perovskite $C_{42}H_{39}N_6Bi_2I_9$ the VBM is at $\Gamma\ (0,0,0)\frac{2\pi}{a_0}$ and CBM between $\Gamma - X\ (\frac{3}{10}, 0, 0)\frac{2\pi}{a_0}$; VBM and CBM are at the same point $R\ (\frac{1}{2}, \frac{1}{2}, \frac{1}{2})\frac{2\pi}{a_0}$ for perovskite $C_{30}H_{25}N_6BiI_6 \cdot 2\,H_2O$. As Figures 15 show, all materials display almost similar density of states contributions. The *p*-states of iodide dominated de VBM, while CBM has comparable contributions of the *p*-states of C and N of organic cations.

4.5 Optical Properties

The absorption coefficient calculations found at the PBE+D3 level consider the direct transitions from the valence to the conduction bands. According to the Figure 16, the optical bandgap energy shows the onset of optical activity, which represents the optical bandgap energy of 1.01 eV, 1.53 eV, and 1.41 eV, respectively, for $C_{20}H_{20}N_4Bi_2I_{10}$, $C_{42}H_{39}N_6Bi_2I_9$, and $C_{30}H_{25}N_6BiI_6 \cdot 2\,H_2O$ perovskites. However, the initial activity associated to the cation-anion transitions is negligible when compared to the intra-octahedra transitions, I(p)→Bi(p), where absorption occurs around 2.5 eV according to the density of states. The poor carrier mobility related to the nature of the interactions between anion and cation justifies the difference in the intensity of cation-anion and intra-octahedra transitions. Thus, to estimate the onset of optical activity, we employed the extrapolation of the absorption coefficient curve. As a result, we found optical bandgap being approximately the same for all 0D perovskites and in better agreement with the experimental findings.

Table 6 – Optical bandgap energy (in eV) found for the perovskites $C_{20}H_{20}N_4Bi_2I_{10}$, $C_{42}H_{39}N_6Bi_2I_9$ and $C_{30}H_{25}N_6BiI_6 \cdot 2\,H_2O$ through the interception of photon energy axis by the extrapolation done to the absorption coefficient curve ($E^{opt}_{g,\mathrm{PBE+D3}}$), employing the HSE06 shift ($E^{opt}_{g,\mathrm{HSE06}}$), and according to experimental data ($E^{opt}_{g,\mathrm{Exp.}}$).

0D Perovskites	$E^{opt}_{g,\mathrm{PBE+D3}}$	$E^{opt}_{g,\mathrm{HSE06}}$	$E^{opt}_{g,\mathrm{Exp.}}$
$C_{20}H_{20}N_4Bi_2I_{10}$	2.30	3.10	2.31
$C_{42}H_{39}N_6Bi_2I_9$	2.20	3.00	2.19
$C_{30}H_{25}N_6BiI_6 \cdot 2\,H_2O$	2.25	3.09	2.22

Source: Reprinted from OZÓRIO, M. S.; OLIVEIRA, W. X. C.; SILVEIRA, J. F. R. V.; NOGUEIRA, A. F.; DA SILVA, J. L. F. **Materials Advances**, v. 1, n. 9, p. 3439–3448, 2020[1]

We applied an HSE06 shift to enhance the description of the bandgap energy. The

Figure 16 – a) Experimental absorption curves from 1 eV to 4 eV for the perovskites $C_{20}H_{20}N_4Bi_2I_{10}$ (**1**), $C_{42}H_{39}N_6Bi_2I_9$ (**2**) and $C_{30}H_{25}N_6BiI_6 \cdot 2\,H_2O$ (**3**) with the corresponding optical bandgap energy b) Theoretical absorption coefficient calculated at PBE+D3 level for perovskites **1**, **2** and **3**. The PBE+D3 fundamental bandgap energy (orange line), the onset of the intra-octahedra transitions (purple line), and the optical banda-gap energy found as x-interception by the extrapolation done to the absorption coefficient curve (gray line) are also given.

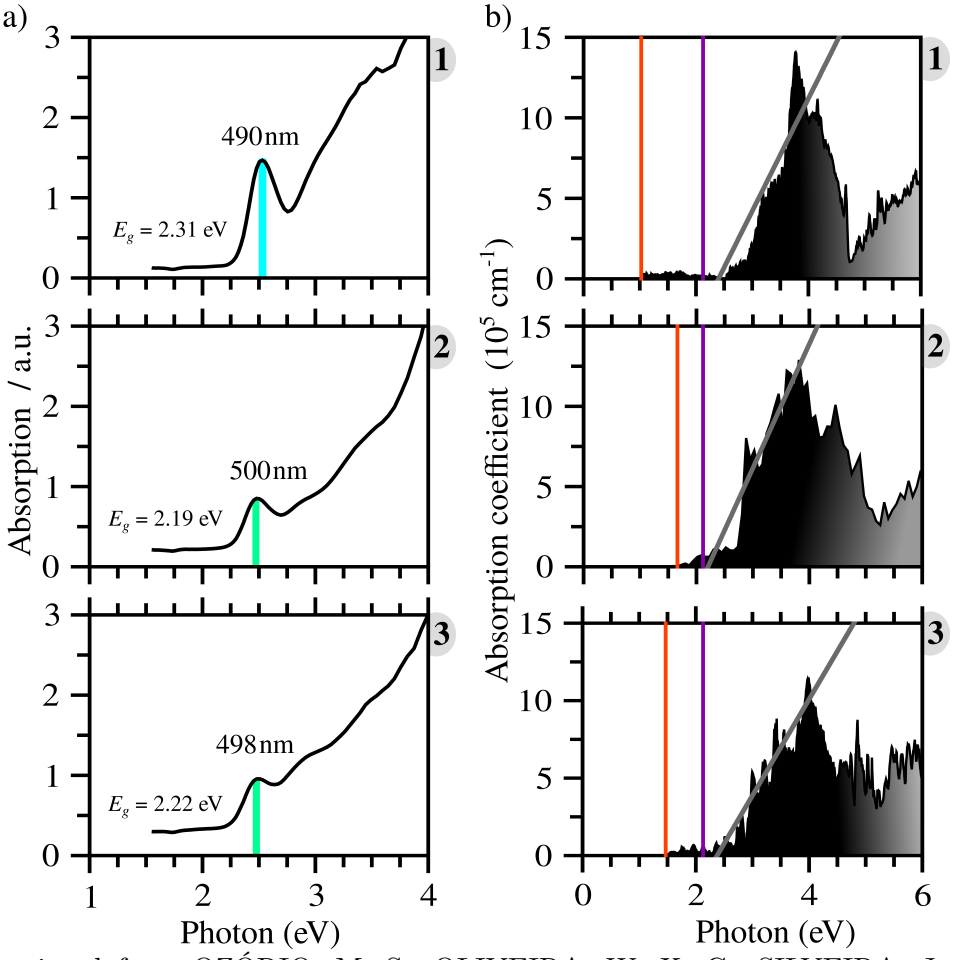

Source: Reprinted from OZÓRIO, M. S.; OLIVEIRA, W. X. C.; SILVEIRA, J. F. R. V.; NOGUEIRA, A. F.; DA SILVA, J. L. F. **Materials Advances**, v. 1, n. 9, p. 3439–3448, 2020[1]

theoretical optical bandgaps are shifted to about 3 eV, close to one another, but displaying quantitative difference with the experimental value. This theoretical-experimental divergence may be related to limiting aspects of theoretical simulations, which do not consider possible defects in experimental samples and exciton effects. In particular, the structural defects can introduce mid-gap states, leading to a smaller optical gap than that found for the calculated perfect crystal structures.

4.6 Chemical Bonding Analysis

Regardless of the kind of connectivity, all 0D perovskites display an ionic behavior for Bi−I bonds as revealed by the Bader charge analysis, Figure 17. Long-range interactions are associated with the small charge difference among $Bi_xI_y^{\delta-}$ octahedra. For instance, two iodides of perovskite $C_{20}H_{20}N_4Bi_2I_{10}$ are transversely symmetric in the apical position ($I_{ap.}$). These apical iodide ions display increased $0.08\,e$ of charge accumulation than the average value observed on the remaining iodide ions because of the $-NH\cdots I_{ap.}$ interaction between H_2bpy^{2+} cation and octahedra. The results explain the close optical behavior of three 0D perovskites and reinforce that the main optical activity comes from the transitions inside the octahedron.

Figure 17 – Effective Bader charge (e) and electron localization function (ELF) calculated at PBE+D3 level for the inorganic moieties of the perovskites a) $C_{20}H_{20}N_4Bi_2I_{10}$, b) $C_{42}H_{39}N_6Bi_2I_9$ and c) $C_{30}H_{25}N_6BiI_6\cdot 2\,H_2O$. In the ELF plots, blue regions mean charge depletion and red represent the regions of charge accumulation.

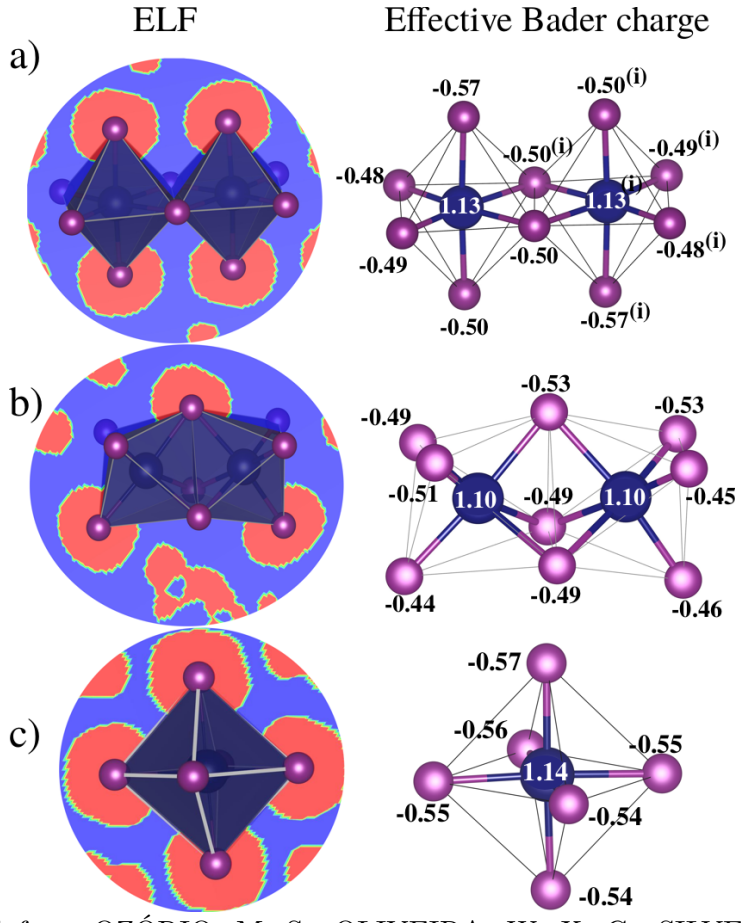

Source: Reprinted from OZÓRIO, M. S.; OLIVEIRA, W. X. C.; SILVEIRA, J. F. R. V.; NOGUEIRA, A. F.; DA SILVA, J. L. F. **Materials Advances**, v. 1, n. 9, p. 3439–3448, 2020[1]

4.7 Summary

We presented a theoretical investigation of the structural and optoelectronic properties of three novel stable and X-Ray determined zero-dimensional perovskites with $C_{20}H_{20}N_4Bi_2I_{10}$, $C_{42}H_{39}N_6Bi_2I_9$, and $C_{30}H_{25}N_6BiI_6 \cdot 2\,H_2O$ chemical formula. We identify an enormous challenge to describe undetermined atom positions to perform the theoretical characterization. For instance, the positions of hydrogen atoms of water molecules could not be defined by X-Ray analysis of $C_{30}H_{25}N_6BiI_6 \cdot 2\,H_2O$. Despite the large degree of freedom to determine those positions, DFT calculations showed to be working to solve this issue, i.e., regarding the lattice parameters and internal properties of $C_{30}H_{25}N_6BiI_6 \cdot 2\,H_2O$, we could determine the hydrogen positions that yield an excellent agreement between calculated and experimental structure. The D3 van der Waals correction made to the DFT calculations has a decisive role in improving the theoretical structural description of those hybrid organic-inorganic systems. Regarding the electronic and optical properties, all three structures are not suitable for a single harvesting layer in solar cells because of the wide optical bandgap energy, which is all larger than 2.10 eV. However, since the structures are stable, they could be tested in the construction of multi-dimensionality structures to improve the stability of devices, for instance, by combining the efficiency of 3D Systems with the stability of low-dimensional 0D perovskites.

5 ROLE OF THE INORGANIC HALIDE COMPLEXES SUBSTITUTION IN THE PHYSICAL PROPERTIES OF LEAD-FREE ZERO-DIMENSIONAL PEROVSKITES

.

The lead toxicity and instability of mainstream perovskites provoked an increased interest in the design of new perovskite materials. In particular, zero-dimensional (0D) hybrid organic-inorganic perovskites are innovative materials given the outstanding potential application for the most diverse purpose, including X-Ray imaging,[124] capacitors,[115] light-emitting diodes,[111] lasers,[112] catalysts,[113] and photodetectors.[123] It is urgent to gain an in-depth understanding of the physical-chemistry properties of 0D perovskites for the control and improvement of 0D perovskite-related technologies. In this sense, experimental and theoretical studies have been done to get clues about the microscopic properties behind 0D perovskite features.[1,113,117] To the best of our knowledge, before our published work,[2] no previous systematic studies were performed to explain how the halide anionic complex substitution affects the properties of 0D perovskites.

This chapter has the theoretical results regarding the structural, electronic, and optoelectronic properties of twelve zero-dimensional perovskites, which were generated by considering the experimental $C_{20}H_{20}N_4Bi_2I_{10}$ and $C_{30}H_{25}N_6BiI_6 \cdot 2\,H_2O$ structures as models.[1] We considered the edge-sharing octahedra B_2X_{10} and the isolated octahedron (BX_6) sites using Bi^{3+} and Sb^{3+} as B-cations and Cl^-, Br^-, and I^- for X-halide sites. To present the theoretical results, the chapter displays the following sections: (*i*) computational details, (*ii*) zero-dimensional perovskite structures, (*iii*) cohesive energy, (*iv*) electronic and optical properties, and (*v*) summary.

5.1 Computational Details

GGA-PBE calculations without the weak van der Waals do not yield accurate modeling of organic-inorganic interactions of the hybrid 0D perovskites systems,[1] thus, our calculations were performed by employing the semi-empirical van der Waals D3 correction[143,151] to the self-consistent DFT-PBE optimizations. To find the equilibrium volume, we performed the stress tensor calculations by employing a **k**-mesh of 2×2×2 and cutoff energy of 632 eV, which is 1.5× higher than the largest cutoff energy among the Bi, Sb, I, Br, Cl, and C, H, N, O species. The convergence criteria for the stress-tensor calculations were values smaller than $0.025\,\text{eV}\,\text{Å}^{-1}$ and of 1×10^{-5} eV for the atomic forces and total energy, respectively. Once we found the stability volume of 0D perovskite structures, we calculated the density of states, band structure, absorption coefficient, and other properties using a **k**-mesh of 4×4×4, and cutoff energy of 474 eV.

Because of the underestimation of the fundamental bandgap energy with GGA-based calculations,[190,191] we enhanced the description of the fundamental bandgap energy with HSE06 functional by considering the frozen PBE+D3 structures and sampling the Γ-point. Moreover, spin-orbit coupling (SOC) effects were observed for many perovskite systems[192,193] and I and Bi are susceptible to SOC effects. Thus, we considered the SOC effects to enhance the optoelectronic properties description. We also increased to twice the number of valence bands of the electronic states to have well-converged SOC results.

5.2 Zero-Dimensional Perovskite Structures

This work was based on two experimental lead-free zero-dimensional structures of our previous work, namely, the Hterpy(H_2terpy)[BiI_6] · 2 H_2O ($C_{30}H_{25}N_6BiI_6 \cdot 2\,H_2O$) and ($H_2$bpy)$_2$[$Bi_2I_{10}$] ($C_{20}H_{20}N_4Bi_2I_{10}$) structures, Figure 18.[1] The crystal structure of those systems displayed distinct octahedra morphologies. The unit cell of $C_{20}H_{20}N_4Bi_2I_{10}$ has one edge-sharing $Bi_2I_{10}^{4-}$ bi-octahedra and two di-protonated 4,4'-bipyridine cations (H_2bpy^{2+}), while the unit cell of $C_{30}H_{25}N_6BiI_6 \cdot 2\,H_2O$ displays an isolated BiI_6^{3-} octahedron surrounded by two protonated 2,2';6',2"-terpyridine organic cations, one is di-protonated (H_2terpy^{2+}) and the other mono-protonated ($Hterpy^{+}$).

We performed an in-depth theoretical analysis of 12 distinct configurations by considering the two experimentally determined perovskites by realizing the replacement of I^- and Bi^{3+} species with Br^-/Cl^- and Sb^{3+}, respectively, Figure 18. In order to identify the candidates for the replacement of I^- and Bi^{3+} species of the $[Bi_xI_y]^{z-}$ sites, we looked for alternatives that display close physical-chemical properties for both I^- and Bi^{3+} species, and with good chances to generate equivalent experimentally halide inorganic complex, i.e., we considered Sb^{3+} replacement for Bi^{3+} because both pair Bi^{3+}/Sb^{3+} have been shown the ability to form isolated and edge-sharing octahedra on 0D perovskites,[117,194–197] and even allowing obtain stable mixed bismuth-antimony perovskite structures.[93,118] Since the organic cation is the same among structures of the same shape, to prevent unnecessary frequency of the same organic cations, we will shortly represent $C_{20}H_{20}N_4B_2X_{10}$ as B_2X_{10}, and $C_{30}H_{25}N_6BX_6 \cdot 2\,H_2O$ as BX_6, where $X = \{Cl^-, Br^-, I^-\}$, and $B = \{Bi^{3+}, Sb^{3+}\}$.

Hereinafter, we will discuss the findings achieved with our calculations. The results give relevant insights and help to understand the effects induced by the inorganic-anionic $[Bi_xI_y]^{z-}$ complexes substitution into the structural, electronic, energetic, and optical properties of 0D perovskites.

5.2.1 Equilibrium Lattice Parameters

As shown in Table 7, we found the equilibrium lattice parameters of all 0D perovskites and compared them with available experimental data.[1] The results suggest an enhanced theoretical-experimental agreement because of the addition of the Van der Waals

Figure 18 – Schematic representation of the experimentally-determined $C_{20}H_{20}N_4Bi_2I_{10}$ and $C_{30}H_{25}N_6BiI_6 \cdot 2\,H_2O$ crystal structures,[1] which were employed as models to investigate the role of inorganic halide complex via the Bi^{3+} and I^- species substitution.

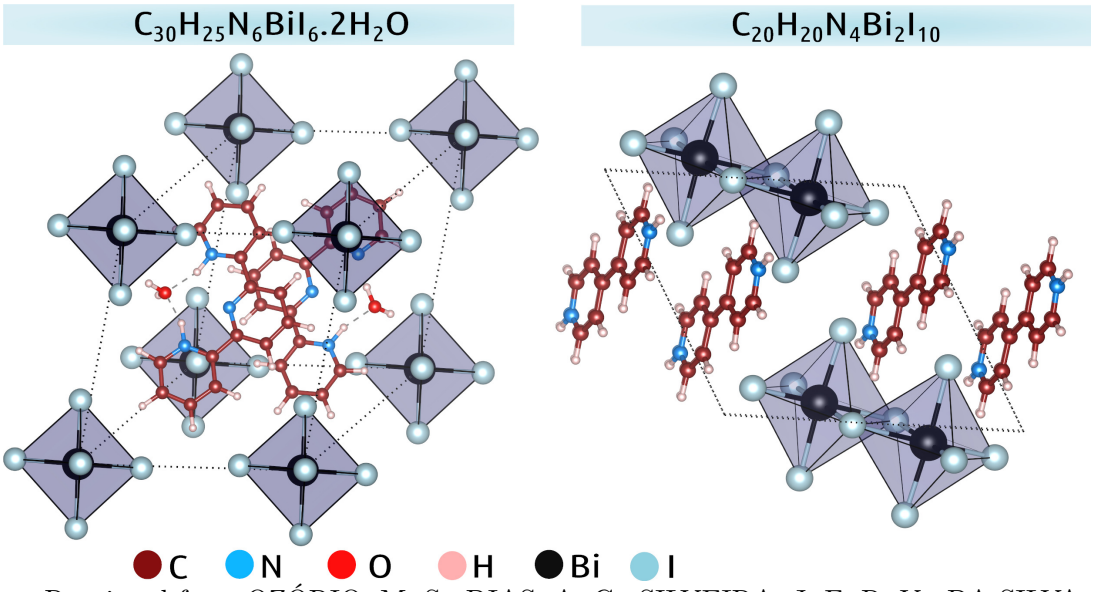

Source: Reprinted from OZÓRIO, M. S.; DIAS, A. C.; SILVEIRA, J. F. R. V.; DA SILVA, J. L. F. **The Journal of Physical Chemistry C**, v. 126, n. 16, p. 7245–7255, 2022.[2]

(vdW) correction term to the plain DFT-PBE results. The lattice parameters absolute deviations range from 0.09 % to 6.16 % without vdW corrections, and by considering the vdW corrections, the absolute deviations range from 0.03 % to 1.29 %. Thus, these results highlight the advantage of including vdW corrections to find improved structural parameters for hybrid organic-inorganic perovskites.

To explain the response of structural parameters provoked by the changes in halide anionic complex composition, we investigated the volume, atomic distances, bond angle variance, and the effective coordination number (see Figure 19). As the lattice parameters increase linearly from Cl^- to Br^-, and then to I^-, the volume and atomic distances are notably affected by the crystal ionic radii of the halides: 1.67 Å, 1.82 Å, and 2.06 Å for Cl^-, Br^-, and I^-, respectively.[77] The average octahedra volume increases in the Cl → Br → I sequence because the $B-X$ bond lengths increase linearly by following the same trend of ionic radii, which are in line with previous works.[198,199] Despite the small difference between the crystal ionic radius of Sb^{3+} (0.90 Å) and Bi^{3+} (1.17 Å),[77] we found a smaller effect on the structural properties for B-cation than the X-halide of both $C_{20}H_{20}N_4B_2X_{10}$ and $C_{30}H_{25}N_6BX_6 \cdot 2\,H_2O$ structures, namely, the equilibrium volume and atomic distances.

The rate in which the equilibrium volume change with the halide substitution is different for the B_2X_{10} and BX_6 structures, so to identify the causes of this behavior, we analyzed the variations in the shortest cation-cation distance (d^{c-c}, C−H), and the

Table 7 – Lattice parameters, volume of the unit cell (V_0), and volume of $[Bi_xI_y]^{z-}$ ($V_{B_xX_y}$) of the $C_{30}H_{25}N_6BX_6 \cdot 2\,H_2O$ and $C_{20}H_{20}N_4B_2X_{10}$ perovskites calculated at PBE and PBE+D3 levels. The chemical formula of the structures were abbreviated as BX_6 and B_2X_{10}, where $B = \{Bi^{3+}, Sb^{3+}\}$, and $X = \{Cl^-, Br^-, I^-\}$. The experimental results (Exp.) are shown for bismuth-iodide systems.[1]

B_xX_y	Method	a_0 (Å)	b_0 (Å)	c_0 (Å)	α (°)	β (°)	γ (°)	V_0 (Å^3)	$V_{B_xX_y}$ (Å^3)
$BiCl_6$	PBE+D3	9.63	9.76	10.95	80.62	62.43	64.09	819.59	27.41
	PBE	10.10	10.01	11.28	79.55	63.14	64.13	915.82	28.00
$BiBr_6$	PBE+D3	10.21	10.20	10.81	80.73	61.84	62.10	874.26	32.14
	PBE	10.58	10.37	11.08	80.50	63.98	62.90	971.66	32.91
BiI_6	PBE+D3	10.66	10.68	10.98	81.17	61.69	61.80	965.60	39.69
	PBE	11.05	10.90	11.30	80.97	63.66	61.75	1071.43	40.60
	Exp.[1]	10.67	10.82	10.95	81.04	61.71	61.46	973.43	38.94
$SbCl_6$	PBE+D3	9.62	9.73	10.91	80.38	62.25	64.16	813.15	25.82
	PBE	10.06	9.99	11.28	79.31	62.95	64.22	908.69	26.38
$SbBr_6$	PBE+D3	10.16	10.16	10.81	80.74	61.84	62.13	866.98	30.47
	PBE	10.53	10.31	11.07	80.42	64.08	63.11	963.78	31.08
SbI_6	PBE+D3	10.63	10.67	10.97	81.13	61.53	61.73	959.65	37.66
	PBE	11.01	10.88	11.24	81.05	63.63	61.78	1061.05	38.49
Bi_2Cl_{10}	PBE+D3	8.20	10.04	11.00	113.70	102.32	99.29	778.27	55.38
	PBE	8.39	10.36	11.57	115.94	100.50	98.83	857.72	55.94
Bi_2Br_{10}	PBE+D3	8.43	10.41	11.24	114.17	101.69	99.69	846.26	64.88
	PBE	8.65	10.80	11.85	116.46	98.92	100.13	940.59	65.80
Bi_2I_{10}	PBE+D3	8.80	11.02	11.74	115.33	100.71	100.13	967.64	80.05
	PBE	9.00	11.36	12.43	117.21	98.88	99.67	1074.82	81.24
	Exp.[1]	8.83	10.70	11.79	114.45	99.70	100.09	962.40	78.11
Sb_2Cl_{10}	PBE+D3	8.20	9.93	10.94	113.57	102.72	98.86	766.34	52.57
	PBE	8.41	10.26	11.60	116.29	100.58	98.24	853.74	53.38
Sb_2Br_{10}	PBE+D3	8.40	10.34	11.18	113.94	102.11	99.31	834.41	61.55
	PBE	8.65	10.70	11.92	116.82	99.26	99.49	935.52	62.26
Sb_2I_{10}	PBE+D3	8.76	10.94	11.69	115.05	100.85	100.06	955.89	76.03
	PBE	9.01	11.26	12.34	117.13	98.96	99.54	1059.89	77.12

Source: Reprinted from OZÓRIO, M. S.; DIAS, A. C.; SILVEIRA, J. F. R. V.; DA SILVA, J. L. F. **The Journal of Physical Chemistry C**, v. 126, n. 16, p. 7245–7255, 2022.[2]

shortest cation-anion distance (d^{c-a}, X–H). The results show a linear increase of both d^{c-a} and d^{c-c} occurs in the perovskite structures with the edge-sharing B_2X_{10} connectivity as the halides change towards large ionic radii. In its turn, the BX_6 structures display similar response for d^{c-a} when halides replacement occur from Cl to Br, then I, while the d^{c-c} values have minor differences. Thus, these results may explain the reason for the steeper increase in volume for B_2X_{10} structures as halides are exchanged.

Figure 19 – Equilibrium volume (V_0), average of B-X bond lengths ($d_{av}^{B\text{-}X}$), effective coordination number of B-cation (ECN^B), $X-B-X$ bond angle variance (BAV), shortest distance of octahedra-cation ($d^{\text{c-a}}$) and cation-cation ($d^{\text{c-c}}$) for all B_2X_{10} and BX_6 studied 0D perovskites.

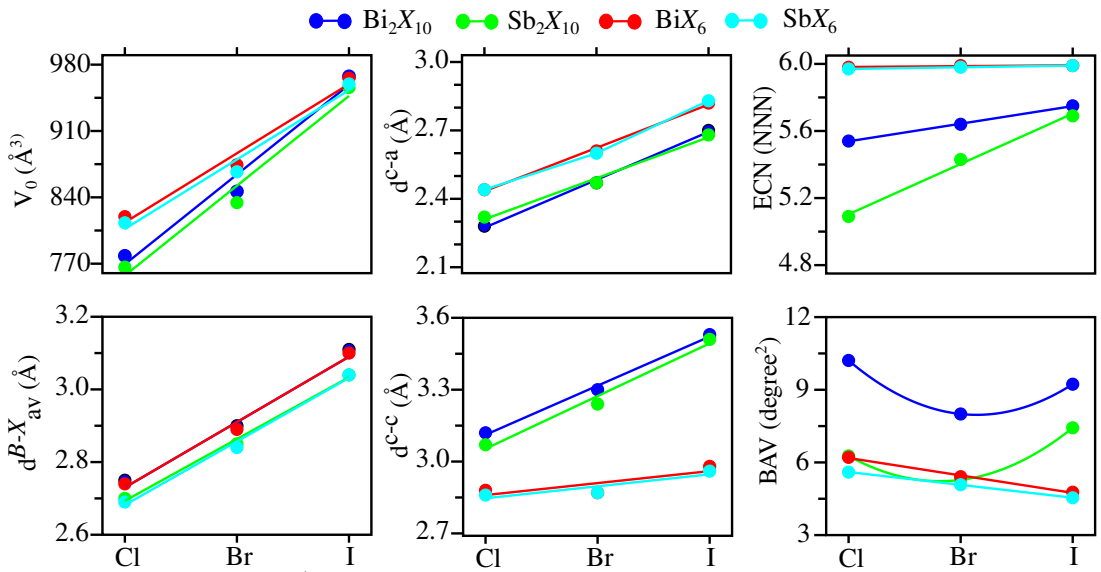

Source: Reprinted from OZÓRIO, M. S.; DIAS, A. C.; SILVEIRA, J. F. R. V.; DA SILVA, J. L. F. **The Journal of Physical Chemistry C**, v. 126, n. 16, p. 7245–7255, 2022.[2]

5.2.1.1 Local Structural Parameters

To analyze the local structural parameters, we calculated the bond angle variance (BAV) and the effective coordination number of the nearest neighbor of B-cations (ECN^B) by considering the self-consistent effective coordination concept.[200] We employed the bond angle variance (BAV) to quantify angular changes of BX_6 octahedra, i.e., the deviations of X-B-X angles from 90° as proposed by Robinson *et al.*.[201] We calculated the BAV values with the equation:

$$\text{BAV} = \frac{1}{n-1}\sum_{i=1}^{n}(\phi_i - \phi_0)^2, \qquad \text{BAV} = \sum_{i=1}^{12}\frac{(\phi_i - 90°)^2}{11} \tag{5.1}$$

where n represents the number of faces multiplied by 3/2, thus in the octahedron $n = 12$, which is the total number of ϕ_i angles involving the bismuth and two adjacent iodide atoms, X-B-X, which in a perfect octahedron are all equal to $\phi_0 = 90°$. In its turn, the effective coordination numbers of B- cations (bismuth/antimony) were obtained by applying the following equation:

$$\text{ECN}^{\text{B}} = \sum_j \exp\left[1 - \left(\frac{d_{ij}}{d_{av}^i}\right)^6\right], \qquad d_{av}^i = \frac{\sum_j d_{ij}\exp\left[1 - \left(\frac{d_{ij}}{d_{av}^i}\right)^6\right]}{\sum_j \exp\left[1 - \left(\frac{d_{ij}}{d_{av}^i}\right)^6\right]}, \tag{5.2}$$

where d_{ij} is the B-X (X = Cl, Br or I) bond-length of octahedra, d_{av}^i is self-consistently obtained weighted average bond length, which starts from d_{min} value, i.e., the shortest

B−X bond length of octahedron. For the particular case of the investigated 0D perovskites, the octahedra in the unit cell have the same structural properties, e.g., the same volume and the same effective coordination number for the B-cation (bismuth/antimony).

The ECN^B values were compared to the value expected from an ideal octahedron ($ECN^B = 6.00\,\mathrm{NNN}$) to evaluate the magnitude of distortions. The BX_6 systems presented an $ECN^B \approx 6\,\mathrm{NNN}$, which suggests that outside interactions within the isolated octahedra are not enough to cause distortions. More significant distortions appear in the edge-sharing B_2X_{10} systems, which suggest that the edge-sharing octahedra connectivity contributes to causing the distortions, which increase as we decrease the ionic radii of both B and X sites. As shown in Figure 19, the different octahedra connectivity presented in BX_6 and B_2X_{10} structures cause distinct BAV behaviors. Among the B_2X_{10} structures, the common aspect is that the $B_2\mathrm{Br}_{10}$ structures have the lowest BAV, and the B cations influence how the halide affects the BAV. On the other hand, regardless of the B species, in the BX_6 structures, the BAV decreases as the crystal ionic radii of halide increase.

5.3 Cohesive Energy

To analyze how the substitution of the B and X species affect the stability of 0D perovskites, we calculated the bulk cohesive energy of 0D perovskites (E_{coh}^{bulk}), which corresponds to the sum of three energy terms: (i) the inorganic complex cohesive energy (E_{coh}^{inorg}), (ii) the organic molecule cohesive energy (E_{coh}^{org}), (iii) and the organic-inorganic binding energy ($E_b^{org-inorg}$) (see Table 8). Thus, E_{coh}^{bulk} is obtained by the expression:

$$E_{coh}^{bulk} = E_{coh}^{inorg} + E_{coh}^{org} + E_b^{org-inorg} \ . \tag{5.3}$$

The decomposition of the bulk cohesive energy stated in the 5.3 is justified henceforward. The bulk cohesive energy of perovskite is found by the energy difference between the total energy of perovskite bulk (E_{tot}^{bulk}) and the total energy of free atoms (E_j), which was calculated by centering the free atom j in a large orthorhombic box to avoid spurious interactions. Thus, the usual cohesive energy expression is given by:

$$E_{coh}^{bulk} = E_{tot}^{bulk} - \sum_{j=1}^{N} E_j \ , \tag{5.4}$$

where N reassemble the total number of elements, hence, $N = N^{inorg} + N^{org}$, where N^{inorg} and N^{org} indicate the total number of inorganic and organic parts, respectively.

Similarly to the whole bulk system, the cohesive energy of inorganic and organic parts can be calculated as:

$$E_{coh}^{org} = E^{tot-org} - \sum_{j=1}^{N^{org}} E_j \qquad E_{coh}^{inorg} = E^{tot-inorg} - \sum_{j=1}^{N^{inorg}} E_j, \tag{5.5}$$

Table 8 – Cohesive energy of the 0D perovskites (E_{coh}), cohesive energy of the inorganic framework ($E_{coh}^{inorg.}$), and organic spacer cations ($E_{coh}^{org.}$). Sum of the organic-inorganic binding energy ($E_b^{inorg-org}$) with the cohesive energy of organic and inorganic moieties with of 0D perovskites ($E_{coh}^{sum} = E_{coh}^{inorg.} + E_{coh}^{org.} + E_b^{inorg-org}$), and their difference with the cohesive energy of the whole system ($\Delta = E_{coh} - E_{coh}^{sum}$).

	E_{coh} (eV)	$E_{coh}^{inorg.}$ (eV)	$E_{coh}^{org.}$ (eV)	$E_b^{inorg-org}$ (eV)	E_{coh}^{sum} (eV)	Δ (eV)
Bi_2Cl_{10}	−263.05	−24.21	−221.95	−16.89	−243.05	0.00
Bi_2Br_{10}	−258.92	−21.95	−221.88	−15.09	−258.92	0.00
Bi_2I_{10}	−254.09	−19.63	−221.79	−12.67	−254.09	0.00
Sb_2Cl_{10}	−262.23	−25.21	−221.96	−15.06	−262.23	0.00
Sb_2Br_{10}	−258.13	−22.39	−221.90	−13.84	−258.13	0.00
Sb_2I_{10}	−253.40	−19.47	−221.80	−12.13	−253.40	0.00
$BiCl_6$	−370.10	−12.19	−344.63	−13.28	−370.10	0.00
$BiBr_6$	−367.67	−10.98	−344.55	−12.14	−367.67	0.00
BiI_6	−364.77	−9.74	−344.43	−10.60	−364.77	0.00
$SbCl_6$	−369.63	−12.75	−344.62	−12.26	−369.63	0.00
$SbBr_6$	−367.24	−11.29	−344.55	−11.40	−367.24	0.00
SbI_6	−364.41	−9.72	−344.44	−10.25	−364.41	0.00

Source: Reprinted from OZÓRIO, M. S.; DIAS, A. C.; SILVEIRA, J. F. R. V.; DA SILVA, J. L. F. **The Journal of Physical Chemistry C**, v. 126, n. 16, p. 7245–7255, 2022.[2]

where $E^{tot-org}$ and $E^{tot-inorg}$ indicate, respectively, the total energy of the organic and inorganic frozen-neutral fragments, and

$$\sum_{j=1}^{N} E_j = \sum_{j=1}^{N^{org}} E_j + \sum_{j=1}^{N^{inorg}} E_j. \tag{5.6}$$

Since the organic-inorganic binding energy is obtained by,

$$E_b^{org-inorg} = E_{tot}^{bulk} - E^{tot-org} - E^{tot-inorg}. \tag{5.7}$$

From the sum of the equations 5.5 with 5.7, we obtain:

$$E_{coh}^{inorg} + E_{coh}^{org} + E_b^{org-inorg} = E_{tot}^{bulk} - \sum_{j=1}^{N^{inorg}} E_j - \sum_{j=1}^{N^{org}} E_j, \tag{5.8}$$

which can be rewritten by considering the equation 5.6 as follow:

$$E_{coh}^{inorg} + E_{coh}^{org} + E_b^{org-inorg} = E_{tot}^{bulk} - \sum_{j=1}^{N} E_j. \tag{5.9}$$

By comparing the equations 5.4 and 5.9, we obtain (equation 5.3):

$$E_{coh}^{bulk} = E_{coh}^{inorg} + E_{coh}^{org} + E_b^{org-inorg}. \tag{5.10}$$

As shown in Table 8 and Figure 20, the principal contribution to the bulk cohesive energy originates from the organic cations. In fact, the binding energy of the C–N, C–C, and C–H covalent bonds are stronger than the binding energy of *B*-*X* bonds, which display primarily ionic behavior. Regarding the trends caused by the octahedra substitutions, we found a negligible effect of organic cation cohesive energy because organic cations are unaltered, i.e., the organic cation is virtually kept the same among the same shape (BX_6 or B_2X_{10}) structures. The most prominent contribution comes from the structural cohesion of the octahedra and their electrostatic interaction with the spacer organic cations. For example, the structural cohesion increases by 8.96 eV from $C_{20}H_{20}N_4Bi_2I_{10}$ to the $C_{20}H_{20}N_4Bi_2Cl_{10}$ perovskite, where 4.58 eV of this value comes from changes in the structural cohesion of the B_xX_y octahedra, and 4.22 eV results from the organic-inorganic binding energy and only 0.16 eV can be attributed to the organic molecule cohesion.

Figure 20 – Decomposition of the bulk cohesive energy of 0D perovskites (E_{coh}^{bulk}) into organic-inorganic binding energy ($E_b^{org-inorg}$), the cohesive energy of the organic (E_{coh}^{org}) and inorganic (E_{coh}^{org}) fragments, and their dependence with the effective Bader charge of the inorganic fragments (Q).

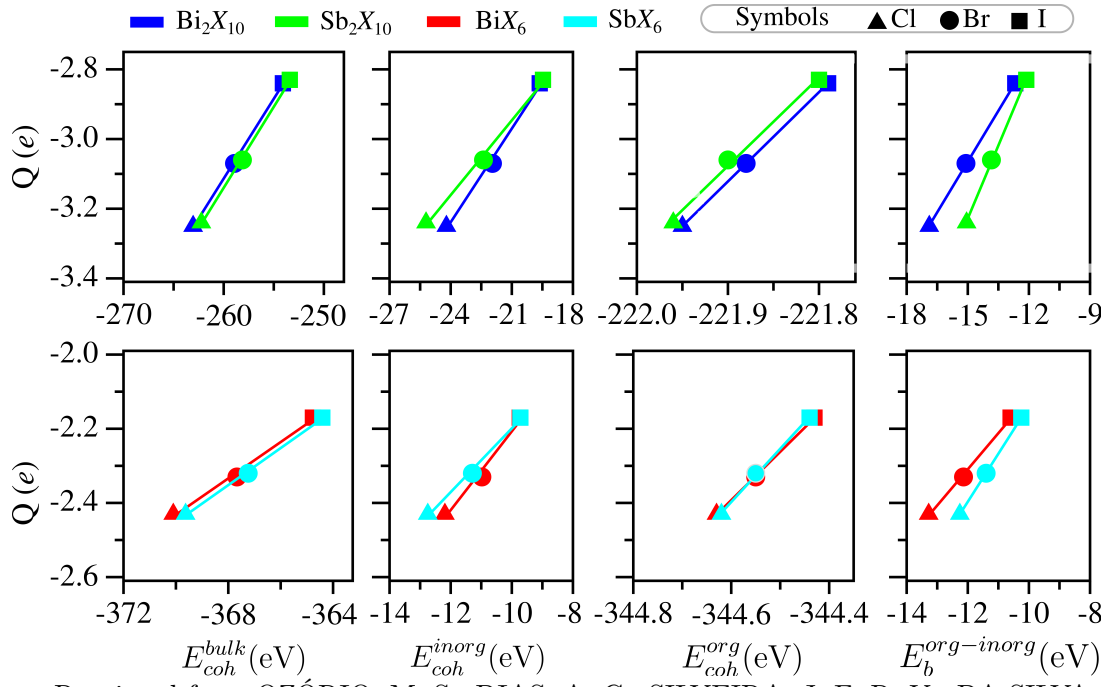

Source: Reprinted from OZÓRIO, M. S.; DIAS, A. C.; SILVEIRA, J. F. R. V.; DA SILVA, J. L. F. **The Journal of Physical Chemistry C**, v. 126, n. 16, p. 7245–7255, 2022.[2]

As are shown in Figure 20, looking closer the *B* and *X* contribution to the total cohesive energy of 0D perovskites, we observe a slight improvement in the structural cohesion when Sb is replaced by Bi, which is of about 0.04 eV/atom and 0.02 eV/atom for BX_6 and B_2X_{10}-based structures, respectively. However, the effect of the metallic *B*-cation on the cohesive energy is minor compared to that of the *X*-site. Independently of the shape (BX_6 or B_2X_{10}), from the cohesive energy results, chlorine systems tend to display

the most stable structures, which are followed by bromine, and then by the less stable iodide systems. To find the source of these cohesive energy trends, we calculated the Bader charge analysis[182,183] which reveals an inverse behavior of ionic radii and effective charge on halide anionic complex, i.e., the effective charge on octahedra increase as halide crystal ionic radii decrease in the $I^- \rightarrow Br^- \rightarrow Cl^-$ sequence. These results relate to differences in the halides electronegativity, which replacement causes the increase of the ionic character of the anionic complex and then contributes to increasing the inorganic-organic interaction. Thus, the inorganic complex becomes more cohesive as the ionicity of octahedra bonds increases.

5.4 Electronic and Optical Properties

5.4.1 Density of States and Band Structure

Figure 21 – Local density of states per octahedra unity for the antimony and bismuth-based zero-dimensional perovskites obtained at PBE+D3 level.

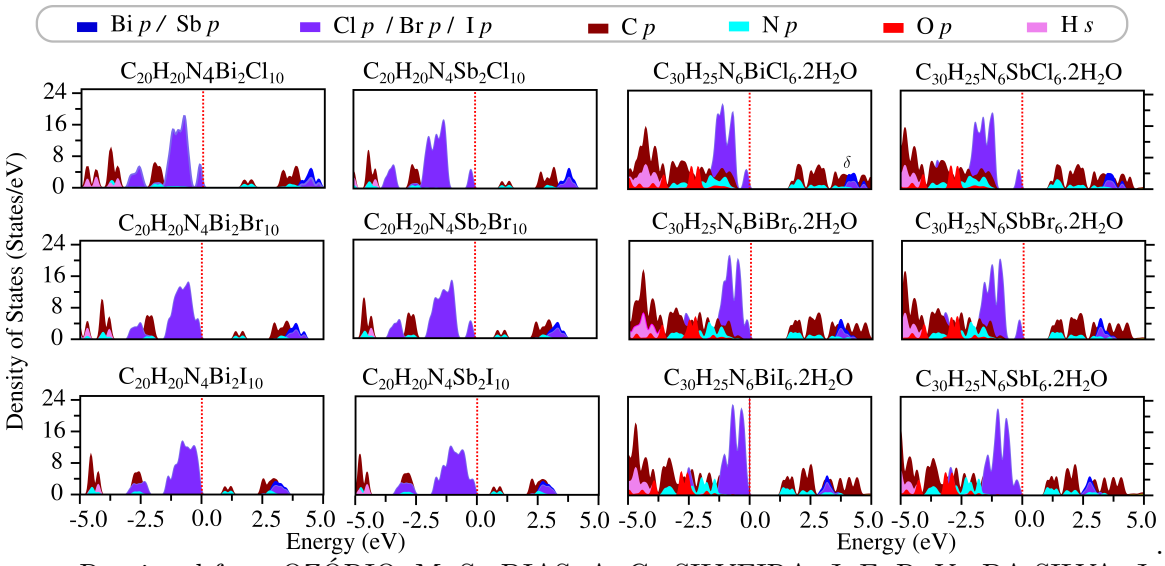

Source: Reprinted from OZÓRIO, M. S.; DIAS, A. C.; SILVEIRA, J. F. R. V.; DA SILVA, J. L. F. **The Journal of Physical Chemistry C**, v. 126, n. 16, p. 7245–7255, 2022.[2]

According to the plots of the density of states shown in Figure 21, the *p*-states of N and C from the organic molecules dominate the CBM of 0D perovskites. The fundamental bandgap energy of perovskites decreases as the halide ionic radii increases from $Cl^- \rightarrow Br^- \rightarrow I^-$, which is related to VBM being mostly composed of *p* states *X*-halide, i.e., the fundamental bandgap energy decrease because of the electron binding decreasing from $3p \rightarrow 4p \rightarrow 5p$.[163] A similar behavior for the bang gap increase/decrease sequence is observed for antimony perovskites in Figure 21. Overall, we identified a smaller effect of *B*-cations in the fundamental bandgap than of the halides, but comparing the effect of Sb and Bi, the last has a slightly larger effect. We noticed a wide fundamental bang

Figure 22 – Band structures were calculated with PBE+D3 without SOC effects (black lines) and considering SOC effects (dashed-blue lines) for all 0D perovskite systems.

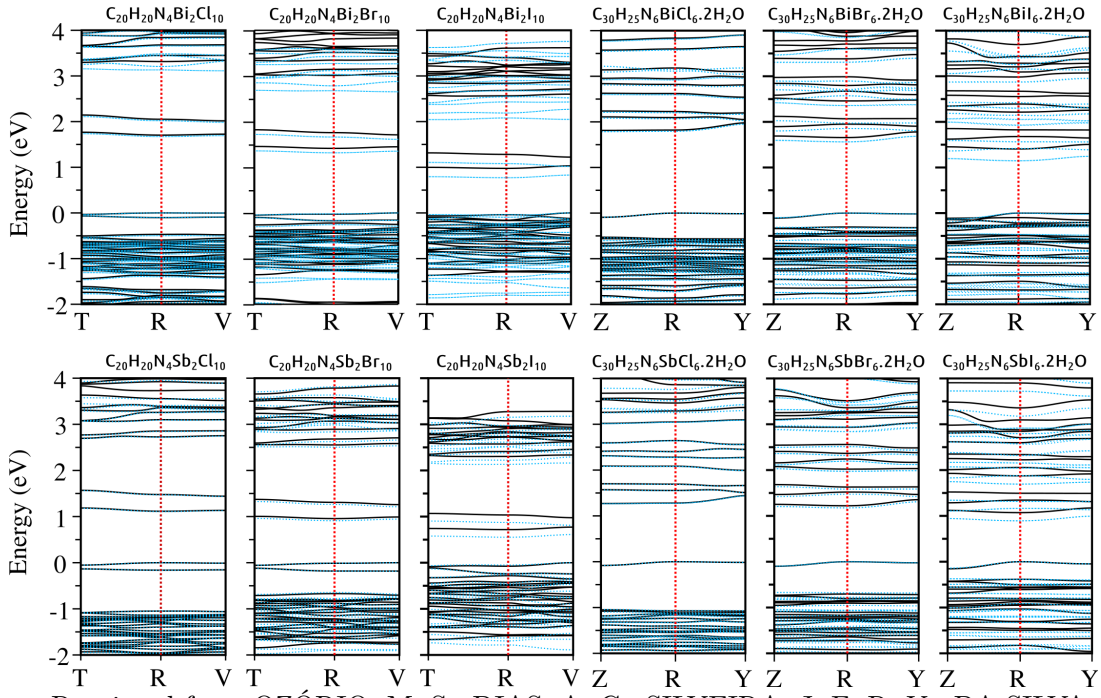

Source: Reprinted from OZÓRIO, M. S.; DIAS, A. C.; SILVEIRA, J. F. R. V.; DA SILVA, J. L. F. **The Journal of Physical Chemistry C**, v. 126, n. 16, p. 7245–7255, 2022.[2]

gap energy for more cohesive perovskites, i.e., structures displaying high absolute cohesive energy of inorganic octahedra and strong organic-inorganic binding.

As shown in Figure 22, the flat band structures indicate a high localization of the electronic states, which implies a negligible difference between direct and indirect fundamental bandgap energy. Heavy Bi and I elements may yield relevant SOC effects; however, the Bi SOC effect is minor for the fundamental bandgap energy because it has a small electronic contribution close to the Fermi level. On the other hand, due to the majoritarian I-*p* states contribution around the Fermi level, we found that SOC effects are significant in I-based systems. We observed a slightly decreasing in the bandgap energy in the range of 0.15 eV to 0.29 eV for iodide-based systems. For comparison, the bandgap reduction on the Cl and Br-based systems is correspondingly 0.05 eV and 0.12 eV. Moreover, as indicated in Table 9, we found a direct to indirect bandgap transition for SbI_6, BiI_6 and $BiBr_6$ due to the relativistic effects.

5.4.2 Absorption Coefficient

To get insights into the optical properties of 0D perovskites and the respective inorganic complex and organic cations fragments separated, we calculated the absorption coefficient between photon energy relevant for photovoltaic applications. As shown in

Table 9 – Fundamental bang gap energy (E_g) of all zero-dimensional bismuth- and antimony-based perovskites with PBE+D3 and PBE+D3+SOC approaches (bold).

Perovskite	E_g (eV)	VBM	CBM	
Bi_2Cl_{10}	1.70	$-0.5, 0.5, -0.5$	$-0.5, 0.5, -0.5$	direct
	1.67	$-0.5, 0.5, -0.5$	$-0.5, 0.5, -0.5$	direct
Bi_2Br_{10}	1.41	$0.5, -0.5, 0.0$	$-0.5, 0.5, -0.5$	indirect
	1.32	$0.5, -0.5, 0.0$	$-0.5, 0.5, -0.5$	Indirect
Bi_2I_{10}	0.98	$0.5, -0.5, 0.0$	$-0.5, 0.5, -0.5$	indirect
	0.77	$0.5, -0.5, 0.0$	$-0.5, 0.5, -0.5$	Indirect
Sb_2Cl_{10}	1.12	$-0.5, 0.5, -0.5$	$-0.5, 0.5, -0.5$	direct
	1.11	$-0.5, 0.5, -0.5$	$-0.5, 0.5, -0.5$	direct
Sb_2Br_{10}	0.96	$0.5, -0.5, 0.0$	$-0.5, 0.5, -0.5$	indirect
	0.91	$0.5, -0.5, 0.0$	$-0.5, 0.5, -0.5$	Indirect
Sb_2I_{10}	0.71	$0.5, -0.5, 0.0$	$-0.5, 0.5, -0.5$	indirect
	0.55	$0.5, -0.5, 0.0$	$-0.5, 0.5, -0.5$	Indirect
$BiCl_6$	1.81	$0.5, 0.5, 0.5$	$0.0, 0.0, 0.5$	indirect
	1.79	$0.5, 0.5, 0.5$	$0.0, 0.0, 0.5$	Indirect
$BiBr_6$	1.66	$0.5, 0.5, 0.5$	$0.5, 0.5, 0.5$	direct
	1.56	$0.5, 0.5, 0.5$	$0.5, 0.47, 0.5$	Indirect
BiI_6	1.41	$0.5, 0.5, 0.5$	$0.5, 0.5, 0.5$	direct
	1.15	$0.5, 0.5, 0.5$	$0.5, 0.45, 0.5$	Indirect
$SbCl_6$	1.27	$0.5, 0.5, 0.5$	$0.0, 0.0, 0.5$	indirect
	1.26	$0.5, 0.5, 0.5$	$0.0, 0.0, 0.5$	Indirect
$SbBr_6$	1.22	$0.5, 0.5, 0.5$	$0.5, 0.5, 0.5$	direct
	1.17	$0.5, 0.5, 0.5$	$0.5, 0.5, 0.5$	direct
SbI_6	1.07	$0.5, 0.5, 0.5$	$0.5, 0.5, 0.5$	direct
	0.89	$0.5, 0.5, 0.5$	$0.5, 0.47, 0.5$	Indirect

Source: Reprinted from OZÓRIO, M. S.; DIAS, A. C.; SILVEIRA, J. F. R. V.; DA SILVA, J. L. F. **The Journal of Physical Chemistry C**, v. 126, n. 16, p. 7245–7255, 2022.[2]

Figure 23, for most 0D perovskites, the absorption contribution of organic cations in a different range of photons energy is narrower than of the inorganic moieties. However, almost the same absorption contribution of organic and inorganic moieties can be observed in such particular cases, for instance, in the $B\mathrm{Cl}_6$-based 0D perovskites. As a matter of fact, the broader absorption observed for the organic cation of the BX_6-structures compared to the B_2X_{10}-structures may be provoked by its one additional heterocyclic ring. Moreover, the difference between the charge frustration (effective charge) and the octahedra formal charge of the BX_6 structures is lower than of B_2X_{10} structures, which might point to substantial optical transitions between organic and inorganic components.

On the other hand, concerning the halide anionic complex part, the absorption coefficient increasing trends follow the sequence Cl→Br→I, which relates to the increase of

Figure 23 – Absorption coefficient of whole 0D perovskite (black lines) and their respective organic cationic (magenta lines) and inorganic anionic (teal lines) fragments. All results were obtained at the PBE+D3 level within DFT formalism.

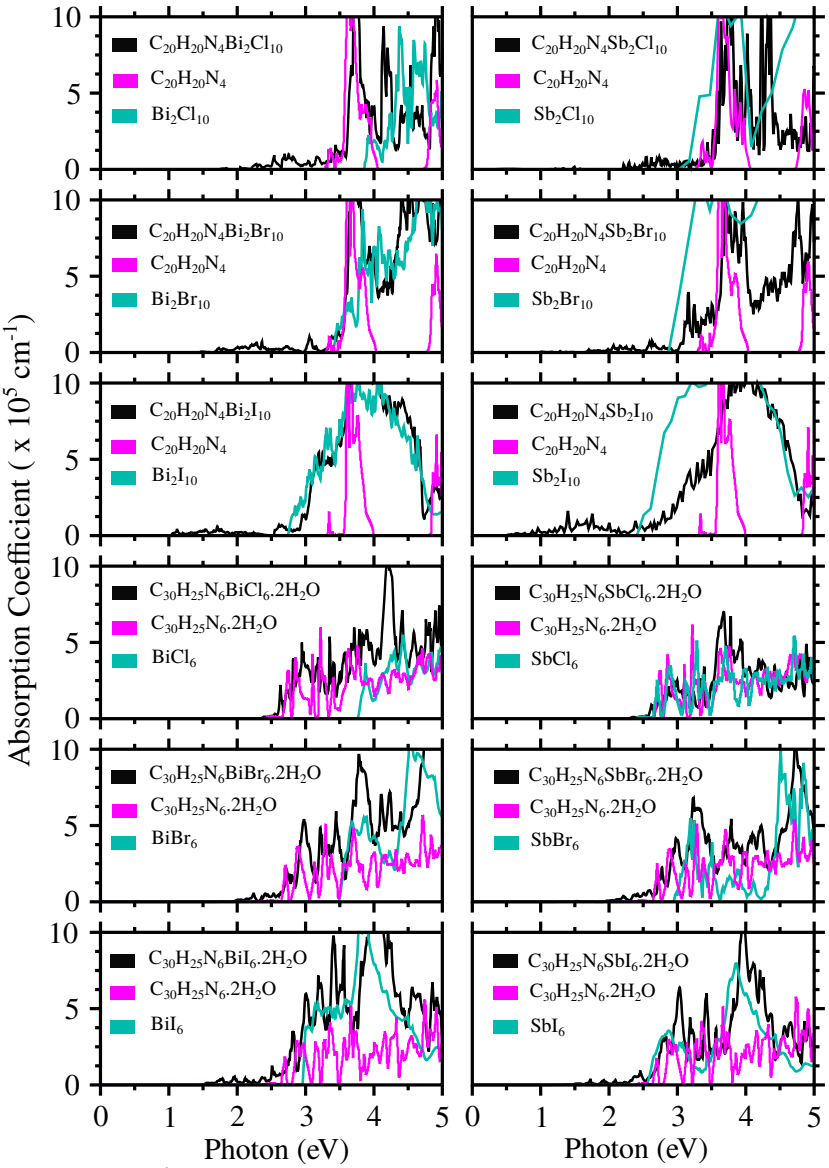

Source: Reprinted from OZÓRIO, M. S.; DIAS, A. C.; SILVEIRA, J. F. R. V.; DA SILVA, J. L. F. **The Journal of Physical Chemistry C**, v. 126, n. 16, p. 7245-7255, 2022.[2]

the electrons concentration that could be excited by the photon energy near the Fermi-level, being smaller for chlorine-based structures and larger for iodide-based ones.

Those 0D perovskites quantum confinement lead to the very flat band structures, and as a result, the complexity of identifying allowed/forbidden from interband optical matrix element increase. In other words, the source of the high absorption coefficient of those 0D perovskites comes from the combination of each isolated optical transition with a small probability. Hence, to achieve the optical bandgap we considered the Tauc-plot procedure by considering the quantity $(\alpha h\nu)^{1/2}$ for each photon energy, where the absorption coefficient

Figure 24 – The blue line interception on the photon energy axes gives the optical bandgap energy of 0D perovskites by considering the Tauc plot procedure for direct-allowed transitions. The absorption coefficient (α) of the ordinate quantity $(\alpha h\nu)^{1/2}$ comes from the TB+scissor+BSE approach, as published in our work.[2]

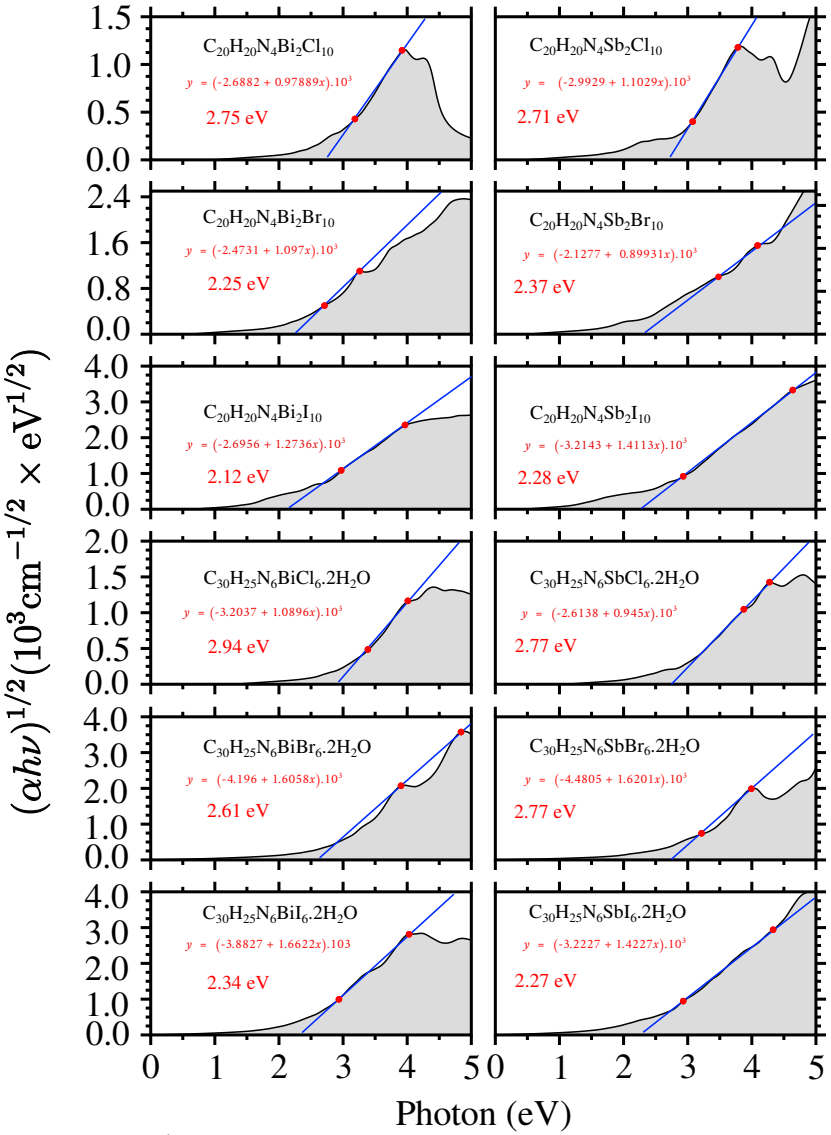

Source: Reprinted from OZÓRIO, M. S.; DIAS, A. C.; SILVEIRA, J. F. R. V.; DA SILVA, J. L. F. **The Journal of Physical Chemistry C**, v. 126, n. 16, p. 7245–7255, 2022.[2]

Table 10 – Band structure properties: Electronic fundamental bandgap energy (E_g) using different level of approximations (PBE+D3, PBE+D3+SOC, HSE06, HSE06+SOC) at the Γ-point. Optical bandgap ($E_g^{optical}$) employing the TB+$\Delta_{scissor}$+BSE framework as described in our published work.[2] The values of the experimental optical bandgap energy ($E_{g,exp.}^{optical}$) are also provided when available.[1] All properties are provided in eV.

B_xX_y	$E_g^{\text{PBE+D3}}$	$E_g^{\text{PBE+D3+SOC}}$	E_g^{HSE06}	$E_g^{\text{HSE06+SOC}}$	$E_g^{optical}$	$E_{g,exp.}^{optical}$
Bi_2Cl_{10}	1.91	1.87	2.94	2.90	2.75	
Bi_2Br_{10}	1.62	1.53	2.57	2.48	2.25	
Bi_2I_{10}	1.12	0.93	2.05	1.81	2.12	2.31
Sb_2Cl_{10}	1.39	1.39	2.34	2.33	2.71	
Sb_2Br_{10}	1.19	1.15	2.05	2.01	2.37	
Sb_2I_{10}	0.95	0.80	1.68	1.53	2.28	
$BiCl_6$	2.14	2.11	3.21	3.18	2.94	
$BiBr_6$	2.02	1.91	3.00	2.90	2.61	
BiI_6	1.73	1.50	2.75	2.46	2.34	2.22
$SbCl_6$	1.59	1.59	2.56	2.56	2.77	
$SbBr_6$	1.59	1.54	2.48	2.44	2.77	
SbI_6	1.51	1.30	2.32	2.13	2.27	

Source: Reprinted from OZÓRIO, M. S.; DIAS, A. C.; SILVEIRA, J. F. R. V.; DA SILVA, J. L. F. **The Journal of Physical Chemistry C**, v. 126, n. 16, p. 7245–7255, 2022.[2]

(α) comes from the TB+scissor+BSE approach described in our published work.[2] As indicated in Table 10 and Figure 24, we found wide optical bandgap energy (> 2.10 eV) for all structures, which agree with previous reports of others 0D perovskites.[116,202] Regarding the iodide-based $[Bi_xI_y]^{z-}$ systems, we found good agreement between calculated and experimental optical bandgap energy, i.e., the absolute theoretical-experimental difference is smaller than 0.19 eV. Moreover, the wide optical gap and the consequent reduction of photons absorption suggest that those 0D perovskites have small potential as solar cell light-absorbing layer.

5.5 Summary

Using as models two-previously reported experimental 0D perovskites ($C_{20}H_{20}N_4Bi_2I_{10}$ and $C_{30}H_{25}N_6BI_6 \cdot 2\,H_2O$) as models, Sb^{3+} was considered as a candidate to replace Bi^{3+}; and I^- was replaced by Cl^- and Br^- yielding to twelve 0D perovskites in an overall combination. Thus, from first-principle calculations, we found significant insights into how the halide anionic complexes affect the physical-chemical properties of 0D perovskites. Our procedure gives an in-depth comprehension of the driving mechanisms affecting the relative structural stability, optical, electronic, and exciton properties of 0D perovskites, which may generate routes to control different applications.

Our results show that the effect of the halide species tends to be larger than of

the octahedra cation (Bi^{3+} and Sb^{3+}). As a consequence of octahedra connectivity, the edge-sharing B_2X_{10} octahedra display increased distortions when compared to isolated BX_6 ones. Regarding the structural cohesion, the chloride-based structures have higher stability, followed by bromide-based perovskites, and then by the iodide ones. The electronic states of the VBM are mainly composed of the *p*-states of halide, while CBM has a majority contribution of the *p*-states of C and N of the organic molecules. Because of the decrease of the X *p*-states binding energy, the fundamental bandgap energy decrease as the crystal ionic radii of halide increase in the $Cl^- \rightarrow Br^- \rightarrow I^-$ sequence. SOC effects show to be significant only for the iodide-based perovskites in reason of their larger mass and the significant role of I *p*-states in the Fermi-level region.

Contrary to the electronic and structural properties, spacer organic cations of some structures contribute to the optical properties. The role of organic cation in the optical properties is more significant for the BX_6 structures (mainly those with Br and Cl in the X_6-site), which may be justified by one extra conjugated heterocyclic ring on the cation compared to the cation of B_2X_{10} structures. The optical bandgap energy is wider than 2.10 eV, which suggests a drawback for the solar cells application; however, we hope that the insights about the halide anionic complex replacement may contribute to addressing applications beyond the photovoltaic field.

6 CONCLUSIONS

Perovskites have well-known and outstanding macroscopic uses despite the poorly understood microscopic properties underlying their properties. Connecting the macroscopic and microscopic scales can be very challenging. Remarkably, computer simulations based on quantum mechanics formalism have given insights regarding microscopic properties. In this Ph.D. thesis, density-functional-theory simulations were used to predict the atomistic properties of lead-free perovskites. We investigated the role of the orientation of the *A*-cations in the inorganic cage of different polymorphic phases of $A\mathrm{SnI_3}$ perovskites, as well as the physical-chemical properties of lead-free bismuth and antimony-based zero-dimensional perovskites. As a result of our effort to better understand the microscopic properties of lead-free perovskites, we published three scientific papers.[1,2,129] The general conclusions from these works are highlighted henceforward.

We observed a broader absorption of energy spectrum for tree-dimensional (3D) $A\mathrm{SnI_3}$ perovskites than the one-dimensional $A\mathrm{SnI_3}$ (pseudo-)hexagonal perovskites and the class of bismuth and antimony-based 0D perovskites. The optical bandgap energy of 3D $A\mathrm{SnI_3}$ perovskites is sharp and of low-dimensional perovskites wider than 2.00 eV. These results suggest that low-dimensional perovskites are not suitable for solar-energy harvesting in single-junction solar cells. Organic cations displayed a minor effect on the electronic and optical properties compared to the inorganic framework. The inorganic-framework dimensionality explains the success or failure of the optoelectronic properties of perovskites. The dimensionality reduction increases the quantum-confinement effects, which explains the high-bandgap energy of low-dimensional perovskites. However, because of the enhanced stability and structural versatility, low-dimensional perovskites may find novel applications beyond the photovoltaic field, including light-emitting diodes, capacitors, and lasers.

For the $A\mathrm{SnI_3}$ perovskites, the weak hydrogen-iodide bond interactions are stronger when involving the hydrogen atoms of the $-\mathrm{NH}_x/-\mathrm{PH_3}$ groups than of the $-\mathrm{CH}_x$ groups. Those H···I interactions are present in all calculated $A\mathrm{SnI_3}$ structures and yield to defects in the $\mathrm{SnI_6}$ octahedra (tin off-center on the I–Sn–I bonds). We found a significant role of the dipole-dipole interactions in determining the relative stability of $A\mathrm{SnI_3}$ phases. Enthalpy of formation of perovskite-like $A\mathrm{SnI_3}$ structures show the orthorhombic crystal structure more stable than tetragonal, which is more stable than cubic. The trend of enthalpy of formation agrees with the experimental phase transitions, which show the orthorhombic structure more stable at low temperature (orthorhombic ← tetragonal ← cubic). The inorganic framework connectivity has a strong contribution to the optoelectronic properties. For instance, the I *p*-, Sn *s*- and Sn *p*-states dominate the density of states, band structures and optical properties. The $A\mathrm{SnI_3}$ systems have different optoelectronic responses

depending on the inorganic framework connectivity, i.e., the $A\mathrm{SnI_3}$ structures displaying 3D corner-sharing $\mathrm{SnI_6}$ octahedra (cubic, orthorhombic, tetragonal, and cubic phases) have closer optoelectronic responses, which are different from the 1D faced-sharing $\mathrm{SnI_6}$ octahedra of non-perovskite (pseudo-)hexagonal $A\mathrm{SnI_3}$ phases. Regarding the differences, the 3D structures present a wider range of absorption of the energy spectrum and smaller bandgap energy than the 1D structures. For instance, The fundamental bandgap values found with HSE06 functional for 3D $A\mathrm{SnI_3}$ perovskites were less than 1.25 eV, whereas the values were as high as 3.00 eV (and above) for 1D $A\mathrm{SnI_3}$ low-dimensional structures. These values were calculated without including SOC effects but allow a clear distinction of the effect of inorganic-framework dimensionality on the optoelectronic properties. In its turn, for all structures, the effect of the A-cations in the optoelectronic properties is minor compared to the inorganic-framework, but the A-cations have a significant role in the energetic and structural stability.

The novel room-temperature stable and experimentally synthesized 0D perovskites were investigated via theoretical-experimental techniques. The theoretical analysis suggests the importance of including van der Waals corrections to the DFT total energy. In particular, we observed that PBE results with D3 van der Waals corrections showed a better theoretical-experimental agreement of structural properties (e.g., bond lengths/angles and lattice parameters) than the calculations without van der Waals corrections. We found greater structural deformation of $\mathrm{BiI_6}$ octahedron displaying shared iodide ions. For instance, the octahedron of face-sharing $[\mathrm{Bi_2I_9}]^{3-}$ (three shared iodide ions) have greater distortion, followed by the edge-sharing $[\mathrm{Bi_2I_{10}}]^{4-}$ (two shared iodide ions), and then by the almost non-distorted $[\mathrm{BiI_6}]^{3-}$ (zero shared iodide ions) of $\mathrm{C_{30}H_{25}N_6BiI_6 \cdot 2\,H_2O}$. Because of the structural nature of 0D perovskites, discrete octahedra separated by spacer cations, we found close optoelectronic responses, i.e., wide optical bandgap energy around 2.2 eV. As noticed for 1D $A\mathrm{SnI_3}$, the wide optical gap energy is in line with the reduced dimensionality of those systems, where quantum confinement effects play an important role. Our results suggest that cation-anions have low-intensity transitions around the fundamental bandgap energy and intense intra-octahedra transitions around 2.5 eV. In a qualitative sense, we found the PBE+D3 optical bandgap close to the experimental values by extrapolating the theoretical absorption-coefficient curves. However, HSE06 deviated by around 1 eV from the experimental values, which suggests limiting factors in the calculations (e.g., absence of exciton effects and defects, which may produce mid-gap states).

To understand the role of halide anionic complex substitution of the microscopic properties in the class of 0D perovskites, we investigated the effect of composition substitution using as models the systems $\mathrm{C_{20}H_{20}N_4}B_2X_{10}$ and $\mathrm{C_{30}H_{25}N_6}BX_6 \cdot 2\,\mathrm{H_2O}$, where $B = \{\mathrm{Bi^{3+}}, \mathrm{Sb^{3+}}\}$ and $X = \{\mathrm{Cl^-}, \mathrm{Br^-}, \mathrm{I^-}\}$. Our results suggest the major importance of the halide substitution in all the investigated properties, which effect is substantially higher than the B-cation substitution. The octahedra of BX_6 structures have small structural

distortions compared to B_2X_{10} because of the increase of the shared halides. We found higher structural cohesive energy for chloride structures, followed by bromide- and next iodide-based 0D perovskites. The p states of X and B from the B_xX_y inorganic moieties (mainly the X p-states) dominate the VBM, while the CBM is composed by C and N p-states of organic cations. Overall, the fundamental bandgap energy decrease as Cl^- is replaced with Br^- and later with I^-, for instance, by changing the X-site in the sequence $I^- \rightarrow Br^- \rightarrow Cl^-$, a tunable bandgap from 0.77 to 1.70 eV is observed for $C_{20}H_{20}N_4Bi_2X_{10}$ perovskites. We found significant SOC effects for iodide-based 0D perovskites, where the fundamental bandgap is 0.77 eV/0.98 eV by considering/non-considering SOC effects for $C_{20}H_{20}N_4Bi_2I_{10}$, while 1.67 eV/1.70 eV for $C_{20}H_{20}N_4Bi_2Cl_{10}$. The organic spacer cations (di-protonated and mono-protonated 2,2';6',2"-terpyridine organic molecules) shown important role in the optical properties of $C_{30}H_{25}N_6BiX_6 \cdot 2\,H_2O$ structures, mainly, on the structures with X = {Br^-,Cl^-}. In its turn, the effect of the octahedra on the optical properties manifested in all systems.

6.1 Scientific Papers

The findings reported in this Ph.D. thesis generated three scientific papers about lead-free perovskite systems. Regarding the collaboration works, we published one article on lead-based perovskites. Two other articles about cerium-oxide clusters were written and published during the Ph.D. studies, which comprise the Master's results. All works developed from August 2018 to August 2022 are listed below.

6.1.1 Perovskites Systems

6.1.1.1 List of Published Articles

- **OZÓRIO, M. S.**; DIAS, A. C.; SILVEIRA, J. F. R. V.; DA SILVA, J. L. F. Theoretical Investigation of the Role of Anion and Trivalent Cation Substitution in the Physical Properties of Lead-Free Zero-Dimensional Perovskites. **The Journal of Physical Chemistry C**, v. 126, n. 16, p. 7245-7255, 2022

- **OZÓRIO, M. S.**; SRIKANTH, M.; BESSE, R.; DA SILVA, J. L. F. The role of the A-cations in the polymorphic stability and optoelectronic properties of lead-free $ASnI_3$ perovskites. **Physical Chemistry Chemical Physics**, v. 23, n. 3, p. 2286–2297, 2021.

- **OZÓRIO, M. S.**; OLIVEIRA, W. X. C.; SILVEIRA, J. F. R. V.; NOGUEIRA, A. F.; DA SILVA, J. L. F. Novel Zero-dimensional Lead-free Bismuth Based Perovskites: From Synthesis to Structural and Optoelectronic Characterization. **Materials Advances**, v. 1, n. 9, p. 3439–3448, 2020

- SRIKANTH, M.; **OZÓRIO, M. S.**; DA SILVA, J. L. F. Optical and dielectric properties of lead perovskite and iodoplumbate complexes: An ab initio study. **Physical Chemistry Chemical Physics**, v. 22, n. 33, p. 18423-18434, 2020

6.1.2 Other Works

- **OZÓRIO, M. S.**; ANDRIANI, K. F.; DA SILVA, J. L. F. A hybrid-DFT investigation of the Ce oxidation state upon adsorption of F, Na, Ni, Pd and Pt on the $(CeO_2)_6$ cluster. **Physical Chemistry Chemical Physics**, v. 22, n. 25, p. 14099-14108, 2020.
- **OZÓRIO, M. S.**; DA SILVA, A. C. H.; DA SILVA, J. L. F. A hybrid density functional theory investigation of the $(CeO_2)_6$ clusters in the cationic, neutral, and anionic states. **Journal of Cluster Science**, v. 31, n. 6, p. 1213-1220, 2020.

BIBLIOGRAPHY

1 OZÓRIO, M. S.; OLIVEIRA, W. X. C.; SILVEIRA, J. F. R. V.; NOGUEIRA, A. F.; DA SILVA, J. L. F. Novel zero-dimensional lead-free bismuth based perovskites: from synthesis to structural and optoelectronic characterization. **Materials Advances**, London, v. 1, n. 9, p. 3439–3448, 2020.

2 OZÓRIO, M. S.; DIAS, A. C.; SILVEIRA, J. F. R. V.; SILVA, J. L. F. D. Theoretical investigation of the role of anion and trivalent cation substitution in the physical properties of lead-free zero-dimensional perovskites. **Journal of Physical Chemistry C**, Washington, v. 126, n. 16, p. 7245–7255, 2022.

3 KOJIMA, A.; TESHIMA, K.; SHIRAI, Y.; MIYASAKA, T. Organometal halide perovskites as visible-light sensitizers for photovoltaic cells. **Journal of the American Chemical Society**, Washington, v. 131, n. 17, p. 6050–6051, 2009.

4 SHIKOH, A. S.; POLYAKOV, A. A quantitative analysis of the research trends in perovskite solar cells in 2009–2019. **Physica Status Solidi A**, Weinheim, v. 217, n. 23, p. 2000441, 2020.

5 KIM, H.; HAN, J. S.; KIM, S. G.; KIM, S. Y.; JANG, H. W. Halide perovskites for resistive random-access memories. **Journal of Materials Chemistry C**, Cambridge, v. 7, n. 18, p. 5226–5234, 2019.

6 FAKHARUDDIN, A.; GANGISHETTY, M. K.; ABDI-JALEBI, M.; CHIN, S.-H.; YUSOFF, A. R. bin M.; CONGREVE, D. N.; TRESS, W.; DESCHLER, F.; VASILOPOULOU, M.; BOLINK, H. J. Perovskite light-emitting diodes. **Nature Electronics**, London, v. 5, n. 4, p. 203–216, 2022.

7 ZHANG, Y.; MA, Y.; WANG, Y.; ZHANG, X.; ZUO, C.; SHEN, L.; DING, L. Lead-free perovskite photodetectors: Progress, challenges, and opportunities. **Advanced Materials**, Weinheim, v. 33, n. 26, p. 2006691, 2021.

8 HUANG, H.; WENG, B.; ZHANG, H.; LAI, F.; LONG, J.; HOFKENS, J.; DOUTHWAITE, R. E.; STEELE, J. A.; ROEFFAERS, M. B. J. Solar-to-chemical fuel conversion via metal halide perovskite solar-driven electrocatalysis. **Journal of Physical Chemistry Letters**, Washington, v. 13, n. 1, p. 25–41, 2021.

9 REN, K.; YUE, S.; LI, C.; FANG, Z.; GASEM, K. A. M.; LESZCZYNSKI, J.; QU, S.; WANG, Z.; FAN, M. Metal halide perovskites for photocatalysis applications. **Journal of Materials Chemistry A**, Cambridge, v. 10, n. 2, p. 407–429, 2022.

10 LUO, J.; WANG, X.; LI, S.; LIU, J.; GUO, Y.; NIU, G.; YAO, L.; FU, Y.; GAO, L.; DONG, Q.; ZHAO, C.; LENG, M.; MA, F.; LIANG, W.; WANG, L.; JIN, S.; HAN, J.; ZHANG, L.; ETHERIDGE, J.; WANG, J.; YAN, Y.; SARGENT, E. H.; TANG, J. Efficient and stable emission of warm-white light from lead-free halide double perovskites. **Nature**, London, v. 563, n. 7732, p. 541–545, 2018.

11 COMBES, C.; DORENBOS, P.; VAN EIJK, C.; KRÄMER, K.; GÜDEL, H. Optical and scintillation properties of pure and Ce^{3+}-doped Cs_2LiYCl_6 and Li_3YCl_6:Ce^{3+} crystals. **Journal of Luminescence**, Amsterdam, v. 82, n. 4, p. 299–305, 1999.

12 PAN, W.; WU, H.; LUO, J.; DENG, Z.; GE, C.; CHEN, C.; JIANG, X.; YIN, W.-J.; NIU, G.; ZHU, L.; YIN, L.; ZHOU, Y.; XIE, Q.; KE, X.; SUI, M.; TANG, J. $Cs_2AgBiBr_6$ single-crystal x-ray detectors with a low detection limit. **Nature Photonics**, London, v. 11, n. 11, p. 726–732, 2017.

13 ANSARI, M. I. H.; QURASHI, A.; NAZEERUDDIN, M. K. Frontiers, opportunities, and challenges in perovskite solar cells: a critical review. **Journal of Photochemistry and Photobiology C:** Photochemistry Reviews, Amsterdam, v. 35, p. 1–24, 2018.

14 WANG, L.; YUAN, G. D.; DUAN, R. F.; HUANG, F.; WEI, T. B.; LIU, Z. Q.; WANG, J. X.; LI, J. M. Tunable bandgap in hybrid perovskite $CH_3NH_3Pb(Br_{3-y}X_y)$ single crystals and photodetector applications. **AIP Advances**, New York, v. 6, n. 4, p. 045115, 2016.

15 DONG, D.; DENG, H.; HU, C.; SONG, H.; QIAO, K.; YANG, X.; ZHANG, J.; CAI, F.; TANG, J.; SONG, H. Bandgap tunable $Cs_x(CH_3NH_3)_{1-x}PbI_3$ perovskite nanowires by aqueous solution synthesis for optoelectronic devices. **Nanoscale**, London, v. 9, n. 4, p. 1567–1574, 2017.

16 JU, D.; DANG, Y.; ZHU, Z.; LIU, H.; CHUEH, C.-C.; LI, X.; WANG, L.; HU, X.; JEN, A. K.-Y.; TAO, X. Tunable band gap and long carrier recombination lifetime of stable mixed $CH_3NH_3Pb_xSn_{1-x}Br_3$ single crystals. **Chemistry of Materials**, Washington, v. 30, n. 5, p. 1556–1565, 2018.

17 LUCARELLI, G.; GIACOMO, F. D.; ZARDETTO, V.; CREATORE, M.; BROWN, T. M. Efficient light harvesting from flexible perovskite solar cells under indoor white light-emitting diode illumination. **Nano Research**, Beijing, v. 10, n. 6, p. 2130–2145, 2017.

18 POPOV, G.; MATTINEN, M.; KEMELL, M. L.; RITALA, M.; LESKELä, M. Scalable route to the fabrication of $CH_3NH_3PbI_3$ perovskite thin films by electrodeposition and vapor conversion. **ACS Omega**, Washington, v. 1, n. 6, p. 1296–1306, 2016.

19 IEFANOVA, A.; ADHIKARI, N.; DUBEY, A.; KHATIWADA, D.; QIAO, Q. Lead free $CH_3NH_3SnI_3$ perovskite thin-film with p-type semiconducting nature and metal-like conductivity. **AIP Advances**, New York, v. 6, n. 8, p. 085312, 2016.

20 YOO, J. J.; SEO, G.; CHUA, M. R.; PARK, T. G.; LU, Y.; ROTERMUND, F.; KIM, Y.-K.; MOON, C. S.; JEON, N. J.; CORREA-BAENA, J.-P.; BULOVIĆ, V.; SHIN, S. S.; BAWENDI, M. G.; SEO, J. Efficient perovskite solar cells via improved carrier management. **Nature**, London, v. 590, n. 7847, p. 587–593, 2021.

21 MIN, H.; LEE, D. Y.; KIM, J.; KIM, G.; LEE, K. S.; KIM, J.; PAIK, M. J.; KIM, Y. K.; KIM, K. S.; KIM, M. G.; SHIN, T. J.; SEOK, S. I. Perovskite solar cells with atomically coherent interlayers on SnO_2 electrodes. **Nature**, London, v. 598, n. 7881, p. 444–450, 2021.

22 JEONG, J.; KIM, M.; SEO, J.; LU, H.; AHLAWAT, P.; MISHRA, A.; YANG, Y.; HOPE, M. A.; EICKEMEYER, F. T.; KIM, M.; YOON, Y. J.; CHOI, I. W.; DARWICH, B. P.; CHOI, S. J.; JO, Y.; LEE, J. H.; WALKER, B.; ZAKEERUDDIN, S. M.; EMSLEY, L.; ROTHLISBERGER, U.; HAGFELDT, A.; KIM, D. S.; GRÄTZEL, M.; KIM, J. Y. Pseudo-halide anion engineering for α-$FAPbI_3$ perovskite solar cells. **Nature**, London, v. 592, n. 7854, p. 381–385, 2021.

23 SHOCKLEY, W.; QUEISSER, H. J. Detailed balance limit of efficiency of p-n junction solar cells. **Journal of Applied Physics**, New York, v. 32, n. 3, p. 510–519, 1961.

24 RÜHLE, S. Tabulated values of the shockley–queisser limit for single junction solar cells. **Solar Energy**, Oxford, v. 130, p. 139–147, 2016.

25 SOLANGI, K.; ISLAM, M.; SAIDUR, R.; RAHIM, N.; FAYAZ, H. A review on global solar energy policy. **Renewable and Sustainable Energy Reviews**, Oxford, v. 15, n. 4, p. 2149–2163, 2011.

26 WANG, R.; MUJAHID, M.; DUAN, Y.; WANG, Z.-K.; XUE, J.; YANG, Y. A review of perovskites solar cell stability. **Advanced Functional Materials**, Weinheim, v. 29, n. 47, p. 1808843, 2019.

27 BERHE, T. A.; SU, W.-N.; CHEN, C.-H.; PAN, C.-J.; CHENG, J.-H.; CHEN, H.-M.; TSAI, M.-C.; CHEN, L.-Y.; DUBALE, A. A.; HWANG, B.-J. Organometal halide perovskite solar cells: degradation and stability. **Energy & Environmental Science**, London, v. 9, p. 323–356, 2016.

28 GRANCINI, G.; ROLDÁN-CARMONA, C.; ZIMMERMANN, I.; MOSCONI, E.; LEE, X.; MARTINEAU, D.; NARBEY, S.; OSWALD, F.; ANGELIS, F. D.; GRÄTZEL, M.; NAZEERUDDIN, M. K. One-year stable perovskite solar cells by 2D/3D interface engineering. **Nature Communications**, London, v. 8, p. 15684, 2017.

29 JIANG, Y.; QIU, L.; JUAREZ-PEREZ, E. J.; ONO, L. K.; HU, Z.; LIU, Z.; WU, Z.; MENG, L.; WANG, Q.; QI, Y. Reduction of lead leakage from damaged lead halide perovskite solar modules using self-healing polymer-based encapsulation. **Nature Energy**, London, v. 4, n. 7, p. 585–593, 2019.

30 ONINGS, B.; BABAYIGIT, A.; BOYEN, H.-G. Fire safety of lead halide perovskite photovoltaics. **ACS Energy Letters**, Washington, v. 4, n. 4, p. 873–878, 2019.

31 LI, J.; CAO, H.-L.; JIAO, W.-B.; WANG, Q.; WEI, M.; CANTONE, I.; Lü, J.; ABATE, A. Biological impact of lead from halide perovskites reveals the risk of introducing a safe threshold. **Nature Communications**, London, v. 11, n. 1, p. 1–5, 2020.

32 JENA, A. K.; KULKARNI, A.; MIYASAKA, T. Halide perovskite photovoltaics: background, status, and future prospects. **Chemical Reviews**, Washington, v. 119, n. 5, p. 3036–3103, 2019.

33 HAN, Q.; BAE, S.-H.; SUN, P.; HSIEH, Y.-T.; YANG, Y. M.; RIM, Y. S.; ZHAO, H.; CHEN, Q.; SHI, W.; LI, G.; YANG, Y. Single crystal formamidinium lead iodide ($FAPbI_3$): Insight into the structural, optical, and electrical properties. **Advanced Materials**, Weinheim, v. 28, n. 11, p. 2253–2258, 2016.

34 ALSALLOUM, A. Y.; TUREDI, B.; ZHENG, X.; MITRA, S.; ZHUMEKENOV, A. A.; LEE, K. J.; MAITY, P.; GEREIGE, I.; ALSAGGAF, A.; ROQAN, I. S.; MOHAMMED, O. F.; BAKR, O. M. Low-temperature crystallization enables 21.9% efficient single-crystal $MAPbI_3$ inverted perovskite solar cells. **ACS Energy Letters**, Washington, v. 5, n. 2, p. 657–662, 2020.

35 SWARNKAR, A.; MARSHALL, A. R.; SANEHIRA, E. M.; CHERNOMORDIK, B. D.; MOORE, D. T.; CHRISTIANS, J. A.; CHAKRABARTI, T.; LUTHER, J. M. Quantum dot-induced phase stabilization of α-$CsPbI_3$ perovskite for high-efficiency photovoltaics. **Science**, Washington, v. 354, n. 6308, p. 92–95, 2016.

36 RAHMAN, M. H.; JUBAIR, M.; RAHAMAN, M. Z.; AHASAN, M. S.; OSTRIKOV, K. K.; ROKNUZZAMAN, M. $RbSnX_3$ (X = Cl, Br, I): promising lead-free metal halide perovskites for photovoltaics and optoelectronics. **RSC Advances**, Cambridge, v. 12, n. 12, p. 7497–7505, 2022.

37 FAN, Q.; BIESOLD-MCGEE, G. V.; MA, J.; XU, Q.; PAN, S.; PENG, J.; LIN, Z. Lead-free halide perovskite nanocrystals: Crystal structures, synthesis, stabilities, and optical properties. **Angewandte Chemie International Edition**, Weinheim, v. 59, n. 3, p. 1030–1046, 2019.

38 ZHANG, J.; XIE, C.; LI, G.; DAI, P.; YANG, L.; LIU, R.; PAN, B. Effect of cation replacement on the phase stability of formamidinium lead iodide perovskite. **The Journal of Chemical Physics**, New York, v. 151, n. 13, p. 134104, 2019.

39 EPERON, G. E.; LEIJTENS, T.; BUSH, K. A.; PRASANNA, R.; GREEN, T.; WANG, J. T.-W.; MCMEEKIN, D. P.; VOLONAKIS, G.; MILOT, R. L.; MAY, R.; PALMSTROM, A.; SLOTCAVAGE, D. J.; BELISLE, R. A.; PATEL, J. B.; PARROTT, E. S.; SUTTON, R. J.; MA, W.; MOGHADAM, F.; CONINGS, B.; BABAYIGIT, A.; BOYEN, H.-G.; BENT, S.; GIUSTINO, F.; HERZ, L. M.; JOHNSTON, M. B.; MCGEHEE, M. D.; SNAITH, H. J. Perovskite-perovskite tandem photovoltaics with optimized band gaps. **Science**, Washington, v. 354, n. 6314, p. 861–865, 2016.

40 SALIBA, M.; MATSUI, T.; SEO, J.-Y.; DOMANSKI, K.; CORREA-BAENA, J.-P.; NAZEERUDDIN, M. K.; ZAKEERUDDIN, S. M.; TRESS, W.; ABATE, A.; HAGFELDT, A.; GRÄTZEL, M. Cesium-containing triple cation perovskite solar cells: improved stability, reproducibility and high efficiency. **Energy & Environmental Science**, London, v. 9, n. 6, p. 1989–1997, 2016.

41 SALIBA, M.; MATSUI, T.; DOMANSKI, K.; SEO, J.-Y.; UMMADISINGU, A.; ZAKEERUDDIN, S. M.; CORREA-BAENA, J.-P.; TRESS, W. R.; ABATE, A.; HAGFELDT, A.; GRÄTZEL, M. Incorporation of rubidium cations into perovskite solar cells improves photovoltaic performance. **Science**, Washington, v. 354, n. 6309, p. 206–209, 2016.

42 GRÄTZEL, M. The rise of highly efficient and stable perovskite solar cells. **Accounts of Chemical Research**, Columbus, v. 50, n. 3, p. 487–491, 2017.

43 JOKAR, E.; CHIEN, C.-H.; TSAI, C.-M.; FATHI, A.; DIAU, E. W.-G. Robust tin-based perovskite solar cells with hybrid organic cations to attain efficiency approaching 10%. **Advanced Materials**, Weinheim, v. 31, n. 2, p. 1804835, 2018.

44 SZOSTAK, R.; SILVA, J. C.; TURREN-CRUZ, S.-H.; SOARES, M. M.; FREITAS, R. O.; HAGFELDT, A.; TOLENTINO, H. C. N.; NOGUEIRA, A. F. Nanoscale mapping of chemical composition in organic-inorganic hybrid perovskite films. **Science Advances**, Washington, v. 5, n. 10, p. 1, 2019.

45 GERMINO, J. C.; SZOSTAK, R.; MOTTI, S. G.; MORAL, R. F.; MARCHEZI, P. E.; SELEGHINI, H. S.; BONATO, L. G.; ARAÚJO, F. L. de; ATVARS, T. D. Z.; HERZ, L. M.; FENNING, D.; HAGFELDT, A.; NOGUEIRA, A. F. Postpassivation of multication perovskite with rubidium butyrate. **ACS Photonics**, Washington, v. 7, n. 8, p. 2282–2291, 2020.

46 YOKOYAMA, T.; CAO, D. H.; STOUMPOS, C. C.; SONG, T.-B.; SATO, Y.; ARAMAKI, S.; KANATZIDIS, M. G. Overcoming short-circuit in lead-free $CH_3NH_3SnI_3$ perovskite solar cells via kinetically controlled gas–solid reaction film fabrication process. **Journal of Physical Chemistry Letters**, Washington, v. 7, n. 5, p. 776–782, 2016.

47 LANZETTA, L.; ARISTIDOU, N.; HAQUE, S. A. Stability of lead and tin halide perovskites: the link between defects and degradation. **Journal of Physical Chemistry Letters**, Washington, v. 11, n. 2, p. 574–585, 2020.

48 SALIBA, M.; CORREA-BAENA, J.-P.; WOLFF, C. M.; STOLTERFOHT, M.; PHUNG, N.; ALBRECHT, S.; NEHER, D.; ABATE, A. How to make over 20% efficient perovskite solar cells in regular (n–i–p) and inverted (p–i–n) architectures. **Chemistry of Materials**, Washington, v. 30, n. 13, p. 4193–4201, 2018.

49 IM, J.-H.; KIM, H.-S.; PARK, N.-G. Morphology-photovoltaic property correlation in perovskite solar cells: one-step versus two-step deposition of $CH_3NH_3PbI_3$. **APL Materials**, New York, v. 2, n. 8, p. 081510, 2014.

50 JAMAL, M.; BASHAR, M.; HASAN, A. M.; ALMUTAIRI, Z. A.; ALHARBI, H. F.; ALHARTHI, N. H.; KARIM, M. R.; MISRAN, H.; AMIN, N.; SOPIAN, K. B.; AKHTARUZZAMAN, M. Fabrication techniques and morphological analysis of perovskite absorber layer for high-efficiency perovskite solar cell: A review. **Renewable and Sustainable Energy Reviews**, Oxford, v. 98, p. 469–488, 2018.

51 HUANG, X.; WANG, K.; YI, C.; MENG, T.; GONG, X. Efficient perovskite hybrid solar cells by highly electrical conductive PEDOT:PSS hole transport layer. **Advanced Energy Materials**, Weinheim, v. 6, n. 3, p. 1501773, 2016.

52 LEE, M. M.; TEUSCHER, J.; MIYASAKA, T.; MURAKAMI, T. N.; SNAITH, H. J. Efficient hybrid solar cells based on meso-superstructured organometal halide perovskites. **Science**, Washington, v. 338, n. 6107, p. 643–647, 2012.

53 YANG, W. S.; PARK, B.-W.; JUNG, E. H.; JEON, N. J.; KIM, Y. C.; LEE, D. U.; SHIN, S. S.; SEO, J.; KIM, E. K.; NOH, J. H.; SEOK, S. I. Iodide management in formamidinium-lead-halide–based perovskite layers for efficient solar cells. **Science**, Washington, v. 356, n. 6345, p. 1376–1379, 2017.

54 GIACOMO, F. D.; RAZZA, S.; MATTEOCCI, F.; EPIFANIO, A. D.; LICOCCIA, S.; BROWN, T. M.; CARLO, A. D. High efficiency $CH_3NH_3PbI_{(3-x)}Cl_x$ perovskite solar cells with poly(3-hexylthiophene) hole transport layer. **Journal of Power Sources**, Amsterdam, v. 251, p. 152–156, 2014.

55 WANG, K.; LIN, Z.; MA, J.; LIU, Z.; ZHOU, L.; DU, J.; CHEN, D.; ZHANG, C.; CHANG, J.; HAO, Y. High-performance simple-structured planar heterojunction perovskite solar cells achieved by precursor optimization. **ACS Omega**, Washington, v. 2, n. 9, p. 6250–6258, 2017.

56 YOON, H.; KANG, S. M.; LEE, J.-K.; CHOI, M. Hysteresis-free low-temperature-processed planar perovskite solar cells with 19.1% efficiency. **Energy & Environmental Science**, London, v. 9, n. 7, p. 2262–2266, 2016.

57 ARORA, N.; DAR, M. I.; HINDERHOFER, A.; PELLET, N.; SCHREIBER, F.; ZAKEERUDDIN, S. M.; GRÄTZEL, M. Perovskite solar cells with CuSCN hole extraction layers yield stabilized efficiencies greater than 20%. **Science**, Washington, v. 358, n. 6364, p. 768–771, 2017.

58 PENG, Y.; YAACOBI-GROSS, N.; PERUMAL, A. K.; FABER, H. A.; VOURLIAS, G.; PATSALAS, P. A.; BRADLEY, D. D. C.; HE, Z.; ANTHOPOULOS, T. D. Efficient organic solar cells using copper(i) iodide (CuI) hole transport layers. **Applied Physics Letters**, New York, v. 106, n. 24, p. 243302, 2015.

59 ISLAM, M. B.; YANAGIDA, M.; SHIRAI, Y.; NABETANI, Y.; MIYANO, K. NiOx hole transport layer for perovskite solar cells with improved stability and reproducibility. **ACS Omega**, Washington, v. 2, n. 5, p. 2291–2299, 2017.

60 YOU, J.; MENG, L.; SONG, T.-B.; GUO, T.-F.; YANG, Y.; CHANG, W.-H.; HONG, Z.; CHEN, H.; ZHOU, H.; CHEN, Q.; LIU, Y.; MARCO, N. D.; YANG, Y. Improved air stability of perovskite solar cells via solution-processed metal oxide transport layers. **Nature Nanotechnology**, London, v. 11, n. 1, p. 75–81, 2015.

61 ANARAKI, E. H.; KERMANPUR, A.; STEIER, L.; DOMANSKI, K.; MATSUI, T.; TRESS, W.; SALIBA, M.; ABATE, A.; GRÄTZEL, M.; HAGFELDT, A.; CORREA-BAENA, J.-P. Highly efficient and stable planar perovskite solar cells by solution-processed tin oxide. **Energy & Environmental Science**, London, v. 9, n. 10, p. 3128–3134, 2016.

62 JIANG, Q.; ZHANG, X.; YOU, J. SnO_2 : A wonderful electron transport layer for perovskite solar cells. **Small**, Weinheim, v. 14, n. 31, p. 1801154, 2018.

63 WANG, W.; TADé, M. O.; SHAO, Z. Research progress of perovskite materials in photocatalysis- and photovoltaics-related energy conversion and environmental treatment. **Chemical Society Reviews**, Cambridge, v. 44, p. 5371–5408, 2015.

64 KIM, J. Y.; LEE, J.-W.; JUNG, H. S.; SHIN, H.; PARK, N.-G. High-efficiency perovskite solar cells. **Chemical Reviews**, Washington, v. 120, n. 15, p. 7867–7918, 2020.

65 ARISTIDOU, N.; SANCHEZ-MOLINA, I.; CHOTCHUANGCHUTCHAVAL, T.; BROWN, M.; MARTINEZ, L.; RATH, T.; HAQUE, S. A. The role of oxygen in the degradation of methylammonium lead trihalide perovskite photoactive layers. **Angewandte Chemie International Edition**, Weinheim, v. 127, n. 28, p. 8326–8330, 2015.

66 LEIJTENS, T.; EPERON, G. E.; NOEL, N. K.; HABISREUTINGER, S. N.; PETROZZA, A.; SNAITH, H. J. Stability of metal halide perovskite solar cells. **Advanced Energy Materials**, Weinheim, v. 5, n. 20, p. 1500963, 2015.

67 LEGUY, A. M. A.; HU, Y.; CAMPOY-QUILES, M.; ALONSO, M. I.; WEBER, O. J.; AZARHOOSH, P.; SCHILFGAARDE, M. van; WELLER, M. T.; BEIN, T.; NELSON, J.; DOCAMPO, P.; BARNES, P. R. F. Reversible hydration of $CH_3NH_3PbI_3$ in films,

single crystals, and solar cells. **Chemistry of Materials**, Washington, v. 27, n. 9, p. 3397–3407, 2015.

68 CHI, W.; BANERJEE, S. K. Achieving resistance against moisture and oxygen for perovskite solar cells with high efficiency and stability. **Chemistry of Materials**, Washington, v. 33, n. 12, p. 4269–4303, 2021.

69 UMARI, P.; MOSCONI, E.; ANGELIS, F. D. Relativistic GW calculations on $CH_3NH_3PbI_3$ and $CH_3NH_3SnI_3$ perovskites for solar cell applications. **Scientific Reports**, London, v. 4, p. 4467, 2014.

70 GREEN, M. A.; HO-BAILLIE, A.; SNAITH, H. J. The emergence of perovskite solar cells. **Nature Photonics**, London, v. 8, p. 506, 2014.

71 YANG, W. S.; NOH, J. H.; JEON, N. J.; KIM, Y. C.; RYU, S.; SEO, J.; SEOK, S. I. High-performance photovoltaic perovskite layers fabricated through intramolecular exchange. **Science**, Washington, v. 348, n. 6240, p. 1234–1237, 2015.

72 HOKE, E. T.; SLOTCAVAGE, D. J.; DOHNER, E. R.; BOWRING, A. R.; KARUNADASA, H. I.; MCGEHEE, M. D. Reversible photo-induced trap formation in mixed-halide hybrid perovskites for photovoltaics. **Chemical Science**, Cambridge, v. 6, p. 613–617, 2015.

73 SLOTCAVAGE, D. J.; KARUNADASA, H. I.; MCGEHEE, M. D. Light-induced phase segregation in halide-perovskite absorbers. **ACS Energy Letters**, Washington, v. 1, n. 6, p. 1199–1205, 2016.

74 BARKER, A. J.; SADHANALA, A.; DESCHLER, F.; GANDINI, M.; SENANAYAK, S. P.; PEARCE, P. M.; MOSCONI, E.; PEARSON, A. J.; WU, Y.; KANDADA, A. R. S.; LEIJTENS, T.; ANGELIS, F. D.; DUTTON, S. E.; PETROZZA, A.; FRIEND, R. H. Defect-assisted photoinduced halide segregation in mixed-halide perovskite thin films. **ACS Energy Letters**, Washington, v. 2, n. 6, p. 1416–1424, 2017.

75 BISCHAK, C. G.; HETHERINGTON, C. L.; WU, H.; ALONI, S.; OGLETREE, D. F.; LIMMER, D. T.; GINSBERG, N. S. Origin of reversible photoinduced phase separation in hybrid perovskites. **Nano Letters**, Washington, v. 17, n. 2, p. 1028–1033, 2017.

76 RAHAMAN, M. Z.; GE, S.; LIN, C.-H.; CUI, Y.; WU, T. One-dimensional molecular metal halide materials: structures, properties, and applications. **Small Structures**, Weinheim, v. 2, n. 4, p. 2000062, 2021.

77 SHANNON, R. D. Revised effective ionic radii and systematic studies of interatomic distances in halides and chalcogenides. **Acta Crystallographica Section A**, Hoboken, v. 32, n. 5, p. 751–767, 1976.

78 KIESLICH, G.; SUN, S.; CHEETHAM, A. K. Solid-state principles applied to organic–inorganic perovskites: new tricks for an old dog. **Chemical Science**, Cambridge, v. 5, n. 12, p. 4712–4715, 2014.

79 TAI, Q.; YOU, P.; SANG, H.; LIU, Z.; HU, C.; CHAN, H. L.; YAN, F. Efficient and stable perovskite solar cells prepared in ambient air irrespective of the humidity. **Nature Communications**, London, v. 7, p. 11105, 2016.

80 CHEN, J.; RONG, Y.; MEI, A.; XIONG, Y.; LIU, T.; SHENG, Y.; JIANG, P.; HONG, L.; GUAN, Y.; ZHU, X.; HOU, X.; DUAN, M.; ZHAO, J.; LI, X.; HAN, H. Hole-conductor-free fully printable mesoscopic solar cell with mixed-anion perovskite $CH_3NH_3PbI_{(3-x)}(BF_4)_x$. **Advanced Energy Materials**, Weinheim, v. 6, n. 5, p. 1502009, 2016.

81 YUAN, L.; GE, L.; SUN, X.; ZHANG, J.; YU, J.; ZHANG, C.; LI, H. Hydrothermal growth of facet-tunable fluoride perovskite crystals KMF_3 (M = Mg, Mn, Co, Ni and Zn). **CrystEngComm**, Cambridge, v. 22, n. 37, p. 6216–6227, 2020.

82 VOLONAKIS, G.; FILIP, M. R.; HAGHIGHIRAD, A. A.; SAKAI, N.; WENGER, B.; SNAITH, H. J.; GIUSTINO, F. Lead-free halide double perovskites via heterovalent substitution of noble metals. **Journal of Physical Chemistry Letters**, Washington, v. 7, n. 7, p. 1254–1259, 2016.

83 MCCLURE, E. T.; BALL, M. R.; WINDL, W.; WOODWARD, P. M. Cs_2AgBiX_6 (X = Br, Cl): new visible light absorbing, lead-free halide perovskite semiconductors. **Chemistry of Materials**, Washington, v. 28, n. 5, p. 1348–1354, 2016.

84 SLAVNEY, A. H.; HU, T.; LINDENBERG, A. M.; KARUNADASA, H. I. A bismuth-halide double perovskite with long carrier recombination lifetime for photovoltaic applications. **Journal of the American Chemical Society**, Washington, v. 138, n. 7, p. 2138–2141, 2016.

85 WOLF, N. R.; CONNOR, B. A.; SLAVNEY, A. H.; KARUNADASA, H. I. Doubling the stakes: the promise of halide double perovskites. **Angewandte Chemie**, Weinheim, v. 133, n. 30, p. 16400–16414, 2021.

86 MAUGHAN, A. E.; GANOSE, A. M.; BORDELON, M. M.; MILLER, E. M.; SCANLON, D. O.; NEILSON, J. R. Defect tolerance to intolerance in the vacancy-ordered double perovskite semiconductors Cs_2SnI_6 and Cs_2TeI_6. **Journal of the American Chemical Society**, Washington, v. 138, n. 27, p. 8453–8464, 2016.

87 SCHWARTZ, D.; MURSHED, R.; LARSON, H.; USPRUNG, B.; SOLTANMOHAMAD, S.; PANDEY, R.; BARNARD, E. S.; ROCKETT, A.; HARTMANN, T.; CASTELLI, I. E.; BANSAL, S. Air stable, high-efficiency, pt-based halide perovskite solar cells with long carrier lifetimes. **Physica Status Solidi Rapid Research Letters**, Weinheim, v. 14, n. 8, p. 2000182, 2020.

88 WANG, X.; LI, T.; XING, B.; FAIZAN, M.; BISWAS, K.; ZHANG, L. Metal halide semiconductors beyond lead-based perovskites for promising optoelectronic applications. **Journal of Physical Chemistry Letters**, Washington, v. 12, n. 43, p. 10532–10550, 2021.

89 JU, M.-G.; DAI, J.; MA, L.; ZHOU, Y.; LIANG, W.; ZENG, X. C. Lead-free low-dimensional tin halide perovskites with functional organic spacers: Breaking the charge-transport bottleneck. **Journal of Materials Chemistry A**, Cambridge, v. 7, n. 28, p. 16742–16747, 2019.

90 ZHOU, T.; WANG, M.; ZANG, Z.; TANG, X.; FANG, L. Two-dimensional lead-free hybrid halide perovskite using superatom anions with tunable electronic properties. **Solar Energy Materials and Solar Cells**, Amsterdam, v. 191, p. 33–38, 2019.

91 MA, C.; SHEN, D.; HUANG, B.; LI, X.; CHEN, W.-C.; LO, M.-F.; WANG, P.; LAM, M. H.-W.; LU, Y.; MA, B.; LEE, C.-S. High performance low-dimensional perovskite solar cells based on a one dimensional lead iodide perovskite. **Journal of Materials Chemistry A**, Cambridge, v. 7, n. 15, p. 8811–8817, 2019.

92 ZHANG, W.; TAO, K.; JI, C.; SUN, Z.; HAN, S.; ZHANG, J.; WU, Z.; LUO, J. $(C_6H_{13}N)_2BiI_5$: A one-dimensional lead-free perovskite-derivative photoconductive light absorber. **Inorganic Chemistry**, Washington, v. 57, n. 8, p. 4239–4243, 2018.

93 ZHANG, R.; MAO, X.; YANG, Y.; YANG, S.; ZHAO, W.; WUMAIER, T.; WEI, D.; DENG, W.; HAN, K. Air-stable, lead-free zero-dimensional mixed bismuth-antimony perovskite single crystals with ultra-broadband emission. **Angewandte Chemie International Edition**, Weinheim, v. 58, n. 9, p. 2725–2729, 2019.

94 HONG, K.; LE, Q. V.; KIM, S. Y.; JANG, H. W. Low-dimensional halide perovskites: review and issues. **Journal of Materials Chemistry C**, Cambridge, v. 6, n. 9, p. 2189–2209, 2018.

95 HAO, M.; BAI, Y.; ZEISKE, S.; REN, L.; LIU, J.; YUAN, Y.; ZARRABI, N.; CHENG, N.; GHASEMI, M.; CHEN, P.; LYU, M.; HE, D.; YUN, J.-H.; DU, Y.; WANG, Y.; DING, S.; ARMIN, A.; MEREDITH, P.; LIU, G.; CHENG, H.-M.; WANG, L. Ligand-assisted cation-exchange engineering for high-efficiency colloidal $Cs_{1-x}FA_xPbI_3$ quantum dot solar cells with reduced phase segregation. **Nature Energy**, London, v. 5, n. 1, p. 79–88, 2020.

96 RICCIARDULLI, A. G.; YANG, S.; SMET, J. H.; SALIBA, M. Emerging perovskite monolayers. **Nature Materials**, London, v. 20, n. 10, p. 1325–1336, 2021.

97 CONNOR, B. A.; BIEGA, R.-I.; LEPPERT, L.; KARUNADASA, H. I. Dimensional reduction of the small-bandgap double perovskite $Cs_2AgTlBr_6$. **Chemical Science**, Cambridge, v. 11, n. 29, p. 7708–7715, 2020.

98 VARGAS, B.; RAMOS, E.; PÉREZ-GUTIÉRREZ, E.; ALONSO, J. C.; SOLIS-IBARRA, D. A direct bandgap copper–antimony halide perovskite. **Journal of the American Chemical Society**, Washington, v. 139, n. 27, p. 9116–9119, 2017.

99 YUAN, Z.; ZHOU, C.; TIAN, Y.; SHU, Y.; MESSIER, J.; WANG, J. C.; BURGT, L. J. van de; KOUNTOURIOTIS, K.; XIN, Y.; HOLT, E.; SCHANZE, K.; CLARK, R.; SIEGRIST, T.; MA, B. One-dimensional organic lead halide perovskites with efficient bluish white-light emission. **Nature Communications**, London, v. 8, n. 1, p. 1–7, 2017.

100 ROCCANOVA, R.; YANGUI, A.; SEO, G.; CREASON, T. D.; WU, Y.; KIM, D. Y.; DU, M.-H.; SAPAROV, B. Bright luminescence from nontoxic $CsCu_2X_3$ (X = Cl, Br, I). **ACS Materials Letters**, Washington, v. 1, n. 4, p. 459–465, 2019.

101 ELLEUCH, S.; LUSSON, A.; PILLET, S.; BOUKHEDDADEN, K.; ABID, Y. White light emission from a zero-dimensional lead chloride hybrid material. **ACS Photonics**, Washington, v. 7, n. 5, p. 1178–1187, 2020.

102 SUN, C.; JIANG, K.; HAN, M.-F.; LIU, M.-J.; LIAN, X.-K.; JIANG, Y.-X.; SHI, H.-S.; YUE, C.-Y.; LEI, X.-W. A zero-dimensional hybrid lead perovskite with highly efficient blue-violet light emission. **Journal of Materials Chemistry C**, Cambridge, v. 8, n. 34, p. 11890–11895, 2020.

103 WANG, Y.; TANG, Z.; LIU, C.; JIANG, J.; LIU, W.; ZHANG, B.; GAO, K.; CAI, H.-L.; WU, X. Room temperature ferroelectricity and blue photoluminescence in zero dimensional organic lead iodine perovskites. **Journal of Materials Chemistry C**, Cambridge, v. 9, n. 1, p. 223–227, 2021.

104 ZHANG, Y.; SAIDAMINOV, M. I.; DURSUN, I.; YANG, H.; MURALI, B.; ALAROUSU, E.; YENGEL, E.; ALSHANKITI, B. A.; BAKR, O. M.; MOHAMMED, O. F. Zero-dimensional Cs_4PbBr_6 perovskite nanocrystals. **Journal of Physical Chemistry Letters**, Washington, v. 8, n. 5, p. 961–965, 2017.

105 WANG, L.; LIU, H.; ZHANG, Y.; MOHAMMED, O. F. Photoluminescence origin of zero-dimensional Cs_4PbBr_6 perovskite. **ACS Energy Letters**, Washington, v. 5, n. 1, p. 87–99, 2019.

106 YANG, J.; LIU, Z.; ZENG, F.; PI, M.; SHI, T.; BIAN, Y.; TANG, X.; DU, J.; LIU, W.; LENG, Y. High-quality single-mode lasers based on zero-dimensional cesium lead halide perovskites. **Solar RRL**, v. 3, n. 10, p. 1900127, 2019.

107 CHA, J.-H.; LEE, H.-J.; KIM, S. H.; KO, K. C.; SUH, B. J.; HAN, O. H.; JUNG, D.-Y. Superparamagnetism of green emissive Cs_4PbBr_6 zero-dimensional perovskite crystals. **ACS Energy Letters**, Washington, v. 5, n. 7, p. 2208–2216, 2020.

108 SUN, R.; LIU, N.; ZHENG, W.; ZHANG, J.; LI, N.; LIAN, H.; LIU, H.; ZHANG, Y. Real-time tracking of emitter generation in a zero-dimensional perovskite. **Chemistry of Materials**, Washington, v. 33, n. 10, p. 3721–3728, 2021.

109 ALMUTLAQ, J.; YIN, J.; MOHAMMED, O. F.; BAKR, O. M. The benefit and challenges of zero-dimensional perovskites. **Journal of Physical Chemistry Letters**, Washington, v. 9, n. 14, p. 4131–4138, 2018.

110 CAI, B.; CHEN, X.; XIE, M.; ZHANG, S.; LIU, X.; YANG, J.; ZHOU, W.; GUO, S.; ZENG, H. A class of pb-free double perovskite halide semiconductors with intrinsic ferromagnetism, large spin splitting and high curie temperature. **Materials Horizons**, Cambridge, v. 5, n. 5, p. 961–968, 2018.

111 TAN, Z.-K.; MOGHADDAM, R. S.; LAI, M. L.; DOCAMPO, P.; HIGLER, R.; DESCHLER, F.; PRICE, M.; SADHANALA, A.; PAZOS, L. M.; CREDGINGTON, D. et al. Bright light-emitting diodes based on organometal halide perovskite. **Nature Nanotechnology**, London, v. 9, n. 9, p. 687–692, 2014.

112 JIA, Y.; KERNER, R. A.; GREDE, A. J.; BRIGEMAN, A. N.; RAND, B. P.; GIEBINK, N. C. Diode-pumped organo-lead halide perovskite lasing in a metal-clad distributed feedback resonator. **Nano Letters**, Washington, v. 16, n. 7, p. 4624–4629, 2016.

113 CHU, K.-B.; XIE, J.-L.; CHEN, W.-J.; LU, W.-X.; SONG, J.-L.; ZHANG, C. A novel bismuth-based hybrid material with highly activity for fast removal of rhodamine b under dark conditions. **Polyhedron**, Oxford, v. 151, p. 146–151, 2018.

114 CHENG, S.; BEITLEROVA, A.; KUCERKOVA, R.; NIKL, M.; REN, G.; WU, Y. Zero-dimensional $Cs_3Cu_2I_5$ perovskite single crystal as sensitive x-ray and γ-ray scintillator. **Physica Status Solidi Rapid Research Letters**, Weinheim, v. 14, n. 11, p. 2000374, 2020.

115 PIOUS, J. K.; LEKSHMI, M. L.; MUTHU, C.; RAKHI, R. B.; NAIR, V. C. Zero-dimensional methylammonium bismuth iodide-based lead-free perovskite capacitor. **ACS Omega**, Washington, v. 2, n. 9, p. 5798–5802, 2017.

116 ELFALEH, N.; KAMOUN, S. Structural characterization, vibrational studies and optical properties of a new luminescent organic-inorganic material $[C_6H_{20}N_3]BiI_6.H_2O$. **Journal of Organometallic Chemistry**, Amsterdam, v. 819, p. 95–102, 2016.

117 ZHOU, C.; LIN, H.; TIAN, Y.; YUAN, Z.; CLARK, R.; CHEN, B.; BURGT, L. J. van de; WANG, J. C.; ZHOU, Y.; HANSON, K.; MEISNER, Q. J.; NEU, J.; BESARA, T.; SIEGRIST, T.; LAMBERS, E.; DJUROVICH, P.; MA, B. Luminescent zero-dimensional organic metal halide hybrids with near-unity quantum efficiency. **Chemical Science**, Cambridge, v. 9, n. 3, p. 586–593, 2018.

118 BENIN, B. M.; MCCALL, K. M.; WÖRLE, M.; MORAD, V.; AEBLI, M.; YAKUNIN, S.; SHYNKARENKO, Y.; KOVALENKO, M. V. The $Rb_7Bi_{3-3x}Sb_{3x}Cl_{16}$ family: A fully inorganic solid solution with room-temperature luminescent members. **Angewandte Chemie International Edition**, Weinheim, v. 59, n. 34, p. 14490–14497, 2020.

119 CHIARA, R.; CIFTCI, Y. O.; QUELOZ, V. I. E.; NAZEERUDDIN, M. K.; GRANCINI, G.; MALAVASI, L. Green-emitting lead-free Cs_4SnBr_6 zero-dimensional perovskite nanocrystals with improved air stability. **Journal of Physical Chemistry Letters**, Washington, v. 11, n. 3, p. 618–623, 2020.

120 PIOUS, J. K.; MUTHU, C.; DANI, S.; SAEKI, A.; VIJAYAKUMAR, C. Bismuth-based zero-dimensional perovskite-like materials: Effect of benzylammonium on dielectric confinement and photoconductivity. **Chemistry of Materials**, Washington, v. 32, n. 6, p. 2647–2652, 2020.

121 ZHANG, Z.; LI, X.; XIA, X.; WANG, Z.; HUANG, Z.; LEI, B.; GAO, Y. High-quality $(CH_3NH_3)_3Bi_2I_9$ film-based solar cells: Pushing efficiency up to 1.64%. **Journal of Physical Chemistry Letters**, Washington, v. 8, n. 17, p. 4300–4307, 2017.

122 BAI, F.; HU, Y.; HU, Y.; QIU, T.; MIAO, X.; ZHANG, S. Lead-free, air-stable ultrathin $Cs_3Bi_2I_9$ perovskite nanosheets for solar cells. **Solar Energy Materials and Solar Cells**, Amsterdam, v. 184, p. 15–21, 2018.

123 PIOUS, J. K.; KATRE, A.; MUTHU, C.; CHAKRABORTY, S.; KRISHNA, S.; NAIR, V. C. Zero-dimensional lead-free hybrid perovskite-like material with a quantum-well structure. **Chemistry of Materials**, Washington, v. 31, n. 6, p. 1941–1945, 2019.

124 LIU, Y.; XU, Z.; YANG, Z.; ZHANG, Y.; CUI, J.; HE, Y.; YE, H.; ZHAO, K.; SUN, H.; LU, R.; LIU, M.; KANATZIDIS, M. G.; LIU, S. F. Inch-size 0D-structured lead-free perovskite single crystals for highly sensitive stable x-ray imaging. **Matter**, Cambridge, v. 3, n. 1, p. 180–196, 2020.

125 ZHANG, J.; BAI, D.; JIN, Z.; BIAN, H.; WANG, K.; SUN, J.; WANG, Q.; LIU, S. F. 3D-2D-0D interface profiling for record efficiency all-inorganic $CsPbBrI_2$ perovskite solar cells with superior stability. **Advanced Energy Materials**, Weinheim, v. 8, n. 15, p. 1703246, 2018.

126 FAN, J.; MA, Y.; ZHANG, C.; LIU, C.; LI, W.; SCHROPP, R. E. I.; MAI, Y. Thermodynamically self-healing 1D-3D hybrid perovskite solar cells. **Advanced Energy Materials**, Weinheim, v. 8, n. 16, p. 1703421, 2018.

127 EGGER, D. A.; BERA, A.; CAHEN, D.; HODES, G.; KIRCHARTZ, T.; KRONIK, L.; LOVRINCIC, R.; RAPPE, A. M.; REICHMAN, D. R.; YAFFE, O. What remains unexplained about the properties of halide perovskites? **Advanced Materials**, Weinheim, v. 30, n. 20, p. 1800691, 2018.

128 WALSH, A. Atomistic models of metal halide perovskites. **Matter**, Cambridge, v. 4, n. 12, p. 3867–3873, 2021.

129 OZÓRIO, M. S.; SRIKANTH, M.; BESSE, R.; Da Silva, J. L. F. The role of the A-cations in the polymorphic stability and optoelectronic properties of lead-free $A\mathrm{SnI}_3$ perovskites. **Physical Chemistry Chemical Physics**, London, v. 23, n. 3, p. 2286–2297, 2021.

130 BORN, M.; OPPENHEIMER, R. Zur quantentheorie der molekeln. **Annalen der Physik**, Berlin, v. 389, n. 20, p. 457–484, 1927.

131 KOHN, W.; BECKE, A. D.; PARR, R. G. Density functional theory of electronic structure. **Journal of Physical Chemistry**, Washington, v. 100, n. 31, p. 12974–12980, 1996.

132 HOHENBERG, P.; KOHN, W. Inhomogeneous electron gas. **Physical Review**, College Park, v. 136, n. 3B, p. B864–B871, 1964.

133 KOHN, W.; SHAM, L. J. Self-consistent equations including exchange and correlation effects. **Physical Review**, College Park, v. 140, n. 4A, p. A1133–A1138, 1965.

134 OZORIO, M. S.; ANDRIANI, K. F.; SILVA, J. L. D. A hybrid-DFT investigation of the Ce oxidation state upon adsorption of F, Na, Ni, Pd and Pt on the $(CeO_2)_6$ cluster. **Physical Chemistry Chemical Physics**, London, v. 22, n. 25, p. 14099–14108, 2020.

135 PERDEW, J. P.; BURKE, K.; ERNZERHOF, M. Generalized gradient approximation made simple. **Physical Review Letters**, College Park, v. 77, n. 18, p. 3865–3868, 1996.

136 HEYD, J.; SCUSERIA, G. E.; ERNZERHOF, M. Hybrid functionals based on a screened coulomb potential. **The Journal of Chemical Physics**, New York, v. 118, n. 18, p. 8207–8215, 2003.

137 HEYD, J.; SCUSERIA, G. E. Efficient hybrid density functional calculations in solids: Assessment of the heyd-scuseria-ernzerhof screened coulomb hybrid functional. **The Journal of Chemical Physics**, New York, v. 121, n. 3, p. 1187–1192, 2004.

138 HEYD, J.; E. SCUSERIA, G. Assessment and validation of a screened coulomb hybrid density functional. **The Journal of Chemical Physics**, New York, v. 120, p. 7274, 2004.

139 HEYD, J.; SCUSERIA, G. E.; ERNZERHOF, M. Erratum: “hybrid functionals based on a screened coulomb potential” [J. Chem. Phys. 118, 8207 (2003)]. **The Journal of Chemical Physics**, New York, v. 124, n. 21, p. 219906, 2006.

140 ADAMO, C.; BARONE, V. Toward realiable density functional methods without ajustable parameters: The pbe0 model. **The Journal of Chemical Physics**, New York, v. 110, p. 6158, 1999.

141 KRUKAU, A. V.; VYDROV, O. A.; IZMAYLOV, A. F.; SCUSERIA, G. E. Influence of the exchange screening parameter on the performance of screened hybrid functionals. **The Journal of Chemical Physics**, New York, v. 125, n. 22, p. 224106, 2006.

142 VAN der Waals forces. *In*: **IUPAC Compendium of Chemical Terminology**. *[S.I.]*: IUPAC,1994.

143 GRIMME, S.; ANTONY, J.; EHRLICH, S.; KRIEG, H. A consistent and accurate *Ab Initio* parametrization of density functional dispersion correction (DFT-D) for the 94 elements H-Pu. **The Journal of Chemical Physics**, New York, v. 132, n. 15, p. 154104, 2010.

144 RECKIEN, W.; JANETZKO, F.; PEINTINGER, M. F.; BREDOW, T. Implementation of empirical dispersion corrections to density functional theory for periodic systems. **Journal of Computational Chemistry**, Hoboken, v. 33, n. 25, p. 2023–2031, 2012.

145 KRESSE, G.; HAFNER, J. *Ab-initio* molecular dynamics for open-shell transition metals. **Physical Review B**, College Park, v. 48, n. 17, p. 13115–13118, 1993.

146 KRESSE, G.; FURTHMÜLLER, J. Efficient iterative schemes for *ab-initio* total-energy calculations using a plane-wave basis set. **Physical Review B**, College Park, v. 54, n. 16, p. 11169–11186, 1996.

147 BLÖCHL, P. E. Projector augmented-wave method. **Physical Review B**, College Park, v. 50, n. 24, p. 17953–17979, 1994.

148 KRESSE, G.; JOUBERT, D. From ultrasoft pseudopotentials to the projector augmented-wave method. **Physical Review B**, College Park, v. 59, n. 3, p. 1758–1775, 1999.

149 TORRENT, M.; HOLZWARTH, N.; JOLLET, F.; HARRIS, D.; LEPLEY, N.; XU, X. Electronic structure packages: Two implementations of the projector augmented wave (PAW) formalism. **Computer Physics Communications**, Amsterdam, v. 181, n. 11, p. 1862–1867, 2010.

150 GAJDOŠ, M.; HUMMER, K.; KRESSE, G.; FURTHMÜLLER, J.; BECHSTEDT, F. Linear optical properties in the projector-augmented wave methodology. **Physical Review B**, APS, College Park, v. 73, n. 4, p. 045112, 2006.

151 GRIMME, S. Semiempirical GGA-type density functional constructed with a long-range dispersion correction. **Journal of Computational Chemistry**, Hoboken, v. 27, n. 15, p. 1787–1799, 2006.

152 TAKAHASHI, Y.; OBARA, R.; LIN, Z.-Z.; TAKAHASHI, Y.; NAITO, T.; INABE, T.; ISHIBASHI, S.; TERAKURA, K. Charge-transport in tin-iodide perovskite $CH_3NH_3SnI_3$: origin of high conductivity. **Dalton Transactions**, Cambridge, v. 40, n. 20, p. 5563, 2011.

153 DANG, Y.; ZHOU, Y.; LIU, X.; JU, D.; XIA, S.; XIA, H.; TAO, X. Formation of hybrid perovskite tin iodide single crystals by top-seeded solution growth. **Angewandte Chemie International Edition**, Weinheim, v. 128, n. 10, p. 3508–3511, 2016.

154 SCHUELLER, E. C.; LAURITA, G.; FABINI, D. H.; STOUMPOS, C. C.; KANATZIDIS, M. G.; SESHADRI, R. Crystal structure evolution and notable thermal expansion in hybrid perovskites formamidinium tin iodide and formamidinium lead bromide. **Inorganic Chemistry**, Washington, v. 57, n. 2, p. 695–701, 2018.

155 ZHANG, H.-Y.; CHEN, X.-G.; ZHANG, Z.-X.; SONG, X.-J.; ZHANG, T.; PAN, Q.; ZHANG, Y.; XIONG, R.-G. Methylphosphonium tin bromide: a 3D perovskite molecular ferroelectric semiconductor. **Advanced Materials**, Weinheim, v. 32, n. 47, p. 2005213, 2020.

156 STOUMPOS, C. C.; MALLIAKAS, C. D.; KANATZIDIS, M. G. Semiconducting tin and lead iodide perovskites with organic cations: phase transitions, high mobilities, and near-infrared photoluminescent properties. **Inorganic Chemistry**, Washington, v. 52, n. 15, p. 9019–9038, 2013.

157 MA, F.; LI, J.; LI, W.; LIN, N.; WANG, L.; QIAO, J. Stable α/δ phase junction of formamidinium lead iodide perovskites for enhanced near-infrared emission. **Chemical Science**, Cambridge, v. 8, n. 1, p. 800–805, 2017.

158 QUARTI, C.; MOSCONI, E.; ANGELIS, F. D. Interplay of orientational order and electronic structure in methylammonium lead iodide: implications for solar cell operation. **Chemistry of Materials**, Washington, v. 26, n. 22, p. 6557–6569, 2014.

159 FILIP, M. R.; EPERON, G. E.; SNAITH, H. J.; GIUSTINO, F. Steric engineering of metal-halide perovskites with tunable optical band gaps. **Nature Communications**, London, v. 5, n. 1, p. 1–9, 2014.

160 STEINER, T. The hydrogen bond in the solid state. **Angewandte Chemie International Edition**, Weinheim, v. 41, n. 1, p. 48–76, 2002.

161 XIE, G.; XU, L.; SUN, L.; XIONG, Y.; WU, P.; HU, B. Insight into the reaction mechanism of water, oxygen and nitrogen molecules on a tin iodine perovskite surface. **Journal of Materials Chemistry A**, Cambridge, v. 7, n. 10, p. 5779–5793, 2019.

162 KACHMAR, A.; BERDIYOROV, G.; MADJET, M. E.-A. Effect of water on the structural, optical, and hot-carrier cooling properties of the perovskite material $MASnI_3$. **Journal of Physical Chemistry C**, Washington, v. 123, n. 7, p. 4056–4063, 2019.

163 FROST, J. M.; BUTLER, K. T.; BRIVIO, F.; HENDON, C. H.; SCHILFGAARDE, M. van; WALSH, A. Atomistic origins of high-performance in hybrid halide perovskite solar cells. **Nano Letters**, Washington, v. 14, n. 5, p. 2584–2590, 2014.

164 FROST, J. M.; WALSH, A. What is moving in hybrid halide perovskite solar cells? **Accounts of Chemical Research**, Columbus, v. 49, n. 3, p. 528–535, 2016.

165 SVANE, K. L.; FORSE, A. C.; GREY, C. P.; KIESLICH, G.; CHEETHAM, A. K.; WALSH, A.; BUTLER, K. T. How strong is the hydrogen bond in hybrid perovskites? **Journal of Physical Chemistry Letters**, Washington, v. 8, n. 24, p. 6154–6159, 2017.

166 MAHESHWARI, S.; PATWARDHAN, S.; SCHATZ, G. C.; RENAUD, N.; GROZEMA, F. C. The effect of the magnitude and direction of the dipoles of organic cations on the electronic structure of hybrid halide perovskites. **Physical Chemistry Chemical Physics**, London, v. 21, n. 30, p. 16564–16572, 2019.

167 THIND, A. S.; HUANG, X.; SUN, J.; MISHRA, R. First-principles prediction of a stable hexagonal phase of $CH_3NH_3PbI_3$. **Chemistry of Materials**, Washington, v. 29, n. 14, p. 6003–6011, 2017.

168 HOWIE, R. A.; MOSER, W.; TREVENA, I. C. The crystal structure of tin(II) iodide. **Acta Crystallographica Section B**, Chichester, v. 28, n. 10, p. 2965–2971, 1972.

169 YAMAMURO, O.; MATSUO, T.; SUGA, H.; DAVID, W. I. F.; IBBERSON, R. M.; LEADBETTER, A. J. Neutron diffraction and calorimetric studies of methylammonium iodide. **Acta Crystallographica Section B**, Chichester, v. 48, n. 3, p. 329–336, 1992.

170 PETROV, A. A.; GOODILIN, E. A.; TARASOV, A. B.; LAZARENKO, V. A.; DOROVATOVSKII, P. V.; KHRUSTALEV, V. N. Formamidinium iodide: Crystal structure and phase transitions. **Acta Crystallographica Section E**, Hoboken, v. 73, n. 4, p. 569–572, 2017.

171 EL-MELLOUHI, F.; MARZOUK, A.; BENTRIA, E. T.; RASHKEEV, S. N.; KAIS, S.; ALHARBI, F. H. Hydrogen bonding and stability of hybrid organic-inorganic perovskites. **ChemSusChem**, Weinheim, v. 9, n. 18, p. 2648–2655, 2016.

172 EL-MELLOUHI, F.; BENTRIA, E. T.; RASHKEEV, S. N.; KAIS, S.; ALHARBI, F. H. Enhancing intrinsic stability of hybrid perovskite solar cell by strong, yet balanced, electronic coupling. **Scientific Reports**, London, v. 6, n. 1, 2016.

173 MENG, X.; ZHANG, R.; FU, Z.; ZHANG, Q. Domain-dependent electronic structure and optical absorption property in hybrid organic–inorganic perovskite. **Physical Chemistry Chemical Physics**, London, v. 18, n. 39, p. 27358–27365, 2016.

174 AKBULATOV, A. F.; TSAREV, S. A.; ELSHOBAKI, M.; LUCHKIN, S. Y.; ZHIDKOV, I. S.; KURMAEV, E. Z.; ALDOSHIN, S. M.; STEVENSON, K. J.; TROSHIN, P. A. Comparative intrinsic thermal and photochemical stability of sn(II) complex halides as next-generation materials for lead-free perovskite solar cells. **Journal of Physical Chemistry C**, Washington, v. 123, n. 44, p. 26862–26869, 2019.

175 PARROTT, E. S.; MILOT, R. L.; STERGIOPOULOS, T.; SNAITH, H. J.; JOHNSTON, M. B.; HERZ, L. M. Effect of structural phase transition on charge-carrier lifetimes and defects in $CH_3NH_3SnI_3$ perovskite. **Journal of Physical Chemistry Letters**, Washington, v. 7, n. 7, p. 1321–1326, 2016.

176 STOKES, H. T.; HATCH, D. M. FINDSYM: Program for identifying the space-group symmetry of a crystal. **Journal of Applied Crystallography**, Chichester, v. 38, n. 1, p. 237–238, 2005.

177 BAIKIE, T.; FANG, Y.; KADRO, J. M.; SCHREYER, M.; WEI, F.; MHAISALKAR, S. G.; GRÄTZEL, M.; WHITE, T. J. Synthesis and crystal chemistry of the hybrid perovskite $CH_3NH_3PbI_3$ for solid-state sensitised solar cell applications. **Journal of Materials Chemistry A**, Cambridge, v. 1, n. 18, p. 5628, 2013.

178 LEE, J.-H.; BRISTOWE, N. C.; LEE, J. H.; LEE, S.-H.; BRISTOWE, P. D.; CHEETHAM, A. K.; JANG, H. M. Resolving the physical origin of octahedral tilting in halide perovskites. **Chemistry of Materials**, Washington, v. 28, n. 12, p. 4259–4266, 2016.

179 GLAZER, A. M. The classification of tilted octahedra in perovskites. **Acta Crystallographica Section B**, Chichester, v. 28, n. 11, p. 3384–3392, 1972.

180 KOH, T. M.; KRISHNAMOORTHY, T.; YANTARA, N.; SHI, C.; LEONG, W. L.; BOIX, P. P.; GRIMSDALE, A. C.; MHAISALKAR, S. G.; MATHEWS, N. Formamidinium tin-based perovskite with low e_g for photovoltaic applications. **Journal of Materials Chemistry A**, Cambridge, v. 3, n. 29, p. 14996–15000, 2015.

181 KAHMANN, S.; NAZARENKO, O.; SHAO, S.; HORDIICHUK, O.; KEPENEKIAN, M.; EVEN, J.; KOVALENKO, M. V.; BLAKE, G. R.; LOI, M. A. Negative thermal quenching in $FASnI_3$ perovskite single crystals and thin films. **ACS Energy Letters**, Washington, v. 5, n. 8, p. 2512–2519, 2020.

182 BADER, R. F. W. **Atoms in Molecules:** a quantum theory. Oxford, Clarendon Press, c1990. 438 p.

183 SANVILLE, E.; KENNY, S. D.; SMITH, R.; HENKELMAN, G. Improved grid-based algorithm for bader charge allocation. **Journal of Computational Chemistry**, Hoboken, v. 28, n. 5, p. 899–908, 2007.

184 WANG, K.; LIANG, Z.; WANG, X.; CUI, X. Lead replacement in $CH_3NH_3PbI_3$ perovskites. **Advanced Electronic Materials**, Weinheim, v. 1, n. 10, p. 1500089, 2015.

185 HERRON, J. A.; KIM, J.; UPADHYE, A. A.; HUBER, G. W.; MARAVELIAS, C. T. A general framework for the assessment of solar fuel technologies. **Energy & Environmental Science**, London, v. 8, n. 1, p. 126–157, 2015.

186 QIAN, J.; XU, B.; TIAN, W. A comprehensive theoretical study of halide perovskites ABX_3. **Organic Electronics**, Amsterdam, v. 37, p. 61–73, 2016.

187 KHANAL, R.; AYERS, N.; BANERJEE, S.; CHOUDHURY, S. Atomic structure and electronic properties of lead and tin based hybrid halide perovskite surface for photovoltaic applications. **AIP Advances**, New York, v. 9, n. 8, p. 085123, 2019.

188 BORRIELLO, I.; CANTELE, G.; NINNO, D. Ab initio investigation of hybrid organic-inorganic perovskites based on tin halides. **Physical Review B**, College Park, v. 77, n. 23, 2008.

189 JIA, Y.; ZENG, Y.; LI, X.; MENG, L. Effect of Sr substitution on the property and stability of $CH_3NH_3SnI_3$ perovskite: a first-principles investigation. **International Journal of Energy Research**, Oxford, v. 44, n. 7, p. 5765–5778, 2020.

190 COHEN, A. J.; MORI-SÁNCHEZ, P.; YANG, W. Fractional charge perspective on the band gap in density-functional theory. **Physical Review B**, College Park, v. 77, n. 11, p. 115123, 2008.

191 CROWLEY, J. M.; TAHIR-KHELI, J.; GODDARD, W. A. Resolution of the band gap prediction problem for materials design. **Journal of Physical Chemistry Letters**, Washington, v. 7, n. 7, p. 1198–1203, 2016.

192 EVEN, J.; PEDESSEAU, L.; JANCU, J.-M.; KATAN, C. Importance of spin–orbit coupling in hybrid organic/inorganic perovskites for photovoltaic applications. **Journal of Physical Chemistry Letters**, Washington, v. 4, n. 17, p. 2999–3005, 2013.

193 ZHU, H.; ERBING, A.; WU, H.; MAN, G. J.; MUKHERJEE, S.; KAMAL, C.; JOHANSSON, M. B.; RENSMO, H.; ODELIUS, M.; JOHANSSON, E. M. J. Tuning the bandgap in silver bismuth iodide materials by partly substituting bismuth with antimony for improved solar cell performance. **ACS Applied Energy Materials**, Washington, v. 3, n. 8, p. 7372–7382, 2020.

194 WANG, Z.; ZHANG, Z.; TAO, L.; SHEN, N.; HU, B.; GONG, L.; LI, J.; CHEN, X.; HUANG, X. Hybrid chloroantimonates(III): Thermally induced triple-mode reversible luminescent switching and laser-printable rewritable luminescent paper. **Angewandte Chemie International Edition**, Weinheim, v. 58, n. 29, p. 9974–9978, 2019.

195 WEI, J.-H.; LIAO, J.-F.; ZHOU, L.; LUO, J.-B.; WANG, X.-D.; KUANG, D.-B. Indium-antimony-halide single crystals for high-efficiency white-light emission and anti-counterfeiting. **Science Advances**, Washington, v. 7, n. 34, 2021.

196 MCCALL, K. M.; BENIN, B. M.; WÖRLE, M.; VONDERACH, T.; GüNTHER, D.; KOVALENKO, M. V. Expanding the 0D $Rb_7M_3X_{16}$ (M = Sb, Bi; X = Br, I) family: Dual-band luminescence in $Rb_7Sb_3Br_{16}$. **Helvetica Chimica Acta**, Weinheim, v. 104, n. 1, p. e2000206, 2021.

197 HAN, L.; WANG, P.; WANG, Z.; LIU, Y.; ZHENG, Z.; CHENG, H.; HUANG, B. Zero-dimensional hydrazine iodobismuthate as a lead-free perovskite-like light absorber in a self-powered photodetector. **Journal of Alloys and Compounds**, Amsterdam, v. 893, p. 162347, 2022.

198 ADONIN, S. A.; SOKOLOV, M. N.; FEDIN, V. P. Polynuclear halide complexes of Bi(III): from structural diversity to the new properties. **Coordination Chemistry Reviews**, Amsterdam, v. 312, p. 1–21, 2016.

199 SILVEIRA, J. F. R. V.; DA SILVA, J. L. F. Mixed halide lead-free double perovskite alloys for band gap engineering. **ACS Applied Energy Materials**, Washington, v. 3, n. 8, p. 7364–7371, 2020.

200 DA SILVA, J. L. F. Effective coordination concept applied for phase change $(GeTe)_m(Sb_2Te_3)_n$ compounds. **Journal of Applied Physics**, New York, v. 109, n. 2, p. 023502, 2011.

201 ROBINSON, K.; GIBBS, G. V.; RIBBE, P. H. Quadratic elongation: a quantitative measure of distortion in coordination polyhedra. **Science**, Washington, v. 172, n. 3983, p. 567–570, 1971.

202 CHEN, D.; DAI, F.; HAO, S.; ZHOU, G.; LIU, Q.; WOLVERTON, C.; ZHAO, J.; XIA, Z. Crystal structure and luminescence properties of lead-free metal halides $(C_6H_5CH_2NH_3)_3MBr_6$ (M = Bi and Sb). **Journal of Materials Chemistry C**, Cambridge, v. 8, n. 22, p. 7322–7329, 2020.

203 BAUR, W. H. The geometry of polyhedral distortions. predictive relationships for the phosphate group. **Acta Crystallographica Section B**, Chichester, v. 30, n. 5, p. 1195–1215, 1974.

APPENDIX A – TIN-BASED PEROVSKITES

A.1 Convergence Test

We performed many tests to get the converged computational parameters of the $A\mathrm{SnI_3}$ perovskites. We selected cubic and orthorhombic structures of $\mathrm{MASnI_3}$ perovskite to analyze the **k**-point density and cutoff-energy convergence. Further, we analyzed the effects of modifying these parameters in the structural properties, i.e., lattice parameters, volume, bond lengths and octahedra distortions.

Figure 25 – a) Different representation of the initial non-optimized cubic $\mathrm{CH_3NH_3SnI_3}$ structure employed on our **k**-points density analyses. Each octahedral of the corner are equivalent, thus each one contributes with $\frac{1}{8}$ for the single cell. The picture shows different projections of the C−N bond length of the organic cation in the cage formed by octahedra. b) Orthorhombic $\mathrm{CH_3NH_3SnI_3}$ perovskite structure.

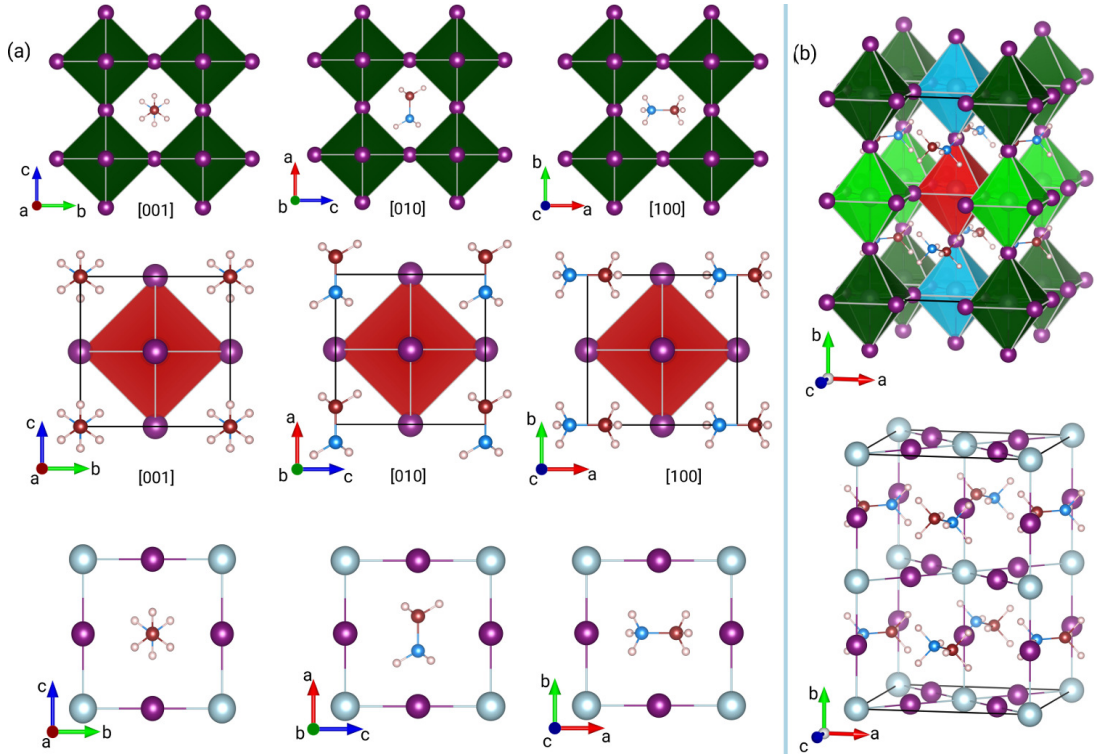

Source: **Source:** Done by Mailde S. Ozório

The initial non-optimized cubic phase ($a_0 = 6.30\,\text{Å}$) of $\mathrm{CH_3NH_3SnI_3}$ displays a C−N bond orientation parallel to the [001] and [010] lattice planes, and perpendicular to the [100]. The $\mathrm{SnI_6}^{4-}$ octahedron is perfect, i.e., six iodide ions occupy the vertices, which are 3.15 Å distanced from the octahedron center where is localized the tin cation. The length of octahedron diagonal is a direct measurement of the lattice parameter of cubic

Table 11 – Cubic $CH_3NH_3SnI_3$ perovskites optimization: **k**-points density (KD), **k**-points mesh (KM), number of **k**-points (NK), volume (V), cubic volume (a_0^c), lattice parameters (a_0, b_0, c_0), cubic deviation (CD) and the relative deviation (considering all significant numbers) of parameters in relation to the highest **k**-points density.

	KD	KM	NK	V ($Å^3$)	ΔV (%)	a_0^c (Å)	Δa_0^c (%)	CD (Å)	Δ CD (%)	a_0 (Å)	Δa_0 (%)	b_0 (Å)	Δb_0 (%)	c_0 (Å)	Δc_0 (%)
NBANDS = 32	10	$1 \times 2 \times 1$	2	242.66	−8.48	6.24	−2.91	1.96	715.91	5.98	−10.60	6.79	4.90	5.97	7.98
	20	$3 \times 3 \times 3$	10	253.05	−4.56	6.33	−1.54	0.08	−68.33	6.30	−3.15	6.30	−0.57	6.38	−0.88
	30	$5 \times 5 \times 5$	39	263.37	−0.67	6.41	−0.22	0.23	−6.46	6.49	−0.30	6.33	−0.05	6.41	−0.31
	40	$6 \times 6 \times 6$	80	267.32	0.82	6.44	0.27	0.26	8.78	6.53	0.38	6.35	0.28	6.44	0.17
	50	$8 \times 8 \times 8$	170	266.36	0.46	6.43	0.15	0.25	3.92	6.52	0.20	6.35	0.16	6.44	0.10
	60	$9 \times 9 \times 9$	205	265.80	0.25	6.43	0.08	0.25	2.12	6.51	0.11	6.35	0.14	6.43	0.00
	70	$11 \times 11 \times 11$	366	265.51	0.14	6.43	0.05	0.24	0.31	6.51	0.05	6.35	0.18	6.43	−0.09
	80	$12 \times 13 \times 12$	518	265.14	0.00	6.42	0.00	0.24	0.00	6.50	0.00	6.34	0.00	6.43	0.00
NBANDS = 50	10	$1 \times 2 \times 1$	2	242.67	−8.31	6.24	−2.85	0.81	237.31	5.98	−8.05	6.78	7.04	5.98	−6.84
	20	$3 \times 3 \times 3$	10	253.27	−4.31	6.33	−1.46	0.16	−34.30	6.29	−3.19	6.31	−0.47	6.38	−0.68
	30	$5 \times 5 \times 5$	39	262.83	−0.70	6.41	−0.23	0.21	−11.54	6.48	−0.37	6.33	−0.11	6.41	−0.22
	40	$6 \times 6 \times 6$	80	267.07	0.91	6.44	0.30	0.25	3.66	6.52	0.34	6.35	0.26	6.44	0.30
	50	$8 \times 8 \times 8$	170	266.09	0.54	6.43	0.18	0.25	3.44	6.52	0.22	6.34	0.10	6.44	0.21
	60	$9 \times 9 \times 9$	205	265.69	0.39	6.43	0.13	0.25	3.57	6.51	0.17	6.35	0.14	6.43	0.07
	70	$11 \times 11 \times 11$	366	266.45	0.67	6.43	0.25	0.25	4.55	6.52	0.28	6.35	0.20	6.44	0.19
	80	$12 \times 13 \times 12$	518	264.67	0.00	6.42	0.00	0.24	0.00	6.50	0.00	6.34	0.00	6.42	0.00

Source: Reprinted from OZÓRIO, M.S.; SRIKANTH, M.; BESSE, R.; DA SILVA, J. L. F. **Physical Chemistry Chemical Physics**, v. 23, n.3, p. 2286–2297, 2021[129]

structure ($a_0 = 6.30\,Å$), i.e., the distance between two adjacent tin cations (Sn–I–Sn) is equivalent to the distance of two non-adjacent iodide ions of octahedron, I–Sn–I. Thus, any deviation in the octahedral I–Sn–I ideal bond lengths (for example, tin out-off center) and diagonal angles (different of 180°) will have a direct effect in the lattice parameters, bond lengths, angles as well as in other structural properties, such as the volume of the unit cell.

Using the cubic structure as reference, we increased the **k**-points from $10\,Å^{-1}$ until 80 Å using the VASP default NBANDS (32), and NBANDS = 50 (total number of valence electrons). As summarized in Table 11, Figure 26 and Figure 27, for a better comprehension of results, among other properties, we compare volume, lattice parameters, and cubic deviations (defined as $CD = |a_0 - b_0| + |a_0 - c_0|$).

Due to the small difference in the structural parameters obtained with NBANDS ≈ 50 and the default value of 32, we concluded that the default value is sufficient for our analyses. Hence, we considered the default NBANDS of the orthorhombic phase to perform its **k**-points convergence test. We employed a perfect orthorhombic *Pnma* (nº 62) perovskite ($a_0 = 9.0\,Å$, $b_0 = 13.1\,Å$, $c_0 = 9.5\,Å$), where the b_0 parameter corresponds twice the octahedral diagonal (d), which are related with a_0 and c_0 lattice parameters by $2d = \sqrt{a_0^2 + c_0^2}$. Thus, since d represents the distance of two non-adjacent iodide atoms of

Figure 26 – PBE results for cubic $CH_3NH_3SnI_3$ perovskite: volume, lattice parameters, and relative cubic deviation in relation to the values found with the highest **k**-points density.

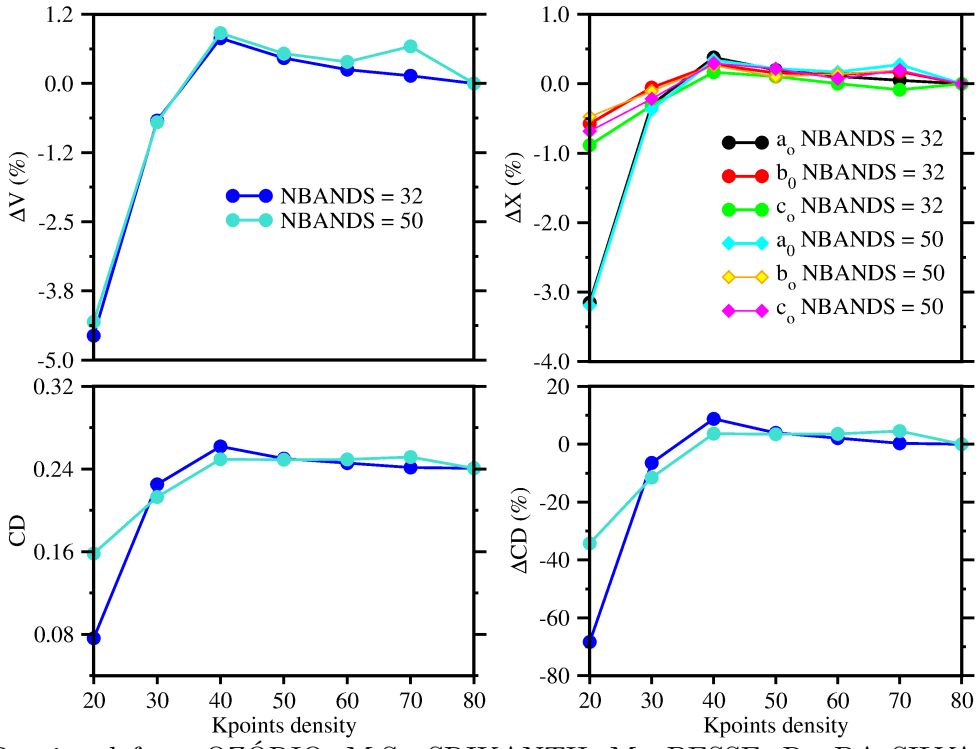

Source: Reprinted from OZÓRIO, M.S.; SRIKANTH, M.; BESSE, R.; DA SILVA, J. L. F. **Physical Chemistry Chemical Physics**, v. 23, n.3, p. 2286–2297, 2021[129]

Figure 27 – PBE results for cubic $CH_3NH_3SnI_3$: relative total energy in relation to the energy found with highest **k**-points density.

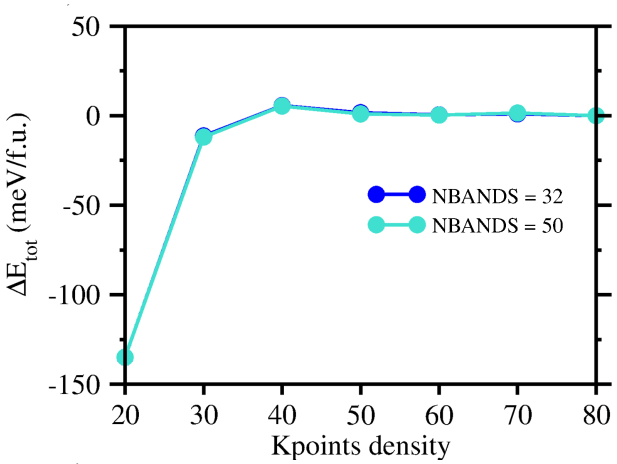

Source: Reprinted from OZÓRIO, M.S.; SRIKANTH, M.; BESSE, R.; DA SILVA, J. L. F. **Physical Chemistry Chemical Physics**, v. 23, n.3, p. 2286–2297, 2021[129]

the octahedron (I–Sn–I diagonal), any angular deviation from 180° and also distortions of I–Sn–I bond length will have a domino effect on the lattice parameters, volume, and other structural properties. To perform the **k**-points convergence test of this orthorhombic

Table 12 – Orthorhombic $CH_3NH_3SnI_3$ perovskites optimization: **k**-points density (KD), **k**-points mesh (KM), Number of **k**-points (NK), volume (V), lattice parameters, and the relative deviation (considering all significant numbers) of aforementioned parameters in relation to the highest **k**-pints density.

KD	KM	NK	V (Å^3)	ΔV (%)	a_0 (Å)	Δa_0 (%)	b_0 (Å	Δb_0 (%)	c_0 (Å)	Δc_0 (%)
10	$1\times1\times1$	1	1025.71	3.49	9.29	1.23	13.27	4.87	8.32	−2.52
20	$2\times2\times2$	8	996.53	0.54	9.17	−0.08	12.70	0.42	8.55	0.19
30	$3\times2\times4$	12	993.22	0.21	9.18	−0.03	12.69	0.31	8.53	−0.07
40	$4\times3\times5$	18	991.50	0.04	9.17	−0.07	12.66	0.09	8.54	0.02
50	$5\times4\times6$	36	991.01	−0.01	9.18	0.06	12.66	0.09	8.52	−0.16
60	$7\times5\times7$	48	991.13	0.00	9.18	0.00	12.65	0.00	8.54	0.00

Source: Reprinted from OZÓRIO, M.S.; SRIKANTH, M.; BESSE, R.; DA SILVA, J. L. F. **Physical Chemistry Chemical Physics**, v. 23, n.3, p. 2286–2297, 2021[129]

structure, we increased in 10 $Å^{-1}$ the **k**-points density from 10 $Å^{-1}$ to 60 $Å^{-1}$. The results of the **k**-point density of the orthorhombic structure are in Table 12.

As summarized in Tables 13 and 14, in addition to the **k**-points analysis indicated in Tables 11 and 12, we also evaluated the octahedra distortions, average length and standard deviation of the three most important H···I interactions involving the hydrogen atoms of $-CH_3$ and $-NH_3^+$ groups, and the following properties:

1. Tin effective coordination number: the effective coordination number (ECN) concept[200] was applied to account the effective number of iodide ions surrounding the Sn-cations in $A SnI_3$ perovskites, ECN^{Sn}. Hence, the following equation was applied:

$$ECN^{Sn} = \sum_j \exp\left[1-\left(\frac{d_{ij}}{d^i_{av}}\right)^6\right], \qquad d^i_{av} = \frac{\sum_j d_{ij}\exp\left[1-\left(\frac{d_{ij}}{d_{\min}}\right)^6\right]}{\sum_j \exp\left[1-\left(\frac{d_{ij}}{d_{\min}}\right)^6\right]}, \tag{A.1}$$

where d_{ij} represent each Sn−I bond length of SnI_6 octahedra, the d^i_{av} represent a weighted average bond length, and $d_{\min}$ the smallest Sn−I bond-length among all six present in the SnI_6 moeity.

2. Bond angle variance: the bond angle variance (BAV) was applied to characterize the changes of ISnI angles in each SnI_6 octahedra. As proposed by Robinson *et al.*,[201] the BAV values were obtained by the following equation:

$$\mathrm{BAV} = \frac{1}{n-1}\sum_{i=1}^{n}(\phi_i-\phi_0)^2, \qquad \mathrm{BAV} = \sum_{i=1}^{12}\frac{(\phi_i-90°)^2}{11} \tag{A.2}$$

where n is the number of faces multiplied by 3/2, thus in the octahedron $n = 12$, which is the total number of ϕ_i angles involving the tin cation and two adjacent iodide atoms, I−Sn−I. For a perfect octahedron $\phi_0 = 90°$.

3. Distortion Index: the Distortion Index (DI)[203] comes from the following

equation:

$$\mathrm{DI} = \frac{1}{6}\sum_{i=1}^{6}\frac{|d_{ij} - d_{av}^{i}|}{d_{av}^{i}} \ , \tag{A.3}$$

where d_{ij} represent the distance from Sn-cation to the ith iodide ion of SnI_6 octahedra, while d_{av} represent the average of Sn−I bond length.

Table 13 – Cubic $CH_3NH_3SnI_3$ perovskites optimization: relative total energy (ΔE_{tot}), average ($d^{N}_{\mathrm{I-H}}$) and standard deviation ($\sigma^{N}_{\mathrm{I-H}}$) of stronger hydrogen bond of $-NH_3{}^{+}$ group, average ($d^{C}_{\mathrm{I-H}}$) and standard deviation ($\sigma^{C}_{\mathrm{I-H}}$) of stronger hydrogen bond of $-CH_3$ group, difference of the average hydrogen bonds of $-NH_3{}^{+}$ and $-CH_3$ ($\Delta d_{\mathrm{I-H}}$), effective coordination number ($\mathrm{ECN}^{\mathrm{Sn}}$), average ($d^{\mathrm{Sn-I}}_{av}$) and standard deviation of Sn−I bond lengths ($\sigma^{\mathrm{Sn-I}}$), octahedra diagonal I–Sn–I angle (Θ) and standard deviation (σ^{Θ}), adjacent I–Sn–I angle (θ) and standard deviation (σ^{θ}), distortion index (DI), and bond angle variance (BAV).

	KD	ΔE_{tot}	$d^{N}_{\mathrm{I-H}}$	$\sigma^{N}_{\mathrm{I-H}}$	$d^{C}_{\mathrm{I-H}}$	$\sigma^{C}_{\mathrm{I-H}}$	$\Delta d_{\mathrm{I-H}}$	$\mathrm{ECN}^{\mathrm{Sn}}$	$d^{\mathrm{Sn-I}}_{av}$	$\sigma^{\mathrm{Sn-I}}$	Θ	σ^{Θ}	θ	σ^{θ}	DI	BAV
	($\mathrm{Å}^{-1}$)	(meV)	(Å)	(Å)	(Å)	(Å)	(Å)	(NNN)	(Å)	(Å)	(deg.)	(deg.)	(deg.)	(deg.)	-	$(\mathrm{deg.})^2$
NBANDS = 32	10	−2452.15	2.82	0.29	3.24	0.25	0.43	5.22	3.13	0.21	178.27	2.03	90.00	1.25	0.06	1.56
	20	−134.90	2.69	0.06	3.41	0.01	0.72	5.91	3.16	0.07	175.70	0.96	89.99	2.28	0.02	5.21
	30	−11.31	2.69	0.06	3.53	0.03	0.84	5.05	3.21	0.21	171.69	4.14	89.85	4.70	0.05	22.09
	40	5.60	2.69	0.08	3.52	0.10	0.83	4.76	3.23	0.24	171.11	4.69	89.82	5.07	0.06	25.77
	50	1.69	2.68	0.08	3.52	0.10	0.83	4.84	3.23	0.23	171.27	4.27	89.84	4.93	0.05	24.30
	60	0.43	2.69	0.07	3.52	0.08	0.84	4.88	3.23	0.23	171.25	4.20	89.84	4.93	0.05	24.30
	70	1.05	2.69	0.07	3.51	0.08	0.82	4.88	3.22	0.23	171.23	4.36	89.83	4.96	0.05	24.63
	80	0.00	2.69	0.06	3.55	0.05	0.86	4.91	3.22	0.23	171.03	4.08	89.83	5.02	0.05	25.18
NBANDS = 50	10	−2463.64	2.79	0.27	3.27	0.27	0.48	5.23	3.13	0.21	177.40	3.15	90.01	1.91	0.06	3.64
	20	−134.85	2.69	0.06	3.41	0.01	0.72	5.92	3.17	0.06	175.98	0.66	89.99	2.12	0.02	4.48
	30	−11.93	2.69	0.06	3.53	0.03	0.84	5.09	3.21	0.20	171.55	4.11	89.85	4.76	0.04	22.66
	40	5.35	2.69	0.08	3.51	0.11	0.82	4.77	3.23	0.24	170.92	4.50	89.82	5.13	0.06	26.39
	50	0.96	2.69	0.07	3.53	0.08	0.84	4.84	3.23	0.23	170.78	4.38	89.82	5.18	0.05	26.90
	60	0.36	2.69	0.08	3.53	0.07	0.83	4.88	3.23	0.23	171.29	4.41	89.83	4.94	0.05	24.41
	70	1.49	2.69	0.08	3.50	0.11	0.81	4.83	3.23	0.23	171.43	4.41	89.84	4.87	0.05	23.76
	80	0.00	2.69	0.06	3.52	0.06	0.83	4.95	3.22	0.22	170.89	4.09	89.84	5.08	0.05	25.79

Source: Reprinted from OZÓRIO, M.S.; SRIKANTH, M.; BESSE, R.; DA SILVA, J. L. F. **Physical Chemistry Chemical Physics**, v. 23, n.3, p. 2286–2297, 2021[129]

Considering the aforementioned results and the computational cost, we considered as converged the **k**-points density of $40\,\mathrm{Å}^{-1}$. Hence, we considered this **k**-points to achieve the converged cutoff energy (ENCUT). Due to a large number of atoms in the orthorhombic structure (4C, 4N, 24H, 4Sn, and 12I), we performed the ENCUT analysis with the cubic structure multiplying the highest ENMAX among all perovskite chemical species by 1.00, 1.25, 1.50, 1.75, 2.00, 2.25, and 2.50. The results for the ENCUT analyses are given in Table 15, Table 16 and Figure 28.

Overall, we can summarize our convergence analysis test as follow:

- The values of pseudo-cubic structure parameters obtained with NBANDS default are very close to that of NBANDS = 50 (twice the number of electrons), which indicates that the default NBANDS is sufficient for structural optimization of $A\mathrm{SnI}_3$

Table 14 – Orthorhombic $CH_3NH_3SnI_3$ perovskites optimization: relative total energy (ΔE_{tot}), average ($d^N_{\mathrm{I-H}}$) and standard deviation ($\sigma^N_{\mathrm{I-H}}$) of stronger hydrogen bond of $-NH_3{}^+$ group, average ($d^C_{\mathrm{I-H}}$) and standard deviation ($\sigma^C_{\mathrm{I-H}}$) of stronger hydrogen bond of $-CH_3$ group, difference of the average hydrogen bonds of $-NH_3{}^+$ and $-CH_3$ ($\Delta d_{\mathrm{I-H}}$), octahedra effective coordination number ($\mathrm{ECN^{Sn}}$), average ($d^{\mathrm{Sn-I}}_{av}$) and standard deviation of Sn–I bond lengths ($\sigma^{\mathrm{Sn-I}}$), octahedra diagonal I–Sn–I angle (Θ) and standard deviation (σ^{Θ}), octahedra adjacent I–Sn–I angle (θ) and standard deviation (σ^{θ}), distortion index (DI), and bond angle variance (BAV).

	KD	ΔE_{tot}	$d^N_{\mathrm{I-H}}$	$\sigma^N_{\mathrm{I-H}}$	$d^C_{\mathrm{I-H}}$	$\sigma^C_{\mathrm{I-H}}$	$\Delta d_{\mathrm{I-H}}$	$\mathrm{ECN^{Sn}}$	$d^{\mathrm{Sn-I}}_{av}$	$\sigma^{\mathrm{Sn-I}}$	Θ	σ^{Θ}	θ	σ^{θ}	DI	BAV
	($\mathrm{Å}^{-1}$)	(meV)	(Å)	(Å)	(Å)	(Å)	(Å)	(NNN)	(Å)	(Å)	(deg.)	(deg.)	(deg.)	(deg.)	-	$(\mathrm{deg.})^2$
NBANDS = 126	10	2718.66	2.68	0.07	3.16	0.02	0.47	5.99	3.32	0.02	180.00	0.00	90.00	8.09	0.00	59.47
	20	166.40	2.64	0.01	3.23	0.13	0.60	6.00	3.21	0.01	180.00	0.00	90.00	2.74	0.00	6.82
	30	51.41	2.65	0.01	3.25	0.12	0.60	6.00	3.20	0.01	180.00	0.00	90.00	2.77	0.00	6.98
	40	5.57	2.65	0.02	3.24	0.13	0.59	6.00	3.20	0.01	180.00	0.00	90.00	2.62	0.00	6.24
	50	1.14	2.66	0.01	3.24	0.11	0.58	6.00	3.20	0.01	180.00	0.00	90.00	2.68	0.00	6.55
	60	0.00	2.66	0.00	3.25	0.11	0.59	6.00	3.20	0.01	180.00	0.00	90.00	2.61	0.00	6.20

Source: Reprinted from OZÓRIO, M.S.; SRIKANTH, M.; BESSE, R.; DA SILVA, J. L. F. **Physical Chemistry Chemical Physics**, v. 23, n.3, p. 2286–2297, 2021[129]

Table 15 – ENCUT analyses (NBANDS default) for cubic hybrid $CH_3NH_3SnI_3$ perovskites optimization: **k**-points mesh (KM), Number of **k**-points (NK), volume (V), cubic volume (a^c_0), lattice parameters (a_0, b_0, b_0), relative total energy (ΔE_{tot}), cubic deviation (CD) and the relative deviation of aforementioned parameters in relation to the highest **k**-pints density.

ENCUT	KM	NK	V	ΔV	a^c_0	Δa^c_0	CD	ΔCD	a_0	Δa_0	b_0	Δb_0	c_0	Δc_0
(eV)			($\mathrm{Å}^3$)	(%)	(Å)	(%)	(Å)	(%)	(Å)	(%)	(Å	(%)	(Å)	(%)
421	$6\times6\times6$	80	243.05	−9.13	6.24	−3.10	0.07	−73.07	6.25	−4.29	6.20	−2.36	6.27	−2.79
526	$6\times6\times6$	80	260.09	−2.76	6.38	−0.93	0.15	−42.31	6.43	−1.53	6.32	−0.47	6.39	−0.93
631	$6\times6\times6$	80	263.33	−1.55	6.41	−0.46	0.24	−0.08	6.49	−0.61	6.33	−0.31	6.41	−0.06
737	$6\times6\times6$	80	266.25	−0.46	6.43	−0.16	0.26	0.00	6.52	−0.15	6.35	0.00	6.43	−0.31
842	$6\times6\times6$	80	267.32	−0.06	6.44	0.00	0.27	3.85	6.53	0.00	6.35	0.00	6.44	−0.16
947	$6\times6\times6$	80	268.21	0.27	6.45	0.16	0.28	7.69	6.54	0.15	6.36	0.16	6.45	0.00
1053	$6\times6\times6$	80	267.48	0.00	6.44	0.00	0.26	0.00	6.53	0.00	6.35	0.00	6.45	0.00

Source: Reprinted from OZÓRIO, M.S.; SRIKANTH, M.; BESSE, R.; DA SILVA, J. L. F. **Physical Chemistry Chemical Physics**, v. 23, n.3, p. 2286–2297, 2021[129]

perovskites. Thus, we used the respective default NBANDS of cubic, tetragonal, orthorhombic, and hexagonal structures.

- Overall, considering the results of the convergence test and computational cost, we considered as converged the value of 40 $\mathrm{Å}^{-1}$ for the **k**-points density, and enough the cutoff energy of 2.00×ENMAX. Hence, we applied a **k**-points density of 40 $\mathrm{Å}^{-1}$ and a cutoff energy of 2.00×ENMAX for all perovskite optimizations.

Table 16 – ENCUT test (NBANDS default) for cubic $CH_3NH_3SnI_3$ perovskites optimization: relative total energy (ΔE_{tot}), average ($d^N_{\mathrm{I-H}}$) and standard deviation ($\sigma^N_{\mathrm{I-H}}$) of stronger hydrogen bond of $-NH_3{}^+$ group, average ($d^C_{\mathrm{I-H}}$) and standard deviation ($\sigma^C_{\mathrm{I-H}}$) of stronger hydrogen bond of $-CH_3$ group, difference of the average hydrogen bonds of $-NH_3{}^+$ and $-CH_3$ ($\Delta d_{\mathrm{I-H}}$), octahedra effective coordination number ($\mathrm{ECN^{Sn}}$), average ($d^{\mathrm{Sn-I}}_{av}$) and standard deviation of Sn–I bond lengths ($\sigma^{\mathrm{Sn-I}}$), octahedra I–Sn–I diagonal angle (Θ), octahedra adjacent I–Sn–I angle (θ), and respective standard deviation (σ^{Θ})/(σ^{θ}), distortion index (DI), and bond angle variance (BAV).

ENCUT	ΔE_{tot}	$d^N_{\mathrm{I-H}}$	$\sigma^N_{\mathrm{I-H}}$	$d^C_{\mathrm{I-H}}$	$\sigma^C_{\mathrm{I-H}}$	$\Delta d_{\mathrm{I-H}}$	$\mathrm{ECN^{Sn}}$	$d^{\mathrm{Sn-I}}_{av}$	$\sigma^{\mathrm{Sn-I}}$	Θ	σ^{Θ}	θ	σ^{θ}	DI	BAV
	(meV)	(Å)	(Å)	(Å)	(Å)	(Å)	(NNN)	(Å)	(Å)	(deg.)	(deg.)	(deg.)	(deg.)	-	$(\mathrm{deg.})^2$
421	208.83	2.67	0.01	3.30	0.02	0.63	5.78	3.13	0.10	171.20	2.40	89.94	4.71	0.02	22.23
526	36.98	2.68	0.07	3.47	0.05	0.79	5.15	3.20	0.19	171.29	4.01	89.85	4.87	0.04	23.75
631	10.70	2.69	0.06	3.53	0.04	0.84	4.99	3.22	0.22	170.87	4.10	89.83	5.09	0.05	25.98
737	4.73	2.69	0.09	3.49	0.11	0.81	4.99	3.22	0.22	171.15	4.65	89.82	5.05	0.05	25.98
842	2.08	2.69	0.08	3.52	0.10	0.83	4.76	3.23	0.24	171.11	4.69	89.82	5.07	0.06	25.77
947	1.93	2.69	0.09	3.51	0.12	0.82	4.69	3.24	0.25	171.28	4.86	89.81	5.02	0.06	25.27
1053	0.00	2.69	0.08	3.53	0.10	0.84	4.75	3.23	0.24	171.07	4.34	89.82	5.04	0.06	25.40

Source: Reprinted from OZÓRIO, M.S.; SRIKANTH, M.; BESSE, R.; DA SILVA, J. L. F. **Physical Chemistry Chemical Physics**, v. 23, n.3, p. 2286–2297, 2021[129]

Figure 28 – Cubic deviation, relative volume, and relative total energy as a function of cutoff energy.

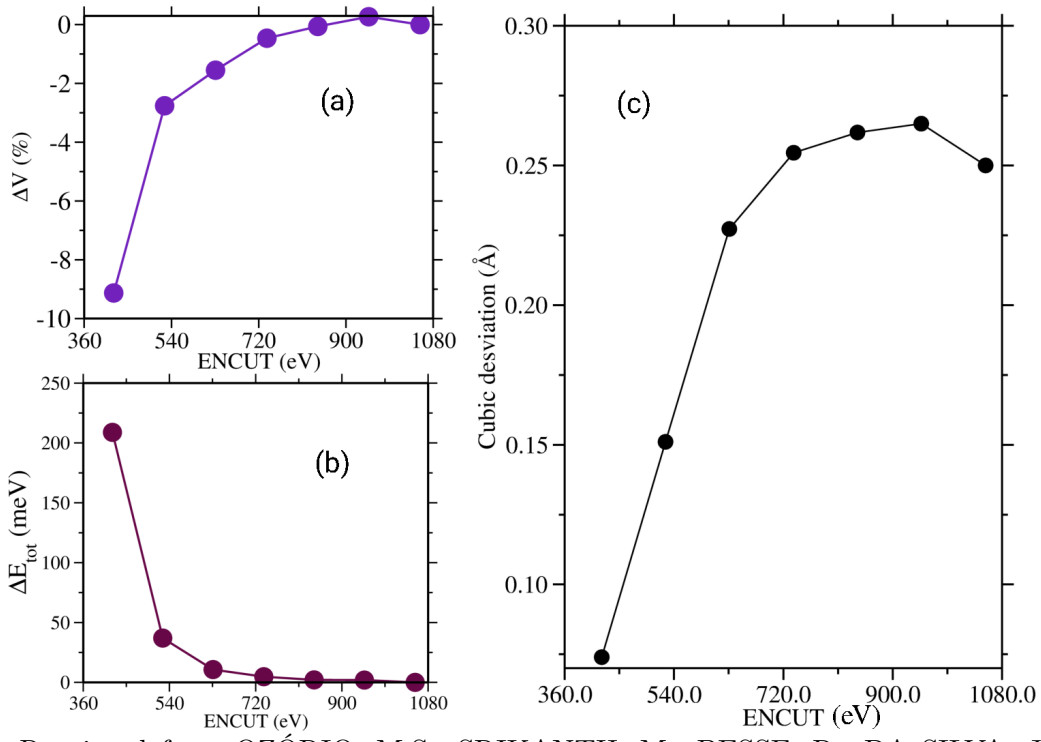

Source: Reprinted from OZÓRIO, M.S.; SRIKANTH, M.; BESSE, R.; DA SILVA, J. L. F. **Physical Chemistry Chemical Physics**, v. 23, p. 2286, 2021[129]

A.2 ASnI$_3$ Perovskites

Table 17 – Structural parameters of the cubic (C), pseudo-cubic (PC), orthorhombic (O), tetragonal (T), hexagonal (H), pseudo-hexagonal (PH) lowest energy phases of ASnI$_3$ perovskites: average ($d^{N/P}_{\mathrm{I-H}}$) and standard deviation ($\sigma^{N/P}_{\mathrm{I-H}}$) of stronger hydrogen bond of $-NH_x{}^+/-PH_3{}^+$ group, average ($d^{C}_{\mathrm{I-H}}$) and standard deviation ($\sigma^{C}_{\mathrm{I-H}}$) of stronger hydrogen bond of $-CH_3$ group, difference of the average hydrogen bonds of $-NH_x{}^+/-PH_3{}^+$ and $-CH_3$ ($\Delta d_{\mathrm{I-H}}$), octahedra effective coordination number (ECN$^{\mathrm{Sn}}$), average ($d^{\mathrm{Sn-I}}_{av}$) and standard deviation of Sn–I bond lengths ($\sigma^{\mathrm{Sn-I}}$), octahedra diagonal I–Sn–I angle (Θ) and standard deviation (σ^{Θ}), octahedra adjacent I–Sn–I angle (θ) and standard deviation (σ^{θ}), distortion index (DI), and bond angle variance (BAV).

	Fase	$d^{N/P}_{\mathrm{I-H}}$ (Å)	$\sigma^{N/P}_{\mathrm{I-H}}$ (Å)	$d^{C}_{\mathrm{I-H}}$ (Å)	$\sigma^{C}_{\mathrm{I-H}}$ (Å)	$\Delta d_{\mathrm{I-H}}$ (Å)	NCE$^{\mathrm{Sn}}$ (NNN)	σ^{NCE} (NNN)	$d^{\mathrm{Sn-I}}_{av}$ (Å)	$\sigma^{\mathrm{Sn-I}}$ (Å)	Θ (deg.)	σ^{Θ} (deg.)	θ (deg.)	σ^{θ} (deg.)	ID (%)	VAL (deg.)^2
MASnI$_3$	CI	2.71	0.05	3.32	0.04	0.61	5.75	0.00	3.14	0.10	171.05	1.81	89.95	4.74	1.93	22.50
	PC	2.71	0.07	3.52	0.40	0.81	5.70	0.00	3.14	0.12	170.75	2.66	89.93	4.97	2.37	24.67
	ORC	2.61	0.05	3.12	0.03	0.51	6.00	0.00	3.16	0.01	180.00	0.00	90.00	2.46	0.21	6.03
	TETR	2.65	0.03	3.18	0.10	0.54	6.00	0.00	3.16	0.01	180.00	0.00	90.00	2.61	0.24	6.79
	PH	2.73	0.15	3.24	0.07	0.51	5.89	0.08	3.20	0.07	176.81	1.79	89.99	3.38	1.49	11.95
MPSnI$_3$	CI	2.93	0.33	3.12	0.27	0.19	5.62	0.00	3.17	0.13	174.75	2.75	89.94	2.98	3.33	8.90
	PC	2.94	0.33	3.13	0.28	0.19	5.53	0.00	3.18	0.15	174.68	4.71	89.91	3.43	2.97	11.79
	ORC	3.02	0.08	3.20	0.04	0.18	5.76	0.08	3.17	0.10	175.13	2.18	89.95	3.79	2.59	15.36
	TETR	3.05	0.02	3.09	0.02	0.04	6.00	0.00	3.16	0.06	180.00	0.00	90.00	1.40	0.33	1.97
	PH	2.89	0.20	3.17	0.23	0.28	5.91	0.04	3.20	0.06	176.84	1.02	90.07	2.91	1.75	9.06
FASnI$_3$	CI	2.78	0.22	3.28	0.00	0.50	5.49	0.00	3.18	0.15	171.13	1.52	90.00	4.67	3.97	21.85
	PC	2.81	0.24	3.22	0.00	0.41	5.21	0.00	3.19	0.21	169.93	2.98	89.93	5.41	4.34	29.27
	ORC	2.77	0.06	3.11	0.00	0.35	5.22	0.00	3.19	0.20	171.63	6.95	89.85	6.94	4.90	48.19
	TETR	3.23	0.27	3.22	0.00	−0.01	5.97	0.00	3.14	0.04	176.69	2.88	90.04	2.12	0.98	4.50
	PH	2.88	0.11	3.15	0.01	0.27	5.73	0.19	3.20	0.11	175.72	2.60	90.00	4.99	2.88	26.07

Source: Reprinted from OZÓRIO, M.S.; SRIKANTH, M.; BESSE, R.; DA SILVA, J. L. F. **Physical Chemistry Chemical Physics**, v. 23, n.3, p. 2286–2297, 2021[129]

Figure 29 – $MASnI_3$ perovskites: bond length of X−H, C−N of *A*-cation and from C and N of to iodide of inorganic framework.

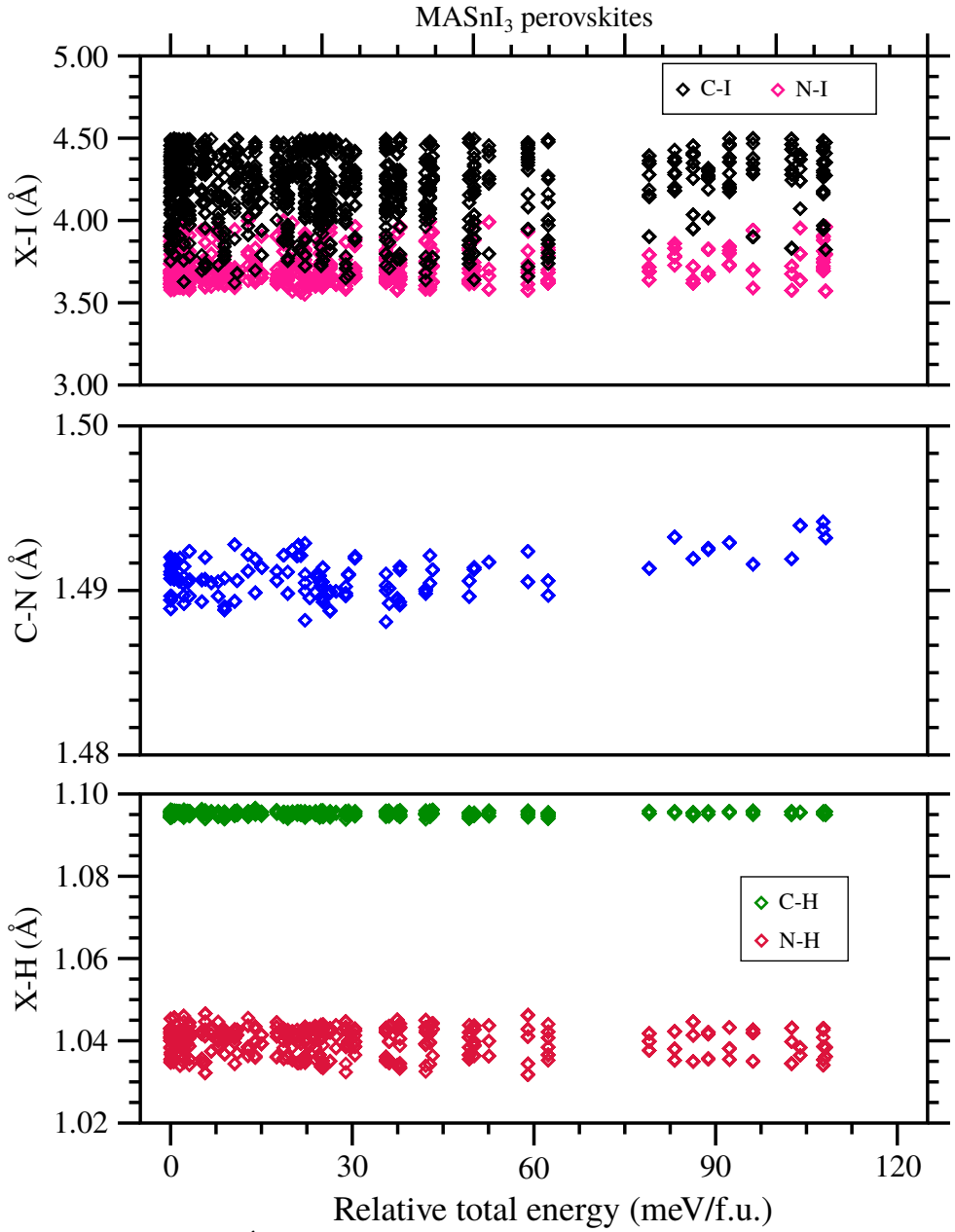

Source: Reprinted from OZÓRIO, M.S.; SRIKANTH, M.; BESSE, R.; DA SILVA, J. L. F. **Physical Chemistry Chemical Physics**, v. 23, n.3, p. 2286–2297, 2021[129]

Figure 30 – $MPSnI_3$ perovskites: bond length of X – H, C – P of *A*-cation and from C and P of to iodide of inorganic framework.

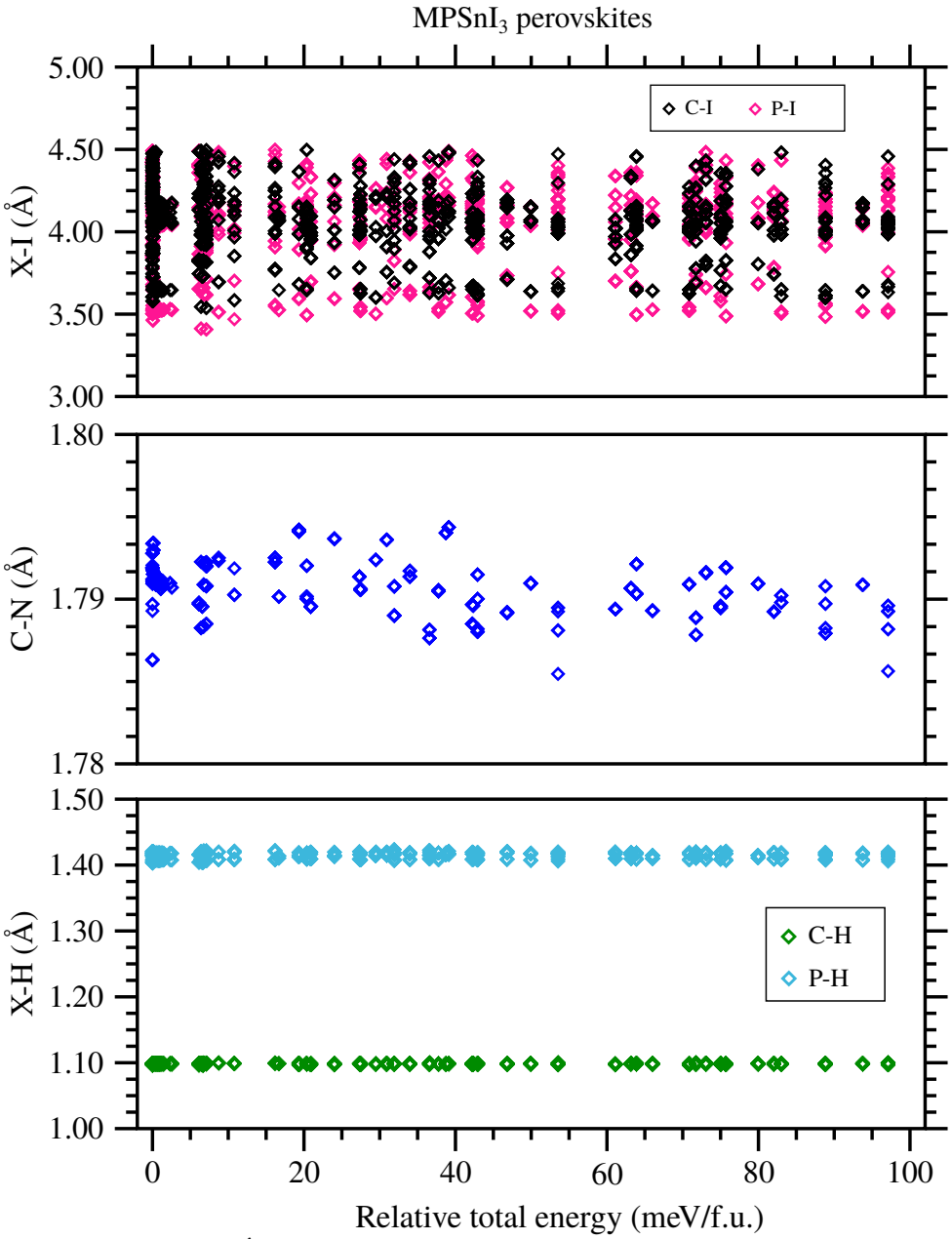

Source: Reprinted from OZÓRIO, M.S.; SRIKANTH, M.; BESSE, R.; DA SILVA, J. L. F. **Physical Chemistry Chemical Physics**, v. 23, n.3, p. 2286–2297, 2021[129]

Figure 31 – $FASnI_3$ perovskites: bond length of X−H, C−N of *A*-cation and from C and N of to iodide of inorganic framework.

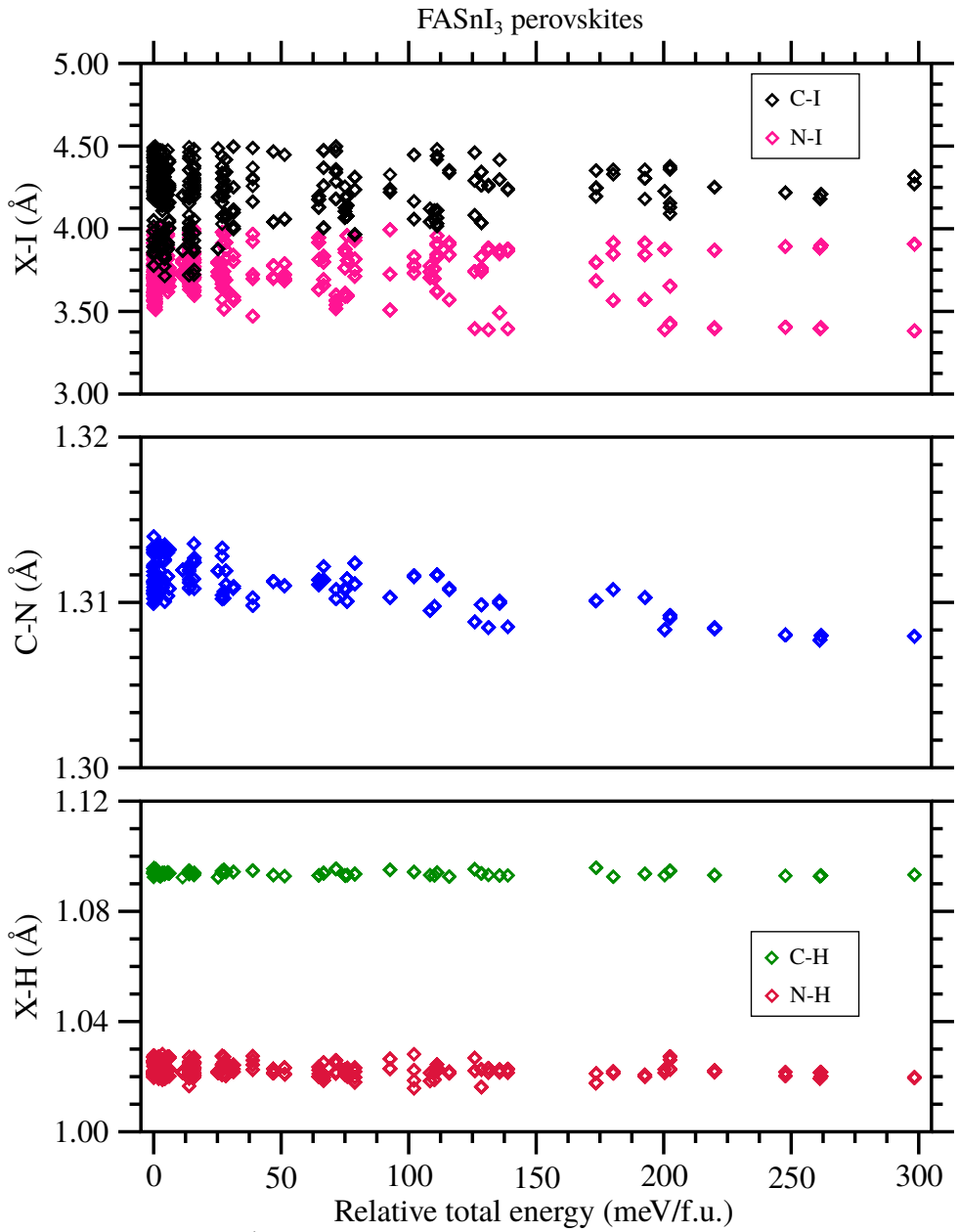

Source: Reprinted from OZÓRIO, M.S.; SRIKANTH, M.; BESSE, R.; DA SILVA, J. L. F. **Physical Chemistry Chemical Physics**, v. 23, n.3, p. 2286–2297, 2021[129]

APPENDIX B – ZERO-DIMENSIONAL PEROVSKITES

B.1 Band Structures

Figure 32 – **k**-path selection for the band structure calculations of a) B_2X_{10}-based and b) BX_6-based zero-dimensional structures.

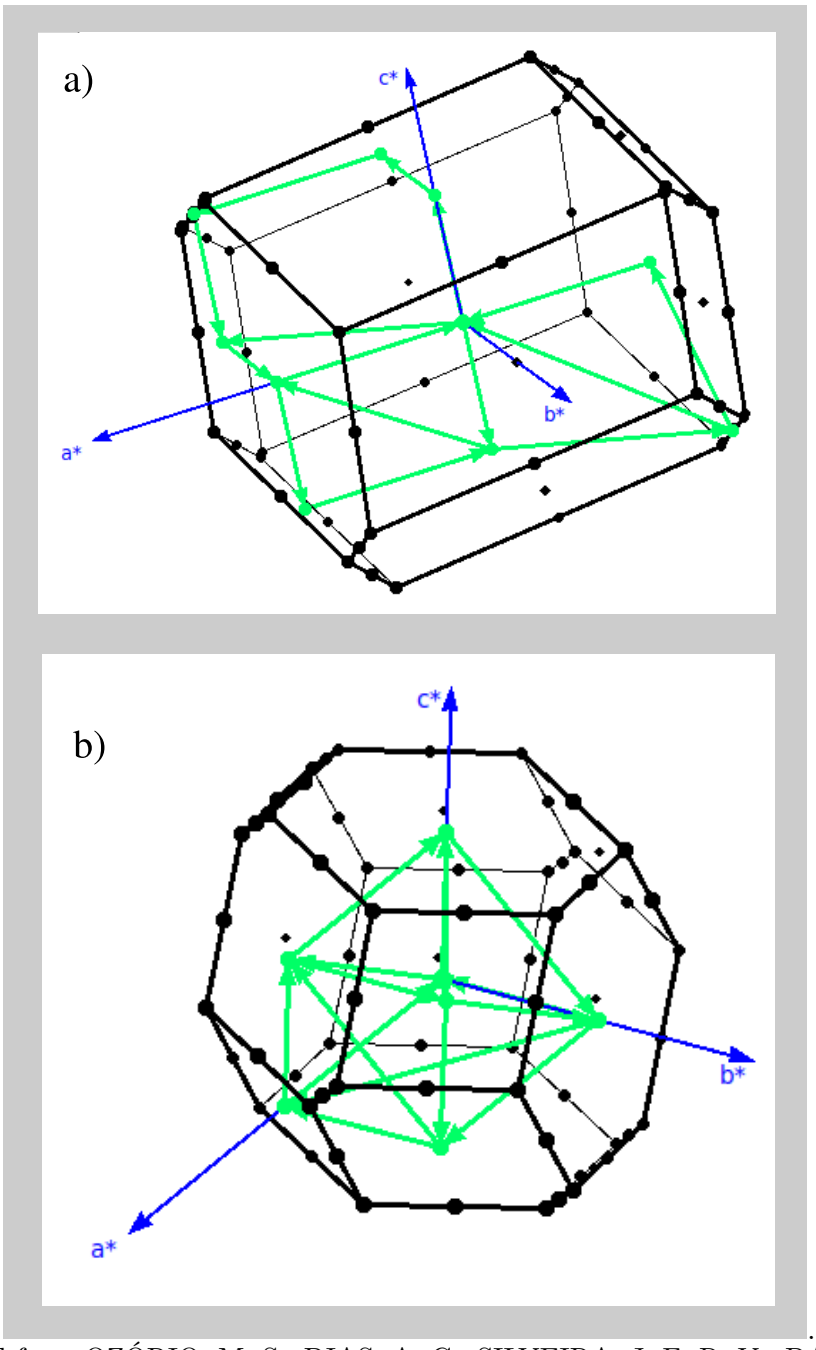

Source: Reprinted from OZÓRIO, M. S.; DIAS, A. C.; SILVEIRA, J. F. R. V.; DA SILVA, J. L. F. **The Journal of Physical Chemistry C**, v. 126, n. 16, p. 7245–7255, 2022.[2]

Figure 33 – Band structure of perovskite $C_{20}H_{20}N_4Bi_2I_{10}$ calculated with PBE+D3. The indirect fundamental bandgap energy is 0.9756 eV with the top of valence band at V point and the bottom of conduction band at R point. The direct fundamental bandgap energy is 1.0143 eV and occurs at R point.

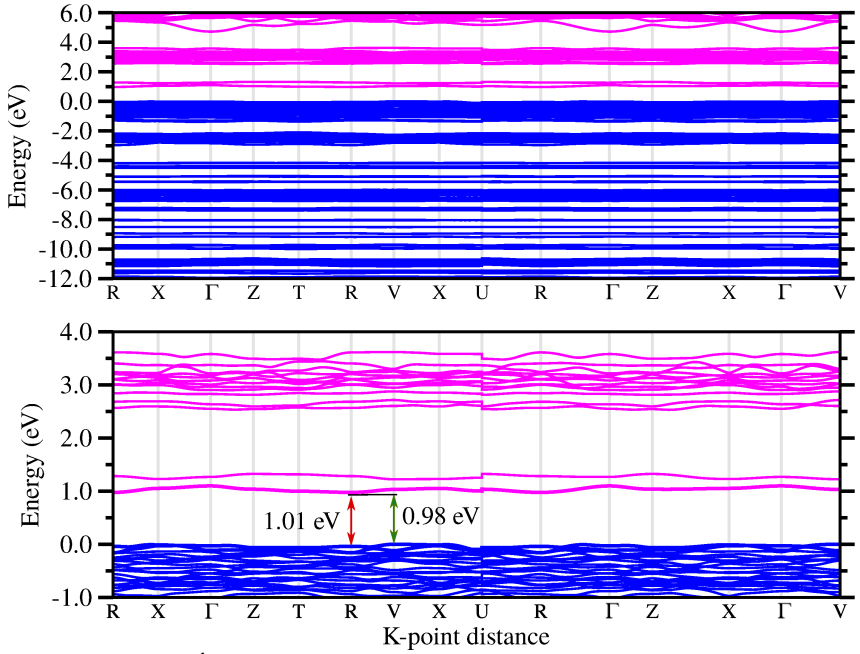

Source: Reprinted from OZÓRIO, M. S.; OLIVEIRA, W. X. C.; SILVEIRA, J. F. R. V.; NOGUEIRA, A. F.; DA SILVA, J. L. F. **Materials Advances**, v. 1, n. 9, p. 3439–3448, 2020[1]

Figure 34 – Band structure of perovskite $C_{42}H_{39}N_6Bi_2I_9$ calculated at PBE+D3 level. The indirect fundamental bandgap energy is 1.53 eV. The top of valence band is at Γ point and the bottom of conduction band in three degenerated points located between the path of Γ and X points. The fundamental direct bandgap energy is 1.53 eV and occurs at Γ point.

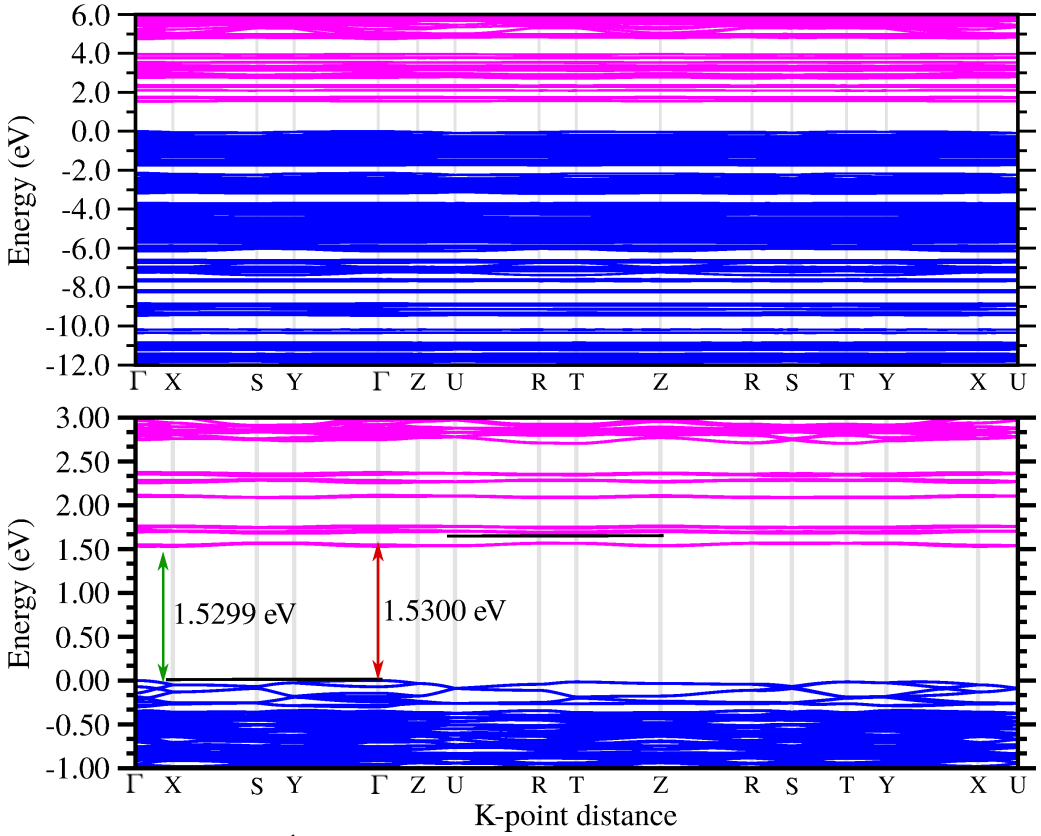

Source: Reprinted from OZÓRIO, M. S.; OLIVEIRA, W. X. C.; SILVEIRA, J. F. R. V.; NOGUEIRA, A. F.; DA SILVA, J. L. F. **Materials Advances**, v. 1, n. 9, p. 3439–3448, 2020[1]

Figure 35 – Band structure of perovskite $C_{30}H_{25}N_6BiI_6 \cdot 2\,H_2O$ calculated with PBE+D3. The direct fundamental bandgap energy is 1.406 eV and occurs at **R** point.

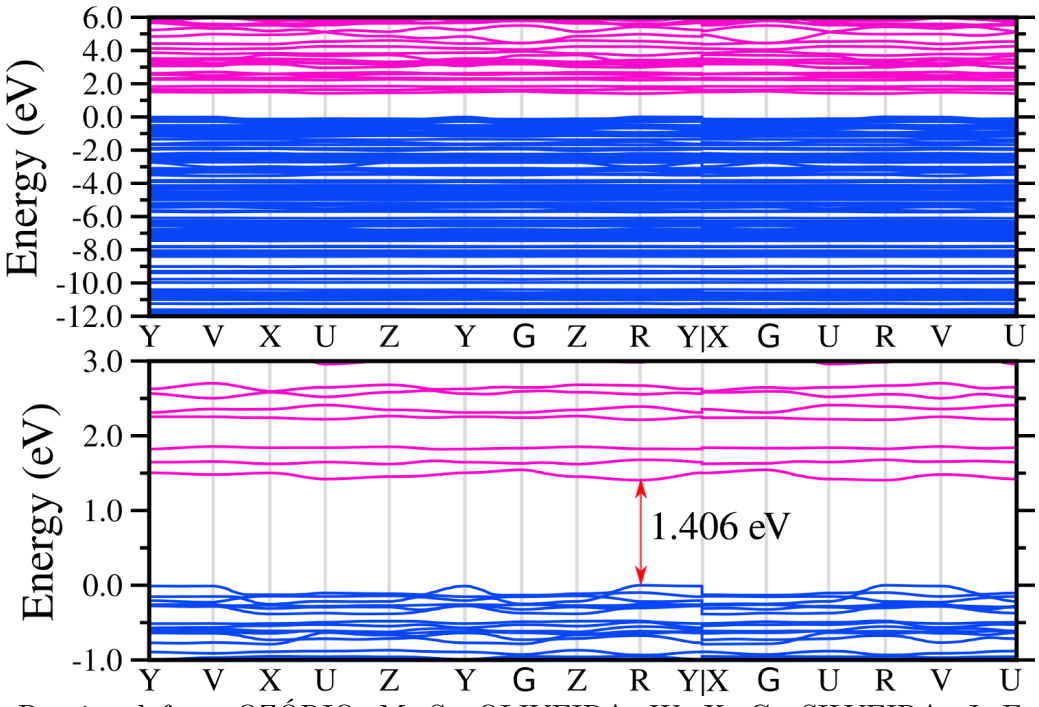

Source: Reprinted from OZÓRIO, M. S.; OLIVEIRA, W. X. C.; SILVEIRA, J. F. R. V.; NOGUEIRA, A. F.; DA SILVA, J. L. F. **Materials Advances**, v. 1, n. 9, p. 3439–3448, 2020[1]

B.2 Density of States

Figure 36 – Total and local density of states for PBE+D3 optimized $C_{20}H_{20}N_4Bi_2I_{10}$ perovskite. The fundamental bandgap energy is 0.9802 eV

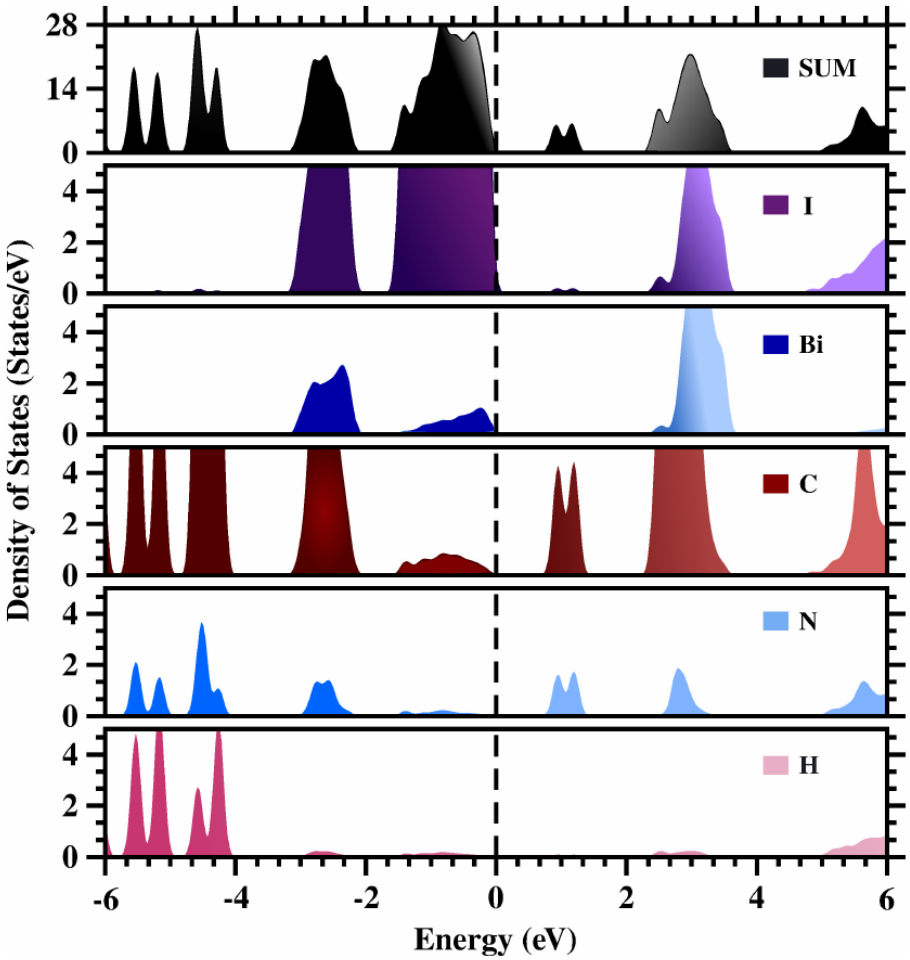

Source: Reprinted from OZÓRIO, M. S.; OLIVEIRA, W. X. C.; SILVEIRA, J. F. R. V.; NOGUEIRA, A. F.; DA SILVA, J. L. F. **Materials Advances**, v. 1, n. 9, p. 3439–3448, 2020[1]

Figure 37 – Total and local density of states for PBE+D3 optimized $C_{42}H_{39}N_6Bi_2I_9$ perovskite. The fundamental bandgap energy is 1.530 eV.

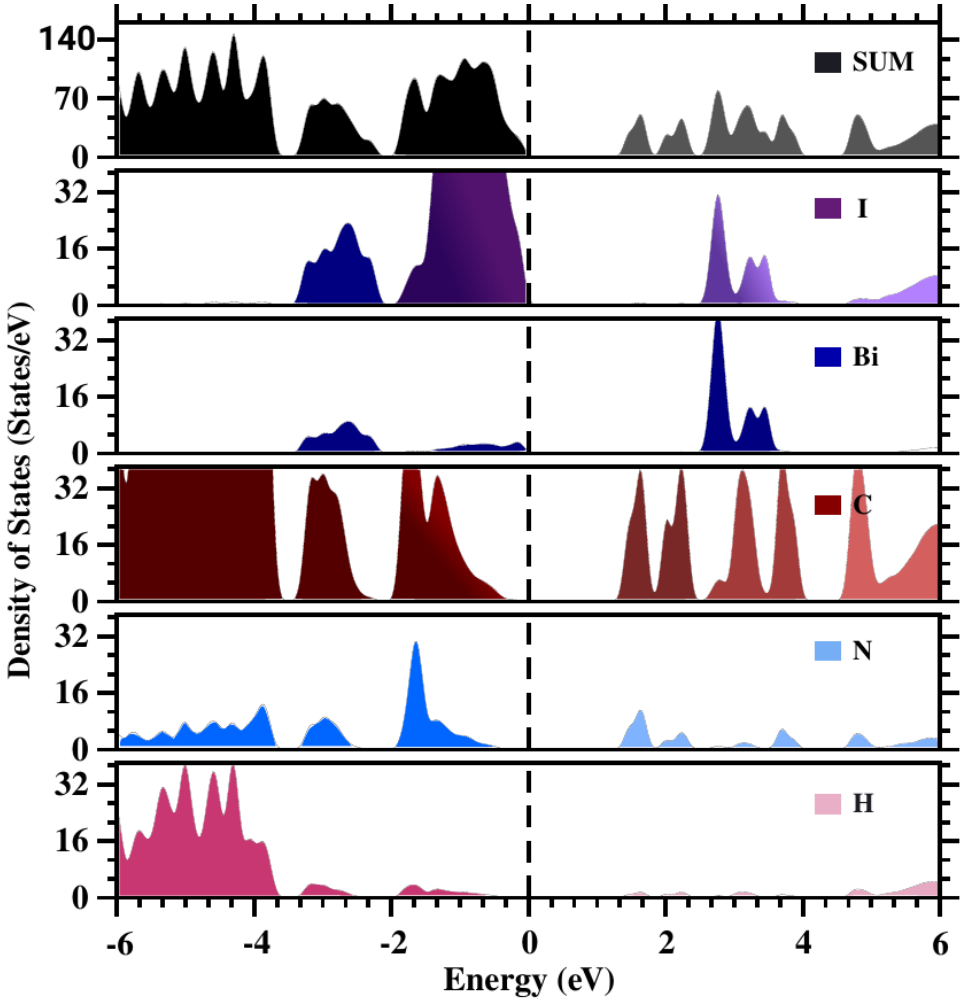

Source: Reprinted from OZÓRIO, M. S.; OLIVEIRA, W. X. C.; SILVEIRA, J. F. R. V.; NOGUEIRA, A. F.; DA SILVA, J. L. F. **Materials Advances**, v. 1, n. 9, p. 3439–3448, 2020[1]

Figure 38 – Total and local density of states for PBE+D3 optimized $C_{30}H_{25}N_6BiI_6 \cdot 2\,H_2O$ perovskite. The fundamental bandgap energy is 1.406 eV.

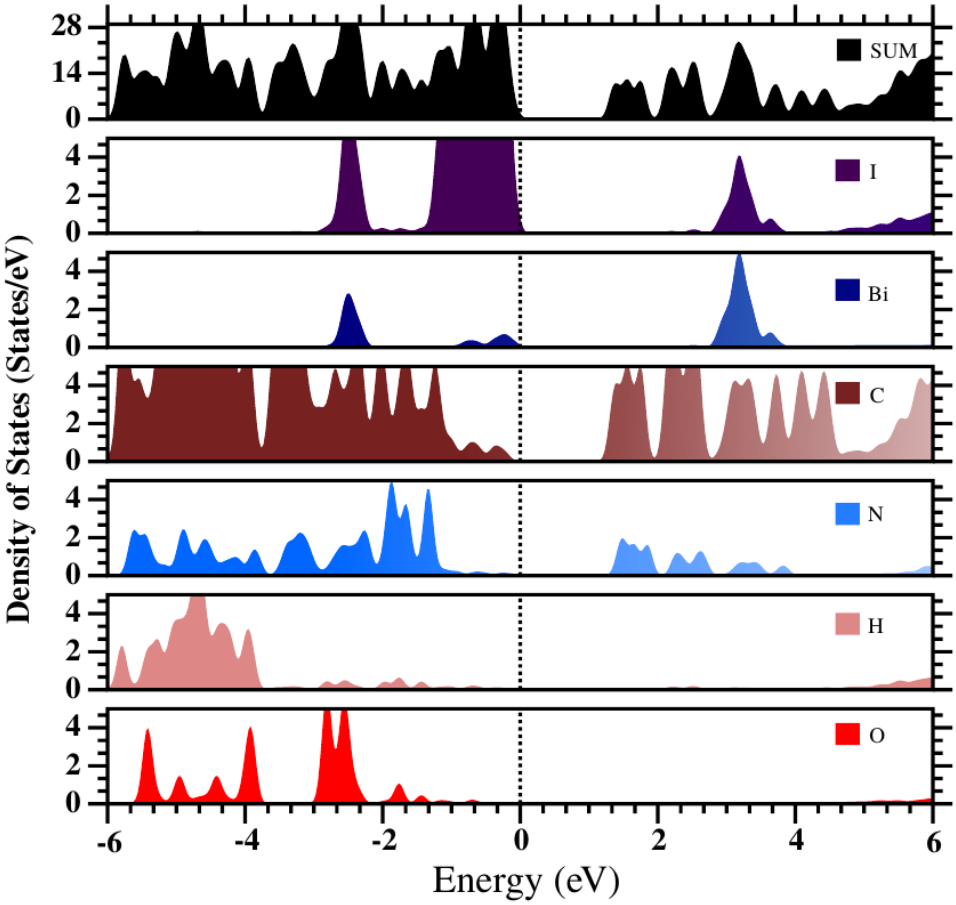

Source: Reprinted from OZÓRIO, M. S.; OLIVEIRA, W. X. C.; SILVEIRA, J. F. R. V.; NOGUEIRA, A. F.; DA SILVA, J. L. F. **Materials Advances**, v. 1, n. 9, p. 3439–3448, 2020[1]

Figure 39 – Density of states calculated with HSE06 for perovskite $C_{20}H_{20}N_4Bi_2I_{10}$. The fundamental bandgap energy is 1.8004 eV

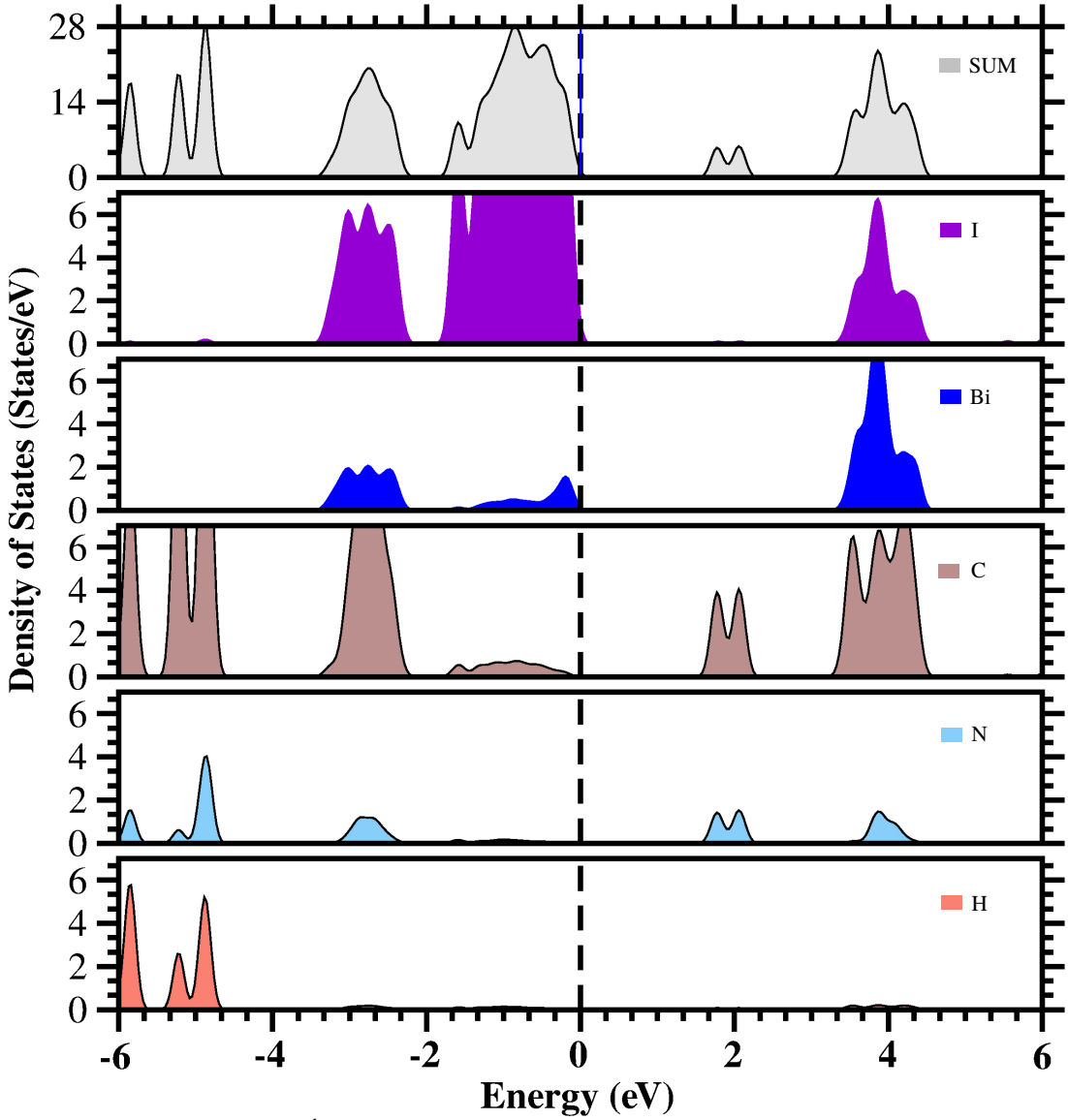

Source: Reprinted from OZÓRIO, M. S.; OLIVEIRA, W. X. C.; SILVEIRA, J. F. R. V.; NOGUEIRA, A. F.; DA SILVA, J. L. F. **Materials Advances**, v. 1, n. 9, p. 3439–3448, 2020[1]

Figure 40 – Density of states obtained with HSE06 for perovskite $C_{42}H_{39}N_6Bi_2I_9$. The fundamental bandgap energy is 2.3525 eV

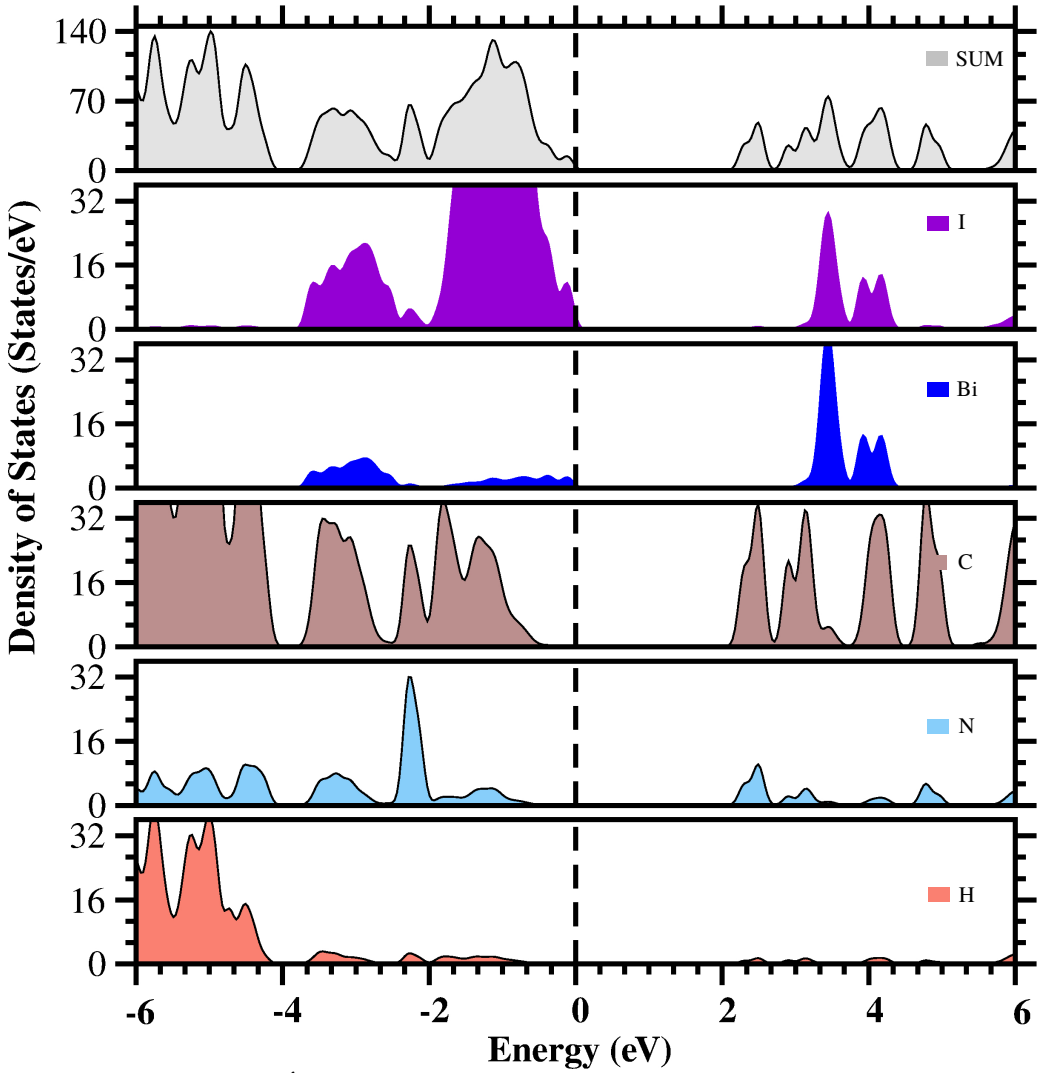

Source: Reprinted from OZÓRIO, M. S.; OLIVEIRA, W. X. C.; SILVEIRA, J. F. R. V.; NOGUEIRA, A. F.; DA SILVA, J. L. F. **Materials Advances**, v. 1, n. 9, p. 3439–3448, 2020[1]

Figure 41 – Density of states obtained with HSE06 for perovskite $C_{30}H_{25}N_6BiI_6 \cdot 2\,H_2O$. The fundamental bandgap energy is 2.24 eV

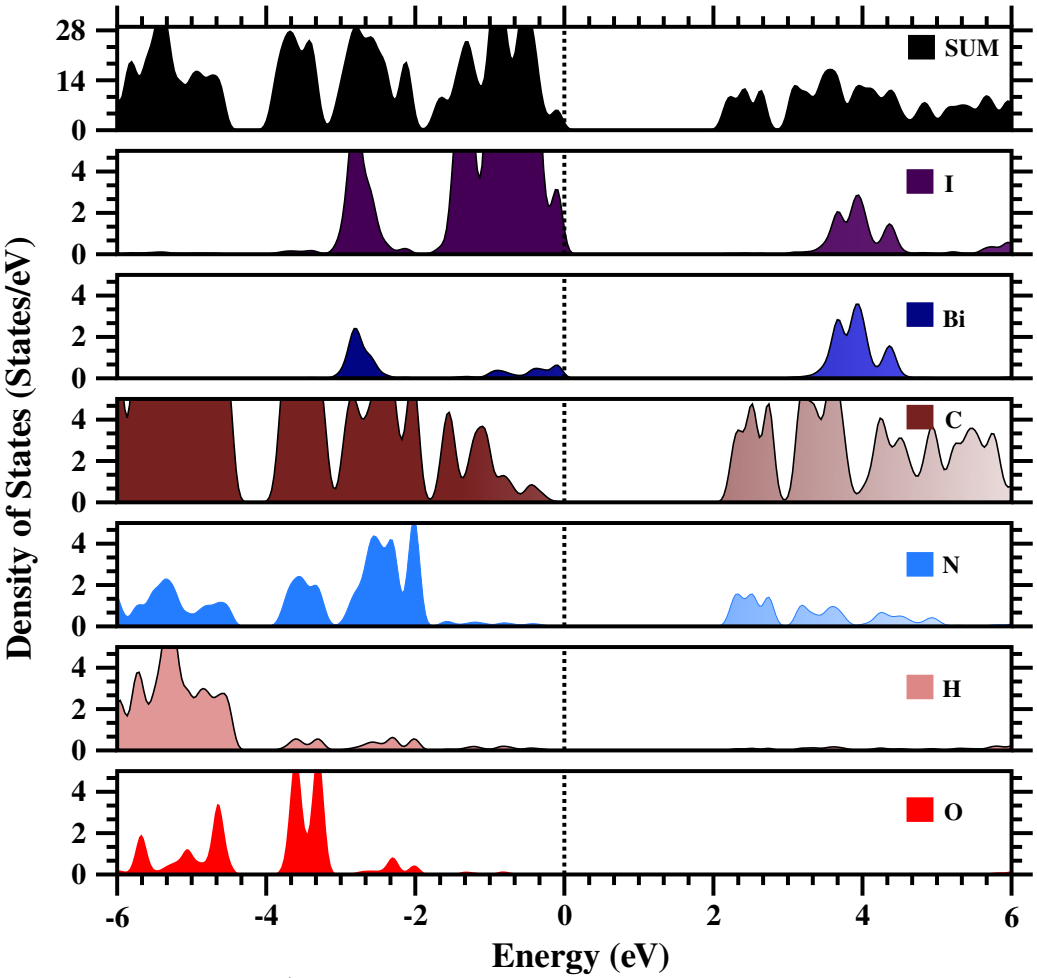

Source: Reprinted from OZÓRIO, M. S.; OLIVEIRA, W. X. C.; SILVEIRA, J. F. R. V.; NOGUEIRA, A. F.; DA SILVA, J. L. F. **Materials Advances**, v. 1, n. 9, p. 3439–3448, 2020[1]

Figure 42 – Local density of states per octahedron unity obtained at PBE+D3 level for the bismuth zero-dimensional perovskites.

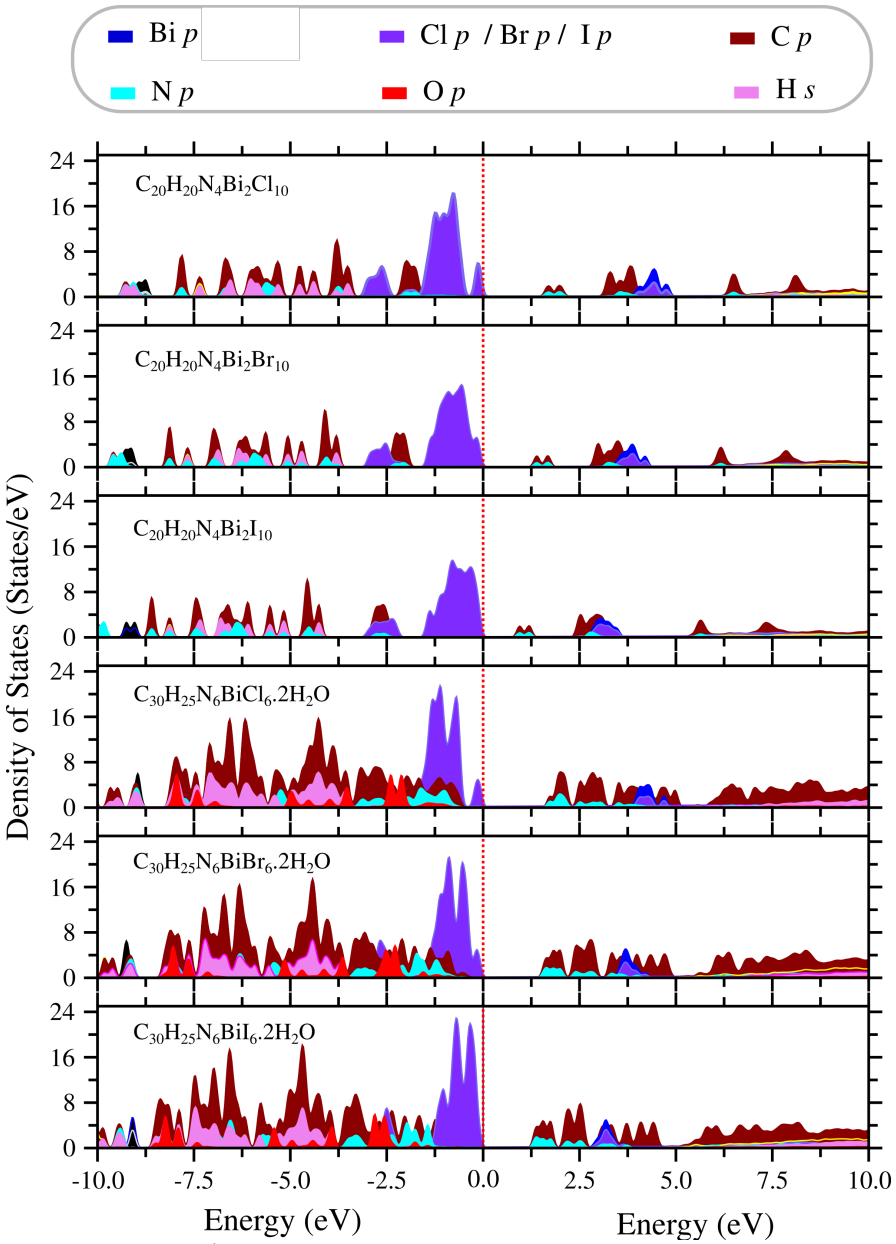

Source: Reprinted from OZÓRIO, M. S.; DIAS, A. C.; SILVEIRA, J. F. R. V.; DA SILVA, J. L. F. **The Journal of Physical Chemistry C**, v. 126, n. 16, p. 7245–7255, 2022.[2]

Figure 43 – Local density of states per octahedron unity obtained at PBE+D3 level for the antimony zero-dimensional perovskites.

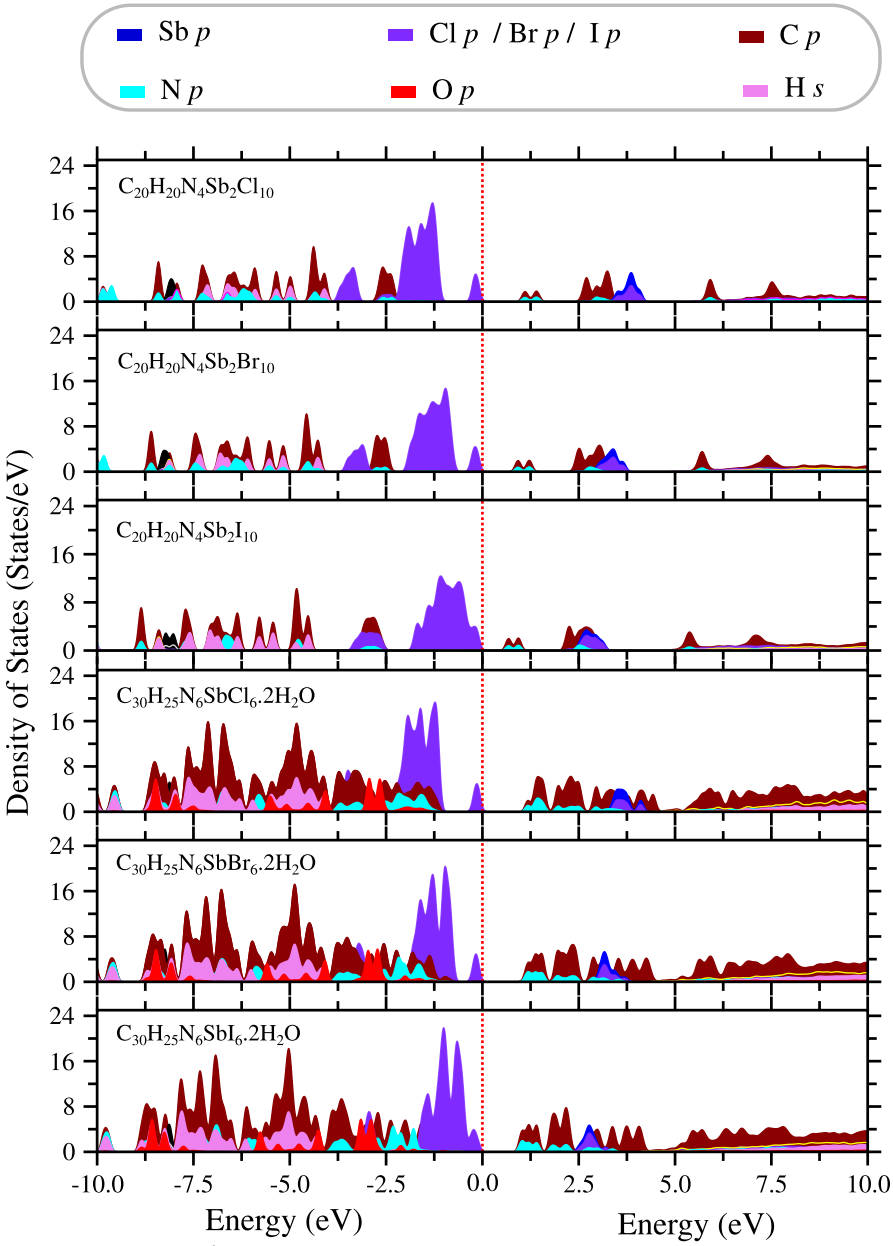

Source: Reprinted from OZÓRIO, M. S.; DIAS, A. C.; SILVEIRA, J. F. R. V.; DA SILVA, J. L. F. **The Journal of Physical Chemistry C**, v. 126, n. 16, p. 7245–7255, 2022.[2]

Figure 44 – Representation of zero-dimensional perovskite structures: $C_{20}H_{20}N_4B_2X_{10}$ and $C_{30}H_{25}N_6BX_6 \cdot 2\,H_2O$.

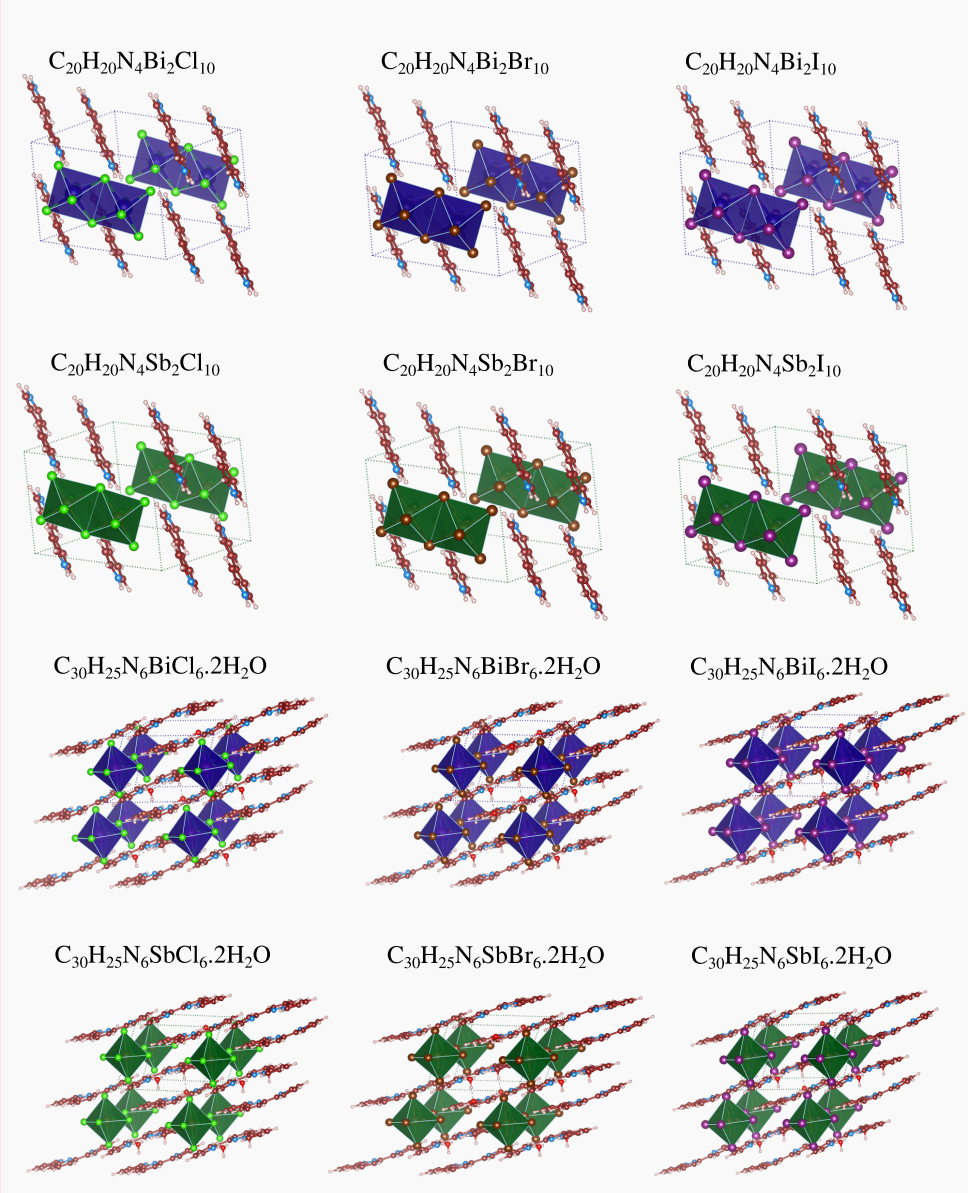

Source: Reprinted from OZÓRIO, M. S.; DIAS, A. C.; SILVEIRA, J. F. R. V.; DA SILVA, J. L. F. **The Journal of Physical Chemistry C**, v. 126, n. 16, p. 7245–7255, 2022.[2]

Figure 45 – Electron localization function of 0D perovskites: charge depletion (blue) and accumulation (red).

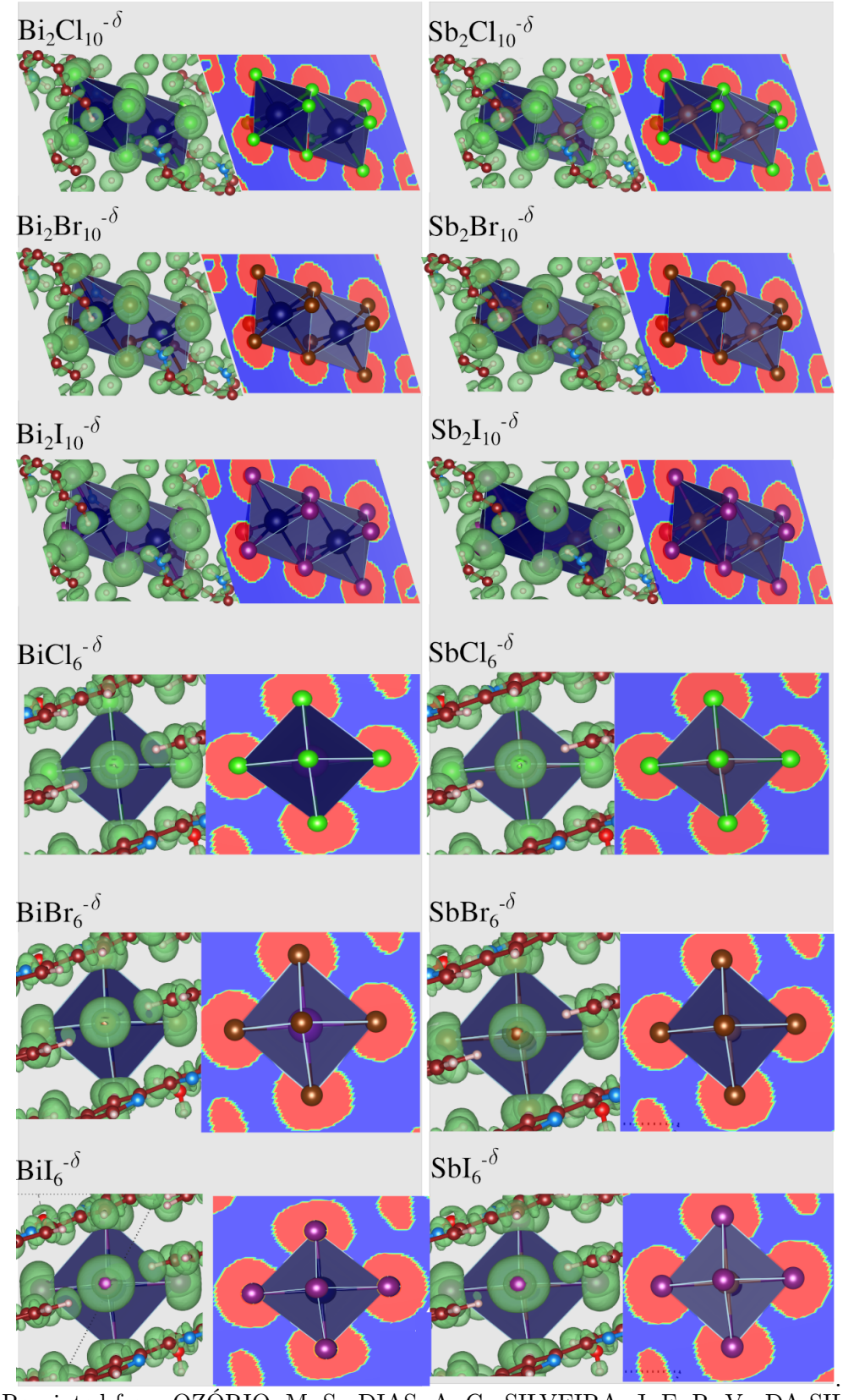

Source: Reprinted from OZÓRIO, M. S.; DIAS, A. C.; SILVEIRA, J. F. R. V.; DA SILVA, J. L. F. **The Journal of Physical Chemistry C**, v. 126, n. 16, p. 7245–7255, 2022.[2]